Precision measurements in the weak interaction framework: development of realistic simulations for the LPCTrap device installed at GANIL

X. Fabian

Université de Caen Normandie

École doctorale : SIMEM

Thèse de doctorat

Présentée et soutenue le 16 décembre 2015

par

M. Xavier Fabian

pour obtenir le

Doctorat de l'Université de Caen Normandie

Spécialité : Constituants Elémentaires et Physique Théorique

Titre :

Precision measurements in the weak interaction framework: development of realistic simulations for the LPCTrap device installed at GANIL.

Directeur de thèse : Monsieur Étienne LIÉNARD

Jury :

M Pierre DELAHAYE, Chargé de recherches, GANIL, Caen	
M Xavier FLÉCHARD, Chargé de recherches, LPC Caen, Caen	
M Stéphane GRÉVY, Directeur de recherches, CENBG, Bordeaux	*(Rapporteur)*
M Étienne LIÉNARD, Professeur des Universités, Université de Caen	*(Directeur de thèse)*
M Bernard PONS, Professeur des Universités, Université de Bordeaux I	
M Nathal SEVERIJNS, Professeur, Katholieke Universiteit, Leuven	*(Rapporteur)*

Remerciements

Tout d'abord, merci aux membres du jury pour l'apport enrichissant à ce travail en particulier à Stéphane Grévy et Nathal Severijns pour avoir acceptés d'être des rapporteurs minutieux.

Dank u Nathal Severijns and thanks to the Leuven group: Martin, Paul, Tomica, Maciek, Leendert for the stimulating discussions et en particulier à Philippe qui m'a fourni le premier TOF simulé ! Mine de rien, ce spectre symbolise beaucoup.

Merci à Bernard Pons pour sa contribution importante sur la partie atomique.

Merci au personnel du GANIL, en particulier Pierre Delahaye et Jean-Charles Thomas.

Avant de rentrer dans le détail, merci au LPC dans son ensemble qui est parfaitement représenté par son directeur, Dominique : un grand respect de la Physique à travers une humanité remarquable. Difficle d'espérer mieux pour un thésard.

Un grand merci aux permanents de GRIFON, spécialement Étienne, mon directeur de thèse officiel, et Xavier, mon directeur de thèse officieux, qui ont bien voulu m'encadrer durant trois ans. C'est grâce à votre disponibilité, votre patience et surtout votre générosité que j'y suis arrivé. Les échanges qu'on a pu avoir sur la Physique (et le reste !) m'ont énormément apporté. Je veux souligner la grande confiance que vous m'avez accordée, notamment pour aller parler de LPCTrap à l'international. Je perçois le tout comme un privilège que je n'oublierai pas.

Merci à Gilles Q. pour m'avoir permi de régler le thermostat ionique. C'était un vrai plaisir de travailler avec toi la journée et de se moquer de l'actualité le midi. Prends bien soin de Clouda ! Trugarez ha kenavo ar c'hentañ !

Merci à François M., notamment pour ta passion de la physique numérique que tu as bien voulu partager.

Merci à Aurélie, Véronique et Lydie pour votre efficacité, votre réactivité et votre gentillesse, en particulier dans les moments administrativement difficiles : l'arrivée et le départ. Pardon d'avoir été à la dernière minute sur deux ou trois choses...

Merci aux informaticiens : Yoann, Thierry, David qui doivent jongler avec un système pas toujours coopératif et des physiciens parfois capricieux (moi le premier).

Merci à mon collègue de bureau Julien Gibelin qui m'en a tant dit sur un tas de sujets, en particulier sur le métier d'enseignant-chercheur.

Merci à la Dream Team : David, Jean, Laurent et M. Carniol. Le LPC ne serait pas pareil sans le repas de Noël ou le BBQ.

Merci aux "jeunes" : Greg pour l'initiation au wake et pour la stratégie moderne qui consiste à réunir des gentlemen en cercle, Sam pour ton efficacité de dialogue d'abord et pour l'intérêt partagé du calcul parallèle ensuite. Benoît, Yves et Arnaud pour votre bonhomie singulière qui contribue beaucoup au quotidien du thésard.

Merci à tout les autres permanents avec qui j'ai pu échanger aux divers repas, cafés et pots divers, mais avec qui je n'ai pas pu travailler, à mon grand regret.

Merci à mes homologues Baptiste, Clovis, Lou, Quentin, Thibault et ceux qui m'en voudront de les oublier (le point étant que j'ai écouté Haken en buvant de l'eau) et en particulier François, Guillaume et Sylvain. Je pourrai mentionner les larmoyants et ô combien distrayants éclats du premier, les phrases plus rebondissantes que pleines de rebondissements du deuxième ou encore les goûts affolants du troisième, mais ce résumé trop succint ne leur rendrait pas justice. Je m'en voudrais d'oublier les nuits gasconne (aussi chaudes que froides), les salutations matinales curieuses ou encore les prédictions évidemment fausses de l'avenir d'un certain jeu.

Merci à ceux qui ont rendu OPTIC possible. Je pense spécialement à Germain, pas juste pour OPTIC, mais pour une vision partagée des choses.

Merci à Flora pour son engagement. À Flora et Paul pour rendre justice à la légendaire hospitalité du Sud.

Merci à Matthieu, Ingrid et surtout Claire pour m'avoir accueilli à Caen (c'est vrai que :FFFFFFFFF en fin de thèse). Même si les nouvelles se font plus rares, je te comptes désormais dans la liste restreinte de ces amis qu'on ne voit qu'une fois par an comme si on s'était quittés la veille.

Merci aux vieux amis présents à la soutenance: Priss, Charlotte, Thomas et Clément, Nico, Pierre, Rose-Marie & Ghislain. J'espère que nous réussirons à nous voir plus souvent que ces dernières années, c'est toujours un grand plaisir de partager un moment avec chacun d'entre-vous.

Merci à Filou et Aymeric, pas seulement pour les weekends décompressions nécessaires à Rennes. Pour prendre la réflexion constructive du moment, notez bien que même si vous ne reculez pas, ça ne m'empêchera pas d'en claquer.

Merci à Amandine, mon namoureuse, qui m'a apporté un soutien infaillible et permanent. C'est grâce à toi que je suis passé à travers la fin de ma thèse (en particulier), là où c'était le moins facile. Je te dois plus que je ne saurai l'exprimer. Puisse M. Poivre vivre de belles et nombreuses années.

Merci à mes parents qui m'ont toujours encouragé à faire ce que je voulais et qui le feront toujours. À ma mère qui a fait (et fait encore) le nécessaire, conjointement avec François. À mon père à qui je dois ce réflexe de questionner les choses. Ils ont, d'une manière différente, contribué à l'aboutissement de ces années d'études. J'aborde l'avenir avec sérénité grâce à cet aboutissement que je vous dois.

Finalement, Clémentine, je te souhaite d'aller où tu veux. Tu as tout le nécessaire pour y arriver et je n'ai pas de doute que ce n'est qu'une question de temps.

Contents

List of Tables

List of Figures

Introduction

Mankind formally discovered radioactivity at the end of the 19^{th} century with the work of H. Becquerel. Neither relativity nor quantum mechanics were established at the time, yet they are the theoretical tools required to understand such a phenomenon. A little more than one century later, the Higgs boson was unveiled at CERN, milestoning the modern comprehension of subatomic physics. What we know of particle physics is embedded in the so-called Standard Model (SM), divided according to the four fundamental interactions governing the universe. One of them, the Weak interaction, is responsible for the very peculiar β^- decay where a quark is spontaneously transmuted in another one, resulting in the ejection of an electron and an anti-neutrino. The mechanisms concealed behind this intriguing curiosity are complex and require the currently dedicated worldwide effort to be fully seized.

Two very different and complementary logics are being followed. On the one hand, the colossal LHC provides the required energy in its collisions to synthesize directly the possible new yet undiscovered particles. On the other hand, the low energy community performs measurements where precision is the keyword. If any new physics lies outside the SM, it is expected to manifest through extremely thin effects in the low energy context. A careful control of all possible sources of uncertainties is thus a major objective. Correlation parameters in β decay were fully formalized by J.D. Jackson *et. al.* in 1957. The present work is part of the measurement of such parameters, more specifically, of the $\beta - \nu$ angular correlation parameter $a_{\beta\nu}$. Experiments are performed where a high statistical count of observables characterizing a relevant β decay is gathered. Extracting $a_{\beta\nu}$ from such data and grasping the error on its value require the full numerical description of the experimental set-up. Therefore, a thorough simulation of all particular aspects is developed. It is only through the comparison between the experimental and simulated data that $a_{\beta\nu}$ emerges. Indeed, the basic idea is to control the value of $a_{\beta\nu}$ in the simulated data and reconstruct the exact same spectra that are experimentally obtained. When this objective is reached, a value of $a_{\beta\nu}$ is established. In the present case, the experimental observable of utmost importance is the Time-Of-Flight (TOF) of the Recoiling Ion (RI).

This work is divided in four uneven chapters. The first one grounds the theoretical landscape in which the present work belongs. A global yet swift description of the SM is given to begin with, in which are introduced the quarks, leptons, gauge bosons and the three interactions relevant to subatomic physics. A particular attention is dedicated to electromagnetism as it is not only relevant for this work in itself, it serves as an excellent transition to the Weak interaction which is built on it. This latter is then detailed in a concise way, starting with a historical perspective, to reach the correlation parameters where a particular interest lies for the present work. The state of the art is thereupon provided and shows that most of the experiments falling in the present framework are requiring the extensive control through simulation that was mentioned above. Indeed, the present precision is reaching a point where higher order contributions cannot be neglected anymore (*e.g.* order-α corrections in the β decay). Lastly, an infringement in atomic physics is done to acquaint with the Shake-Off (SO) effect.

The second chapter focuses on the experimental apparatus installed at GANIL: the LPCTrap. The used ions sources, whether online or offline, are described first. The very distinct experiments which are performed in the present context require the conversion of a continuously incoming ion beam to slowed cooled ion bunches. The required devices to perform such a task are thus detailed. Ensues the presentation of the Paul trap for which only the prepared ion bunches are suited for confinement. With trapped radioactive ions, β decay can be observed and this is done with what follows, *i.e.* the detection set-up. It is an ensemble made with the combination of a MicroChannel Plate (MCP) able to detect slowly-recoiling ions and a β telescope which is the coupling of Double Sided Stripped Silicon Detector (DSSSD) and a plastic scintillator. This experimental section ends with a review of all the experiments

performed with LPCTrap, from the first one accomplished with $^{6}He^{+}$ in 2005 to the 2012 $^{35}Ar^{+}$ dataset to the last one with $^{19}Ne^{2+}$ in 2013. A quick summary of the experimental results so far is given, including the status of $a_{\beta\nu}$ extraction and Shake-Off probabilities. An important conclusion is that two important systematic uncertainties remain: the proper modeling of the trapped ion cloud and of the β scattering.

The major chapter of this work is the third one and is dedicated to simulations. After a quick introduction, the modeling of initial decaying events in a Paul trap is detailed. The full description of the numerical β decay is provided first. It is followed by where the present effort was concentrated: The program CLOUDA for which the objective is to account for all the possible sources of uncertainty in the dynamics of the trapped ion cloud using modern Graphics Processing Units (GPU). A microscopic approach was followed where a realistic description of the confining field, the collision with the buffer gas and the space-charge due to the Coulomb repulsion (N-body effect) is achieved. CLOUDA sheds light on aspects that were not finely known and is expected to yield a better control of the relevant uncertainties. Once a decay occurs, the BAYEUX package takes over to track both the β particle and the RI in a realistic geometry. BAYEUX is a GEANT4 wrapper amongst other things and, as such, benefits from its powerful modeling of the β scattering.

The fourth and last chapter rapidly reviews the ongoing data analysis of $^{35}Ar^{+}$. The methodology around it is summarized through an estimation of the SO probabilities in the $^{35}Ar^{+}$ system with the 2012 dataset. The future of LPCTrap is finally discussed with the possible minimal upgrade or the larger project WINNINGMOTIONS in which D, yet another correlation parameter, becomes the target.

Introduction (Français)

L'humanité a formellement découvert la radioactivité à la fin du 19^e siècle à travers le travail d'H. Becquerel. À l'époque, ni la relativité ni la mécanique quantique étaient établies alors qu'il s'agit des outils théoriques nécessaires pour comprendre un tel phénomène. Un peu plus d'un siècle plus tard, le CERN confirme l'observation du boson de Higgs, couronnant notre compréhension moderne de la physique subatomique. Ce que nous savons de la physique des particules est intégré dans ce que l'on appelle le Modèle Standard (MS) qui est divisé selon les quatre interactions fondamentales qui gouvernent l'univers. L'une d'elles, l'interaction Faible, est responsable de l'étrange décroissance β^- où un quark est spontanément transmuté en un autre, résultant en l'éjection d'un électron et d'un anti-neutrino. Les mécanismes dissimulés derrière cette curiosité intriguante sont complexes et nécessitent l'effort international actuellement dédié pour être totalement compris.

Deux logiques très différentes et complémentaires sont suivies. D'une part, le gigantesque LHC fournit l'énergie nécessaire dans ses collisions pour synthétiser directement les nouvelles particules possibles qui ne sont pas encore découvertes. D'autre part, la communauté de la basse énergie effectue des mesures où la précision est le maître-mot. Si de la nouvelle physique se trouve au-delà du MS, il est attendu qu'elle se manifeste par des effets extrêmement fins dans le contexte de la basse énergie. Par conséquent, le contrôle minutieux de toutes les sources possibles d'incertitude est un objectif majeur. Les paramètres de corrélation dans la décroissance β furent entièrement formalisés par J.D. Jackson *et. al.* en 1957. Ce travail fait partie intégrante des mesures de tels paramètres et, plus spécifiquement, du paramètre de corrélation angulaire $\beta - \nu$ $a_{\beta\nu}$. Des expériences sont menées où l'idée est d'accumuler une statistique importante des observables qui caractérisent la décroissance β d'intérêt. L'extraction de $a_{\beta\nu}$ ainsi que la compréhension de l'erreur sur sa valeur nécessitent une description numérique complète du dispositif expérimental. Pour cette raison, une simulation fine comportant tous les aspects caractéristiques est développée. Une comparaison entre les données simulées et expérimentales est alors essentielle pour faire émerger la valeur de $a_{\beta\nu}$. En effet, l'idée fondamentale est de contrôler la valeur de $a_{\beta\nu}$ dans les données simulées et de reconstruire précisément les spectres expérimentaux obtenus. Lorsque cet objectif est atteint, la valeur de $a_{\beta\nu}$ est établie. Dans le cas présent, l'observable expérimentale la plus importante est le temps de vol de l'ion de recul.

Ce travail est divisé en quatre chapitres inégaux. Le premier ancre le contexte théorique auquel appartient ce travail. Une description globale mais brève est d'abord donnée dans laquelle sont introduits les quarks, les leptons, les bosons de jauge et les trois interactions d'intérêt pour la physique subatomique. Une attention particulière est dédiée à l'électromagnétisme qui non seulement présente un intérêt pour ce travail, mais qui sert également de transition vers l'interaction Faible qui fut construite dessus. Cette dernière est ensuite détaillée de manière concise en débutant par une perspective historique pour terminer avec les paramètres de corrélation où se trouve un intérêt particulier pour ce travail. L'état de l'art est alors fourni et montre que la plupart des expériences appartenant au contexte présent requièrent le contrôle étendu par simulation abordé ci-haut. En effet, la précision actuelle atteint un point où il n'est plus possible de négliger certaines contributions d'ordre supérieur. Enfin, une transgression en physique atomique est faite pour se familiariser avec l'effet Shake-Off.

Le second chapitre se concentre sur le dispositif expérimental installé au GANIL: le LPCTrap. Les sources d'ions en-ligne et hors-ligne utilisées sont d'abord décrites. Les expériences très particulières effectuées dans le présent contexte nécessitent la conversion d'un faisceau continu d'ions en paquets refroidis et ralentis. Les appareils requis pour accomplir cette tâche sont donc détaillés. S'ensuit la présentation du piège de Paul pour lequel seulement les paquets d'ions préparés sont adaptés au confinement. Les ions radioactifs désormais piégés permettent alors l'observation de décroissances β, ce qui

est accompli avec ce qui vient ensuite, *i.e.* le dispositif de détection. Il s'agit d'un tandem fait de la combinaison d'une galette à micro-canaux adaptée à la détection d'ions de recul lents et d'un télescope β qui est l'assemblage d'un silicium à piste et d'un scintillateur plastique. La section expérimentale termine avec une revue de toutes les expériences effectuées avec LPCTrap, de la première accomplie en 2005 avec l'ion $^{6}He^{+}$ jusqu'à la dernière en 2013 avec l'ion $^{19}Ne^{2+}$, en passant par l'expérience de 2012 avec l'ion $^{35}Ar^{+}$. La conclusion qui s'impose est qu'il reste deux effets systématiques importants qui ne sont pas encore maîtrisés : la modélisation correcte du nuage d'ions piégé et la diffusion du β.

Le chapitre le plus important de ce travail est le troisième et est dédié aux simulations. Après une introduction rapide, la modélisation des décroissances initiales dans le piège de Paul est détaillée. La description complète des décroissances β est fournie d'abord. Elle est suivie par là où s'est concentré ce travail: le programme Clouda dont l'objectif est l'étude de toutes les éventuelles sources d'incertitude cachées dans la dynamique du nuage d'ions piégé en s'appuyant sur des cartes graphiques (GPU) modernes. Une approche microscopique fut appliquée où une description réaliste qui comporte le champ de piégeage, les collisions avec le gaz tampon et la charge d'espace due à la répulsion coulombienne (effet à N-corps) est accomplie. Clouda met en lumière certains aspects jusqu'alors méconnus et devrait permettre un meilleur contrôle des incertitudes d'intérêt. Lorsqu'une décroissance a lieu, l'application Bayeux prend la relève pour traquer à la fois la particule β et l'ion de recul au sein d'une géométrie réaliste. Bayeux est en fait un "enveloppeur" de Geant4 entre autres choses et bénéficie ainsi de sa modélisation puissante de la diffusion des β.

Le quatrième et dernier chapitre passe rapidement en revue l'analyse des données $^{35}Ar^{+}$ qui est en cours. Sa méthodologie est résumée via l'estimation des probabilités de Shake-Off dans le système $^{35}Ar^{+}$ en utilisant le lot de données de 2012. Le futur de LPCTrap est finalement abordé, que ce soit à court terme avec une évolution minimale possible ou à plus long terme avec le projet winningmotions où D, un autre paramètre de corrélation, devient l'objectif.

Chapter 1

Context

Résumé français – Le contexte théorique dans lequel s'inscrit cette thèse est celui du modèle standard des particules. Après une brève introduction des particules élémentaires, les trois interactions d'intérêt pour la physique des particules sont présentées. L'accent est mis sur l'électromagnétisme d'abord où les idées fondamentales de l'intéraction faible sont établies. Cette dernière est ensuite détaillée de manière concise, en commençant avec une revue historique des événements marquants depuis la découverte de la radioactivité en 1896 jusqu'à la première observation du boson de Higgs en 2012. Un cheminement complet est alors suivi en partant de la règle d'or de Fermi pour aboutir à l'élément de matrice de transition nucléaire qui caractérise complètement une décroissance β en tenant compte des violations de symétries, des hélicités leptoniques observées ainsi que des différents courants faibles (pseudoscalaire, scalaire, vector, axial-vecteur et tenseur). Une section dédiée aux tests possibles de l'interaction faible est ensuite abordée. On y introduit la matrice de Cabibbo-Kobayashi-Maskawa (CKM), en particulier l'élément V_{ud}, ainsi que l'hypothèse du courant vecteur conservé (CVC). La valeur ft corrigée est alors présentée. Les paramètres de corrélation sont ensuite discutés en mettant l'accent sur le paramètre de corrélation angulaire $\beta-\nu$, $a_{\beta\nu}$. S'ensuit une revue de l'état de l'art sur, d'une part, l'existence potentielle de courants dits exotiques et, d'autre part, la valeur de V_{ud}. La conclusion est sans équivoque : il est nécessaire de contrôler de manière extrêmement fine les sources d'erreur systématiques, en particuler en utilisant des simulations de pointe. Enfin, la dernière section consiste en la présentation du phénomène de "Shake-Off" qui appartient à la physique atomique.

Contents

The theoretical framework in which this thesis is written is essentially the Standard Model of particle physics (SM). More specifically, we will focus on the weak sector of the SM through the study of the (nuclear) beta decay. A transgression in atomic physics will be made to introduce the Shake-Off (SO) effect.

1.1 Standard Model landscape

The SM strives to describe the fundamental constituents of matter and the way they interact. Satisfying the requirements of both special relativity and quantum mechanics, it correctly accounts for what we henceforth know as the electromagnetic (EM), weak and strong interactions. Although the SM is quite successful on many aspects, several phenomena are testing its limits. For instance, the mechanisms underlying quantum gravity or dark matter are still speculative. Moreover, the gravitation is by far the weakest of all interactions as its coupling constant[1] is around 10^{-39} where the three others range from 10^{-2} to 1. For these reasons, we will be neglecting gravity (but obviously not mass !). Most of the data, conventions and reasonings comes from [Beri12; BJ95; GM01; HG01].

1.1.1 Particles

Sixteen elementary "bricks" are embedded in the SM. They are divided into three categories: the gauge bosons, the quarks and the leptons. The two latter, fermion in nature, differ for one another in the way they interact. The four gauge bosons will be discussed in the next section dedicated to the interactions. Each charged particle has an associated anti-particle with the same mass and opposite charge.

1.1.1.1 Quarks

Six different quark flavors regrouped into three generations compose the quark family, namely, in ascending order of mass:

- 1^{st} generation: *up* (u) and *down* (d)
- 2^{nd} generation: *strange* (s) and *charm* (c)
- 3^{rd} generation: *bottom* (b) and *top* (t)

[1] When normalized to the strong interaction coupling constant.

Gn	Flavor	Mass	Q	T_3
1st	up	$2.3\,^{+0.7}_{-0.5}$ MeV	$+2/3$	$+1/2$
	down	$4.8\,^{+0.5}_{-0.3}$ MeV	$-1/3$	$-1/2$
2nd	charm	1.275 ± 0.025 GeV	$+2/3$	$+1/2$
	strange	95 ± 5 MeV	$-1/3$	$-1/2$
3rd	top	$173.07 \pm 0.52 \pm 0.72$ GeV	$+2/3$	$+1/2$
	bottom	4.18 ± 0.03 GeV	$-1/3$	$-1/2$

Q: EM charge - T_3: Weak isospin

Table 1.1: Quarks – the up quark has the lowest mass, explaining the amplitude of the $|V_{ud}|^2$ term discussed in section 1.2.4.1.

Gn	Flavor	Mass (MeV)	Q	L	$\mathcal{L}_e$	$\mathcal{L}_\mu$	$\mathcal{L}_\tau$
1st	e	0.510998928 (11)	-1	+1	+1	0	0
	ν_e	$< 2 \times 10^{-6}$	0	+1	+1	0	0
2nd	μ	105.6583715 (35)	-1	+1	0	+1	0
	ν_μ	$< 2 \times 10^{-6}$	0	+1	0	+1	0
3rd	τ	1776.82 (16)	-1	+1	0	0	+1
	ν_τ	$< 2 \times 10^{-6}$	0	+1	0	0	+1

Q: EM charge - L: Lepton number - T_3: Weak isospin
$\mathcal{L}_e$: Electron lepton number - $\mathcal{L}_\mu$: Muon lepton number - $\mathcal{L}_\tau$: Tau lepton number

Table 1.2: Leptons – See text for remark on the neutrino masses.

These elementary particles are subjugated to all three interactions because they are (electrically) charged, have a non-zero weak isospin and are *colored* (see section 1.1.2.1). As of today, no quark was observed in an unbound state [Beri12]. Indeed, they always form objects made of two (*mesons*) or three (*baryons*) quarks[2]. The prevalent forms of baryon in the universe are the proton (uud) and the neutron (udd). The quarks have particular quantum numbers which are important for the different conservation laws governing the possible interactions. It is important to note that the anti-quarks have the same quantum numbers, but with opposite sign. Table 1.1 sums up their features.

1.1.1.2 Leptons

The leptons are divided into three couples :

$$\begin{pmatrix} e \\ \nu_e \end{pmatrix} \begin{pmatrix} \mu \\ \nu_\mu \end{pmatrix} \begin{pmatrix} \tau \\ \nu_\tau \end{pmatrix} \tag{1.1}$$

The *electron* (e), *muon* (μ) and *tau* (τ) are massive particles with an electric charge equal to -1. They only interact through EM and weak interactions and are, just like the quarks, elementary particles without known substructure. Each of these charged leptons has an associated neutrino with a rather tiny mass. Experimental evidence interpreted with the proper theoretical model seems to point out that neutrinos do have a mass because oscillation between the different neutrino states was observed [GGMa07]. These elusive particles interact only through the W interaction (since they are both chargeless and colorless) with a very low cross section, making them amazingly hard to detect directly (see next section). Moreover, it is rather complicated to measure the mass of a single neutrino flavor since their weak interacting-states are a mixture of the three possible flavors. Exactly like the quarks, when considering the anti-leptons one needs to take the opposite sign for all the quantum numbers regrouped in table 1.2.

[2] An object made with any number of quarks is called a *hadron*.

Interaction	Coupling constant	Range (m)	Reaction time (s)	Effective strength	Gauge boson
Strong	1	10^{-15}	10^{-23}	1	gluon (g)
Weak	∼0.04	10^{-18}	$\geq 10^{-12}$	10^{-9}	$W^{\pm}$, Z^0
EM	∼0.01	∞	$\leq 10^{-16}$	10^{-2}	photon (γ)

Table 1.3: Interactions – This table is mainly adapted from [BJ95].

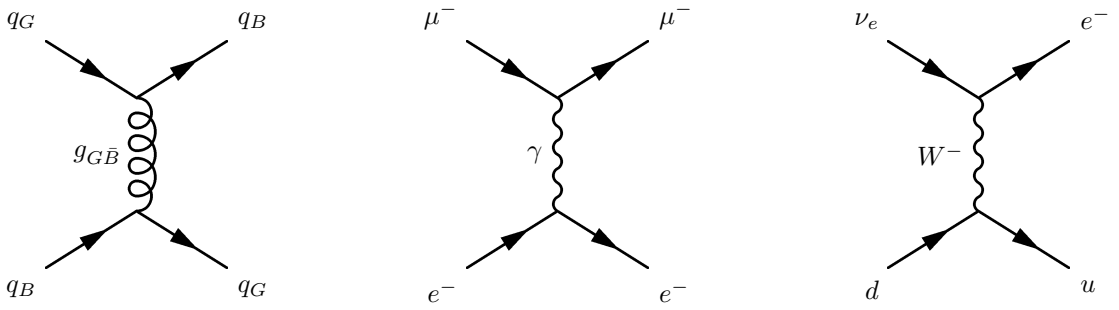

(a) Gluon exchange (b) (Virtual) photon exchange (c) (Virtual) W^- exchange

Figure 1.1: Typical Feynman diagrams for each fundamental interaction.

1.1.2 Interactions

There are three fundamental interactions through which the different particles interacts: the *electromagnetic* (EM), the *weak* and the *strong* interactions. In this work, we will be focusing on the weak interaction and since it was built with ideas coming from electromagnetism, it is useful to introduce the two of them. The strong interaction discussion will be short and is there mainly for the sake of completeness. We will be using Feynman diagrams to represent the fundamental interactions (see fig. 1.1). The relative "strength" of the different interactions are given in table 1.3 at the nuclear scope (and not the quark scope) since the couplings depend on the considered scale[3]. The four gauge bosons mentioned above are the interaction information carriers. Excepted the Higgs boson which gives particles their masses, they are all shown in the table as well.

1.1.2.1 Strong interaction

A problem rose when the Δ^{++} baryon was discovered: it was composed of three u quarks, thus violating ostensibly the Pauli exclusion principle. The idea to add a new quantum number, defined as the *color*, was then put forward to explain such an apparent contradiction. Three were defined for the quarks, namely *Red* (R), *Green* (G) and *Blue* (B) with three associated anti-colors ($\bar{R}\bar{G}\bar{B}$)[4] for the anti-quarks and the constraint that any hadron is *white* or *colorless* was established. The gauge theory studying this aspect of the SM was then named accordingly as Quantum Chromo-Dynamics (QCD). The gauge boson responsible for the information exchange in this sector is the massless gluon which carries one color and one anti-color, yielding nine possibilities :

$$R\bar{R}, R\bar{G}, R\bar{B}, G\bar{R}, G\bar{G}, G\bar{B}, B\bar{R}, B\bar{G}, B\bar{B}$$

The color wavefunctions can be linear combination of those possibilities, leading to eight actual gluons. Since these latter are colored themselves, they can interact with each other, unlike an electrically-chargeless photon carrying the EM information. The strong interaction always conserves the baryon and "sub"-baryon numbers and couples only to quarks. An example of interaction is given in figure 1.1a. A specificity of this interaction is that its related potential energy increases very rapidly with distance. A

[3] Indeed, gravitation contributes much more than the strong interaction at the galactic scale !
[4] Some authors refer to the anti-colors as *Cyan*, *Magenta* and *Yellow*.

quark and an anti-quark pair being sufficiently brought apart yields a scenario where it is more energetically favorable to break the confinement field into a new pair of anti-quark/quark. This effect, named hadronization, is believed to be the reason why quarks were always observed in bound states.

1.1.2.2 Electromagnetism

The concept of radiative correction is important in the present work and a base for the theoretical development of the *weak* interaction itself is required. This section is thus useful to introduce the fundamentals behind these ideas: We will start with familiar concepts and end up with more modern ones.

The classical electromagnetism description was fully formalized by Maxwell at the end of the 19^{th} century with its four well-known equations. In their differential form:

$$\begin{aligned} \nabla \cdot \mathbf{E} &= \frac{\rho}{\epsilon_0} \qquad & \nabla \times \mathbf{E} &= -\frac{\partial \mathbf{B}}{\partial t} \\ \nabla \cdot \mathbf{B} &= 0 \qquad & \nabla \times \mathbf{B} &= \mu_0 \left(\mathbf{j} + \epsilon_0 \frac{\partial \mathbf{E}}{\partial t} \right) \end{aligned} \tag{1.2}$$

with $\mathbf{E}$ and $\mathbf{B}$ the electric and magnetic fields, ρ and $\mathbf{j}$ the charge and current densities.

As it is detailed in [BJ95] section 8.12, one can then apply an appropriate gauge transformation with an arbitrary scalar function to the scalar and vector potentials from which the vectors $\mathbf{E}$ and $\mathbf{B}$ can be derived. Imposing the Lorenz gauge constraint will imply that the two potentials will follow the wave equations and then, by rewriting these potentials as four vectors, the initial Maxwell equations can be rewritten as:

$$\Box A_\mu = j_\mu \tag{1.3}$$

with $\Box = \partial_\mu \partial^\mu$ the D'Alembertian, $A_\mu = (\phi, \mathbf{A})$ the four-potential from which the EM fields can be derived and $j_\mu = q\bar{\Psi}\gamma_\mu\Psi$ the EM current. We will come back at this below.

The Lagrangian[5] of a spinor is defined as:

$$\mathcal{L} = i\bar{\Psi}\gamma^\mu\delta_\mu\Psi - m\bar{\Psi}\Psi \tag{1.4}$$

Imposing *local* gauge invariance to the spinor, this Lagrangian requires the introduction of the gauge covariant derivative (which will be subjected to the same transformations as the field themselves) in order to preserve gauge invariance. Such a step will yield an additional gauge field A_μ associated with the photon field. Then, by adding the kinetic energy term, one can reach the full QED[6] Lagrangian which is:

$$\mathcal{L} = \bar{\Psi}(i\gamma^\mu\partial_\mu - m)\Psi - j^\mu A_\mu - \frac{1}{4}F_{\mu\nu}F^{\mu\nu} \tag{1.5}$$

with $F_{\mu\nu} = \partial_\mu A_\nu - \partial_\nu A_\mu$ the Faraday tensor. The first term is associated to the Dirac equation for a free spin $^1/_2$ particle, the second term is the interaction between matter and the EM radiation and the third term describes the propagation of the free photon.

Restricting this Lagrangian to the terms associated to the EM field yields:

$$\mathcal{L} = -\frac{1}{4}F_{\mu\nu}F^{\mu\nu} - j^\mu A_\mu \tag{1.6}$$

We then recall the generalized Euler-Lagrange equation:

$$\frac{\partial \mathcal{L}}{\partial \phi_i} - \partial_\mu \left[\frac{\partial \mathcal{L}}{\partial(\partial_\mu \phi_i)} \right] = 0 \tag{1.7}$$

with the fields $\phi_i = f(x_1, \ldots, x_j)$.

Injecting 1.6 in 1.7 yields:

$$\partial_\mu F^{\mu\nu} = j^\nu \tag{1.8}$$

[5] The word "Lagrangian" will in fact designate the Lagrangian density $\mathcal{L}$ defined as $L = \int \mathcal{L}\, d^3x$, with L the "true" Lagrangian.

[6] Quantum ElectroDynamics

(a) 1^{st} order (b) 2^{nd} order

Figure 1.2: EM effective interactions between an electron and a proton

which are the Maxwell equations in covariant form, an expression similar to equation 1.3.

We have rewritten the well-known Maxwell equations from their *classical* differential form to a tensorial form. In parallel, with reasonings coming from *quantum* field theory, thus requiring the introduction of the Lagrangian concept, we derived an equivalent tensorial expression. This shows the elegance and power of such a formalism. As we will see in the next section, the basis of the *weak* interaction was built on this.

Fine structure constant and higher order contributions Using the second term in expression 1.5, one can compute the matrix element of the processes shown in fig. 1.2. At first order, the interaction between an electron and a proton is done through a single virtual photon. During this exchange, it is possible for this photon to form a virtual electron-positron pair such as in the 2^{nd} order diagram. We showed here only two examples of Feynman diagrams, but one could imagine a multitude of higher order processes, for instance the self-interaction of an electron with itself through another virtual photon and so on. In Feynman diagrams, each vertex is associated with a coupling constant which depends on the specific interaction. In the QED case, the well-known fine structure constant takes this role:

$$\alpha = \frac{e^2}{4\pi\varepsilon_0\hbar c} \simeq \frac{1}{137} \tag{1.9}$$

Furthermore, α shows a very interesting peculiarity: it is universal, meaning that the EM interaction is governed by some intrinsic coupling strength which is the same for all charged particles, regardless of its nature. Since $\alpha \ll 1$, summing up higher order contribution (α^n) is not an issue since it does not require renormalization and can thus be done perturbatively. We will come back to this in section 1.2.4.3, when approaching the corrected $\mathcal{F}$t values.

1.2 Weak interaction

Among the three fundamental interactions relevant to particle and nuclear physics, the *weak* one is the most elusive. It does not form bound states such as the *strong* interaction's baryon or the EM's atom. Its Z^0 gauge bosons are EM-neutral unlike the charged $W^{\pm}$. It is actually pretty hard to picture because there is no analogy possible with our daily existence. Let us start off with a brief history which might give us an overall view of it then we will jump in the heart of things.

1.2.1 Historical perspective

1896 H. Becquerel explains that *phosphorescent substances* like uranium salts ($K(UO)SO_4$) are able to mark a photographic plate protected by black fabric and even thin layers of metal [Bec96b]. During the same year, he finds out that these substances are not phosphorescent because they do not need to be exposed to sunlight to emit their own radiation: Radioactivity is discovered [Bec96a].

1897 J.J. Thomson presents an experiment where he finds evidence that *cathode rays*, or electric discharges, are probably carried by corpuscules, with a specific $\frac{m}{q}$ ratio that he measures, rather than being solely aetherial: Electrons are discovered [Thom97].

1899 E. Rutherford classifies the different kinds of radiation according to their penetrating power. α particles penetrate less than β particles [Ruth99]. Later that year, he performed quantitative measurements and found out that the $\frac{m}{q}$ ratio of the β particles was the same that what Thomson found two years earlier: β particles are, in fact, electrons.

1914 J. Chadwick shows that the β particle energy spectrum is continuous. At the time, this is a major issue because β decay involves only two bodies [CJ14]. Some people even propose to revise energy conservation.

1928 P.A.M. Dirac derives the first relativistic quantum wave equation for the electron [Dira28]. It is in this period that Dirac, Heisenberg and Pauli develop a complete *quantum field theory* which unites quantum mechanics and relativity and is applicable to all fundamental interactions.

1930 W. Pauli sends an open letter to "the group of radioactive people at the Gauverein meeting in Tübingen" stating that a *neutron* may be emitted during β decay, making it a three-body process and preserving energy conservation. As he said himself, this was an *almost improbable remedy*, but still, why not consider it. This *neutron* should have a mass between that of an electron and 1% of the proton mass, travel slower than the speed of light and be a fermion. Pauli actually postulated the existence of the neutrino[7] for the first time [Paul30].

1932 J. Chadwick wraps up evidence available at the time and provides insights to testify the existence of another nucleon: the *neutron* (the modern one this time). He suggests that the neutron is composed of a proton and an electron since its mass is between 1.005 m_p and 1.008 m_p [CJ32]. Later that year, Heisenberg presents a new nucleus formed only by protons and neutrons [Heis32]. In the very same year, C. D. Anderson observes antimatter for the first time through the detection of positrons [Ande33], granting him half the Nobel Prize of 1936.

1934 E. Fermi establishes a complete theory for the β decay which includes Pauli's "neutron". In his work, he uses analogies with electromagnetism, treating the relevant particles just like photons emitted from atoms. As far as experimental evidence available at the time is concerned, this theory accounts for the observed β energy spectra. It has a powerful predicting potential, foreseeing, for instance, the possibility of electron capture. This could be considered the first Weak interaction theory [Ferm34][8].

[7] From [Amal84], p.306:

> The name "neutrino" (a funny and grammatically incorrect contraction of "little neutron" in Italian: neutronino) entered the international terminology through Fermi, who started to use it sometime between the conference in Paris in July 1932 and the Solvay Conference in October 1933 where Pauli used it. The word came out in a humorous conversation at the Istituto di Via Panisperna. Fermi, Amaldi and a few others were present and Fermi was explaining Pauli's hypothesis about his "light neutron". For distinguishing this particle from the Chadwick neutron Amaldi jokingly used this funny name, – says Occhialini, who recalls of having shortly later told around this little story in Cambridge.

[8] Translated and commented in [Wils68].

1937 S.H. Neddermeyer and C.D. Anderson observe a particle that is less massive than a proton, more massive than an electron and behaves like an electron. The muon is discovered. [NA37]

Late 1940s Feynman, Tomonaga, Schwinger and Dyson developed independently what we henceforth know as the Quantum ElectroDynamics[9], which was the first quantum *gauge* field theory. All the following work on gauge field theories were based on what was done for QED.

1953 F. Reines and C.L. Cowan detect neutrinos for the first time through the detection in coincidence of a neutron and a positron coming from an inverse β decay reaction [ReCo53].

1956 T.D. Lee and C.N. Yang outline that although parity conservation was observed in strong and EM interactions, it was not tested for weak interactions. They express a few experimental ideas which might test such a conservation [LY56].

1957 C.S. Wu *et al.* performed a parity conservation test through the observation of polarized ^{60}Co β decay. They found an important asymmetry in the counting rate of βs with respect to the nuclei orientation, detectors position and to the de-polarizing time: Parity is discovered to be highly violated, if not maximally [Wu57].

1958 E.C.G. Sudarshan and R.E. Marshak [SM58] and independently R.P. Feynman and M. Gell-Mann [FGM58] review the experimental evidence available at the time and suggest that, except for a few experiments which could be wrong, the so-called universal Fermi interaction is most probably Vector and Axial-Vector, thus setting aside the Scalar and Tensor currents. Moreover, the discovery of C.S. Wu *et al.* is followed by intense research to understand the fundamental nature of the Weak interaction. As an example, M. Goldhaber *et al.* set up an experiment to check the neutrinos helicity using polarized Eu^{152}. They conclude that the Gamow-Teller transitions, that is with a final spin triplet state, are of an Axial-Vector nature [GGS58].

1961 S.L. Glashow publishes the first work that formalizes the ressemblances between the weak and EM interactions [Glas61] through the introduction of the relevant gauge bosons (from fig. 1.3a to 1.3b). This could be considered the premises of the SM.

1963 N. Cabibbo introduces the angle which now bears his name as an assumption on J_μ, the "weak current of strong interacting particles" [Cabi63]. In the same year, a precise measurement of the $\beta - \nu$ angular correlation parameter $a_{\beta\nu}$ is performed by C. H. Johnson, F. Pleasonton and T. A. Carlson in the decay of ^{6}He$^+$ [JPC63].

1964 G. Zweig establishes the *aces* model (now named *quarks*) [Zwei64]. Three of them should account for all the particles discovered at the time, namely the u, d and s. In the same year, J. W. Cronin and V. L. Fitch discover evidence of indirect CP-violation awarding them the 1980 Nobel prize [CJH64].

1970 S. L. Glashow, J. Iliopoulos and L. Maiani predict the existence of a fourth quark [GIM70].

1972 M. Kobayashi and T. Maskawa shows that CP-Violation requires the introduction of other new quark fields and establish what we henceforth know as the Cabibbo-Kobayashi-Maskawa (CKM) matrix which includes three quark generations [KM73].

1975 Electron-positron annihilation were observed to populate an exit channel made of an electron, a muon and missing energy. This is, in fact, the first observation of the τ lepton [Perl75]. The same year, the teams of B. Richter and S.C.C. Ting observed independently the J/Ψ for the first time, thus discovering the *charm* quark [Augu74; Aube74]

1977 S.W. Herb *et al.* discover the bottom quark [Herb77].

1983 As the accelerators technology evolves, the available energy to perform experiments reaches the mass of the different gauge bosons of the Weak interaction, namely the W^-, the W^+ and the Z^0. The Super Proton Synchrotron (SPS) built at CERN was the machine used to discover these bosons. In 1984, the two main team leaders, C. Rubbia and S. van der Meer were awarded the Nobel prize for this discovery.

1995 First observation of the top quark at Fermilab [Abea95].

[9] Feynman, Tomonaga and Schwinger were jointly awarded the Nobel Prize in 1965 "for their fundamental work in quantum electrodynamics, with deep-ploughing consequences for the physics of elementary particles" [FN65].

1998 The Super Kamiokande collaboration published evidence of neutrino oscillations [Fuku98]. This was confirmed by another experiment that took place at SNO[10] [Ahma01]. T. Kajita and A.B. McDonald were conjointly awarded the 2015 Nobel prize for the discovery of neutrino oscillations.

2012 The Higgs boson was discovered, as announced conjointly by the CMS and ATLAS collaborations at CERN [Chat12; Aad12].

1.2.2 Application of the Fermi theory to nuclear β decay

In order to assess it, we need to reach a full theoretical description of the (nuclear) β decay. We will start with what Fermi had done in 1934, when he established a first complete description of such a phenomenon. This will be followed by the inclusion of adjustements required by the ever-accumulating experimental evidence. As an example, the maximal parity violation, discovered in 1957, is now embedded in the formal description of a β decay. This process will end with the expression of the V-A theory.

1.2.2.1 Fermi golden rule

Perturbation theory is applicable in the case of a nuclear β transition since the implied weak interaction is characterized by a weak coupling constant. Defining λ as a transition probability between two given states, $\mathcal{M}_{fi}$ as the transition matrix element between the two same states and $\frac{dN}{dE_0}$ as the density of final states per energy unit, the Fermi golden rule states that:

$$\lambda = \frac{2\pi}{\hbar}|\mathcal{M}_{fi}|^2 \frac{dN}{dE_0} \tag{1.10}$$

This equation summarizes, more or less, all one needs to know about β decay. Looking quite simple, it is in the details that complications and stakes rise. Let us first take a closer look at the term $\mathcal{M}_{fi}$. As said above, it is a transition matrix element that could be defined, using the Dirac formalism, as:

$$\mathcal{M}_{fi} = \langle \bar{f} | \mathcal{H} | i \rangle \tag{1.11}$$

with $|i\rangle$ the initial state, $\mathcal{H}$ the Hamiltonian of such a transition, which is the key term here as we will see below, and $\langle \bar{f}|$ the final state.

The initial state is a specific nuclear state with a given parity and spin. In this initial nucleus, a neutron transforms into a proton and two leptons: an electron (the so-called β particle) and an electronic anti-neutrino. The final state is the group formed by these two leptons and the new nucleus which has one more proton and one less neutron. This last sentence describes the β^- decay and reversing the words "proton" and "neutron" from it describes the β^+ decay. In fact we will only refer to the β^- decay as of now and assert that the β^+ decay is nothing more than the Hermitian conjugate of the former.

Depending on the relative spin orientation of the emitted leptons, the daughter nuclear state has either changed its spin or not when compared to the initial nuclear state. The former case is known as a Gamow-Teller (GT) transition while the latter is named a Fermi transition (F). In the case of a mixed transition, the mixing ratio ρ between the F and GT components is yet another important observable.

The derivation of the final states density is done in *e.g.* [LiUH10]. Considering a β with a momentum between p_e and $p_e + dp_e$ we have:

$$\frac{dN}{dE_0} = \frac{2\pi V^2}{c^3 h^6} p_e^2 (E_0 - E_e) \sin\theta dp_e d\theta d\Omega_e \tag{1.12}$$

with V a normalization volume, E_0 the total available energy for the decay, E_e the β energy, θ the angle between the leptons and Ω_e the solid angle covered by the β.

1.2.2.2 Weak Hamiltonian

We saw in equation 1.5 that the term $j^\mu A_\mu$ embodies the interaction between matter and EM radiation. Moreover, the Maxwell equations 1.3, $\Box A_\mu = j_\mu$, give us a correspondance between the EM current and

[10] Sudbury Neutrino Observatory

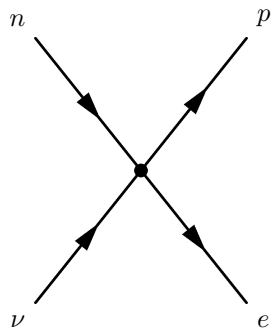

(a) Point-like β^- decay

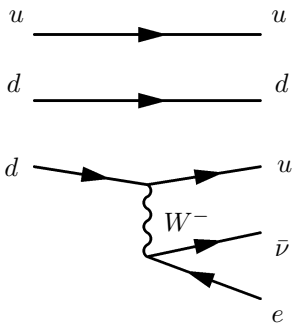

(b) β^- decay with propagator

Figure 1.3: *Weak* effective interactions

the four-potential. This leads us to write the matrix element of this current-current interaction shown in fig. 1.2a:

$$\mathcal{M}_{fi} \simeq j^\mu A_\mu \simeq -\frac{1}{q^2} j_\mu(e) j^\mu(p) \tag{1.13}$$

with $j_\mu(e) = \bar{u}_e \gamma_\mu u_e$ the electron current, $j^\mu(p) = \bar{u}_p \gamma^\mu u_e$ the proton current and -1/q^2 the photon propagator term. Fermi originally saw that the interactions pictured in fig. 1.2a and fig. 1.3a were pretty much alike[11]. As we said above, nuclear β decay occurs at low energies (few MeVs) comparing to the mass of the W boson (∼80 GeV). This justifies the fact that we do not need to explicit the propagator term in the expression of the matrix element as it is done in fig. 1.3b. In other words, we will assume the nuclear β decay to be pointlike. The exiting anti-neutrino will also be considered an entering neutrino in the appropriate Feynman diagram. Fermi then replaced respectively the proton current and the electron current with a hadron current $j^\mu(h) = \bar{u}_n \gamma^\mu u_p$ and a lepton current $j_\mu(l) = \bar{u}_\nu \gamma_\mu u_e$ and changed the EM fine structure constant for a *weak* coupling constant $\mathcal{G}$ (which we will discuss later) [Ferm34]:

$$\mathcal{M}_{fi} = \mathcal{G} j_\mu(l) j^\mu(h) \tag{1.14}$$

This *weak* matrix element is usually named the general hamiltonian density of the β decay.

[11] Of course, the Feynman diagrams were still not invented at the time: Feynman himself was only 15 years old!

Operator	Definition
Scalar	1
Vector	γ_μ
Tensor	$\sigma_{\mu\nu} = \frac{i}{2}[\gamma_\mu, \gamma_\nu]$
Axial-vector	$\gamma_5\gamma_\mu$
Pseudoscalar	γ_5

Table 1.4: Mathematically possible operators in weak currents.

1.2.3 Towards a general description

We will now use equation 1.14 as our entry point to reach a general expression where all observed experimental features are accounted for.

1.2.3.1 Operator generalization

In each current j_μ of equation 1.14, the operator between the initial and final state is γ^μ. This operator is vector in nature, but any combination of the five γ matrices which covers exhaustively the possible behavior under a Lorentz transformation coupled with a Parity transformation is mathematically acceptable. O_i will designate such operators with i belonging to {S,V,T,A,P}. These letters stand respectively for Scalar, Vector, Tensor, Axial-vector and Pseudoscalar and each one behaves differently under the combined Lorentz and Parity transformations. They are defined in table 1.4. Including all possibilities and expliciting the currents, equation 1.14 becomes:

$$\mathcal{M}_{fi} = \mathcal{G} \sum_i C_i (\bar{u}_\nu O_i u_e)(\bar{u}_n O^i u_p) \tag{1.15}$$

with C_i the coupling constant weighting the contribution of each operator.

1.2.3.2 Symmetries violation

Fermi established his theory in 1934 [Ferm34] and for more than two decades it worked nicely, until Wu *et al.* discovered evidence to maximal parity violation in 1957 [Wu57]. This kind of symmetry feature needs to be included in the matrix element we are computing. The way to perform this is to add a pseudoscalar term (γ_5) which exhibits the behavior we are looking for under the parity transformation. Weighting this new term with a coupling constant C_i', our matrix element turns into:

$$\mathcal{M}_{fi} = \mathcal{G} \sum_i C_i \left(\bar{u}_\nu O_i \left(1 + \frac{C_i'}{C_i} \gamma_5 \right) u_e \right) (\bar{u}_n O^i u_p) \tag{1.16}$$

Putting constraints on C_i and C_i' enables to embed the symmetry features of this matrix element. For instance, C-symmetry happens when C_i are real and C_i' are purely imaginary, maximal P-symmetry violation is accounted for if $|C_i| = |C_i'|$ and T-symmetry invariance is ensured if both coupling constants are real. Thus, our matrix element transforms to:

$$\mathcal{M}_{fi} = \mathcal{G} \sum_i C_i \left(\bar{u}_\nu O_i \left(1 \pm \gamma_5 \right) u_e \right) (\bar{u}_n O^i u_p) \tag{1.17}$$

1.2.3.3 Handedness

At this point, it is useful to introduce the notion of *helicity* which is defined as the projection of the spin direction on the momentum direction. It is equal to 1 (-1) when the spin and the momentum are parallel (anti-parallel). We thus say that the considered particle is *right-handed*/RH (*left-handed*/LH). If we consider u and v to be a particle spinor and an anti-particle spinor, respectively, the operators $\frac{1}{2}(1 \pm \gamma^5)$ project the handedness[12] of that particle in the following way:

$$\frac{1}{2}(1 + \gamma^5)u = u_R \qquad \frac{1}{2}(1 - \gamma^5)u = u_L \tag{1.18}$$

[12] This holds true when the γ matrices are chosen in the Weyl basis.

$$\frac{1}{2}(1+\gamma^5)v = v_L \qquad \frac{1}{2}(1-\gamma^5)v = v_R \tag{1.19}$$

Experimental evidence showed that neutrinos and anti-neutrinos are respectively LH and RH. We will then only keep the negative part in the helicity operator projection of our matrix element which therefore becomes:

$$\mathcal{M}_{fi} = \mathcal{G}\sum_i C_i \left(\bar{u}_\nu O_i \left(1-\gamma_5\right) u_e\right)\left(\bar{u}_n O^i u_p\right) \tag{1.20}$$

1.2.3.4 V-A theory

We will now discriminate among the possible operators we found out in 1.2.3.1. The easiest one is O_P which vanishes in a non relativistic approximation. The remaining four terms can be divided into two categories. Axial-vector and Tensor couplings allow a spin change, ergo, they are associated to Gamow-Teller (GT) transitions whereas Vector and Scalar couplings do not allow a spin change and are thus associated to Fermi transitions. Experimental evidence showed that both the Scalar and the Tensor couplings are tiny, if there are any [SNC11]. This lead to the elaboration of the V-A theory in which $C_S = C_T = 0$ (and $C_A/C_V < 0$):

$$\mathcal{M}_{fi} = \mathcal{G}C_V \left(\bar{u}_\nu \gamma_\mu \left(1-\gamma_5\right) u_e\right)\left(\bar{u}_n \gamma^\mu u_p\right) + \mathcal{G}C_A \left(\bar{u}_\nu \gamma_5 \gamma_\mu \left(1-\gamma_5\right) u_e\right)\left(\bar{u}_n \gamma^5 \gamma^\mu u_p\right) \tag{1.21}$$

In order to simplify and explicit the F and GT parts, one can rewrite this expression in the following manner:

$$|\mathcal{M}_{fi}|^2 = C_V^2 |M_F|^2 + C_A^2 |M_{GT}|^2 \tag{1.22}$$

where C_V and C_A are now expressed in $\mathcal{G}$ units. This expression will be useful later.

1.2.4 Testing the Weak interaction

This section is dedicated to the ways experiments can test the weak interaction. Although there are many possibilities, we will focus on what can be done with the LPCTrap experiments. Indeed, through our measurement of $a_{\beta\nu}$, which we will be presenting below, either a test of the exotic current existence or of the unitarity of the CKM matrix (defined below) can be performed.

1.2.4.1 CKM Matrix

Quarks *weak* eigenstates differ from their mass eigenstates. In a way, a β decay is the transformation of an up-type quark mass-eigenstate to a down-type quark weak-eigenstate[13] which is then projected in the down-type quark mass-eigenstates space, resulting in any of the three possible down-type mass-eigenstate with a probability closely tied to the relevant elements of a particular matrix. Noting q_W and q_m the weak and mass eigenstates, the following relation holds:

$$\begin{pmatrix} d_W \\ s_W \\ b_W \end{pmatrix} = \begin{pmatrix} V_{ud} & V_{us} & V_{ub} \\ V_{cd} & V_{cs} & V_{cb} \\ V_{td} & V_{ts} & V_{tb} \end{pmatrix} \begin{pmatrix} d_m \\ s_m \\ b_m \end{pmatrix} \tag{1.23}$$

Where the central matrix is the Cabibbo-Kobayashi-Maskawa (CKM) matrix. The Particle Data Group recommends the following values [O14]:

$$V_{CKM} = \begin{pmatrix} 0.97427 \pm 0.00014 & 0.22536 \pm 0.00061 & 0.00355 \pm 0.00015 \\ 0.22522 \pm 0.00061 & 0.97343 \pm 0.00015 & 0.04140 \pm 0.00120 \\ 0.00886^{+0.00033}_{-0.00032} & 0.0405^{+0.0011}_{-0.0012} & 0.99914 \pm 0.00005 \end{pmatrix} \tag{1.24}$$

[13] Flavor-Changing Neutral Current (FCNC) are supposed inexistant in the frame of this work, thus, quarks undergoing a β decay may transform only to the other-type quark, *i.e.* a up-type to a down-type or vice-versa.

The unitarity requirement of the CKM matrix is an important problematic since any disparity could lead to new physics [HT15]. The most useful data linked to this allows to check that:

$$|V_{ud}|^2 + |V_{us}|^2 + |V_{ub}|^2 = 1 \tag{1.25}$$

Since V_{ud} is the most contributing term, a good precision on it is crucial.

1.2.4.2 CVC hypothesis

We now take a closer look at $\mathcal{G}$, the weak coupling constant. A measurement in the case of the purely leptonic decay of the muon yielded $\mathcal{G} \simeq 0.89619 \times 10^{-4}$ MeV.fm^3. In nuclear β decay, this value is $C_V\mathcal{G} \simeq 0.88526 \times 10^{-4}$ MeV.fm^3. These values are quite similar and suggest that even for different decay types, some universal *weak* constant governs the amplitude of the decay rate as it is the case in the EM interaction with the constant α. The nuclear scenario has an important specificity: It is not purely leptonic and the hadronic part of it, that is the quark transmutation, implies that one needs to include a specific factor linked to the existence of the quark generation themselves. This factor is in fact V_{ud} and was introduced in section 1.2.4.1.

Another hint advocates the path to a universal *weak* coupling constant. A proton in some nuclear medium may emit virtual pions. Consequently, one expects nuclear β decay to be altered because such higher order Feynman diagrams exists. It happens that it is not the case, *i.e.* the proton *weak* charge is not renormalized because of such processes, as it was validated by measurements done in the case of non-virtual pions (see [BJ95], section 11.7).

We thus call the Conserved Vector Current (CVC) hypothesis the assumption that in Vector-type interactions the same coupling rests underneath [FGM58]. Using the above notation (eq. 1.22), this means that:

$$C_V = \mathcal{G}V_{ud} \tag{1.26}$$

Precisely measuring V_{ud} in different decays is consequently a way to test the CVC hypothesis.

1.2.4.3 $\mathcal{F}t$

$\mathcal{F}t$, the corrected ft value[14] is classically extracted in the superallowed pure Fermi decay ($0^+ \rightarrow 0^+$) through:

$$\mathcal{F}t = ft(1+\delta'_R)(1+\delta_{NS}-\delta_C) = \frac{K}{\mathcal{G}^2 V_{ud}^2 (1+\Delta_R^V)} \tag{1.27}$$

- $\mathcal{F}t$ is expected to be a unique value for all such transitions.
- δ_i and Δ_R^V are correction terms which are discussed below.
- K regroups fundamental constants [Beri12]:

$$K = \frac{2\pi \ln(2) \hbar^7 c^6}{(m_e c^2)^5} = 8120.2776(9) \times 10^{-10} GeV^{-4} s \tag{1.28}$$

- $\mathcal{G}$ is the universal *weak* constant.
- V_{ud}, described in the last section, appears explicitly here.

The objective here is to reach V_{ud}, thus one needs to know all the other quantities with the greater possible precision. We will give some more details on the superallowed pure Fermi decays in section 1.3. The experiments around LPCTrap were done with quite different nuclei. One can take advantage of mirror nuclei undergoing mixed (GT/F) transitions between $T = 1/2$ isospin doublets to obtain $\mathcal{F}t$, the corrected ft value [Sev14a; NS09]. In such a case, expression 1.27 becomes:

$$\mathcal{F}t = ft(1+\delta'_R)(1+\delta_{NS}-\delta_C)[1+(f_A/f_V)\rho^2] = \frac{K}{\mathcal{G}^2 V_{ud}^2 (1+\Delta_R^V)} \tag{1.29}$$

where a few terms have been added, namely:

[14] This value is usually presented as $\log ft = \log f + \log t$, where f is associated to theoretical calculations (Fermi function) while t is linked to specific nuclear data of a given nucleus.

- f_A/f_V is the ratio to account for the slight discrepancy in the statistical rate function between F and GT transitions.
- ρ is the GT to F mixing ratio.

Once again, we are interested in V_{ud}. The relevant nuclear data (mass, halflife, branching ratio) is known with a better precision than the mixing ratio ρ, which is thus the greatest source of (statistical) uncertainty [Sev14a]. As we will see in section 1.2.4.4, this is where $a_{\beta\nu}$, the β-ν angular correlation parameter, may play a role.

Now, regarding the correction terms (computed in [Seve08] for the mirror transitions):

- δ'_R and Δ^V_R are pure QED corrections [MS06]. Can go up to ∼1.5%.
- δ_{NS} is a nuclear structure correction.
- δ_C is the isospin symmetry breaking correction, usually computed from shell-model calculations [TH08], although other approaches exist [LVGM10] [Auer09]. Combined with δ_{NS}, they can have a contribution in 0.3% – 1.5%.

1.2.4.4 Correlation parameters

In 1957, using natural units ($c = \hbar = 1$), Jackson *et al.* developped an expression for the angular distribution of the electron and neutrino as a function of the coupling constants C_i and kinematic quantities [JTW57a; JTW57b]. For unoriented nuclei and including Coulomb corrections to order α, we have:

$$\omega(\sigma|E_e,\Omega_e,\Omega_\nu)dE_e d\Omega_e d\Omega_\nu = \frac{F(\pm Z,E_e)}{(2\pi)^5} p_e E_e (E^0-E_e)^2 dE_e d\Omega_e d\Omega_\nu \frac{1}{2}\xi\left\{1 + a\frac{\mathbf{p_e}\cdot\mathbf{p}_\nu}{E_e E_\nu} + b\frac{m_e}{E_e} + [\ldots]\right\} \quad (1.30)$$

where the subscripts e and ν are associated to the electron and the neutrino, p and E are momentum and energy. $F(\pm Z, E_e)$ is the Fermi function. $a = a_{\beta\nu}$ is called the β-ν angular correlation parameter and b the Fierz interference term. The coupling constants are regrouped in $a_{\beta\nu}$ and b in the following manner:

$$a\xi = |M_F|^2\Big(-|C_S|^2+|C_V|^2-|C'_S|^2+|C'_V|^2 \mp \frac{\alpha Z m}{p_e} 2\Im(C_S C_V * + C'_S C'_V *)\Big) + \frac{|M_{GT}|^2}{3}\Big(|C_T|^2-|C_A|^2+|C'_T|^2-|C'_A|^2 \pm \frac{\alpha Z m}{p_e} 2\Im(C_T C_A * + C'_T C'_A *)\Big) \quad (1.31)$$

$$b\xi = \pm 2Re\Big[|M_F|^2(C_S C_V^* + C'_S C'^*_V) + |M_{GT}|^2(C_T C_A^* + C'_T C'^*_A)\Big] \quad (1.32)$$

with ξ defined as:

$$\xi = |M_F|^2\Big(|C_S|^2+|C_V|^2+|C'_S|^2+|C'_V|^2\Big) + |M_{GT}|^2\Big(|C_T|^2+|C_A|^2+|C'_T|^2+|C'_A|^2\Big) \quad (1.33)$$

Other correlation parameters exist as we will see in the next section. For pure currents, $a_{\beta\nu}$ takes the values presented in table 1.5. As we illustrate in fig. 1.4a and 1.4b, the shape of the Recoil Ion (RI) momentum distribution following a nuclear β decay depends on the value of $a_{\beta\nu}$. In the LPCTrap case, we actually measure the TOF for multiple nuclei (see sections 3.2.1 and 2.4).

It is worth noting that, experimentally, $a_{\beta\nu}$ is not measured directly and alone. Indeed, the Fierz interference term, b, has an effect on the observed kinematics. Detecting the β particle makes us dependent on this term in the following manner:

$$\tilde{a} = \frac{a_{\beta\nu}}{1 + b\frac{m_e}{E_e}} \quad (1.34)$$

Although this is inexact, we will be referring to $\tilde{a}$ in this document when evoking $a_{\beta\nu}$.

Current	$a_{\beta\nu}$ value
Vector (SM, F)	+1
Axial-vector (SM, GT)	-1/3
Scalar (Exotic, F)	-1
Tensor (Exotic, GT)	+1/3

Table 1.5: $a_{\beta\nu}$ values

Extracting a precise value of $a_{\beta\nu}$ is very useful since it allows to check either of two hypothesis.

Hypothesis 1 (V_{ud}) V-A theory is true, *i.e.* there are no exotic currents. Thus, the following relation holds:

$$a_{\beta\nu} = \frac{1-\rho^2/3}{1+\rho^2} \tag{1.35}$$

$a_{\beta\nu}$ is then extracted from the TOF data and considered to be the SM value. This yields an experimental value for ρ which contributes to the global dataset mentioned in section 1.2.4.3. Consequently, it serves the purpose of testing the unitarity of the CKM matrix through V_{ud}.

Hypothesis 2 (Exotic currents) For mixed mirror transitions, we consider the value of V_{ud} recommended by the PDG[15] to be the SM value. Combined with other nuclear data, one can then compute a mixing ratio ρ which yields a "SM value" for $a_{\beta\nu}$. It is then possible to compare this latter value with the one extracted from the TOF spectrum. Any deviations would suggest the existence of non-SM coupling, namely Tensor for GT transitions or Scalar for F transitions.

Pure transitions, either of F or GT nature, are nevertheless better suited to constrain one specific exotic current. These transitions are characterized by the disappearance of either the $|M_F|^2$ or $|M_{GT}|^2$ term in equation 1.31, allowing to choose what exotic current to focus on.

[15] Particle Data Group

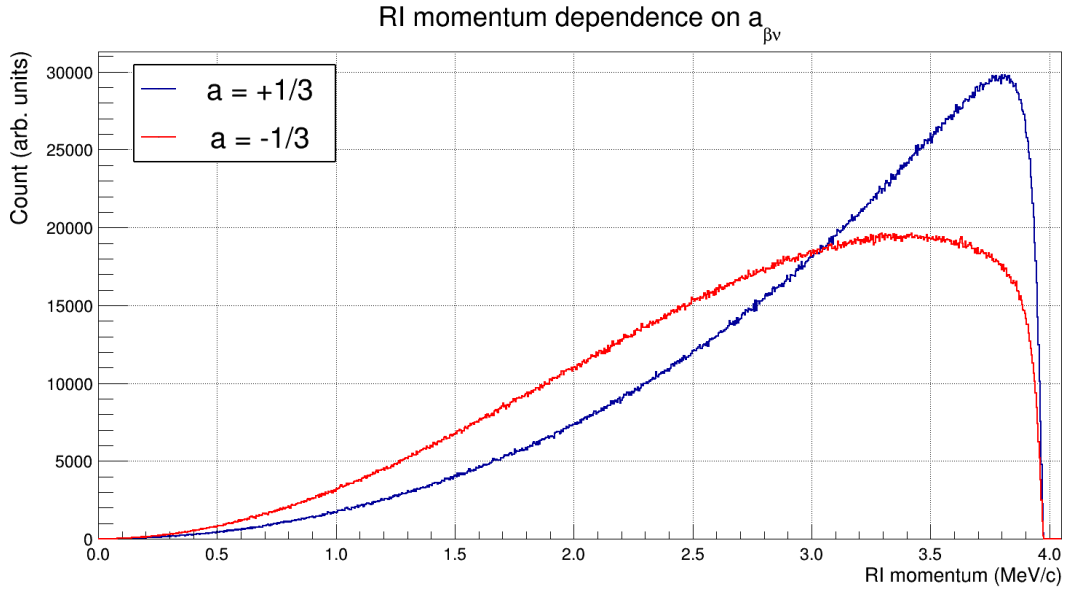

(a) RI momentum distribution following the GT transitions in the decay of $^{6}He^{+}$.
Axial: $a_{\beta\nu}= -\frac{1}{3}$ & Tensor: $a_{\beta\nu}= \frac{1}{3}$. The SM states that the tensor current is nil (V-A theory).

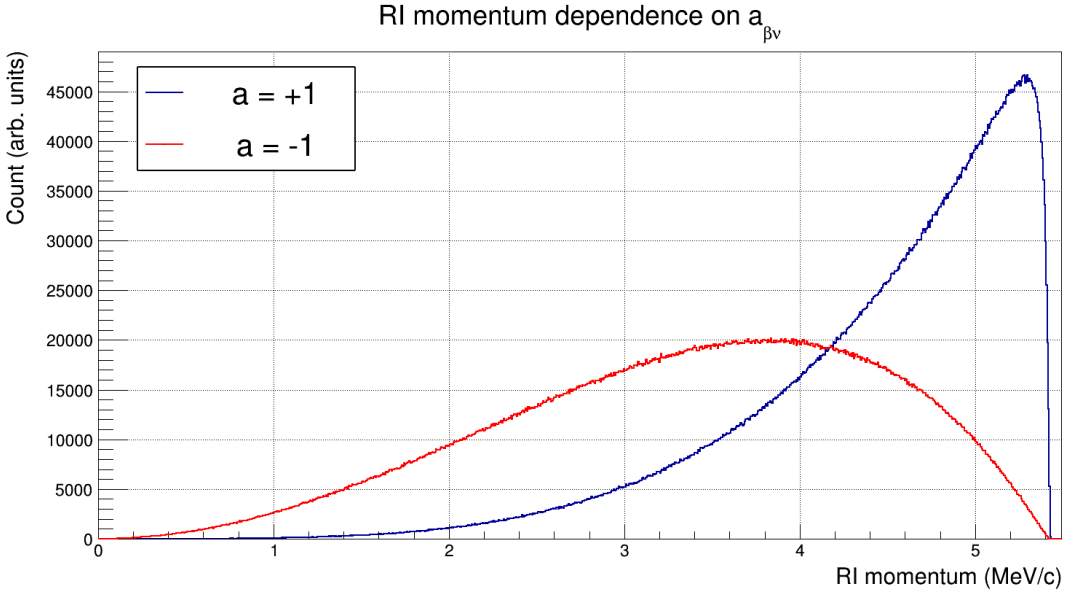

(b) RI momentum distribution following the F transitions in the decay of $^{35}Ar^{+}$.
Vector: $a_{\beta\nu}= 1$ & Scalar: $a_{\beta\nu}= -1$. The SM states that the scalar current is nil (V-A theory).

Figure 1.4: RI momentum distributions following GT & F transitions.

1.3 State of the Art

The LPCTrap experiments, which the present work is part of, are based on the detection in coincidence of the decay products following a nuclear β transition. The decaying nuclei are confined in a Paul trap. The achieved Time-of-Flight (TOF) spectrum of the recoiling ion is thoroughly analyzed to extract $a_{\beta\nu}$ using realistic simulations of the whole experiment (see chapter 3). As it will be more detailed in chapter 2, three nuclei were studied with the LPCTrap device: ^{6}He$^+$, ^{35}Ar$^+$and $^{19}Ne^+$. The measurement of $a_{\beta\nu}$ is the objective in each of these experiments, but the studied transitions are very different. In the case of ^{6}He$^+$, the pure GT transition allows to test the existence of exotic tensorial currents. ^{35}Ar$^+$ decays through a mixed mirror transition, mostly F in nature. ^{19}Ne^{2+}is a mixed transition as well, but with a dominating GT component. The $a_{\beta\nu}$ value thus allows to increase the constraint on the current V_{ud} value or, with another interpretation, to test the existence of the exotic scalar current. The present section is a quick overview of the other existing experiments which follow similar goals with variants.

Experimentally, Paul traps to limit β scattering and to provide a well-localized source are not the only trapping techniques in usage: Penning traps and Magneto-Optical Traps (MOT) are used as well. This being said, confining the radioactive source is not mandatory, ergo, some experiments do not use traps at all.

On the theoretical side, $a_{\beta\nu}$ is not the only angular correlation parameter existing. To illustrate this, let us write the complete expression 1.30, *i.e.* account also for possibly-oriented nuclei. A more general expression is [JTW57a; JTW57b]: re

$$\omega(\langle J\rangle|E_e,\Omega_e,\Omega_\nu)dE_e d\Omega_e d\Omega_\nu = \frac{F(\pm Z,E_e)}{(2\pi)^5} p_e E_e (E^0-E_e)^2 dE_e d\Omega_e d\Omega_\nu$$
$$\xi\Bigg\{1 + a\frac{\mathbf{p_e}\cdot\mathbf{p}_\nu}{E_e E_\nu} + b\frac{m}{E_e} + c\left[\frac{1}{3}\frac{\mathbf{p_e}\cdot\mathbf{p}_\nu}{E_e E_\nu} - \frac{(\mathbf{p_e}\cdot\mathbf{j})(\mathbf{p}_\nu\cdot\mathbf{j})}{E_e E_\nu}\right]\left[\frac{J(J+1)-3\langle(\mathbf{J}\cdot\mathbf{j})^2\rangle}{J(2J-1)}\right]$$
$$+\frac{\langle\mathbf{J}\rangle}{J}\cdot\left[A\frac{\mathbf{p_e}}{E_e} + B\frac{\mathbf{p}_\nu}{E_\nu} + D\frac{\mathbf{p_e}\times\mathbf{p}_\nu}{E_e E_\nu}\right]\Bigg\} \quad (1.36)$$

This expression still shows $a_{\beta\nu}$, but other correlation parameters such as A, B and D appear when they are not integrated out over the polarization. Measuring these other parameters grants access to various aspects of the SM. For example, section 4.2 presents the experimental future of LPCTrap where a measurement of D is foreseen. The value of this parameter is linked to the existence of a possible source of CP-violation.

Choosing to study a specific aspect of a particular baryon undergoing a β decay changes what is tested underneath. To access the value of V_{ud}, we mentioned the case of the mirror transitions where $a_{\beta\nu}$ is extracted (see equation 1.29), which is the chosen path in the LPCTrap case. Yet, the same could be done in the free neutron, a very different system where several effects coming from the nuclear medium are not present. We also introduced the superallowed pure Fermi decays through equation 1.27 where the precision on specific nuclear data (mass, lifetime, BR, ...) becomes the challenge. An important number of measurements using superallowed decays have been carried out for the past decades [HT14]. Experiments with pions where the same logic applies exist as well [Poca14]. These different systems and their observables are all a complementary source of precious input to increase the current constraint on the value of V_{ud}.

As mentionned in the the previous section, pure transitions, whether of F or GT nature, are well-suited to test the existence of exotic currents.

The section will be divided according to the LPCTrap timeline. The first part will be dedicated to the search of exotic currents in pure (GT/F) decays while the second will focus on V_{ud}. The neutron case actually belongs to both studies, we arbitrarily placed it in the second part.

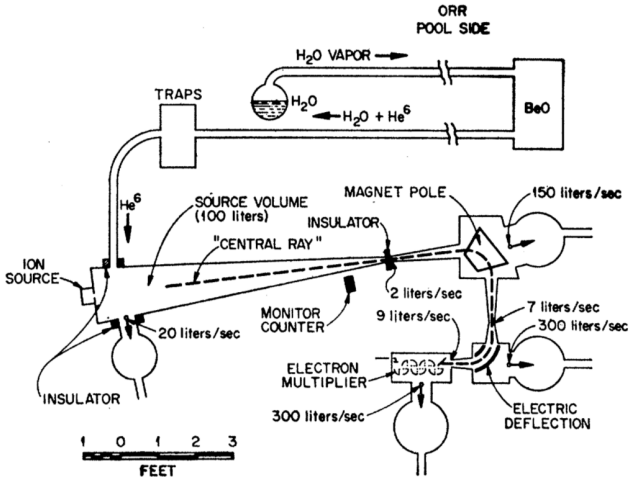

(a) Oak Ridge 1963 Experiment setup [JPC63].

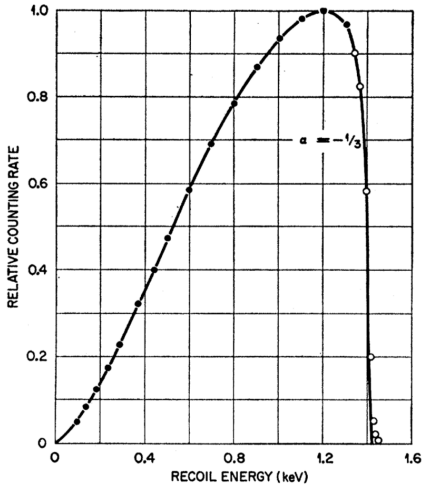

(b) Oak Ridge 1963 experiment typical spectrum [JPC63]. The statistical uncertainties are lower than the size of the points which show the experimental results of a typical dataset. The curve is from theory with SM assumption, the agreement is excellent.

Figure 1.5: 1963 Oak Ridge Experiment

1.3.1 Exotic currents in pure transitions

1.3.1.1 Oak Ridge Research Reactor (1963)

One of the most stringent constraints on the existence of exotic currents comes from a measurement done in 1963 [JPC63]. The Oak Ridge Research Reactor provided the neutrons required for the relevant production reaction: ^{9}Be(n, α)^{6}He. The produced gaseous ^{6}He was routed using water vapor to the detection setup as pictured in fig. 1.5a. Cold traps on the way were used to capture the water and other contaminants. The recoiling ^{6}Li$^+$ resulting from the pure GT nuclear β decay of ^{6}He was steered using magnetic and electric fields, thus allowing a selection on energy, to an electron multiplier. A typical spectrum presenting the recoil ion energy counts is shown in fig. 1.5b. The error control was very thorough and yielded this result:

$$\frac{|C_T|^2 + |C'_T|^2}{|C_A|^2 + |C'_A|2} \leq 0.4\% \tag{1.37}$$

implying $a_{GT} = -0.3343(30)$. Glück modified this value with the inclusion of radiative corrections to $a_{GT} = -0.3303(30)$ [Gluc98]. This value is still today one of the most precise results on tensor currents.

1.3.1.2 ANLTrap@CENPA

A team at Argonne National Laboratory (ANL) has been developing an experiment to measure $a_{\beta\nu}$ in the pure GT decay of ^{6}He [Mull14; Robe15; Lere15]. The atoms are produced using the ^{7}Li(d, ^{3}He)^{6}He reaction with the tandem accelerator at CENPA[16] in Seattle with a high yield: 10^{10} atoms/s. The high intensity deuteron beam caused issues as the rapid degradation of the stainless-steel foil which houses the Lithium was observed. This was mend through the replacement of this stainless-steel foil with Tantalum, one of the few elements that do not react chemically with Lithium. Tantalum has a melting point twice as high when compared to stainless-steel (1400 vs 3020 ^{o}C). The whole target can now operate for weeks instead of days.

The experiment consists of two coupled MOTs where the first receives and shapes an atom bunch while the second (see fig. 1.6a) is equipped with the detectors. Although the transfer efficiency is around 30%, possible non-trapped ^{6}He contamination is reduced in the process. The total efficiency is around 2×10^{-7}. This results in a few thousands atoms trapped per second inside the detection zone. Using

[16] Center for Experimental Nuclear Physics and Astrophysics

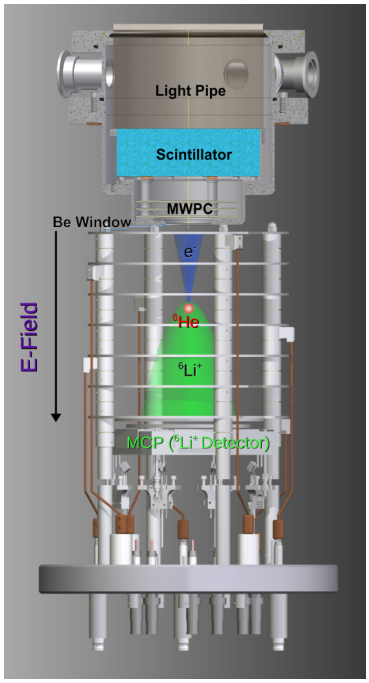

(a) CENPA Detection MOT [Lere15].

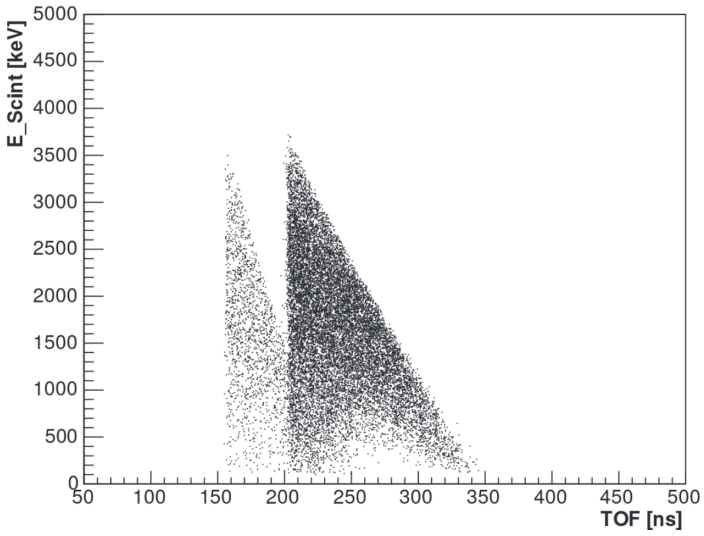

(b) CENPA spectra (Feb. 2015 data) [**CENP15**].

Figure 1.6: CENPA ^{6}He Experiment

MOTs provides a few assets. A high selectivity is possible and no space-charge effects or RFP[17] enables to have a quasi-punctual cold source. The bunch dynamics is an important source of systematic uncertainty in Penning or Paul trap experiments and is thus avoided here. The detector setup is similar to what LPCTrap is equipped with. Detection in coincidence of the decay products, namely the β particle and the recoil ion $^6Li^+$, is done using respectively a plastic scintillator and a MCP (see section 2.3).

A full simulation of the whole setup using GEANT4 and COMSOL was developed in this framework. The last experiments yielded ~ 0.3 coincidences/second for a total of $\sim 2 \times 10^4$ events (see fig. 1.6b), representing a 4% relative statistical error on $a_{\beta\nu}$. An update of the detection efficiency is foreseen and should allow to reach $\Delta a_{\beta\nu}/a_{\beta\nu} = 0.1\%$.

1.3.1.3 Paul trap at Argonne (ATLAS)

A collaboration working at Argonne is performing a correlation measurement in the ^{8}Li β decay in a Paul trap [Scie14]. The transition is almost pure GT with a F component smaller than 10^{-3}. The daughter nucleus is an excited ^{8}Be which fissions in two delayed-α particles. The detection of these products changes the "usual" dependence of the kinematic distribution on the correlation parameter [Li13]. The end result is that the experiment really measures $|C_T/C_A|^2$ through the energy difference of the alphas, thus constraining the possible existence of exotic currents. The coincidence detection with the β allows to clear background.

The radioactive ions are produced through the ^{7}Li(d,p)^{8}Li reaction with a beam provided by ATLAS[18] where 24 MeV ^{7}Li imping on a cryogenic D_2 target. As it is shown in fig. 1.7 the Paul trap is surrounded by DSSSDs[19] which allows the detection of the triple β-α-α coincidence. The back-to-back coincidences of the two αs were used to measure the cloud dimensions which is approximated as a 3D Gaussian distribution with 1.8 mm of FWHM. A full simulation including the setup geometry, the ion cloud distribution, the β scattering and the detector response was used to better understand the possible systematic

[17] Radio-Frequency Phase, see section 3.2.2
[18] Argonne Tandem-Linac Accelerator System
[19] Double-Sided Striped Silicon Detector, see section 2.3.1.1

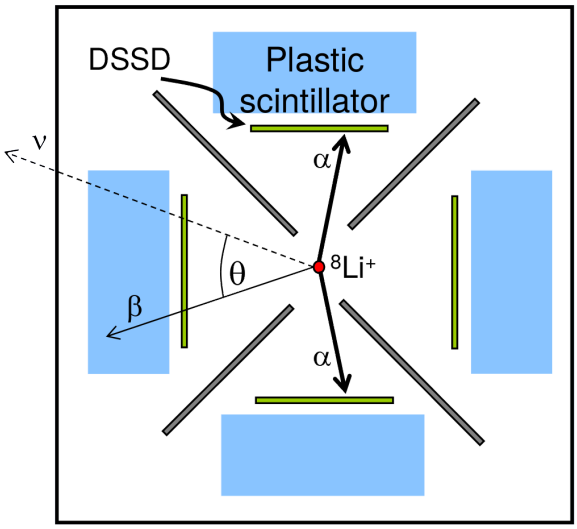

Figure 1.7: Argonne experiment detection setup [Scie14].

effects. Unlike LPCTrap, the effects from the RF field, the ^{4}He buffer gas and the ion temperature were neglected in the first campaign [Li13] which yielded the following result:

$$|C_T/C_A|^2 = 0.004 \pm 0.009_{stat} \pm 0.010_{syst} \tag{1.38}$$

A second campaign took place where ten times more statistics were gathered. Detailed simulations and fine theoretical corrections are required for a good control of the systematic effects. The preliminary result is [Ster13]:

$$|C_T/C_A|^2 = 0.0018 \pm 0.0036_{stat} \pm 0.0041_{syst} \tag{1.39}$$

which implies:

$$a_{\beta\nu} = -0.3321 \pm 0.0036 \tag{1.40}$$

The collaboration published more recent results as well [Ster15]:

$$|C_T/C_A|^2 = -0.0013 \pm 0.0038_{stat} \pm 0.0043_{syst} \tag{1.41}$$

which implies:

$$a_{\beta\nu} = -0.3342 \pm 0.0026_{stat} \pm 0.0029_{syst} \tag{1.42}$$

1.3.1.4 TRINAT@TRIUMF

The TRINAT collaboration at TRIUMF studied the superallowed pure F decay $^{38m}\mathrm{K} \rightarrow ^{38}\mathrm{Ar} + \beta^+ + \nu_e$. The TRIUMF ISAC facility provided the ^{38m}K beam, the metastable state being the only one captured in a first MOT. A 75% efficiency transfer towards a second MOT lowers the background. The coincidence detection of the β particle and the recoil ion with, respectively, a Double Sided Silicon Stripped Detector (DSSSD) and a Micro-Channel Plate (MCP) is performed for 150 ms in the second MOT. The TOF spectrum of the RI, from which $a_{\beta\nu}$ is extraced with the proper fit, is thus collected as shown in fig. 1.8b. An experiment in 2005 yielded [GMAA05]:

$$a_{\beta\nu} = 0.9981 \pm 0.0030(\mathrm{stat})^{+0.0032}_{-0.0037}(\mathrm{syst}) \tag{1.43}$$

A TOF spectrum is shown in fig. 1.8a. The collaboration is working on an upgrade that would lower the error on $a_{\beta\nu}$ to 0.001 [BG14; Behr14]. The update relies on the idea of collecting all recoil ions with a proper electric field, a larger MCP and a larger β detector.

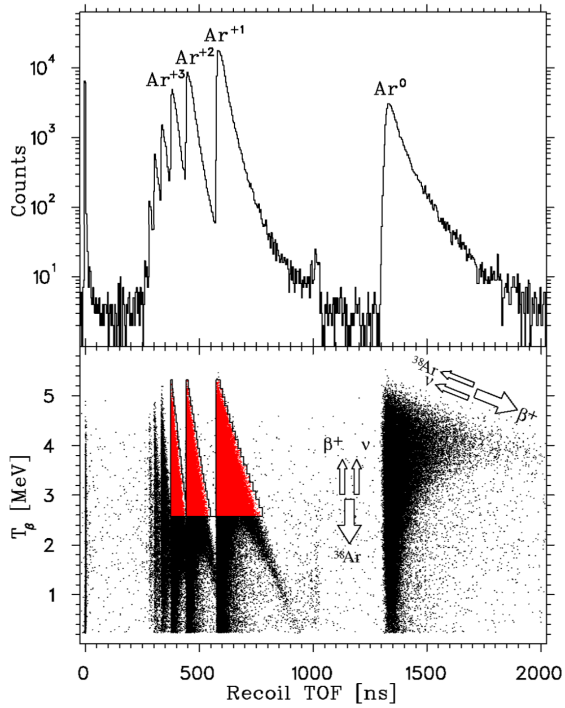

(a) Results from the 2005 experiment. The different charge states of the recoiling Ar appear clearly, the red regions in the bottom canvas correspond to the analysis cuts [GMAA05].

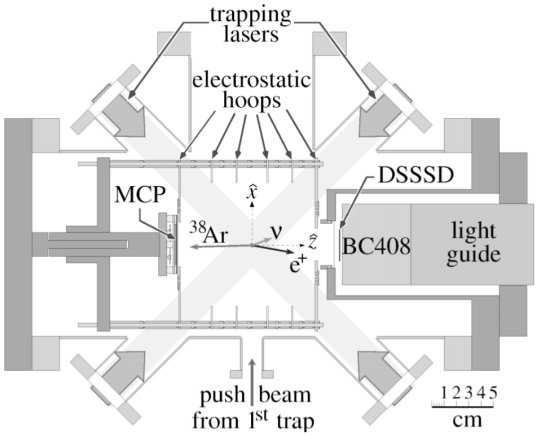

(b) TRINAT Detection setup around the second MOT [GMAA05].

Figure 1.8: TRINAT ^{38m}K Experiment

1.3.1.5 WITCH

The WITCH experiment is installed after the REXTRAP device at ISOLDE, CERN. The objective of WITCH is the measurement of $a_{\beta\nu}$ in the ^{35}Ar β decay, a mirror transition mostly Fermi in nature (see section 2.4.2). The apparatus consists of a double Penning trap system as it is pictured in fig. 1.9a [Sev14b]. The first cooler trap cools the ions with buffer gas collisions in order to bunch them, readying them for injection in the second so-called decay trap. In this second region, a potential barrier is present and, depending on the set voltage, allows selected ion energies to pass. A typical dataset is shown in fig. 1.9b. Varying this voltage allows to construct a full inclusive spectrum of the RI energies with which the fit of $a_{\beta\nu}$ is done.

Like most trap-based experiment reaching a high level of precision, the control and understanding of the systematic effects becomes crucial. For example, the decay trap dynamics generate three specific eigenmotions because of the overlapping electro- and magneto-static fields (see section 3.2.2.1). The space-charge effect comes into play and must not be neglected as well. All of this contributes to a non-pointlike dynamic source and its proper modeling is required in order to control the errors it causes. A recent study of these effects is available [Poro15] where the simulation work was done using SIMBUCA [VG11]. Just like for LPCTrap, the analysis is ongoing and now depends on the commissioning of thorough simulations. A few % of precision is expected on $a_{\beta\nu}$.

1.3.1.6 TAMUTRAP

Installed at the Texas A&M University (TAMU), the TAMUTRAP experiment is based on a singly cyclindrical-shaped Penning trap of which the goal is to measure $a_{\beta\nu}$ through the study of β-delayed proton emitters [Melc14; Mehl13], the pure Fermi ^{32}Ar case being considered first. A global layout is shown in fig. 1.10a. This endeavor is very promising since it is expected to yield a high statistical count as its geometrical efficiency is nearing 4π. Indeed, the path of the decay products is anticipable, allowing the design of an appropriate Penning geometry to maximize the collection of the protons and the βs using proper EM fields combined with detectors placed on the ends of the chamber. Unlike the LPCTrap

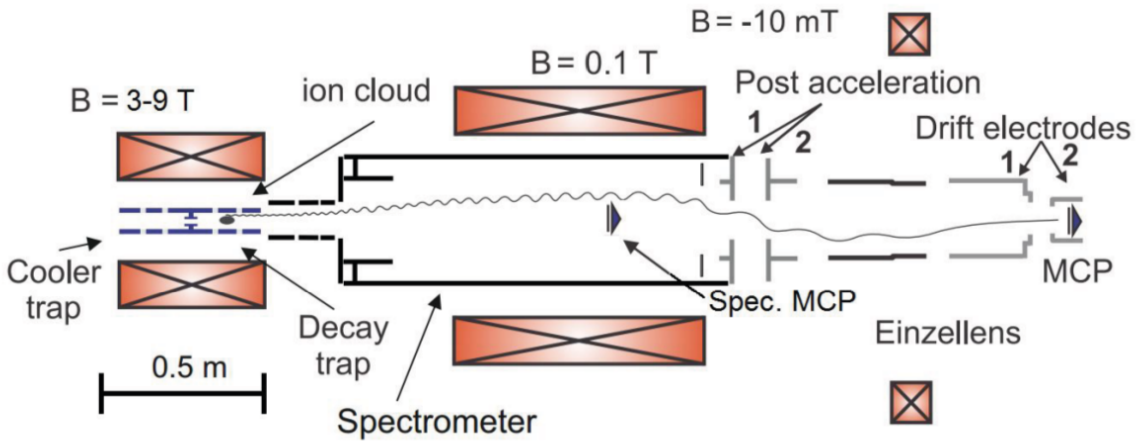

(a) WITCH Setup [Poro15].

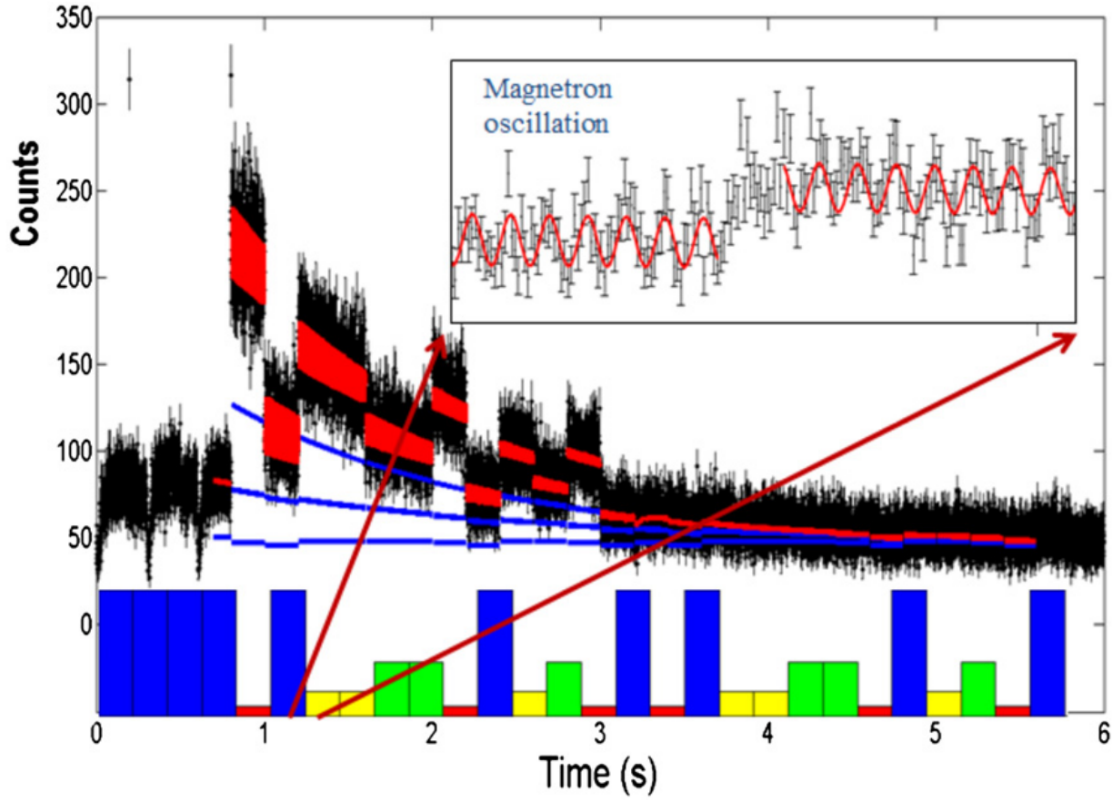

(b) Typical WITCH dataset [Sev14b]. The transfer from the cooler to the decay trap occurs at 0.8 s while the decay trap is emptied at 3.2 s. The retardation voltages are shown as the down histogram. The radioactive decay of ^{35}Ar appears clearly with slices offsets due to the lower counting rate associated with a higher potential barrier. The lines are fits to account for all the components generating the signal.

Figure 1.9: WITCH ^{35}Ar Experiment

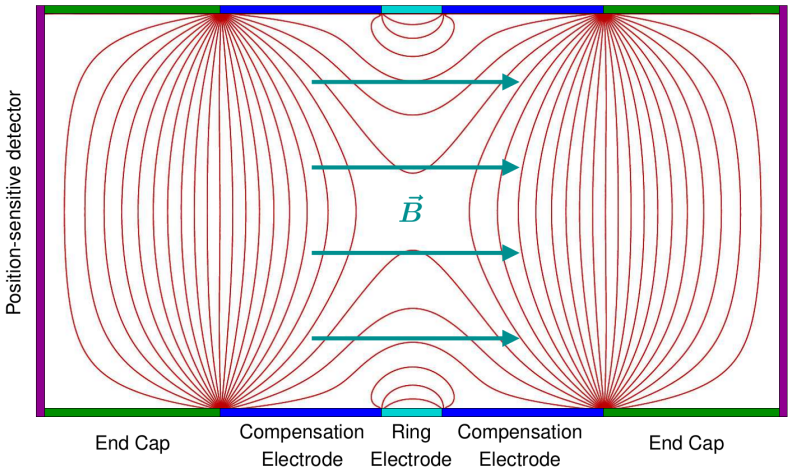

(a) TAMUTRAP layout [Melc14].

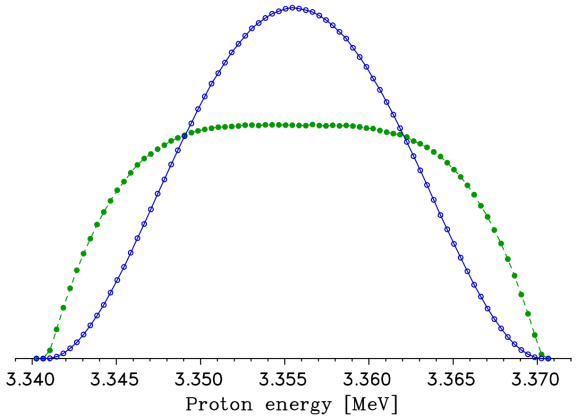

(b) TAMUTRAP – Proton spectrum in the ^{32}Ar case for S (blue) and V (green) currents [Melc14].

Figure 1.10: TAMUTRAP Experiment

expe riment where $a_{\beta\nu}$ is obtained through the analysis of the RI TOF spectrum, TAMUTRAP aims to extract this correlation parameter using the proton energy where a detection of proton-β coincidences occurs. The effect of possible exotic (S) currents is shown in fig. 1.10b.

This experiment is rather new and still in its R&D phase as the required apparatus to bunch and cool the relevant ions, the RFQCB (see section 2.2.2), has recently been commissioned [Mehl15]. The measurement trap itself as well as the full detection setup is still in development. The first test runs are estimated for the year 2017. In the future, it is not excluded to use this apparatus to measure other observables, *e.g.* through a coupling with lasers, thus polarizing chosen ions.

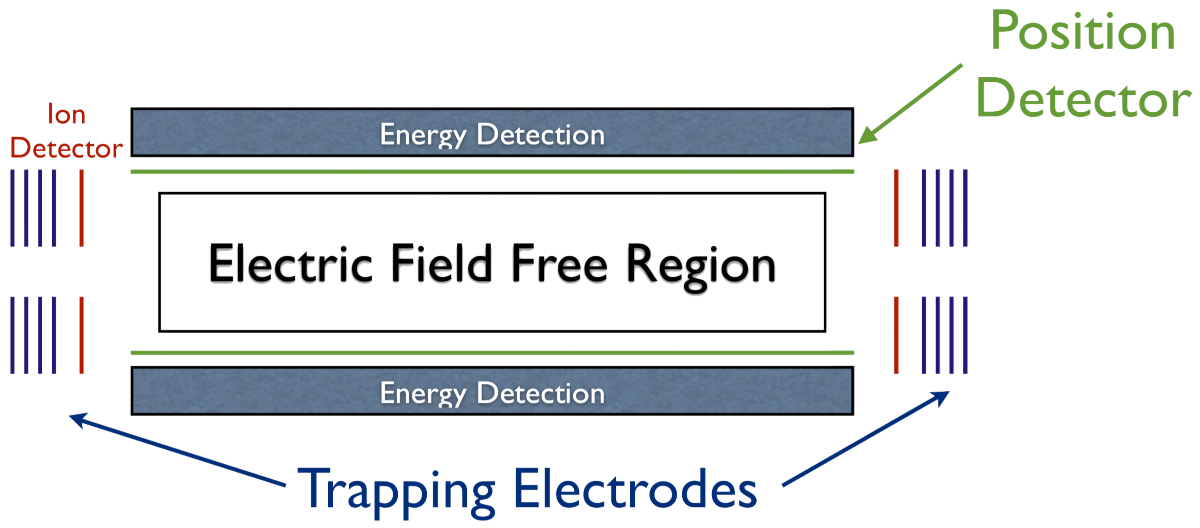

Figure 1.11: WIRED scheme, adapted from [Ron14].

1.3.1.7 WIRED

Experiments using the WIRED[20] apparatus are being developed at the Weizmann Institute [Ron14; Dhal13; Aviv12]. Fig. 1.11 illustrates the experimental setup which allows for a high-resolution mass selection. Indeed, the ions travel back and forth through multiple reflection around the detectors and get separated according to their mass. When in the free field region, β decay can occur and the decay products are captured by the detectors. The collaboration is aiming at measurements of correlation parameters with a coincidence detection of the RI and the β in ^{6}He. To this end, the SARAF[21] accelerator is being constructed to deliver the required exotic beams.

1.3.2 V_{ud} measurements

1.3.2.1 Lawrence Berkeley National Laboratory (LBNL)

The LBNL extracted $a_{\beta\nu}$ in the β decay of $^{21}\mathrm{Na} \rightarrow ^{21}\mathrm{Ne} + \beta^+ + \nu_e$ [Vett08]. The studied Sodium nuclei are provided by a cyclotron at LBNL using $^{24}\mathrm{Mg(p,\ }\alpha)^{21}\mathrm{Na}$. The produced ^{21}Na atoms are injected in a MOT where the detection setup is mounted (see fig. 1.12a). The detection in coincidence of the ^{21}Ne and the β yields a TOF spectrum, a sample of which is shown in fig. 1.12b. The studied mixed (F/GT) transition produced a first faulty result because of the presence of molecular Sodium [Scie04]. A new experiment ensured that less atoms were trapped, preventing the formation of undesired molecules yielding a wrong TOF. In this new experiment the TOF was constructed with the detection in coincidence of the RI and the Shake-Off electrons. The value for $a_{\beta\nu}$ was then later corrected to [Vett08]:

$$a_{\beta\nu} = 0.5502 \pm 0.0038(stat) \pm 0.0046(syst) \tag{1.44}$$

which is in agreement with the SM-predicted value of $a_{\beta\nu}$= 0.553(2).

1.3.2.2 Non-nuclear β decay

Pions A recent summary reviews the results from the PEN[22] experiments using the PIBETA array [Poca14]. From a theoretical point of view, pions are the easiest systems to study because of their low number of decay channels and very good understanding of radiative corrections. The pion β decay rate is given by:

$$\Gamma = \frac{\mathcal{G}^2|V_{ud}^2|}{30\pi^3}\Delta^5 f(\varepsilon,\Delta)\left(1-\frac{\Delta}{2m_+}\right)^3(1+\delta_\pi) \tag{1.45}$$

[20] Weizmann Institute Radioactive Electrostatic Device
[21] Soreq Applied Research Accelerator Facility
[22] http://pen.phys.virginia.edu/

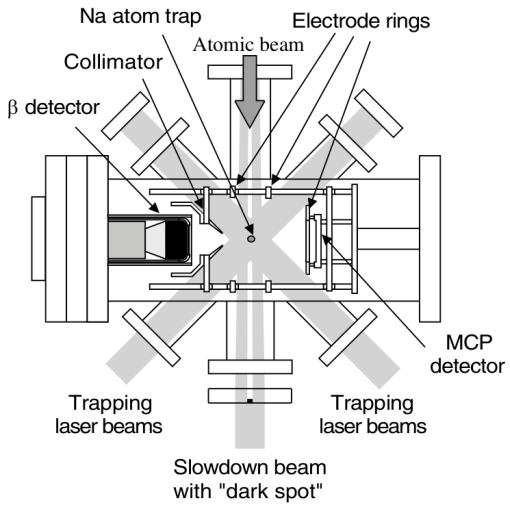

(a) Setup of the LBNL experiment [Scie04].

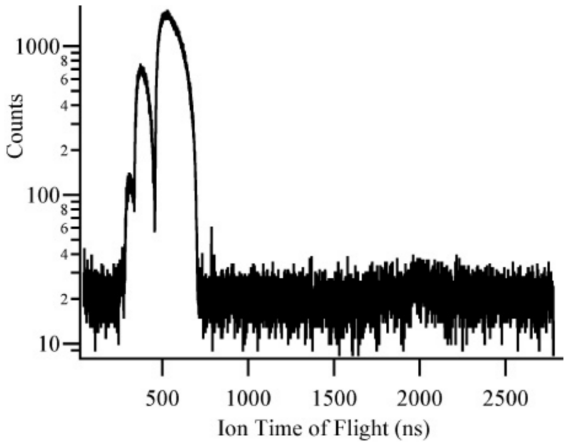

(b) A typical run spectrum from the LBNL experiment on ^{21}Na [Vett08].

Figure 1.12: Berkeley ^{21}Na Experiment

with $\Delta = M_+ - M_0$, $\varepsilon = \left(\frac{m_e}{\Delta}\right)^2$, M_+, M_0 and m_e are respectively the π^+, π^0 and electron masses. f is the Fermi function while δ_π is a well-controled theoretically-computed correction term.

Accessing V_{ud} is thus possible by precisely measuring the decay rate Γ or, as it is done experimentally to cancel out several uncertainties, the branching ratio to the β decay. It is important to note that the major difficulty of this measurement is that this branching ratio is very low ($\sim 10^{-8}$). Normalizing to either the average experimental π_{e2} branching ratio ($R^\pi_{e/\mu} = (1.230 \pm 0.004) \times 10^{-4}$ – exp. nor.) or to the established theoretical value ($R^\pi_{e/\mu} = (1.2352 \pm 0.0005) \times 10^{-4}$ – theo. nor.), yields:

$$V_{ud}^{\text{exp. nor.}} = 0.9728 \pm 0.0030 \tag{1.46}$$

$$V_{ud}^{\text{theo. nor.}} = 0.9748 \pm 0.0025 \tag{1.47}$$

Neutrons The free neutron decay is a powerful tool to search for exotic currents or increase the constraint on V_{ud} (currently, $V_{ud} = 0.9774 \pm 0.017$ from the neutron [O14]). Regarding the exotic currents, we notice that the beta asymmetry parameter A appears in equation 1.36. It is through the measurement of this parameter that free neutron decay provides an accurate method to constrain the existence of possible exotic currents. The polarization of the neutrons is thus mandatory [Bae14; YCFG14]. The corrected $\mathcal{F}t$ value in the case of neutron decay is [SBNC06]:

$$f_n \tau_n (1 + \delta_R) = \frac{K/\ln 2}{G_F^2 V_{ud}^2 (1 + \Delta_R^V)(1 + 3\lambda^2)} \tag{1.48}$$

where τ_n is the lifetime of the free neutron, $f_n(1+\delta_R)$ is the phase space factor and λ is the ratio between Axial and Vector coupling including some radiative corrections. It is this ratio that grants access to the parameter A:

$$A_{SM} = -2\frac{\lambda^2 + \lambda}{1 + 3\lambda^2} \tag{1.49}$$

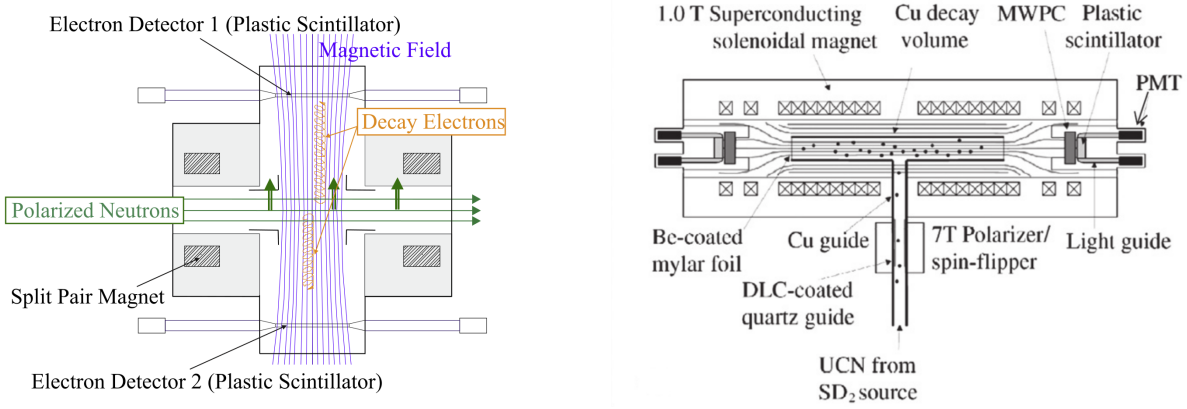

(a) Perkeo II setup [Bae14].

(b) UCNA setup [YCFG14].

Figure 1.13: (Ultra) Cold neutron experiments

Neutron has the ease of not being in a nuclear environment, thus avoiding possible nuclear or isospin breaking corrections. This simplicity is similar to the pion case we just discussed. In this context, we could cite two experiments:

PERKEO II Using cold neutrons[23], the PERKEO II experiment detects the decays from a polarized neutron beam passing through the detection setup (see fig. 1.13a). A recent measurement yielded [Mund13]:

$$A = -0.11972 \pm 0.00045\ (\text{stat})\ {}^{+0.00032}_{-0.00044}\ (\text{syst}) \tag{1.50}$$

$$\lambda = \frac{g_A}{g_V} = -1.2761 \pm 0.0012\ (\text{stat})\ {}^{+0.0009}_{-0.0012}\ (\text{syst}) \tag{1.51}$$

The upgrade of this experiment is being developed: PERKEO III, where more statistics is expected.

UCNA In this other experiment, ultra cold neutrons[24] decay in a chamber where the proton and the β are detected. A recent measurement yielded [Mend13]:

$$A = -0.11954 \pm 0.00055\ (\text{stat})\ \pm\ 0.00098\ (\text{syst}) \tag{1.52}$$

$$\lambda = \frac{g_A}{g_V} = -1.2756 \pm 0.0030 \tag{1.53}$$

[23] Cold neutrons: at thermal equilibrium with matter at 40 K, mean neutron kinetic energy of 5 meV.
[24] Ultra cold neutrons: $E_K \leq 335$ neV

SM test	Transition	Nucleus	Experiment	Results
Exotic	Pure GT	^{6}He	Oak Ridge (1963)	$a_{GT} = -0.3303(30)$ (Glück correction)
Exotic	Pure GT	^{6}He	CENPA	Expecting 0.1% of rel. precision on $a_{\beta\nu}$
Exotic	∼Pure GT (negl. F)	^{8}Li	Argonne	$a_{\beta\nu} = -0.3342 \pm 0.0026_{stat} \pm 0.0029_{syst}$
Exotic	Superall. pure F	^{38m}K	TRINAT	$a_{\beta\nu} = 0.9981 \pm 0.0030(\text{stat})^{+0.0032}_{-0.0037}(\text{syst})$
Exotic	Mostly F	^{35}Ar	WITCH	Expecting a few % of rel. precision on $a_{\beta\nu}$
Exotic	Pure F	^{32}Ar	TAMUTRAP	in development
Exotic	Pure GT	^{6}He	WIRED	in development
V_{ud}	mirror	^{21}Na	LBNL	$a_{\beta\nu} = 0.5502 \pm 0.0038(stat) \pm 0.0046(syst)$

Table 1.6: State of the art – summary

1.3.3 Conclusion

An important experimental effort is being dedicated to the study of the weak interaction through precision measurements at (very) low energy. Whether it is in pion, neutron or nuclear (superallowed, mirror) β decays, the information that has been accumulating for the past decades is beginning to reach very high sensitivities on an important number of systematic effects. For most of the experiments using trapping techniques, this translates in important theoretical and simulation efforts. A summary is showed in table 1.6.

The LHC also provides an important input at high energy. The approach is radically different since instead of verifying tiny possible Beyond-Standard-Model (BSM) effects, the LHC rather follows the logic of producing possible *e.g.* BSM bosons directly. The key of comparing the results between low energy and high energy experiments is through the selection of the relevant theoretical framework. See [NCGA13; GA14] for further details on the comparison between low and high energy domains.

Although the constraints on possible physics beyond the SM are tightening, experimental results are still all consistent with the SM for now [Hols14]. The recent evolution of the constraints on the exotic currents are shown in fig. 1.14. Although we focused on GT tensorial currents research, the field is active in its F counterpart as well, *i.e.* the possible scalar contribution as we show on the figure.

Regarding V_{ud}, we list the results coming from four different sources:

- Superallowed $|V_{ud}| = 0.97425 \pm 0.00022$, is the most precise (PDG value) [O14].
- Pions $|V_{ud}| = 0.9728 \pm 0.0030$ (PDG value) [O14].
- Neutrons $|V_{ud}| = 0.9774 \pm 0.0017$ (PDG value) [O14]).
- Mirror $|V_{ud}| = 0.9719 \pm 0.0017$ [NS09; Sev14b]

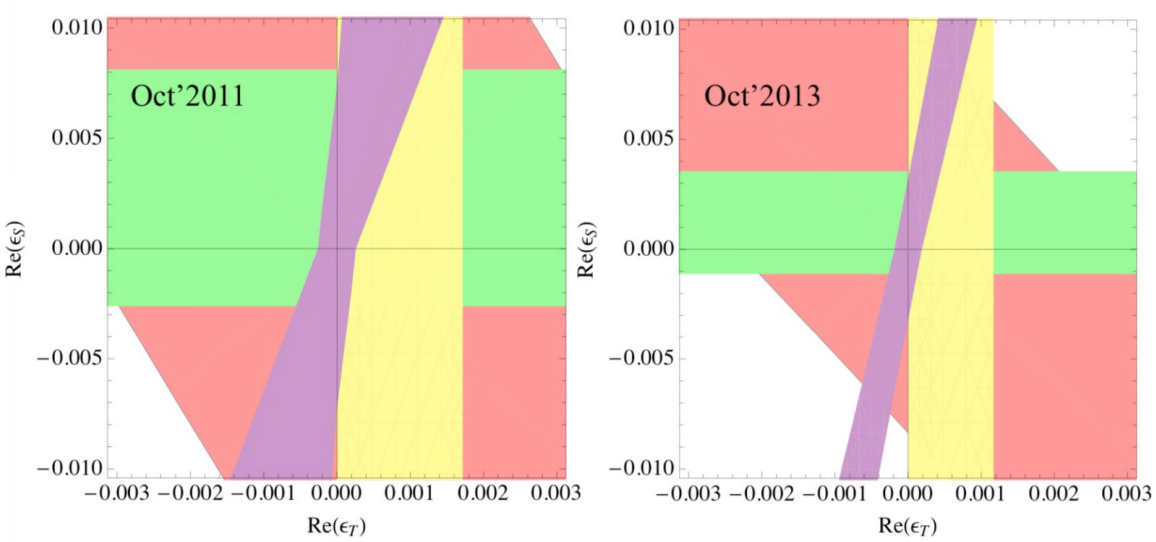

Figure 1.14: Evolution of the constraints on exotic current existence. ε_S and ε_T can be interpreted as the exotic contribution of the Scalar and Tensor currents. The purple region comes from the free neutron decay, the green region is associated to superallowed nuclear β decays and the yellow region is the result of a global fit done on nuclear and neutron decays. The red region was established using measurements in the polarization of ^{14}O and ^{10}C. Taken from [GA14].

1.4 Atomics: Shake-Off effect

The abrupt change of the charge of a given nucleus, through any available nuclear process, has an effect on the bound electronic cloud. Electronic excitation processes may take place such as the Shake-up (SU) or the Shake-off (SO) effects which are respectively the excitation toward a higher orbital or to the continuum. The sudden approximation provides a framework to compute the probabilities of such processes. The validity of such an approximation depends on the speed at which the central potential changes when compared to the relaxation time of the electrons in the new potential. In our specific nuclear β decay case, this charge change happens in less than 10^{-18} s which corresponds to the transit time of the emitted β particle through the electronic cloud. Moreover, this assumption is valid in the case that $\alpha Z_{\text{eff}} \ll 1$, α and Z_{eff} being respectively the fine structure constant and the effective nuclear charge. Indeed, the sudden approximation makes sense only if the β particle does not "have time" to interact with the electronic cloud (see [CPJ63]).

The first computations of the probabilities of such processes were done using hydrogen like wave functions [Migd41; Fein41; Levi53]. More sophisticated calculations were performed using numerical self-consistent wave functions for many-electron atoms [CNT68]. A hole in the inner shells of the electronic cloud may be filled with a higher orbital electron. A way to preserve energy conservation is through the ejection of another high orbital electron: this is the Auger emission which constitutes a possible secondary process. The comparison between theoretical predictions and experimental results is not easily done because of such processes [Scie03]. A calculation was performed in the ^{6}He case [WV96] and although the prediction for the single ionization was in good agreement with experimental results, the 2+ state was overestimated by one order of magnitude. Indeed, this probability was predicted to be 0.32% but its measurement yielded $0.024\% \pm 0.009$ in [CPJ63]. It is thus important to include possibly contributing secondary processes in such predictions.

Since 2010, LPCTrap is capable of providing the SO probabilities following the β decay of interest and has done so for the the decay of three ions. These results are addressed in section 2.4. Z. Patyk and B. Pons computed precisely the SO probabilities from a theoretical point of view in ^{6}He and ^{35}Ar, providing a stringent test of the sudden approximation in ^{6}He and showing the importance of including the Auger effect in ^{35}Ar [Cour12; Cour13b]. A measurement was done with ^{19}Ne as well, the theoretical and experimental analysis is underway.

Chapter 2

LPCTrap Experiments

Résumé français – Ce chapitre présente tous les aspects expérimentaux qui touchent au dispositif LPCTrap qui est installé au GANIL. On aborde en premier lieu la production des ions qui sont envoyés au dispositif expérimental. Ces ions sont produits soit par des sources d'ionisation de surface soit par l'ensemble SPIRAL, lorsqu'il est disponible, qui fournit un faisceau stable en phase de test ou un faisceau qui contient les ions radioactifs d'intérêts pour les "vraies" mesures physiques. Le dispositif LPCTrap est ensuite détaillé, il permet de s'attaquer à deux problématiques intrinsèquement liées. La première est la mise en forme d'un faisceau d'ions continu pour le préparer à son piégeage par paquet dans un piège de Paul transparent. Le deuxième est la détection des produits issus de la désintégration bêta des ions ainsi piégés. L'ensemble de détection est ensuite discuté, il est constitué d'une galette à micro-canaux avec lignes à retard pour l'ion de recul ainsi que d'un télescope bêta (pistes de silicium couplées à un scintillateur plastique). Ces deux détecteurs sont montés face-à-face pour, historiquement (premières expériences avec $^{6}He^{+}$), maximiser la sensibilité aux éventuels courants exotiques tensoriels actuellement exclut du Modèle Standard par la théorie V-A. Finalement, un résumé de toutes les campagnes de mesures effectuées avec LPCTrap est établi. Il en ressort que LPCTrap a largement prouvé sa capacité à récolter des données de très bonne qualité avec une statistique suffisante pour, en principe, atteindre une grande précision sur $a_{\beta\nu}$ (supérieure à 1%). Par ailleurs, les probabilités de Shake-Off ont été mesurées dans le cas de $^{6}He^{+}$ et $^{35}Ar^{+}$ et s'accordent très bien avec les prédictions théoriques alors que la même comparaison dans le cas de $^{19}Ne^{+}$ présente des anomalies. Malgré tout, extraire une valeur de $a_{\beta\nu}$ requiert un bon contrôle des effets systématiques, ce qui est possible en développant une simulation complète de l'expérience. En particulier, la (rétro) diffusion de la particule bêta et la modélisation fine de la dynamique du nuage d'ions piégé sont les deux plus gros contributeurs à ces erreurs qu'il reste à étudier minutieusement.

Contents

In this chapter, we present all the experimental aspects around LPCTrap. We start with the radioactive beams production in 2.1. Details about the LPCTrap device are thereafter given concerning both the incoming ions injection in the Paul trap (2.2) and the detection set-up (2.3). A generic description of all these parts is given first and is followed in section 2.4 by the explicit configuration of each component and experimental specificities for each of the three studied ions, namely $^{6}He^{+}$, $^{35}Ar^{+}$and $^{19}Ne^{2+}$, with a focus on the second one.

Multiple theses were written prior to this one [Cour13a] [Velt11] [MA07] [Dari04] [Dela02]. In section 2.2 in particular, we merely sum up the work done during these past years. The earlier the reference thesis, the higher the experimental/instrumental development done in it while the recent thesis are more focused on data analysis and set-up simulation. English material is available as well through several articles published by the LPCTrap group. They either sum up the LPCTrap functionning [Rodr06] or focus on specific aspects of it [LiHB05]. If the reader is interested in details about the elements given in this chapter, these references are available.

2.1 Ions production

The nuclei we are working with are unstable isotopes with rather short lifetimes and thus must be produced at an accelerator facility. For the LPCTrap experiments this is done at GANIL[1] with the SPIRAL[2] facility which is using the ISOL[3] technique [Lind04]. This method requires a few components: A primary/driver beam of stable ions, a thick target on which the beam impinges, an ion source to ionize the formed atoms and an electromagnetic mass analyzer to roughly select and send the proper nuclei to the chosen beam line. This technique allows a high production yield of mostly contaminants among which the nuclei we are interested in are formed through fragmentation.

The SPIRAL facility accelerates its primary stable beam with three cyclotrons (C0, CSS1 and CSS2) and sends it on a thick graphite target. The resulting radioactive gas is routed through an ECR[4] source (Nanogan III) where it is not fully ionized. A magnetic dipole (ICD1) then allows the separation of the different species according to their $\frac{q}{m}$ ratio (mass separation resolution of $\frac{m}{\Delta m} \sim 250$) [CC15a]. The roughly-selected radioactive ions are thereupon delivered to LIRAT[5] (the low-energy branch), CIME[6] (a post-acceleration cyclotron) or an identification station. As shown in figure 2.1, the LPCTrap device is located at the end of LIRAT. This is where our beam is driven using multiple magnetic quadrupoles and steerers. Its maximum emittance, *i.e.* when the slits are open, is limited by the beam tube size and is roughly equal to 100 $\pi.mm.mrad$.

The radioactive beams we are interested in are not always available. Since we need to prepare the whole LPCTrap set up for each different beam, we can do that prerequisite work using stable beams with the same $\frac{q}{m}$ than the beam of interest (enables a fine tuning of our apparatus) or beams made of the stable counterpart of the ion of interest (has the same chemical behavior). Unfortunately, even stable beams are not always available at SPIRAL, this is why we also work with two different offline ion sources (see section 2.2.1).

The first one is a home-made surface ionization source and is retractable. A first voltage applied on

[1] *Grand Accélérateur National d'Ions Lourds.* In English: large national accelerator of heavy ions.
[2] *Système de Production d'Ions Radioactifs Accélérés en Ligne.* In English: production system of on line accelerated radioactive ions.
[3] Isotope Separation On Line.
[4] Electron Cyclotron Resonance.
[5] *Ligne d'Ions Radioactifs À Très basse énergie.* In English: very low energy radioactive ions line.
[6] *Cyclotron pour Ions de Moyenne Énergie.* In English: cyclotron for intermediate energy ions.

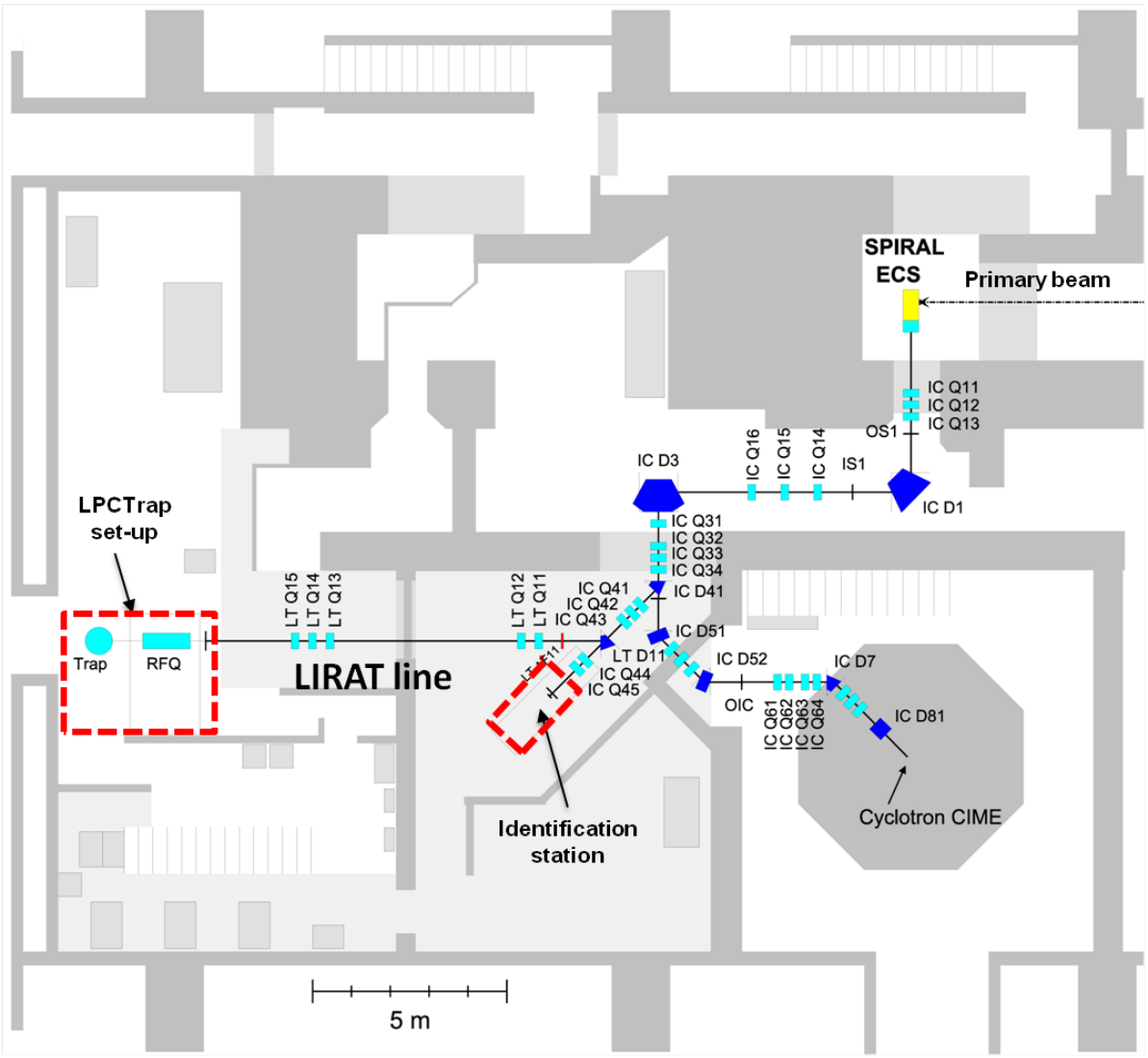

Figure 2.1: Layout showing the incoming primary beam, the different steering dipoles and quadrupoles and the LIRAT line ending with the LPCTrap ensemble [CC15b].

the filament inside the alkaline silicate compound, which the source is made of, enables to ionize the atoms of interest. The resulting alkaline ions are then extracted at a chosen energy using a second voltage. A few more voltages enable to modify the intensity and geometry of this offline beam. The experiments performed at LPCTrap were done with radioactive noble gas which are chemical neighbors of the alkali elements and as such, they have a close $\frac{q}{m}$ ratio when working with singly-charged ions. This makes these sources useful tools to adjust the timings of the apparatus presented below when neither radioactive nor stable beams from GANIL are available (see section 2.1).

The second available source, which is more constraining, is a Phrasor type source working in the same way as above but requiring to be mounted instead of the connection between the LPCTrap set-up and LIRAT. This process obviously requires to break the vacuum of the line and wait at least half a day to recover the needed vacuum. It has an asset nonetheless: this bulky source is capable of reaching higher energies than the retractable one. It also yields a higher number of ions, though the other one is already able to deliver more ions than what is reachable with radioactive beams and handleable with the Radio Frequency Quadrupole Cooler Buncher (RFQCB) (see section).

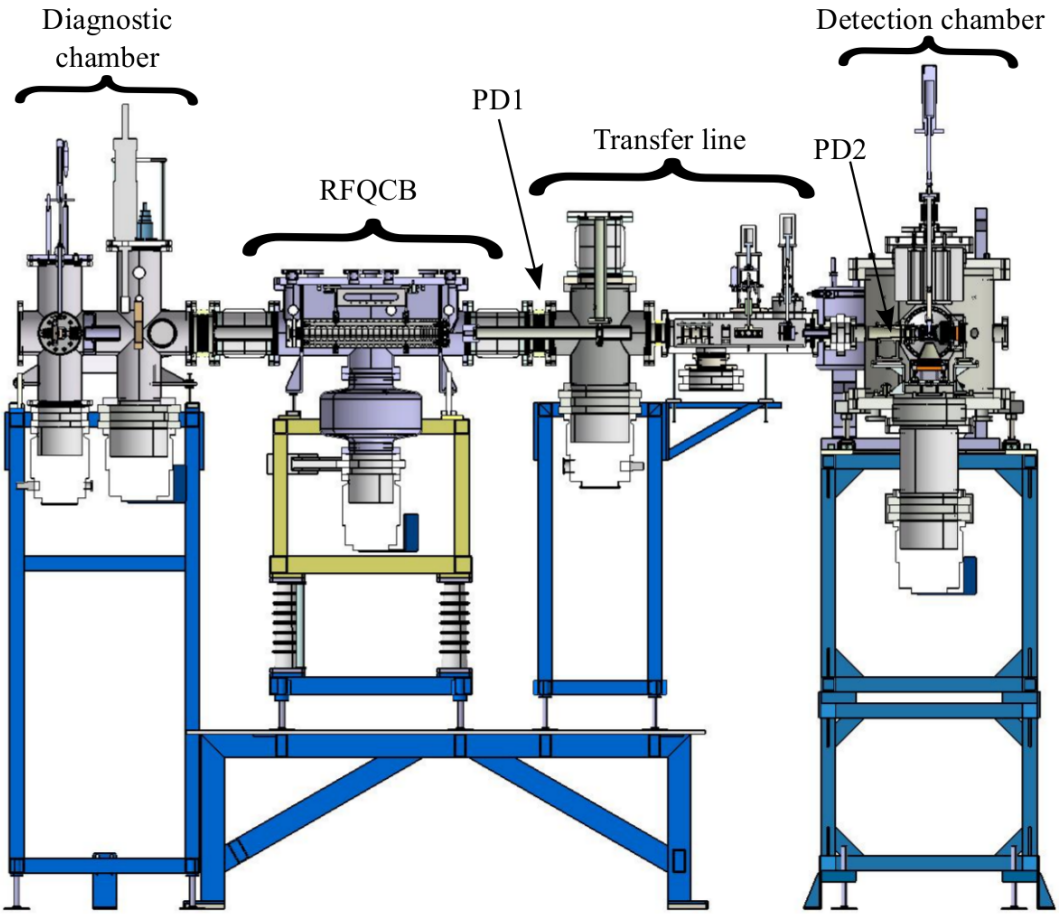

Figure 2.2: 2D Overview of the LPCTrap device. PD1 and PD2 are pulse drift tubes (see section 2.2.3).

2.2 From the accelerator to the Paul trap

Once an exotic beam of interest is created at SPIRAL, we must prepare it to be able to inject the exotic nuclei into the Paul trap situated at the end of the LPCTrap line. Indeed, the trap cannot receive a high-energy continuous beam. The LPCTrap device is thus separated into multiple components which allow the incoming beam to be processed into low-energy bunched ions, the suitable "format" for injection into a Paul trap. The main apparatus used for this task is the Radio Frequency Quadrupole Cooler Buncher (RFQCB) which is detailed in section 2.2.2. Smaller yet important components are also explained in the following sections. An overview of LPCTrap is shown in fig. 2.2 and 2.3.

From a global point of view, the radioactive beam gets bunched into the RFQCB. A cycle time has to be decided so that these bunches get injected regularly into the Paul trap. Based on this cycle length, multiple timings throughout the device must be tuned so that the passage of the bunch in each component is correctly synchronized with the current component function up to the Paul trap (see fig. 2.4). The typical cycle length is 200 ms, distributed unevenly between 160 ms of trapping and 40 ms of background measurement.

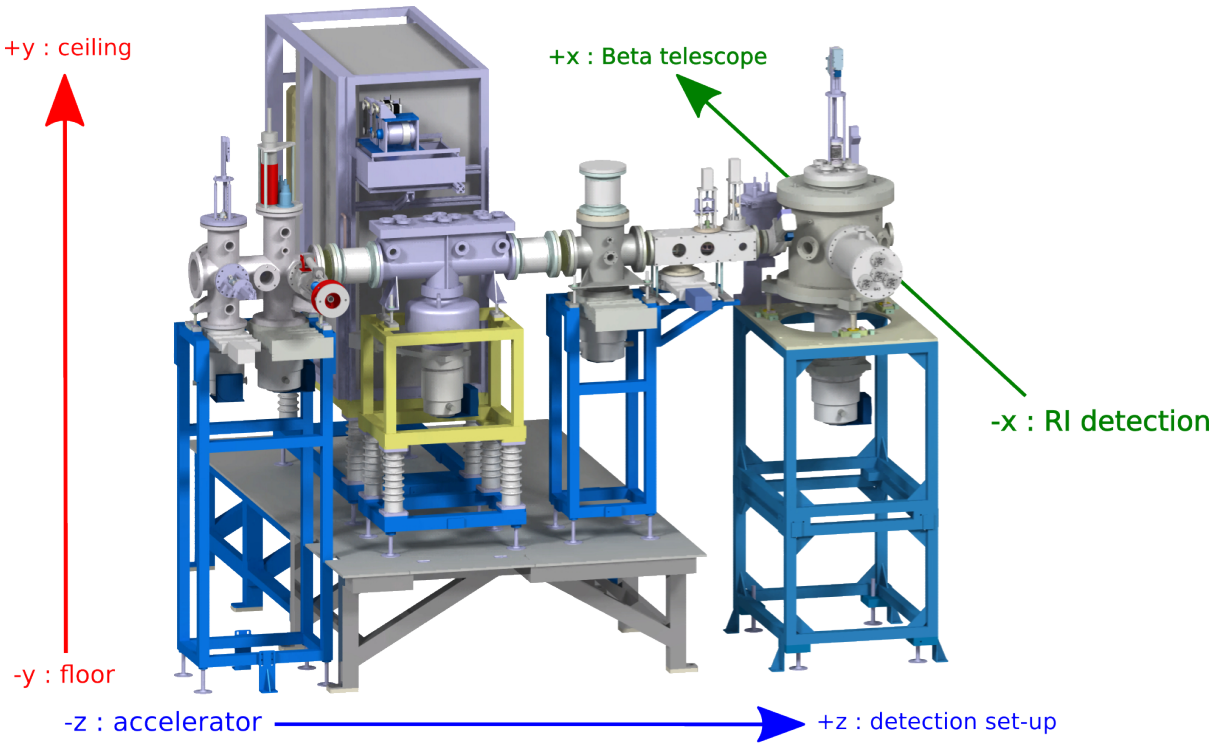

Figure 2.3: 3D Overview of the LPCTrap device. The insulator beneath the RFQCB and the ceramic parts of the line itself appears clearly, pointing out the location of the high voltage platform (yellow part). The axis of reference are also shown.

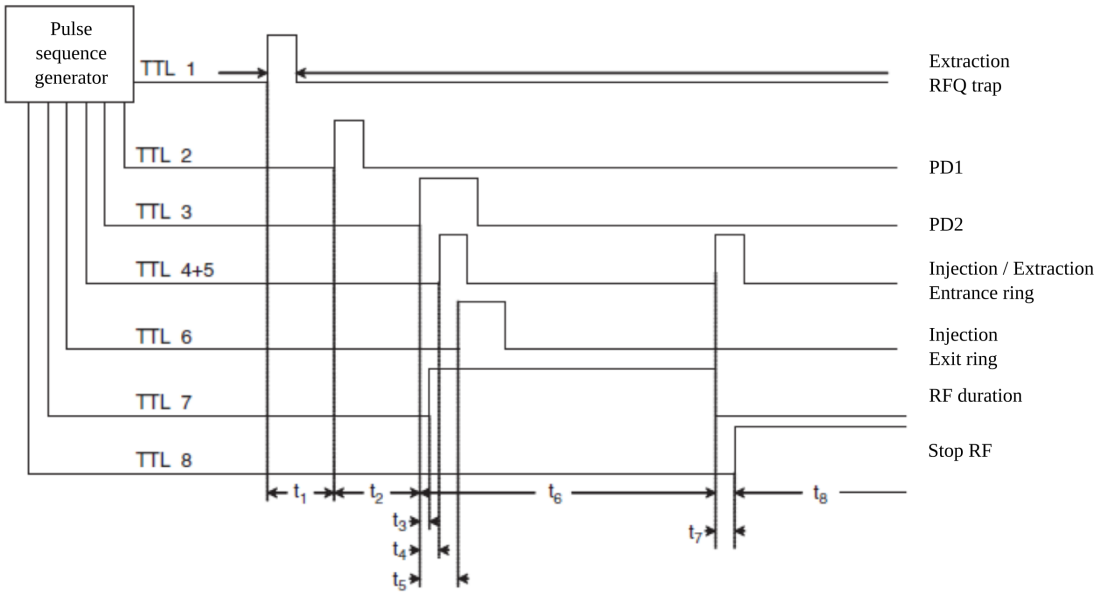

Figure 2.4: Timings overview of the LPCTrap device. For each specific timing, an associated duration is defined such that a given signal starts at its time t_i and has a duration of D_i. PD1 and PD2 are pulse drift tubes (see section 2.2.3).

2.2.1 Beam diagnostic

The first part of the LPCTrap device is a beam diagnostic chamber which includes the retractable offline ion source (see section 2.1). The vacuum in this part is $\sim 10^{-5}$ mbar due to buffer gas leaking from the RFQ. Multiple diagnostic tools are present:

- **A silicon diode**: Of LER Eurisys Mesures kind, this silicon diode has a surface of $45 \times 45\ mm^2$ and a thickness equal to 4 mm. It comprises a thick dead layer (300 μm) where the radioactive beam gets implanted. The β radiation is then detected with a geometrical efficiency of ∼50%. This is useful to quantify the amount of radioactive ions reaching the entrance of LPCTrap and let the accelerator operators optimize the transmission in the line before our set-up. This diode being slow and somewhat fragile, an attenuation factor of several 10^5 must be applied to the incoming beam to perform a proper counting and to prevent any damage on it when it is in usage.
- **A Faraday cup** ("CF14"): This Faraday cup yields the integrated beam intensity ranging from a few pA to several A.
- **A beam profiler** ("PR14"): The profiler gives information on the beam position prior to its injection in the RFQCB.

2.2.2 Radio Frequency Quadrupole Cooler Buncher (RFQCB)

The RFQCB is a key component of the LPCTrap device and its development is summed up in [Ban04]. At first glance, it can be described as a 2D Paul trap whose purpose is to receive a "high-energy" beam (10 keV ± 20 eV) and convert it into cooled ion bunches (0 eV ± 1 eV). In order to do so, after the incoming beam injection has been optimized using the appropriate lenses, it must be cooled. This is done using a neutral buffer gas (either molecular H_2 or monoatomic He, see 2.4) where the effect of the collisions is optimized for ions having a few tens of eVs compared to the gas. This is why the whole RFQCB is mounted on a high voltage platform set at a few tens of eVs lower than the energy of the incoming beam. The ion deceleration at the entrance of the RFQCB and the required collisions induce a straggling of the beam which is compensated with a quadrupole RF field. This confining RF field is applied on four parallel rods running throughout the RFQCB in the z direction (see fig. 2.3 for the reference frame). These rods are segmented themselves and on top of the RF field, each segment has a continuous potential applied on it such that a global tub-like potential is seen by the ions as shown in fig. 2.5.

The main challenge with the RFQCB is to optimize the transmission (the ratio between the exiting and entering ions). A few parameters were studied in order to do so:

- **Buffer gas pressure**: Increasing this parameter yields better cooled ions (with a lower energy), but a critical value cannot be exceeded because the extraction becomes inefficient afterwards. Depending on the studied ion and on the nature of the appropriate gas, this value varies (typically 10^{-2} mbar).
- **Mathieu parameter**: This concept will be explained in section 2.2.4, but we can say here that it is a characteristic of a given Paul trap. Regions of stability are defined for given Mathieu parameters and scanning these regions may yield a better transmission.

To give a number, 10% is a nominal transmission for the $^6He^+ + H_2$ system (limited by losses due to charge exchange with the buffer gas). Another interesting figure which brings its own constraints is the cooling time. It is defined as the time required for the entering ions to reach the bunching section of the device and has been found to be typically a few hundreds of μs. The trapping lifetime of the ions inside the RFQCB is yet another important observable because it can further constrain the chosen cycle length or the gas pressure, for instance.

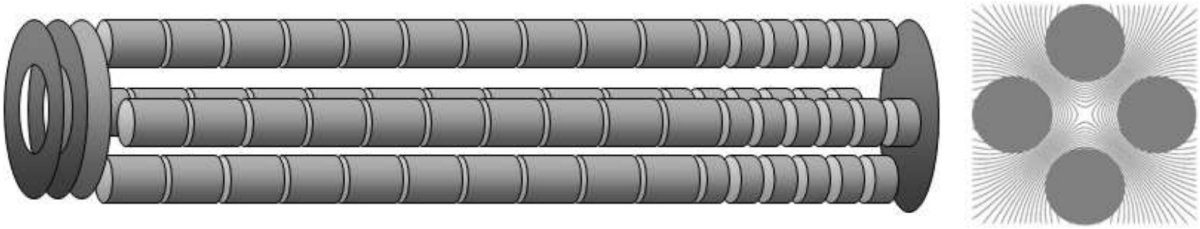

(a) View of the four segmented rods of the RFQCB (left) and the equipotentials of the confining field (right).

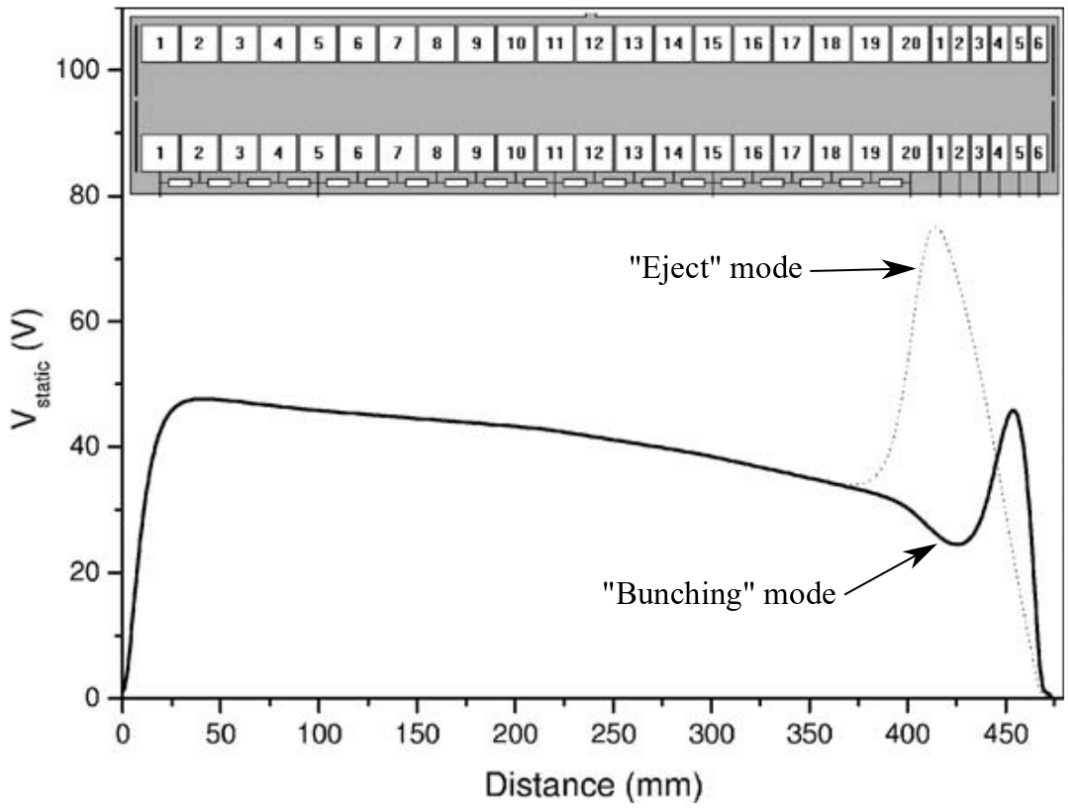

(b) RFQCB potential structure. 26 segments separated by 300 μm constitute the four parallel rods of the RFQCB. Among them, 20 are "cooling" segments and the 6 remaining are switchable to either "bunch" or "eject" mode [Ban04].

Figure 2.5: RFQCB features

2.2.3 Transfer line

Whenever an ion bunch gets ejected from the RFQCB, it needs to be brought toward the Paul trap. First of all, the RFQCB is secluded on a high voltage platform and as such, the ion bunch has a high potential energy which needs to be lowered when exiting this platform and returning to the grounded line. Indeed, we reiterate that the objective here is to trap a low-energy ion bunch. The technique used in the LPCTrap device for such a task is through the usage of a Pulse Drift Tube (PDT)[7]. The operation principle is quite simple: whenever a full ion bunch (or most of it) is inside the PDT, it is switched from a high voltage to a lower one. The time it takes to switch the voltage is about 500 ns, around one quarter of the time needed for *e.g.* an ion of mass 6 to go through the tube. In the case of LPCTrap, the first PDT (PD1), which is located right after the RFQCB switches from the platform voltage to 1 kV, leaving 1 keV of kinetic energy to the ions. Another PDT (PD2) is just before the Paul trap and allows to further lower the bunch energy, going from about 1 keV to 120 eV. Between these two tubes, there is a "bunch manager" portion of the LPCTrap which we call the *transfer line* where the vacuum is the same as in the first chamber (10^5 mbar) and which contains multiple tools:

- **Lens & X-Y Deflector**: This system allows to adjust the focus and the alignment of the bunch.
- **"Le hamster"**: The name given to the attenuator wheel. Viewed from the top, it has a dodecagon shape that can be rotated around its central point. It thus has six different attenuation settings. In decreasing order of transmitted bunch size: H1(100%), H2(40%), H3(10.7%), H4(1%), H5(0.25%), H6(0.0087%=$\frac{1}{115}$%).
- **"L'espion"**: The French word for "spy". It is a retractable MicroChannel Plate (MCP) detector[8] which allows to measure the time structure and the energy dispersion of the bunches. Transparent polarizable grids are mounted on it. For a given voltage, an incoming ion will be stopped by the potential barrier unless it has enough energy to cross it. By setting different voltages, it is possible to scan the energy dispersion of the bunches for specific tuning of the whole apparatus. Moreover, another MCP located on the beam axis behind the Paul trap can be used conjointly with "L'espion" to perform Time-Of-Flight (TOF) measurements, allowing us to identify the different masses present in the ion bunches. Of course, when "L'espion" is in use the bunch is stopped on it. These ToF measurements must be done first by using one of the two MCPs, then the other one and assume that the characteristic of the ion bunch did not change in the meantime. This is how we reach an estimate of the contaminants present in the bunch.

Just before the entrance of the Paul trap, there is another simple device which allows to chop out unwanted neutral gas: the vacuum conductance. Indeed, while the ions are cooled and get bunched in the RFQCB, neutralization occurs as well, increasing the number of neutral radioactive atoms. Those atoms are not subjected to the EM fields guiding the bunch throughout the line and as such, they move freely in all directions, including towards the entrance of the Paul trap. The vacuum conductance is a thin tube (diameter of 20 mm) on the bunch axis which decreases the number of contaminants inside the Paul trap. This allows not only to perform cleaner measurements by having less out-trap decays, but it is also a way to better control the real pressure in the chamber and, ergo, the buffer gas injection in the measurement Paul trap (see next section).

2.2.4 Transparent Paul Trap

Along with the RFQCB, the Paul trap is the main key piece of the LPCTrap device. Lots of work was done on the design of the transparent Paul trap to finally reach its current blueprint (fig. 2.6). This final layout is the result of a compromise between the generation of a field as close as possible to an ideal trapping field while maximising the geometrical efficiency of detection. This Paul trap has been working successfully for years, enabling to accumulate multiple high-quality experimental datasets. The reader might note three ring-electrode pairs in the actual design[9]. Fig. 2.6c shows these rings in more details and each has a specific voltage V_i associated with the ring A_i. We will get back to these voltages right after having presented the working of the Paul traps.

[7] a.k.a. Pulse Down Tube or Pulsed Cavity.

[8] More details on such detectors are given in section 2.3.2.

[9] The design with three electrode pairs is the only one that was constructed in two different versions. The addition of "fins" to the bare rings is intended to lower the asymmetry coming from the proximity of the trap power supply. This constitutes the second version now in usage.

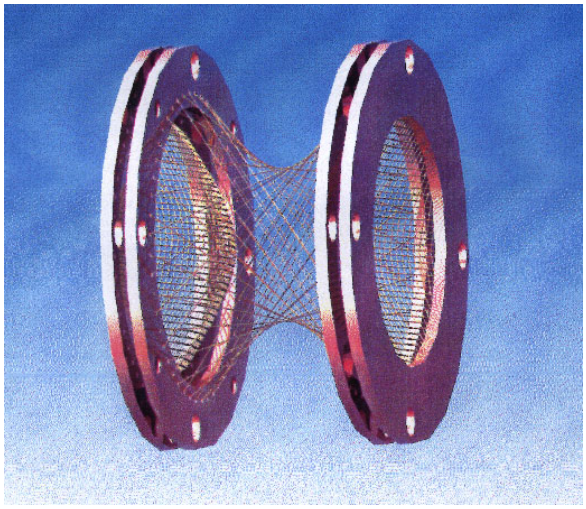

(a) Historical design. It was found that the scattering on the fishnet-like structure was too important through simulation, consequently this design was never used with radioactive beams.

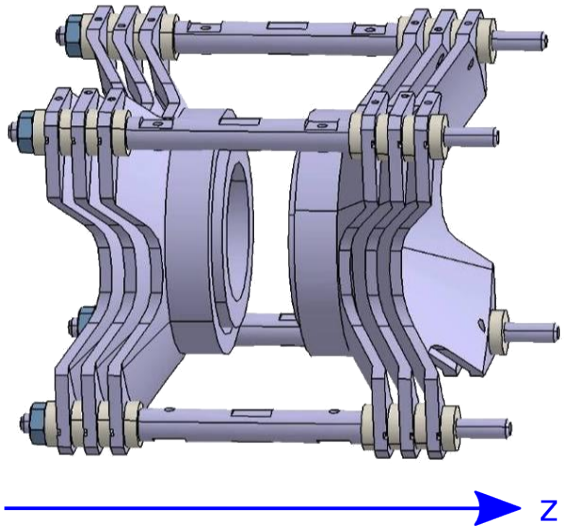

(b) Current design

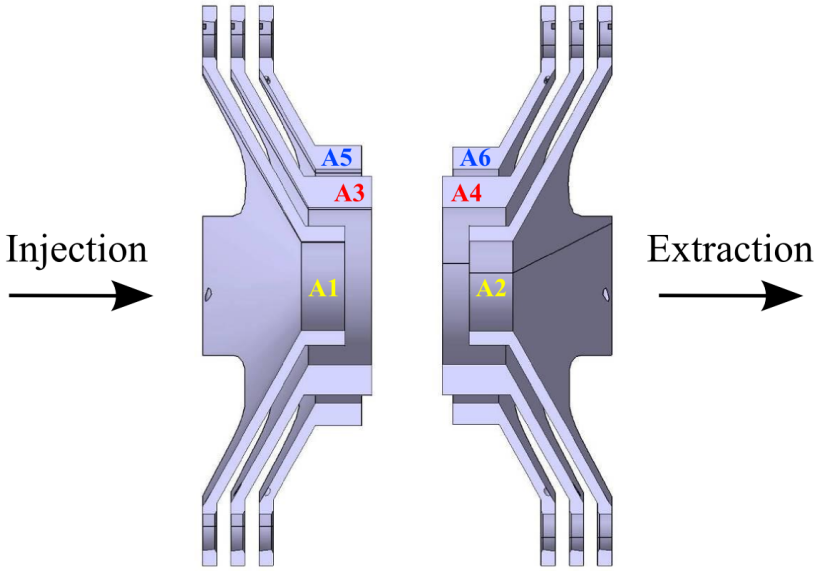

(c) Layout of the three electrode pairs constituting the Paul trap.

Figure 2.6: LPCTrap's Paul trap designs

The concepts behind the Paul trap are rather simple and elegant to the point that Hans G. Dehmelt and Wolfgang Paul were conjointly awarded half of the 1989 Nobel prize. While Dehmelt developed the Penning traps, Paul lead the team which invented the trap which bears his name. Both the Penning and the Paul traps are devices which make use of electromagnetic fields in order to confine ions. The difference lies in the way they do it. Indeed, while the Penning trap is using both electric and magnetic static fields, the Paul trap requires a RadioFrequency (RF)[10] voltage yielding a confining dynamic electric field without magnetic field. In chapter 3, we will be modeling both devices, although we will focus on Paul traps. This is why it is useful to give some details on its operation. The following is taken from the summary Paul published ensuing his Nobel prize award [Paul90].

The fundamental idea behind Paul traps is that we want a confining field towards the origin (taken at the center of the trap):

$$\mathbf{F} = -\alpha\ \mathbf{r} \tag{2.1}$$

with α some constant and $\mathbf{r}$ the radial direction[11]. We are looking for a potential expression which could generate such a force. In the absence of charge, Gauss's law states that:

$$\nabla \cdot \mathbf{E} = 0 \tag{2.2}$$

And we know that for any electric field, we have:

$$\mathbf{E} = -\nabla V \tag{2.3}$$

with V the potential we are looking for. Injecting 2.3 in 2.2 yields the Laplace equation:

$$\Delta V = 0 \tag{2.4}$$

The general expression for such a potential is:

$$V = V_0(ax^2 + by^2 + cz^2) \tag{2.5}$$

where two different solution sets exist for a, b and c (apart from the trivial $a = b = c = 0$). They are as follows:

- *2D Paul trap*: $a = -b$ and $c = 0$ yields nothing less than a RFQCB field. Equipotentials of such a potential are represented in fig. 2.5a.
- *3D Paul trap*: $a = b = -c/2$ bestows our transparent Paul trap, see fig. 2.7c.

Although these are solutions of the Laplace equation, it is still inadequate to trap ions because there is always an escape direction. The way to mend this is through the application of a periodic RF voltage on the relevant electrodes emitting the field, thus changing this escape direction continuously. In practice this is done by adding a RF component in the potential such that:

$$V_0 = \varphi_0 + \varphi_1 \cos(2\pi f_{RF} t) \tag{2.6}$$

with f_{RF} the applied RF. Now we want to reach the equations of motion to see if there is anything remarkable hidden in them. We are only in the presence of an electric field, thus we have the Lorentz force:

$$\frac{d^2\mathbf{r}}{dt^2} = \frac{e}{m}\mathbf{E} \tag{2.7}$$

with e the charge of the trapped particle[12] and m its mass. With 2.6 and the configuration of a 3D Paul trap, we can explicit equation 2.5.

[10] The typical frequencies for trapping purposes are in MHz, thus the RF name.
[11] It will become clearer below that this coordinate may be associated to either a cylindrical or a spherical frame, depending on the kind of Paul trap.
[12] e was taken instead of q because q will be a Mathieu parameter later on.

We will be adding a term to account for the quadrupolar geometry which will generate our parabolic potential (see [Paul90]):

$$V = \frac{1}{r_0^2}(\varphi_0 + \varphi_1 \cos(2\pi f_{RF} t))(x^2 + y^2 - 2z^2) \tag{2.8}$$

with r_0^2 being related to the geometry of the electrodes. Reusing equation 2.3, we can find our electric field:

$$\mathbf{E} = -\frac{2}{r_0^2}(\varphi_0 + \varphi_1 \cos(2\pi f_{RF} t))(\mathbf{x} + \mathbf{y} - 2\mathbf{z}) \tag{2.9}$$

and our motion:

$$\frac{d^2\mathbf{r}}{dt^2} = -\frac{2e}{mr_0^2}(\varphi_0 + \varphi_1 \cos(2\pi f_{RF} t))(\mathbf{x} + \mathbf{y} - 2\mathbf{z}) \tag{2.10}$$

We now introduce the Mathieu parameters a and q and we rewrite the time expression:

$$a = \frac{2e\varphi_0}{mr_0^2\pi^2 f_{RF}^2} \qquad q = \frac{e\varphi_1}{mr_0^2\pi^2 f_{RF}^2} \qquad \tau = \pi f_{RF} t \tag{2.11}$$

It is now possible to explicit our equations of motion:

$$\begin{aligned} \frac{d^2x}{d\tau^2} + \ (a + 2q\cos(2\tau))x = 0 \\ \frac{d^2y}{d\tau^2} + \ (a + 2q\cos(2\tau))y = 0 \\ \frac{d^2z}{d\tau^2} - 2(a + 2q\cos(2\tau))z = 0 \end{aligned} \tag{2.12}$$

which happen to be the Mathieu equations [Math68]. The so-called stability diagrams for different values of a and q are shown in fig. 2.7a, while fig. 2.7b gives the first stability region we are referring to when listing the possible optimizations of the transmission for the RFQCB in section 2.2.2. A typical configuration for $^{35}Ar^+$ yields the couple:

$$(a, q) = (0.0, 0.2189) \tag{2.13}$$

when applying only a RF potential of 120 V_{pp} ($\varphi_1 = 60$ V) at $f_{RF} = 0.7$ MHz in a trap of size $r_0 = 12.5$ mm. The solutions of the equations 2.12 can be written as the following infinite series [WSL59]:

$$u = A \sum_{n=-\infty}^{+\infty} C_{2n} \exp((\eta + 2ni)\tau) + B \sum_{n=-\infty}^{+\infty} C_{2n} \exp(-(\eta + 2ni)\tau) \tag{2.14}$$

with u any coordinate, A and B constants depending on the initial conditions and η a complex number. Since our physical case implies to avoid any divergence, *i.e.* we wish to stay in a bound state, in $\eta = \alpha + \beta i$, α must be set to 0. We are thus left with:

$$u = A \sum_{n=-\infty}^{+\infty} C_{2n} \exp((\beta + 2n)i\tau) + B \sum_{n=-\infty}^{+\infty} C_{2n} \exp(-(\beta + 2n)i\tau) \tag{2.15}$$

Each term of this solution is a motion harmonic of order n with the angular frequency:

$$\omega_n = (\beta + 2n)\pi f_{RF} \tag{2.16}$$

In practice, the first two harmonics are dominant:

$$\begin{aligned} \omega_0 = \beta\pi f_{RF} \\ \omega_{-1} = (\beta - 2)\pi f_{RF} \qquad \omega_{+1} = (\beta + 2)\pi f_{RF} \end{aligned} \tag{2.17}$$

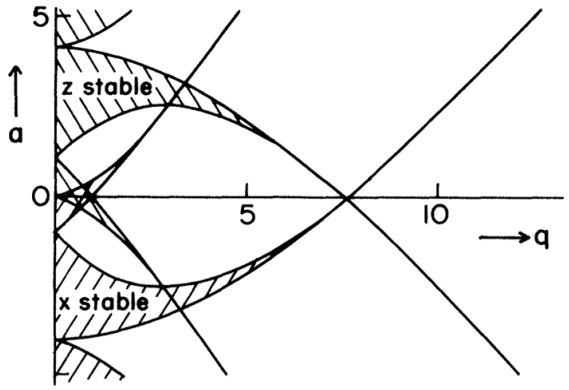

(a) Stability diagram

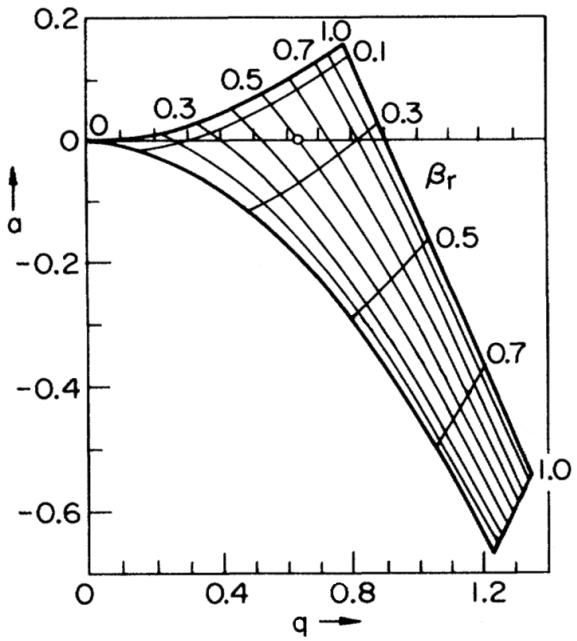

(b) Stability diagram (zoom)

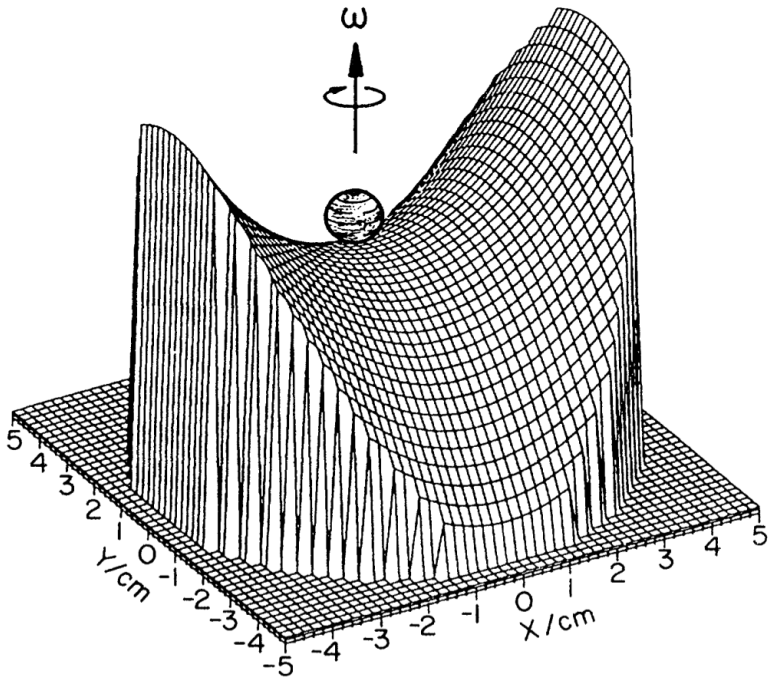

(c) 3D trapping potential representation. Applying a RF voltage in addition to a constant one with a driving frequency ω allows to constantly change the escape direction and successfully trap charged particles.

Figure 2.7: Paul trap stability diagrams as a function of the Mathieu parameters and 3D trapping potential representation [Paul90].

For experimental ease reasons, we tend to stay in the first stability region (see fig. 2.7b) which happens to be delimited by integer values of β [Dela02]. In this region, considering β small is a good approximation and this implies that ω_0 will be associated with a slowly-changing component. On the other hand, $\omega_{\pm 1}$ will almost be equal to the driving RF frequency $\omega_{RF} = 2\pi f_{RF}$ and will correspond to a swiftly-changing component. Thereby, the motions associated with ω_0 and $\omega_{\pm 1}$ are called respectively macromotion (or secular motion) and micromotion.

Now that we have some understanding of the Paul trap main features, it is important to note that all these periodic or quasi-periodic motions as well as the trapping itself are not possible unless the ions have reached a suitable low-energy thermal equilibrium[13]. Just like a constant flow of neutral gas is ensured in the RFQCB for the same purpose, a buffer gas is also injected in the Paul trap to provide the required thermalization. In fact, there is a specific thermalization time during the initial moments of a trapped bunch. This evaporation[14] phase lasts for a few μs experimentally and once it is complete, we are able to work with a smoother, from the phase space point of view, trapped ion cloud. It was calculated elsewhere [MA07] that the typical potential depth of the Paul trap is a few electronvolts, hence advocating both the chosen gas features and the PD2 setting. Without this gas, the vacuum inside the trap chamber is $\sim 5 \times 10^{-8}$ mbar and with gas injection it is $\sim 1.5 \times 10^{-5}$ mbar.

The simulations described in chapter 3 begin with the trapping of a randomly generated bunch. Indeed, the thermalization kills most of the information about the initial state prior to the injection in the Paul trap. In a way, the smoothing mentionned above is a constant "reset" of the incoming bunch, providing a constant initial state to work with from a detection point of view.

As we said at the beginning of the section, in fig. 2.6c there are three pairs of ring-electrodes. Each pair has a specific function:

- $[A_1 - A_2]$: Quadrupolar RF confining field. The amplitude provided by the power supply is chosen so that the potential is as deep as possible (always set at 120 V). In order to stay in the chosen stability region (constant Mathieu parameter), we can play on another parameter: f_{RF} (see equation 2.11).
- $[A_3 - A_4]$: These voltages depend on the ion bunch energy and that energy is always brought to the same value for all studied ions.
  - injection: $V_3 = 130\ V$; $V_4 = 300\ V$
  - during trapping: $V_3 = V_4 = 0\ V$
  - extraction: $V_3 = 300\ V$; $V_4 = 0\ V$. $V_3 = 300\ V$ was chosen so that the ejection kick is important enough to ensure detection on the extraction MCP (the one on the beam axis).
- $[A_5 - A_6]$: The real trapping field is not perfect. These two voltages bring some corrections to the imperfect field.

[13] This concept will be referred to as "thermalization" in the following.

[14] This analogy with boiling liquid which subsides through both the ejection of its most energetic parts and the cooling of the remnant is correct since it is exactly what happens when trapping an ion bunch.

2.3 Detection set-up

As was explained in the first chapter, the LPCTrap device is designed to measure two quantities, both of which are extracted from the TOF spectrum of the Recoil Ion (RI). On the one hand, we are interested in the value of $a_{\beta\nu}$which is extracted from the shape of the TOF spectrum. On the other hand we reach for the ShakeOff (SO) probabilities of the RI which is taken from the relative count in the different peaks of the same spectrum. These two aspects are the fundamental ideas justifying the whole detection set-up design.

In the last section, we ended with the description of the Paul trap which is actually sitting in the center of the detection chamber. This will be our starting point here: once the radioactive ion cloud is trapped and thermalized, the relevant data for the two quantities just mentioned begins to accumulate through the detectors. In β decay, the neutrino can hardly be detected because of its remarkably low cross section for any interaction with matter. To reconstruct a full decay, we are thus left with the remaining products, namely the RI and the β particle. From theory, we know that the *tensor* value of $a_{\beta\nu}$ tends to maximize the discrepancies of kinematic observables when compared to the expected V-A $a_{\beta\nu}$ values whenever the angle between the two detectable decay products is π rad. This is not so true for a *scalar* interaction, nevertheless, the statistical count is always maximized at this angle. Moreover, we must have a consistency between this theoretical fact and the design of the Paul trap electrodes. This leads to the current detector layout where both the β telescope and the RI detection device are facing each other on the x axis while being perpendicular to the beam (z axis) as shown in fig. 2.8.

As specified in section 2.2.3, there is an extraction detector, a MCP, located inside the detection chamber along the beam axis. This MCP is not directly used to collect data, it is rather yet another possible diagnostic check tool. Apart from the possible TOF measurement when used conjointly with "L'espion" (see 2.2.3), this MCP allows us to roughly count the number of ions of an ejected bunch from the trap and let us see if there are any trapped ions at all !

Finally, the TOF of a given decay is the time between the detection of a β particle and of its associated RI. Since we are able to detect the energy of the β particle, we can account for it in the TOF calculation.

2.3.1 β Telescope

The β telescope is not in the same vacuum as the Paul trap. Indeed, its electronic components degas, which could bring an important contamination in the trap, thereby a thin (1.5 μ m) aluminized mylar foil isolates this device. Instead of being under 5×10^{-8} mbar (without buffer gas), its vacuum is less extensive, being set at 2×10^{-3} mbar. Two distinct detectors constitute the β telescope: A Double-Sided Striped Silicon Detector (DSSSD) and a plastic scintillator. An overview is shown in fig. 2.9.

2.3.1.1 DSSSD

The 60×60 mm^2 DSSSD features 60 vertical strips on the Junction side (J) and 60 horizontal strips on the Ohmic (Ω) side, each strip being 1 mm wide (the resolution in position is thus 1 mm^2). It is 300 μm thick and its nominal working voltage is 30 V in order to maximize the signal-to-noise ratio. This structure allows to detect the position where the β particle passed. Like any semiconductor, its signal comes from the capture of created electrons (negative charges) and holes (positive charges) whenever a β particle interacts with the depleted zone. Both the J and the Ω sides have their own embedded chip (VA-Rich) whose role is to pre-amplify, shape and multiplex the signal coming from each distinct strip group. A CAEN V550 module (standard VME ADC) is responsible for un-multiplexing and digitalizing the DSSSD information. Each strip thus has its energy spectrum, although most of the time it reads only background since the reading of all the strips is triggered by the signal provided by the plastic scintillator. This is why the energy spectrum has two distinct components: the first one being the prevalent background pedestal and the second one being the signal. The good separation of these two parts is essential to perform a correct fit on the "real" energy signal. This separation is related to the electronic noise and is very sensitive to a proper shielding of the relevant wires.

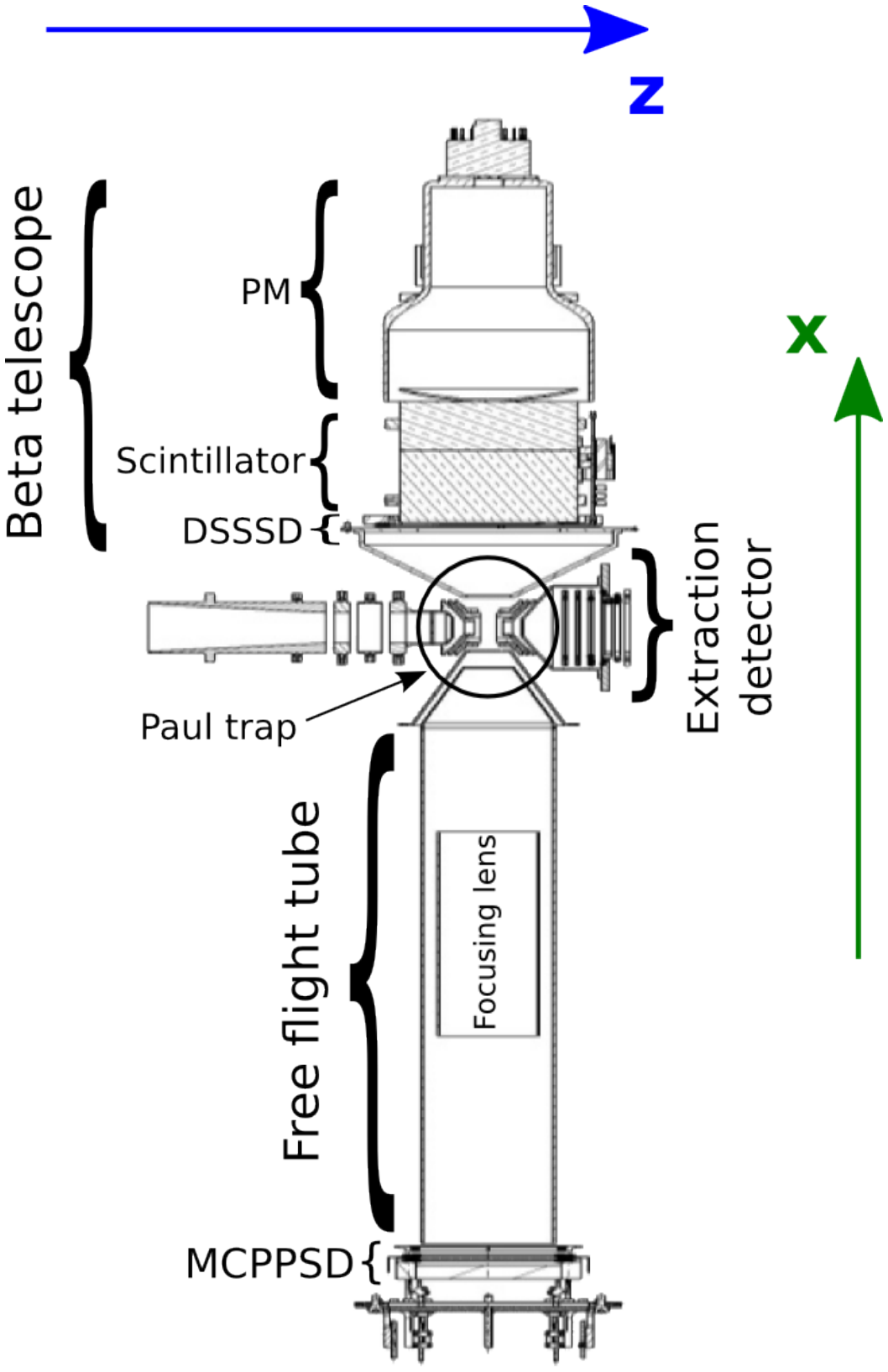

Figure 2.8: Detection set-up overview

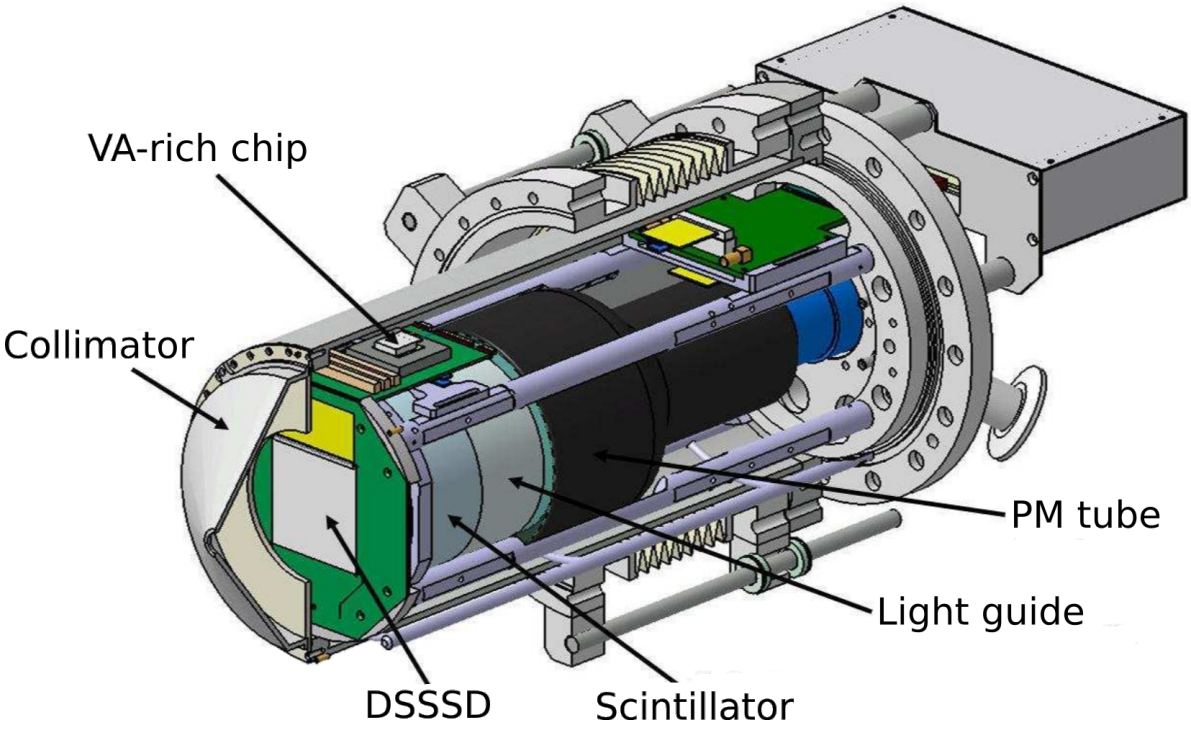

Figure 2.9: β telescope overview

2.3.1.2 Plastic scintillator

The plastic scintillator is a BC-400 type scintillating around 430 nm. It has a cylindrical shape with a diameter of 110 mm, about twice the side of the DSSSD, and a thickness of 70 mm, more than enough to stop the β we are interested in. These features allow us to detect the full energy of the β particles and to focus the interaction around the center of the scintillator, implying a homogeneous light collection. This piece is coupled to a PhotoMultiplier (PM) through a light guide in order to match the geometry of both. The PM is a XP4592B model of Photonis and posseses these characteristics[15]:

- Number of stages: 8
- Operating voltages:
  - Minimum: 1.1 kV
  - Typical: 1.5 kV
  - Maximum: 2.0 kV
- Gain at typical voltage: 5.0×10^5
- Time response:
  - Risetime: 2.5 ns
  - Resolution: 100 ps. This is obtained with a proper tuning of the CFD coupled to the PM.
- Relative energy resolution: $\frac{\Delta E}{E} \simeq 25\%$ for the scintillator-PM ensemble.

This second part of the β telescope is responsible for sending the START signal to the whole acquisition which includes the starting time mark for the TOF measurement of the RI, the saving of the current applied RF[16] and the time in the cycle. The latter is recorded using a $0-10$ V ramp synchronized with the beginning and ending of each cycle. The RF information comes directly from the generator used to send the signal to the Paul trap electrodes.

[15] Taken from an old datasheet on http://www.photonis.com

[16] This is a systematic effect. Indeed, depending on the RF we are in, the position of the TOF rising edge will slightly shift.

Calibration source Inside the Paul trap chamber, there is another "offline" retractable source made of ^{90}Sr $-^{90}Y$ (β^- emitter) and it is employed for the calibration of the β telescope.

2.3.2 Recoil ion detection

Sitting on the opposite side of the β telescope is the RI detection device (see fig. 2.10c). After entering its collimator, the RI first passes through a grounded transparent grid providing insulation from the Paul trap fields. A little further sits yet another grid which is polarized (typically at -2 kV), thus accelerating the RI proportionnaly to its charge. Indeed, the idea is to separate the different charge states that may rise following the β decay itself (the so-called shakeoff effect, see 1.4). After reaching the second grid, the RI enters a free flight tube where the separation is given time to occur. To avoid any loss, a lens, whose role is to focus the RI towards the axis of the device, is installed in the tube. Finally, the RI reaches its detector: a MicroChannel Plate Position Sensitive Detector (MCPPSD).

Prior to the MCP itself, another grid at -2 kV provides a proper field homogeneity toward the MCP polarized at -4 kV. The consequent post-acceleration allows to reach the efficiency plateau plotted in fig. 2.10a. The MCP is made with a dielectric material and pierced regularly with holes, or channels, making half the surface sensitive. When a RI enters a channel and impinges on the edge, electrons are ejected which themselves continue to impinge and create more electrons and so on. An avalanche is thus triggered and gets detected on the other side of the MCP, providing the signal t_{gal} which is the STOP signal for the TOF measurement. The avalanche does not stop here and continues until it reaches the anode (see fig. 2.10b) which provides the PS part of the MCPPSD, another systematic effect control tool. Indeed, delay lines sit underneath the MCP and are made of two perpendicular wires winding: one for each dimension. At the end of each wire (there is one wire winded multiple times for x and another one for y), the signal is collected with its timestamp. With t_{gal} the "timewatch" START, each four signals has an associated STOP time. The difference between t_{X1} and t_{X2} is related to the position in x with the same for y and the sum of each time pair is related to the wire length. With the difference, we have the position and with the sum, we have a way to discriminate non-physical signals yielding absurd values. The resolution for the position is around 140 μm. A full characterization of our MCPPSD was done earlier [LiHB05].

2.3.3 Acquisition

Let us recap the signals recorded during an experiment:

- RI side:
  - t_{gal}: the STOP time for the TOF measurement.
  - t_{X1}, t_{X2}, t_{Y1} and t_{Y2}: the information on the position of the RI.
  - Q_{MCP}: the deposited charge on the MCP.
- β side:
  - The energy deposited in the DSSSD (signal amplitude of each strip).
  - $Q_{scint.}$: The energy deposited in the plastic scintillator with the photomultiplication.
- Systematic effects purpose:
  - T_{cycle}: Timestamp of the event in the measurement cycle.
  - φ_{RF}: The current applied RF phase (between 0 and 2π).

Reconstructing the kinematic only requires the TOF of the RI and the position of the two detected decay products. The other observables allow a more thorough data control and a better systematic effects study.

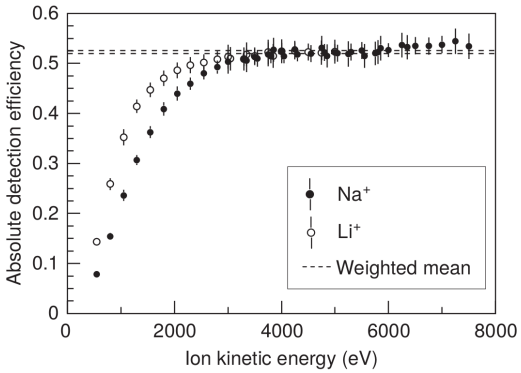

(a) MCP absolute detection efficiency where the highest efficiency appears as a plateau a little lower than 50%. This is due to the fact that only half the surface is sensitive, *i.e.* pierced with channels [LiHB05].

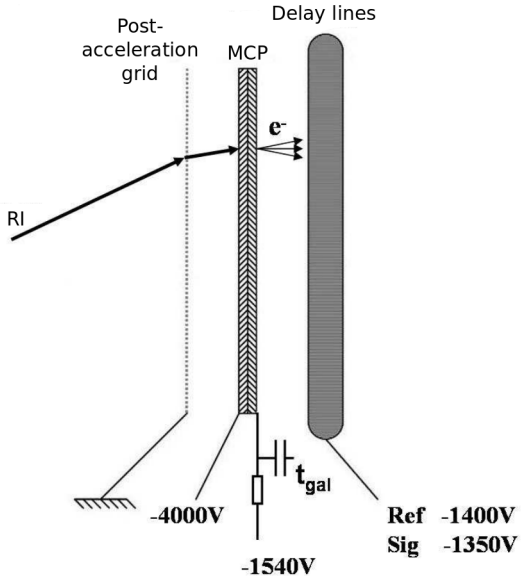

(b) MCPPSD scheme showing the post-acceleration grid required to reach the highest possible efficiency, the MCP itself which lets the RI create an electron avalanche which gets detected at the end of the channels and the delay lines which provide the sensitivity to position.

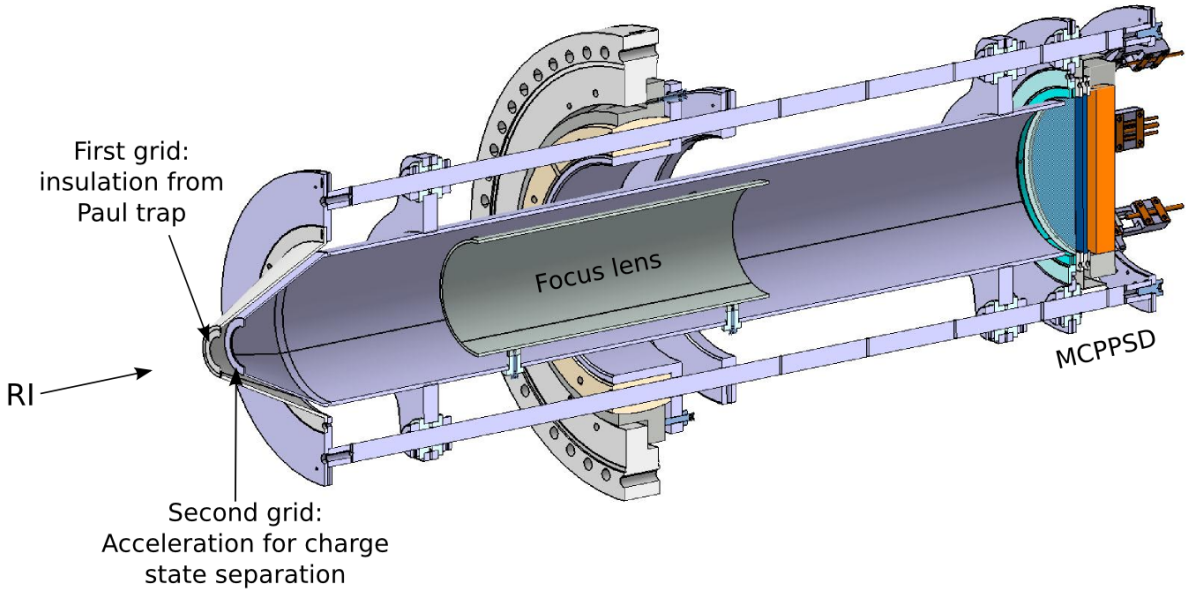

(c) RI full detection device. The biggest part is the free flight tube which gives enough time to the accelerated ions to separate according to their charge state.

Figure 2.10: MCPPSD features

Regarding the signal conversion modules, LPCTrap features:

- Two QDCs for the charge coding of the scintillator and the MCPPSD;
- One TDC for the TOF of the RI;
- One TDC to reconstruct the position of the RI (delay lines signal);
- One ADC to measure the timestamp in the current cycle;
- One TDC to record the current applied RF phase;
- One ADC to save the DSSSD signals.

Except for the DSSSD, all signals are converted with VXI modules (XDC_3214) developed at GANIL, allowing an asynchronous processing (all triggered channels must be ascertained by the trigger that their validation point is inside the validation gate). The acquisition trigger (scintillator START) is sent to a Grand Master Trigger, thus opening the validation gate the length of which depends upon the studied nucleus. This length is the maximum time allowed for the detection of a RI. The validation point of the QDC_{MCP} and TDC_{TOF} VXI modules are delayed, thus casting aside negative timestamps (STOP before START). These events are fortuitous coincidences to subtract during the analysis phase.

Concerning the DSSSD, the silicon strips signals are recorded in a synchronous manner using a VME module suitable for signal multiplexing.

Section 4.1 reviews these signals and quickly shows how they are used in the data analysis.

2.4 Campaigns

For almost ten years now, three nuclei were studied with LPCTrap through eight experiments, namely $^6He^+$, $^{35}Ar^+$ and $^{19}Ne^+$. This section is a global summary of all these experiments and the main results of them. For all these nuclei, the objectives were more or less the same: measure $a_{\beta\nu}$ to constrain the existence of exotic current and, in mirror transitions, increase the precision on V_{ud} (see chapter 1). Moreoever, LPCTrap is able, since 2010, to measure the SO probabilities following a given β decay. A timeline representing all the experiments done is shown in fig. 2.11.

From a global scope, an important feature of the LPCTrap device is the total efficiency (ε_{tot}). It represents the percentage of ions being actually trapped compared to the number of ions delivered at the entrance of the apparatus and is equal to:

$$\varepsilon_{tot} = \varepsilon_{RFQCB} \times \varepsilon_{transfer} \times \varepsilon_{trapping} \tag{2.18}$$

where $\varepsilon_{transfer} = \varepsilon_{PD1} \times \varepsilon_{line} \times \varepsilon_{PD2}$. Indeed, the efficiency was measured for each LPCTrap part. The $transfer$ subscript refers to the part between PD1 and PD2. It is important to note that this efficiency depends upon the chosen cycle length, this is why this total efficiency will be presented as a function of that time. This same efficiency will also be presented on a *per second* basis using the notation ε_{tot}^{sec}.

Thorough work was done to optimize the transmission throughout the line. The obtained parameters are listed in appendix 5.1.

2.4.1 $^6He^+$

$^6He^+$ was the first ion to be studied with LPCTrap and multiple reasons motivated that choice at the time and later on:

1. **Daughter state:** The most obvious reasons are shown in the decay scheme of fig. 2.12. We can see that the only possible transition is toward a stable fundamental level of the ^6Li daughter nucleus. Having no excited levels with possible gamma de-excitation is an asset in that the RI kinematic will not be altered, thus avoiding a systematic error source.

2. **Lifetime:** In the same scheme, we also note that the lifetime of $^6He^+$ is 806.7 ms. This is high enough to be able to drive the beam toward the trap and low enough to provide a high number of detectable decay events.

3. **Q-value:** the Q-value is rather important in this transition ($Q_\beta = 3.5078$ MeV), yielding a high kinetic energy ($T_{RI_{max}} \simeq 1.4$ keV) for the RI since it is light ($m = 6$). This facilitates the detection of the RI.

4. **Pure GT:** In 1963, Johnson et al. published a high precision measurement of $a_{\beta\nu}$ in pure GT transition for ^6He [JPC63]. Years of effort were then dedicated to reach the highest possible precision in F decays where the pinnacle was reached in 1999 with the work presented in [Adel99]. After decades of experimental development, it was natural to return to GT transitions and $^6He^+$ goes through a pure one.

5. **Production:** SPIRAL is able to produce high amounts of $^6He^+$with up to 2×10^8 ions/s.

6. **Shake-off:** The daughter Lithium ion is expected to have a 2+ charge state since this is a β^- decay, if it was not for the SO effect. The latter may ionize the Lithium further by ejecting the remaining electron. This is a textbook case where only two charge states are possible in the final state and only one is induced by the SO effect.

As was discussed in chapter 1, there is a dependence between the value of $a_{\beta\nu}$ and the kinetic energy and momentum statistical distribution in the decay products. For exotic decays in GT transition, *i.e.* going through a tensor interaction, the RI and the β particle are preferably emitted back-to-back. This influenced the π rad geometry of the LPCTrap detection set-up.

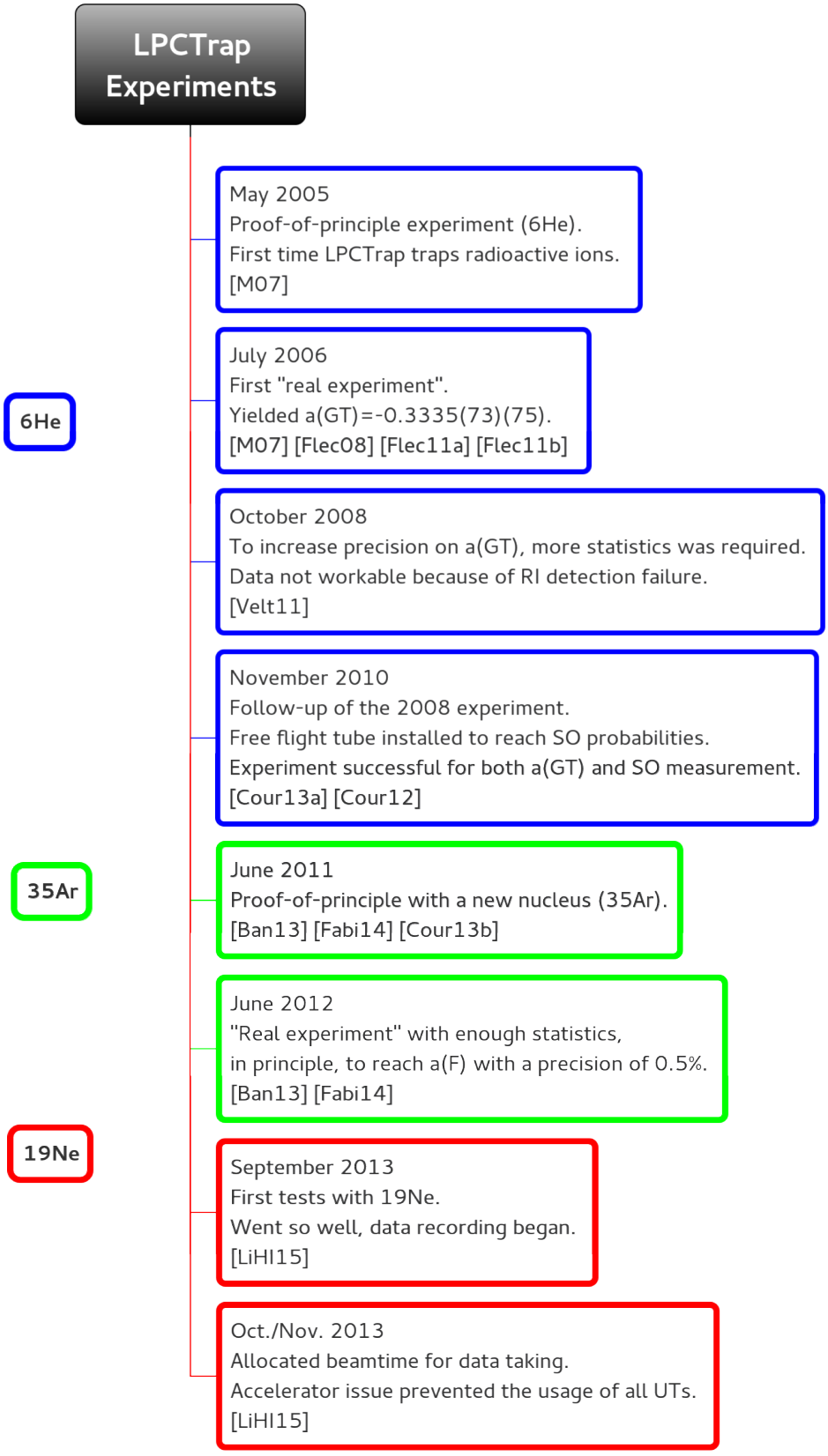

Figure 2.11: Experiments timeline at LPCTrap.

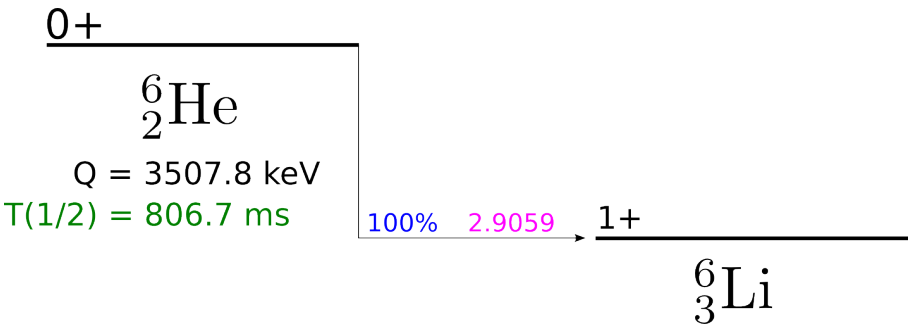

Figure 2.12: $^{6}He^{+}$ full decay scheme. Only one possible daughter state through a pure GT transition. A $^{6}He^{+}$ ion decaying results in a monoelectron Lithium ion: the perfect case to study the SO following β decay.

The buffer gas utilized in the RFQCB and the Paul trap was the molecular H_2, the choice of an element lighter than Helium being rather limited. Moreover, the cross section for charge exchange between neutral and ionized Helium being resonant, neutral Helium was not withheld as a buffer gas solution. This led to the choice of H_2 where this cross section is still high, leading to non-negligible losses in the RFQCB during the bunching phase.

Four different experiments took place with $^{6}He^{+}$.

2.4.1.1 May 2005

This was the first experiment done with $^{6}He^{+}$ and served as a proof-of-principle [MA07; M07]. It showed that radioactive ions coming from the SPIRAL facility and going all the way through the LPCTrap device could actually get trapped and detection in coincidence of the decaying products was possible. This objective was achieved during this first experiment where about 150 good[17] coincidences were gathered, milestoning multiple years of experimental development. At the time, the group observed a huge contamination of $^{12}C^{2+}$ coming from the source. With $\frac{q}{m} = \frac{1}{6}$ for $^{6}He^{+}$ and for the $^{12}C^{2+}$, the resolution of the mass separator at the source is not high enough to jettison the contaminant. The LPCTrap line was not well optimized as well, leaving room to a lot of improvement in the statistical accuracy, especially through the lowering of out-trap coincidences. Fig. 2.13 shows the TOF spectrum obtained at the time. Let us sum up the main features of this experiment:

- **Efficiency:** $\varepsilon_{tot}(10\text{ ms}) = 1.5 \times 10^{-3}$ %
- **Typical extracted bunch size:** 225 ions
- **Total coincidences:** 1000
- **"Good" coincidences:** 150
- **Estimated "good" coincidences rate:** 0.007 Hz
- **Beam intensity:** 3×10^{7} $^{6}He^{+}$ (4.5 pA) ions for a total of 200 nA. The vast majority of the beam is made of $^{12}C^{2+}$ contaminants.

Conclusion: the project is good to go with a thorough optimization of the whole apparatus and enough beamtime to reach a high statistics count, granting access to a precision of less than 1% on $a_{\beta\nu}$.

[17] Detecting the β and the RI in coincidence allows to clear up an important background count. Nonetheless, *bad* coincidences may still get detected and are of multiple origins, *e.g.* out-trap decays.

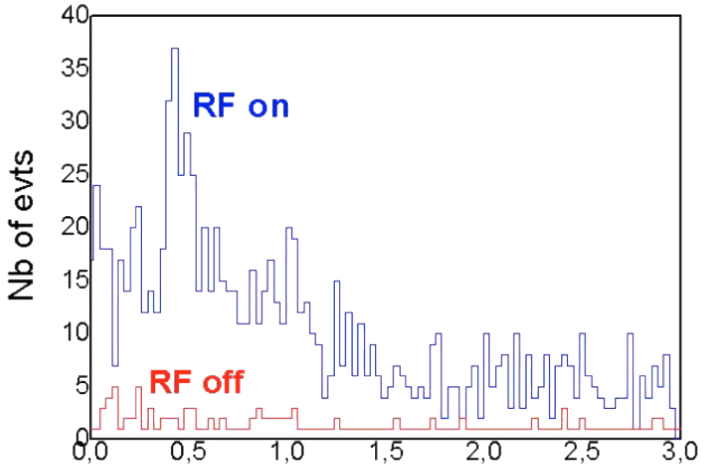

Figure 2.13: 2005 TOF spectrum, adapted from [M07].

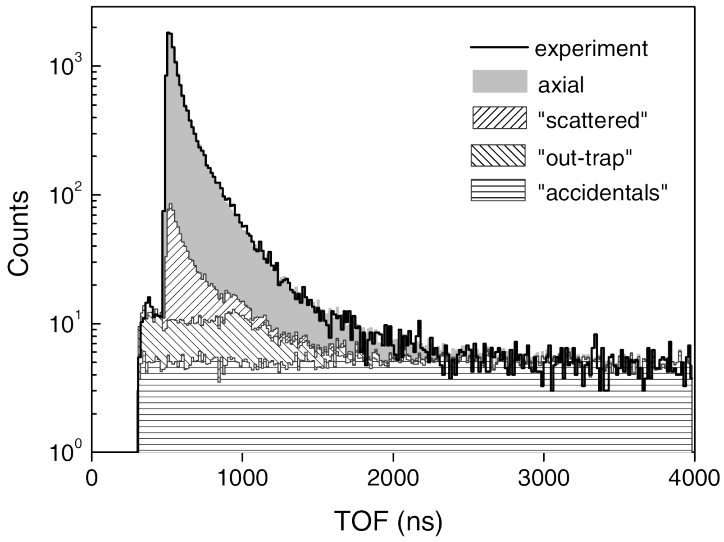

Figure 2.14: 2006 TOF spectrum. Before from the main TOF peak, a small out-trap contribution is visible - not to be mistaken with a SO peak. The detail of the different background and contributions are explained in [Flec11a].

2.4.1.2 July 2006

With the successful completion of the 2005 experiment, beamtime was allocated one year later to perform a full experiment to reach the value for $a_{\beta\nu}$. The results and the analysis were published in [Flec08], followed by a more detailed analysis in [Flec11a]. The TOF spectrum is shown in fig. 2.14. From a global point of view, the experiment was a success, enabling to stressfully test the apparatus. Nonetheless, the relative precision reached on $a_{\beta\nu}$ was around 3.1%, knowing the aim is to reach the subpercent level. $a_{\beta\nu}$ was found equal to:

$$a_{\beta\nu} = -0.3335\ (73)_{stat.}\ (75)_{syst.} \tag{2.19}$$

which is compatible with the SM for a pure Gamow-Teller transition.

Cycle (ms)	ε_{RFQCB} (%)	$\varepsilon_{transfer}$ (%)	$\varepsilon_{trapping}$ (%)	ε_{tot} (%)	ε_{tot}^{sec} (%)
20	8	2.5	4	8.0×10^{-3}	0.4
100	3.5	2	9	6.3×10^{-3}	6.3×10^{-2}

Table 2.1: 2006 experiment efficiencies. The 20 ms cycle was first chosen to optimize the line, then 100 ms was the proper cycle length for measurements, especially to give time to the trapped cloud to reach thermalization ($\sim$ 25 ms to reach 0.1 eV of mean kinetic energy).

Here is a list of the main features:

- **"Good" coincidences:** 5.0×10^4
- **Beam intensity:** $1 - 2 \times 10^8$ ^{6}He$^+$produced. The contamination of ^{12}C^{2+} was still present, but a fine tuning of a specific slit and an octupole enabled to chop out a vast part of it. The best repartition reached was 7×10^7 pps of ^{6}He$^+$ and 3×10^8 pps of ^{12}C^{2+}.
- **Efficiencies:** see table 2.1.
- **Incoming energy:** Usually, setting the source at high energies is better since it implies a better extraction from the ECR source and steering to LIRAT. However, it was observed that the total efficiency drops when the energy of the incoming ions is too high. The compromise was to set that energy at 10 kV [MA07].
- **Pressures:** $p_{RFQCB} = 7.0 \times 10^{-3}$ mbar and $p_{trap} = 2.0 \times 10^{-6}$ mbar
- **Typical bunch size:** 700 ions
- **Typical cloud size:** 2.4 mm diameter
- **Lifetimes:** $\tau_{RFQCB} = 37 \pm 5$ ms and $\tau_{trap} = 240$ ms

This important experiment allowed for the first time to establish a detailed list of the systematic error sources (p.17 in [Flec11a]). It is interesting to see that the majority of these can be extracted from data, while a few require offline measurements. The two most contributing ones, namely the proper ion cloud modeling inside the Paul trap and the dim knowledge on β scattering processes, are extracted from simulations. The work done at the time for the cloud is reported in [Flec11b].

The conclusion is that there is not enough statistics to reach the desired precision of 0.5% on $a_{\beta\nu}$. More events will not only increase the precision associated to the statistics, but the one associated with the systematic effects as well, since the uncertainty on most of them is extracted from the data themselves.

2.4.1.3 October 2008

Following the need for more statistics, the 2008 experiment amassed thirty times the "good" coincidence count of the 2006 experiment ($\sim 1.5 \times 10^6$). This was promising, enabling to reach, in principle, a statistical precision of 0.5% on $a_{\beta\nu}$. During the data analysis, it was found that the MCP had not functioned properly, having in fact a very low efficiency and erroneous readings on the delay lines. Unfortunately, this resulted in an unconclusive value for $a_{\beta\nu}$ [Velt11].

2.4.1.4 November 2010

It was for this experiment that the free flight tube was installed on the RI detection side and the fins on the Paul trap electrodes. This permitted to measure the SO probability of the ^{6}Li^{2+} following the β decay of ^{6}He$^+$ for the first time. Furthermore, the gathered data led to 1.2×10^6 "good" coincidences, which allows to reach the desired 0.5% precision on $a_{\beta\nu}$, in principle. No disfunctioning of the MCP was found this time, enabling a fine data analysis of the gathered data. Digging further into the data revealed a very high sensitivity to systematic effects that were not an issue previously. The conclusion of the analysis at the time was that controlling these systematic effects, especially through realistic simulations, rose as the new challenge to further sharpen the precision on $a_{\beta\nu}$ [Cour13a].

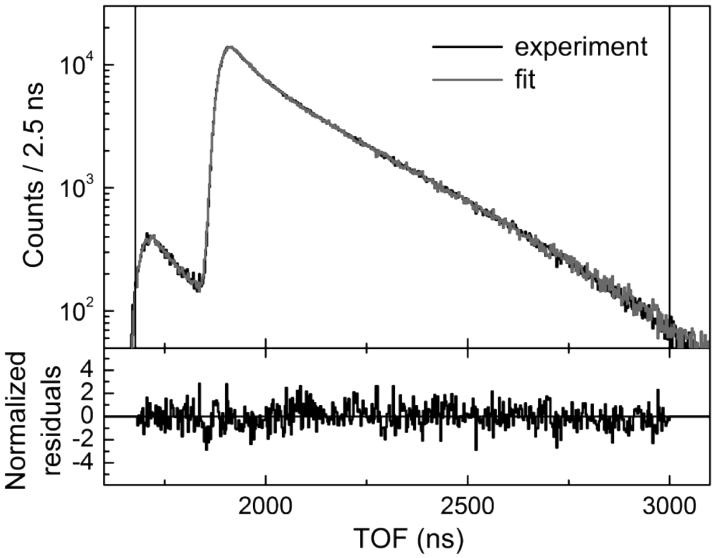

Figure 2.15: 2010 TOF spectrum. The different charge state peaks now clearly appear since the free flight tube was installed at this time. Adapted from [Cour12].

Ion	Cycle (ms)	ε_{RFQCB} (%)	$\varepsilon_{transfer}$ (%)	$\varepsilon_{trapping}$ (%)	ε_{tot} (%)	ε_{tot}^{sec} (%)
$^6Li^+$	8	$8-15$	$30-34$	$10-20$	$0.24-1$	$30-125$
$^6Li^+$	80	<10	$27.3-32.0$	$10-20$	$0.273-0.64$	$3.4125-8$
$^6Li^+$	200	<10	$27.3-31.9$	$10-20$	$0.273-0.638$	$1.365-3.19$
$^6He^+$	200	$1-1.5$	50	20	$0.1-0.15$	$0.5-0.75$

Table 2.2: 2010 experiment achieved efficiencies.

The radioactive beam had its nominal characteristics with some 10 nA of $^{12}C^{2+}$ for 30 pA of $^6He^+$(2.0×10^8 pps), with the usage of the slit spoke of above. It was found that a longer bunching time obviously yielded bigger bunches, but lowered the transmission of the RFQCB. A good compromise was found for a cycle length of 200 ms since the plateau for the bunch size is reached. This cycle length also responds to the fact that $\tau_{trap} = 146$ ms, that the radioactive lifetime of $^6He^+$ is ~ 800 ms, that we need a few tens of ms to reach the thermalization and that we want to perform a background measurement of 50 ms each cycle. Regarding the efficiencies, they are shown in table 2.2.

Although $a_{\beta\nu}$ was not extracted from this dataset yet, the needs to reach the SO probabilities are less and the work done was reported in [Cour12], with the TOF spectrum displayed in fig. 2.15. The $^6He^+$ decay is a textbook case since only one electron is subjugated to SO in the daughter Lithium. In the article, a simple calculation is done to predict the SO probability of that single electron and leads to $\langle P_{\mathrm{SO}}\rangle = 0.02322$. The experimental result is in perfect agreement with it: $P_{\mathrm{SO}}^{\mathrm{exp}} = 0.02339 \pm 0.00036$.

Conclusion: the data is of high quality, the results on the SO are concluding, but the analysis to reach $a_{\beta\nu}$ requires the completion of a thorough simulation of all aspects.

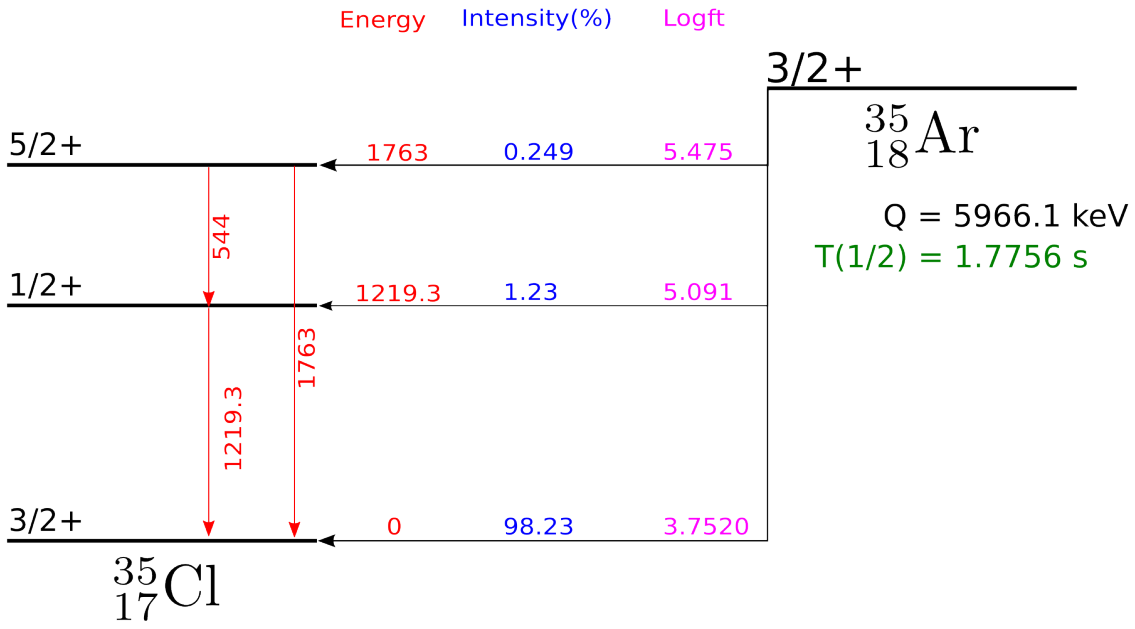

Figure 2.16: $^{35}Ar^{+}$ simplified decay scheme. Here, only the main contributing excited levels are shown

2.4.2 $^{35}Ar^{+}$

After having successfully gathered data with $^{6}He^{+}$, the group decided to perform a similar measurement in $^{35}Ar^{+}$, another element available at LIRAT. As explained in the chapter 1, it is important to remember that the measurement of $a_{\beta\nu}$ has not the sole purpose of finding exotic currents. Depending on the initial hypothesis, it may also serve the goal to increase the precision on V_{ud}, the first element of the CKM matrix. This is possible through the extraction of the mixing ratio ρ from our measurement of $a_{\beta\nu}$ and coupling it with other nuclear measurements (lifetime, transition intensities and Q-value). As shown on the decay scheme in fig. 2.16, $^{35}Ar^{+}$ is harder to work with for several reasons:

- The direct decay to the daughter Chlorine fundamental level has an intensity of 98%, a mirror transition mostly Fermi in nature. The remaining $\sim 2\%$ lands on short-lived excited states, implying an alteration of the RI momentum. The high precision context we are in implies that we should not neglect such a systematic effect.
- $^{35}Cl^{+}$ can be ionized in not only one but multiple charge states with the SO effect, rising up the challenge when compared to the ideal $^{6}Li^{+}$ case.
- Although the Q-value of the $^{35}Ar^{+}$decay (~ 6 MeV) is higher than the Q-value of $^{6}He^{+}$, the ^{35}Cl mass is also higher than the mass of ^{6}Li. All in all, this yields a maximum kinetic energy of 450 eV, three times less than what we had previously.
- In the Fermi transitions, the exotic Scalar current does not favor an emission at 180° (see chapter 1). Consequently, a high event count will be important.
- We are considering a β^{+} decay from a singly-charged ion, meaning that most of the daughters are non-ionized atoms which are undetectable with our apparatus. This fact lowers the statistic count by a factor of 4 ($\sim 25\%$ of ionization through SO).
- The lifetime of $^{35}Ar^{+}$ is around 1.8 s, a little more than twice the value for $^{6}He^{+}$.

From an experimental point of view, hosting a new nucleus in LPCTrap requires to test two important features prior to a new experiment: the chemical behavior of Argon with the buffer gas and the tuning of the apparatus for a new $\frac{q}{m}$ ratio (timings, Mathieu parameters). The former is checked with stable Argon for two different charge states ($^{36,40}Ar^{+}$ and $^{40}Ar^{2+}$) and the latter with $^{35}Cl^{+}$. The retained buffer gas is He for both the RFQCB and the Paul trap. Since it is a noble gas, its ionization potential is rather high, preventing charge exchange with incoming Ar^{+}. Ar^{2+} was also tried as the input ion with

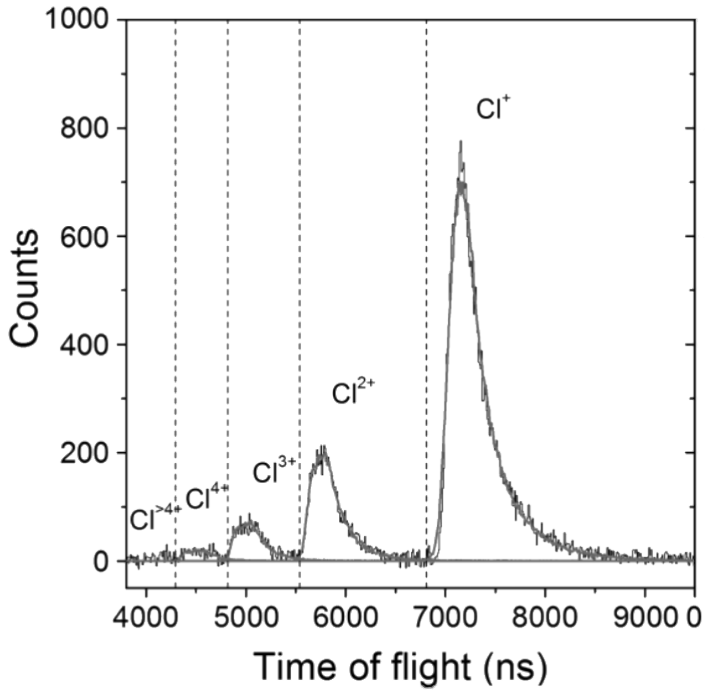

Figure 2.17: 2011 TOF spectrum. Since ^{35}Cl has multiple electrons in its final state which can be ionized through SO, multiple charge state peaks appear here. Adapted from [Cour13b].

the hope that it would lower an important molecular $m = 35$ contamination and that charge exchange with the buffer gas would yield enough singly charged ions, but transmission throughout the line was found to be two to three times lower.

It was seen with stable Argon that there was an important loss due to water contamination. The addition of a Liquid Nitrogen (LN2) trap connected to the RFQCB enabled the capture of that water through adsorption and increased the RFQCB transmission by a factor between 1.5 and 2. This LN2 device has now become an important part of LPCTrap for the collapse of the ion number in the trapped bunch is noticeable when the LN2 has run out. There was another large contamination coming from an unknown molecule with the same $\frac{q}{m}$ ratio. The production of $^{35}Ar^{+}$ is ensured with a primary beam of ^{36}Ar fragmentating on a thick graphite target at 95 MeV/A.

Two experiments were done with $^{35}Ar^{+}$and the preliminary results are discussed in [Ban13; Fabi14].

2.4.2.1 June 2011

This first experiment resulted in a success with the finding of the different timings and parameters of LPCTrap as well as the collection of some 3.7×10^4 "good" coincidences for the newcomer, where the main TOF spectrum is shown in fig. 2.17. Unfortunately, an unnoticed issue with the RF amplitude applied on the RFQCB segment lowered by a factor 10 the transmission of this part. Although the statistic count is enough to extract the SO probabilities of the resulting Chlorine [Cour13b], it is not enough to increase significantly the precision on $a_{\beta\nu}$. Here is a summary of a few experimental aspects:

- **"Good" coincidences:** 3.7×10^4
- **Beam intensity:** $0.5 - 2 \times 10^7$ $^{35}Ar^{+}$/s with 55 pA on CF14, *i.e.* 93% of contaminants.
- **Trapped bunch size:** 3.0×10^4 ions/cycle, including 2.1×10^3 $^{35}Ar^{+}$

Charge	Expt. results	With recoil, with Auger	Without recoil, with Auger	With recoil, without Auger	Without recoil, without Auger
1	74.75 ± 1.07	74.37	74.44	87.07	87.37
2	17.24 ± 0.44	16.98	16.91	11.92	11.66
3	5.71 ± 0.27	6.03	6.04	0.95	0.91
4	1.58 ± 0.21	1.79	1.79	0.05	0.05
>4	0.71 ± 0.18	0.82	0.82	<0.002	<0.002

Table 2.3: 2012 - Final SO results adapted from [Cour13b].

Ion	ε_{RFQCB} (%)	$\varepsilon_{transfer}$ (%)	$\varepsilon_{trapping}$ (%)	ε_{tot} (%)	ε_{tot}^{sec} (%)
$^{36,40}Ar^{+}$	32	22	15	1	50
$^{40}Ar^{2+}$	9	22	20	0.37	18.5
$^{35}Cl^{+}$	4.2	55	11	0.25	12.5
$^{35}Ar^{+}$	32	25	10	0.8	40

Table 2.4: 2012 experiments efficiencies for a cycle of 20 ms ($^{35}Ar^{+}$). The low efficiency for $^{35}Cl^{+}$ is explained by the fact that no optimization was done, E.G. on the different injection optics throughout the line. Indeed, only the timings were relevant at the time to prepare for $^{35}Ar^{+}$.

Ion	ε_{RFQCB} (%)	$\varepsilon_{transfer}$ (%)	$\varepsilon_{trapping}$ (%)	ε_{tot} (%)	ε_{tot}^{sec} (%)
$^{36,40}Ar^{+}$	12	22	15	0.37	1.85
$^{40}Ar^{2+}$	3	22	20	0.13	0.65
$^{35}Cl^{+}$	43	55	11	2.6	13.0
$^{35}Ar^{+}$	15	25	10	0.38	1.9

Table 2.5: 2012 experiments efficiencies for a cycle of 200 ms ($^{35}Ar^{+}$).

Regarding the SO study, it was found that the inclusion of the Auger effect in the theoretical calculations contributes significantly to further ionize a given recoil ion. Indeed, without this effect, the predicted population of 1+ is overestimated by 13% and the abundance of charges beyond 3+ is not accounted for. Taking into account not only the Auger effect but also the recoil energy only slightly alters the predicted populations, the differences being smaller than the experimental error bars (2.3). Since the $^{35}Ar^{+}$ ion decays through a β^{+} transition, most of the resulting Clorine are neutral atoms. Theory predicts that the population of neutral RI is equal to 73.9% while experiment yields a probability of 72(10)%. This is in agreement, although the error on the experimental side is high.

Conclusion: with an incoming 4×10^7 pps and one week of beam, 2×10^6 good coincidences is reachable. In principle, this would allow to reach 0.7% on the precision of $a_{\beta\nu}$.

2.4.2.2 June 2012

With a beam comprising 3.5×10^7 pps, 1.5×10^6 good coincidences were recorded, as it was predicted. A new effect appeared as well: since the line was well optimized and the trap reached a saturation point, the deadtime was unusually high and erroneous readings began to appear on the recorded buffers. The spectrum representing the number of events as a function of the time in the cycle was not presenting its usual smooth decreasing exponential shape. New random-like structures appeared, as shown in fig. 4.1, and went away when the number of ions injected in the trap was cut (using the Hamster first and by degrading the beam with the injection optics of the RFQCB later on). With such data, it was calculated that a statistical precision of 0.3% is reachable on $a_{\beta\nu}$. The data of this experiment is still under analysis. Summing up the main features:

- **Beam intensity:** 3.5×10^7 pps (5.5 pA) with 40 pA of stable contaminants
- **Cycle length:** 200 ms
- **Trapped bunch size:** $0.75 - 1.5 \times 10^5$ ions/cycle (total with contaminants)
- **Detection rate:** $2 - 4$ coincidences/s
- **"Good" coincidences:** 1.5×10^6
- **Efficiencies:** See tables 2.4 and 2.5.

Conclusion: just like for $^6He^+$, precise simulations are required because of the impeding systematic effects, although the data is potentialy of high quality as well.

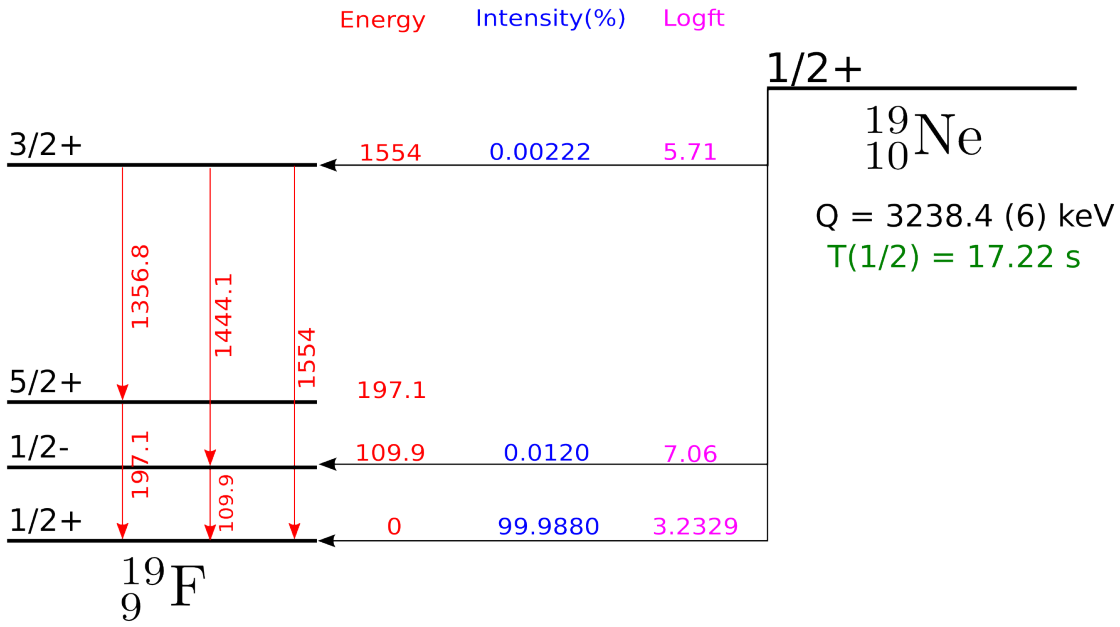

Figure 2.18: $^{19}Ne^{+}$ full decay scheme.

2.4.3 $^{19}Ne^{+}$

$^{19}Ne^{+}$ is a stressful test case for the LPCTrap device. With a rather long lifetime of 17 s and a very low recoil energy (200 eV maximum), it is not obvious that the apparatus can yield interesting results when studying such an ion. The tests showed that for $\frac{q}{m} = \frac{1}{19}$, the beam was too strongly contaminated. Going with $^{19}Ne^{2+}$, contamination was sharply reduced, even though transmission loss was observed like for doubly ionized Argon.

Two radioactive beamtimes were allowed in 2013: in September and October/November. The first one was to further test the apparatus and went so well that it was possible to begin data recording, enabling to accumulate a first batch of 3.7×10^4 good coincidences. During the late automn runs, 8.7×10^4 coincidences were recorded, giving a total of $\sim 1.25 \times 10^5$ coincidences. Unfortunately, an electronic default provoked a sudden breakdown of the vacuum, inducing an important failure on the RFQCB before the end of the allocated beam time, preventing the usage of all the UTs. The accumulated data is still high enough to extract the SO probabilities of the daughter ^{19}F nucleus (see fig. 2.19). The same complete calculation done for the $^{35}Ar^{+}$ case, with the inclusion of the Auger effect, was applied to compute the resulting charge states of the resulting Fluorine (see table 2.6). Discrepancies appear and are under investigation, the main lead being the inclusion of the Shake-Up process which was neglected in the $^{35}Ar^{+}$ study.

- **Beam intensity:** $0.8 - 3.4 \times 10^8$ pps, $170 - 210$ pA total
- **Efficiencies:** See table 2.7.
- **Detection rate:** 0.45-0.50 coincidences/s
- **Cycle length:** 200 ms
- **Primary beam:** ^{20}Ne at 95 MeV/u
- **Incoming energy:** $9950 \times 2 = 19900$ keV
- **Typical bunch size:** $1.7 - 2.0 \times 10^4$ total trapped ions
- **Lifetime** τ_{trap}
  - ^{20}Ne+: 110 ms with LN2, 40 ms without LN2
  - ^{20}Ne2+: $>$ 200 ms with LN2, 170 ms without LN2

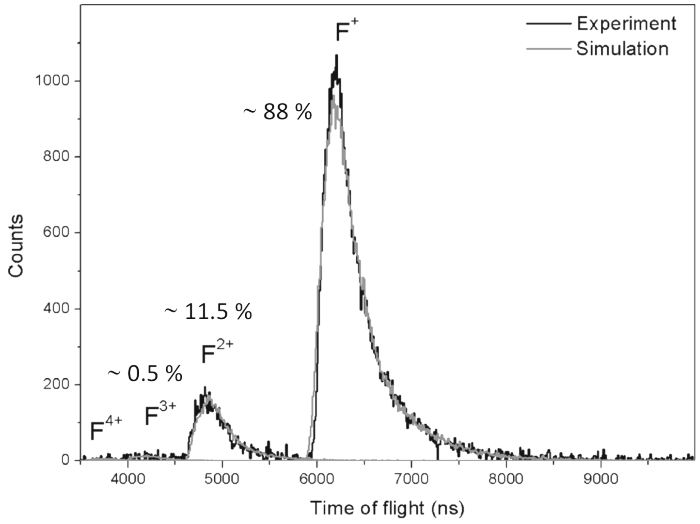

Figure 2.19: 2013 TOF spectrum. We can clearly see the different charge state peaks of the resulting Fluorine [LiHI15].

Charge	**Exp. result (%)**	**Exp. error (%)**	**Theory (%)**	**Theory (no Auger) (%)**
1+	0.87479	0.00892	0.8425	0.888
2+	0.11836	0.00264	0.1384	0.104
3+	0.00685	0.00146	0.0174	0.00699
>4+	0	0.0012	0.0018	2.9×10^{-4}

Table 2.6: 2013 Shake-Off results ($^{19}Ne^{+}$).

Ion	ε_{RFQCB} (%)	$\varepsilon_{transfer}$ (%)	$\varepsilon_{trapping}$ (%)	ε_{tot} (%)	ε_{tot}^{sec} (%)
$^{19}M^{+}$	25	56	24	3.4	17.0
$^{20}Ne^{+}$	15	56	24	2	10
$^{20}Ne^{2+}$	4.8	45.5	27	0.6	3.0
$^{19}Ne^{+}$	4	25 – 35	1 – 10	0.01 – 0.14	0.05 – 0.7

Table 2.7: 2013 experiments efficiencies for 200 ms cycles ($^{19}Ne^{+}$).

Chapter 3

Simulations

Résumé français – Après une brève introduction, ce chapitre majeur décrit la modélisation numérique d'un événement initial de décroissance puis la traque des deux produits de décroissance d'intérêt (la particule β et le neutrino). Le générateur d'événements de décroissance est d'abord présenté. L'effet de la valeur de $a_{\beta\nu}$ est montré puisque c'est ici qu'elle est paramétrée, ainsi que celui la correction de Fermi et des désexcitations γ possibles. Le coeur de ce travail est ensuite abordé : la description complète du programme CLOUDA qui se veut générique (exploitable pour d'autres dispositifs expérimentaux). On y présente dans l'ordre les trois intégrateurs implémentés, la manière de modéliser à la fois un piège de Paul (idéal ou réaliste) et un piège de Penning (idéal), la description, la modélisation et la validation des collisions ion-atome par quatre modèles différents (dont trois réalistes) et l'effet à N-corps de la charge d'espace – le tout sur carte graphique *via* CUDA. Une fois les différents modules décrits, on montre l'effet qu'un modèle ou un autre a sur les différents profils de nuages finaux. La conclusion à propos de CLOUDA est claire : le degré de réalisme des différents modules modifie de manière importante les profils de nuage, on ne peut donc pas fonctionner avec des modèles idéaux. Une fois un événement fixé dans le référentiel du laboratoire par le générateur de décroissances bêta et CLOUDA, la traque des deux produits de décroissance peut démarrer. C'est ainsi que l'application BAYEUX prend la relève et assure le calcul des trajectoires de ces particules dans une géométrie et des champs électromagnétiques réalistes. *In fine*, la simulation est complète et désormais fonctionnelle. Elle permettra, dans le cadre de l'analyse des données à poursuivre, de bien mieux maîtriser les incertitudes systématiques que jusqu'alors.

Contents

3.1 Introduction

The complete and thorough simulation of the LPCTrap device is mandatory to extract $a_{\beta\nu}$ from the TOF spectrum and evaluate the systematic error on it. As said before, the two main remaining systematic uncertainties come from the complex and not yet fully known β scattering processes and the modeling of the ion cloud inside the Paul trap. The complete simulation package developed to achieve these main objectives is detailed in this chapter.

Before entering details, let us describe the global structure of the simulation for which a general layout is shown in fig. 3.1. As was mentionned in section 2.2.4, a confined ion bunch in the Paul trap loses its initial state information since collisions occur with the buffer gas. After a given thermalization time, a smoothed state remains as the ion cloud. The simulation package begins when the bunch is just trapped and not yet thermalized. We do not have much information on the bunch getting injected in the Paul trap. However, it is reasonable to generate some initial state from a Maxwell-Boltzmann distribution and let it thermalize in the trap as we will show in section 3.2.2.3. The dynamics and thermalization of the trapped ion bunch constitute a major part of this work and is encapsulated in the program named CLOUDA[1].

Just like CLOUDA provides the initial vertices positions and velocities of the trapped ions depending on the dynamics of the Paul trap environment, a proper β decay generator was written to supply the kinematics of both the RI and the β particle. This generator coupled to CLOUDA yields a decay event in the laboratory frame.

In order to construct a TOF spectrum, it is required to track the two decay products. This is done using BAYEUX, a multi-purpose simulation package developed at LPC Caen [Maug14]. Roughly speaking, BAYEUX embeds GEANT4 while providing powerful tools to configure the Monte Carlo (MC) engine

[1] CUDA + cloud = CLOUDA

inside. Whether it is the geometry description, the initial events setting or the recorded events data, this package allows to perform realistic simulations without writing a single C++ line. Instead, ASCII configuration files (with their own language) are required and allow to describe all aspects of the simulation. We remind that the TOF spectrum is the central part of the LPCTrap experiments from which the Shake Off (SO) is extracted by means of the integral under each charge peaks and $a_{\beta\nu}$ is obtained from the shape of the TOF peaks (see section 1.2.4.4).

Specific technical choices were made to address the problems at hand. One of them was taking advantage of Graphical Processing Units (GPUs) through CUDA[2] instead of classic Central Processing Units (CPUs) to perform massive computation. Even if modern CPUs have in general eight available threads[3] to work with, GPUs grant access to a number of threads ranging in a few hundreds to a few thousands without the need to buy a complete computationnal facility since it can be embedded in a standard high-end desktop computer. For the past decade or so, available frequencies to perform raw calculus for a thread has capped to a few GHz. The solution to continue the improvement in computational power is to increase the number of these high speed threads and GPUs were designed to work on highly parallelizable problems, namely, image computation. Images are nothing more than matrices in their mathematical representation, ergo, it is natural to associate a thread for each cell so all of these are treated simultaneously. Such parallel programmation requires the learning of a very different logic, even more for GPUs. Apart from that learning cost, the assets granted are rather high, giving access to performances measured in TFLOPS[4] with a standard machine. It is not a simple task to properly compare this number with what a classical CPU-program would yield because of the parallelization cost that needs to be taken into account and so on. Nevertheless, the N-body example provided in the Nvidia's samples has 1000 times more FLOPS when running in GPU instead of CPU. This gives an idea of the power at hand.

A question now rises: why is so much computing power required? The main answer resides in that we need to model in the most accurate way the dynamic of a N-body problem which is particulary greedy in terms of computational needs. Indeed, the confined ions in the Paul trap exert on one another a repulsive Coulomb force. We wish to compute this effect for up to a million ions, thus providing a higher limit, at each timestep for an important number of timesteps in a reasonable computing time. The resulting need in computing power is extensive and thus GPUs are a good solution to undertake such a task. The side effect of developing simulations on GPUs is that once the learning is done, it may as well serve other modeling purposes, *e.g.* the buffer gas models assessment done with CLOUDA as discussed in section 3.2.2.3.

The simulation package developed here is intended to be generic. In other words, a special effort was made so that others can use it for other experiments.

This chapter is dedicated to the physics embedded in the models. The technical documentation and *How To*s will be included in the programs archive themselves.

[2](The) Compute Unified Device Architecture, or CUDA, is the C++ extension provided by Nvidia to execute instructions on GPUs.

[3]The word *thread* in this context designates the computation worker quantum. Whether a thread is virtual or not, it is the basic entity that can fulfill a computational task.

[4]Stands for Tera FLOPS (FLoating-point Operation Per Second): it is a standard unit to evaluate the computing throughput of a given machine.

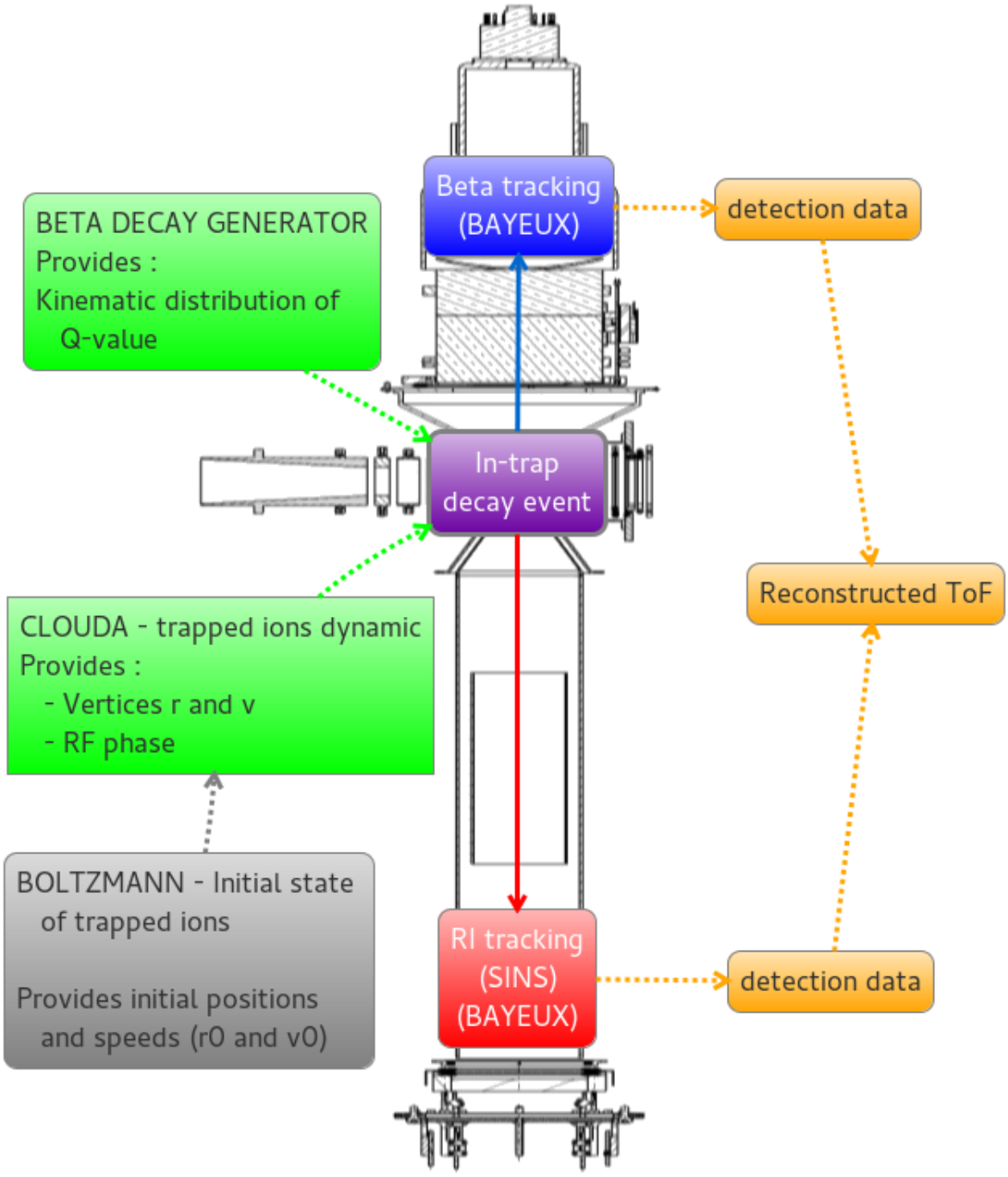

Figure 3.1: LPCTrap simulation package overview

3.2 Initial event

In order to generate an initial event, we require the distribution of the Q-value between the decay products and the dynamics of the decaying vertexes in the laboratory frame. These two aspects are answered to with the β decay generator and CLOUDA.

3.2.1 β decay generator

The goal of the generator is to be able to have big enough sets of events in the decay frame with specific features. For instance, as we described in chapter 1, we want to reach a specific value for $a_{\beta\nu}$ and this is the part in the simulation where we decide which value we want to simulate. Fermi corrections and gamma de-excitation are also available. Although a small stand-alone generator is available, a more extended and accurate one (finer description of the Fermi correction) was included in BAYEUX. The detailed algorithm that was used is provided as in appendix 5.3. We show here typical distributions for several parameters.

Glück computed order-α corrections (*e.g.* photon bremsstrahlung) that apply to the β decay recoil spectrum which goes up to a few % in some cases [Gluc97; Gluc98]. It is worth noting that these kind of corrections are not included in the present generator, although the Fermi function is.

3.2.1.1 Value of $a_{\beta\nu}$

The main objective of LPCTrap is to extract the value of $a_{\beta\nu}$ for multiple ions. As shown in fig. 3.2 and 3.3, the shape of the RI TOF distribution depends on $a_{\beta\nu}$ (see section 1.2.4.4). The fundamental idea of the simulations presented here is to find a linear combination of final TOF distribution for different values of $a_{\beta\nu}$ which matches the experimental data. The beta decay generator is where the value of $a_{\beta\nu}$ is set.

3.2.1.2 Fermi correction

The Fermi correction is simply the Coulomb correction one has to apply to the wavefunction of the outgoing electron because of its interaction with the nucleus charge [GM01]. Indeed, it slows down the β^- particles and accelerate the β^+ particles. We show in fig. 3.4 the effect it has on the electron kinetic energy of the $^{35}Ar^+$ β^+ decay. The figure illustrates the relative difference in event counts between distributions generated without and with this correction. In this case, we see that for βs under 1 MeV, it yields non-negligible differences.

3.2.1.3 γ de-excitation

In the $^{35}Ar^+$ and $^{19}Ne^+$ cases, the β decay can end up on excited states of the daughter nucleus (see fig. 2.16 and 2.18). This has two effects: it lowers the Q-value of the given reaction and it causes a kick in the de-exciting RI, changing its momentum. The lifetimes of these levels are rather low (10^{-12} s) and the RI are rather slow (A=35, $\sim 10^2$ eV of kinetic energy), ergo, the approximation to consider that this decay happens at the same point as the β decay is made[5]. There are several ways to represent the effect of the γ de-excitation, we chose here to show the effect it has on the RI momentum in fig. 3.5, where an explanation is given in the figure caption.

[5]This does not mean that the β decay becomes a four-body reaction. It is still a three-body reaction (β, ν, RI) *immediately* followed by a γ emission.

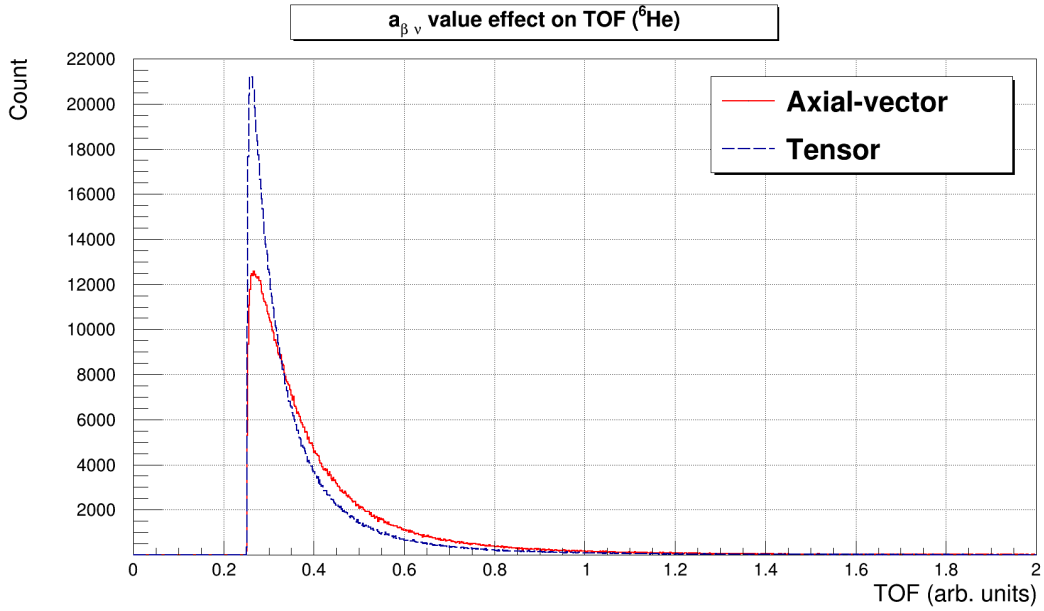

Figure 3.2: RI TOF following the GT transitions in the decay of $^{6}He^{+}$.
Axial: $a_{\beta\nu}= -\frac{1}{3}$ & Tensor: $a_{\beta\nu}= \frac{1}{3}$. The SM states that the tensor current is nil (V-A theory).

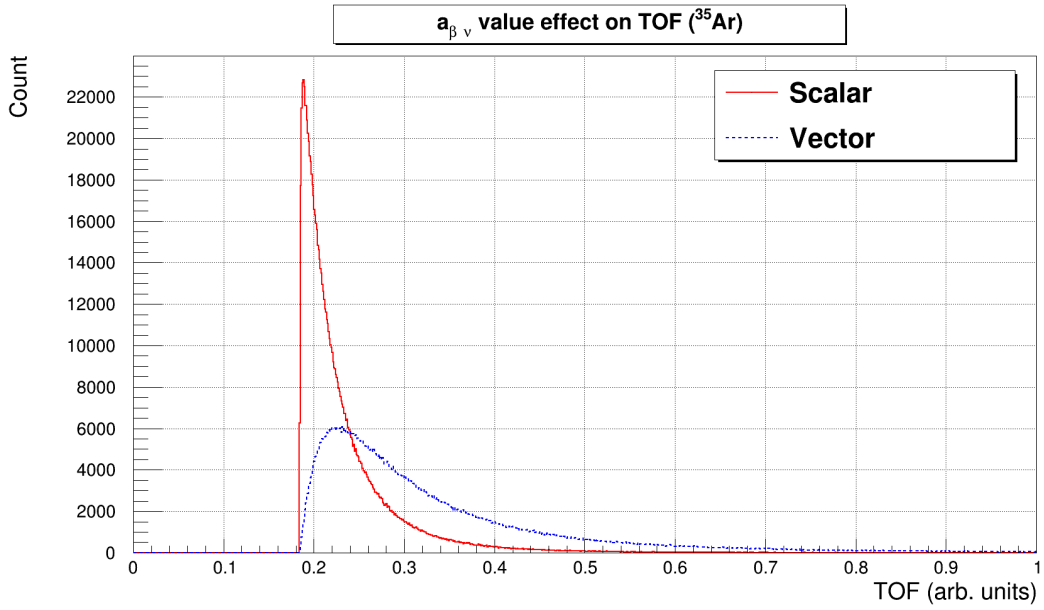

Figure 3.3: RI TOF distribution following the F transitions in the decay of $^{35}Ar^{+}$.
Vector: $a_{\beta\nu}= 1$ & Scalar: $a_{\beta\nu}= -1$. The SM states that the scalar current is nil (V-A theory).

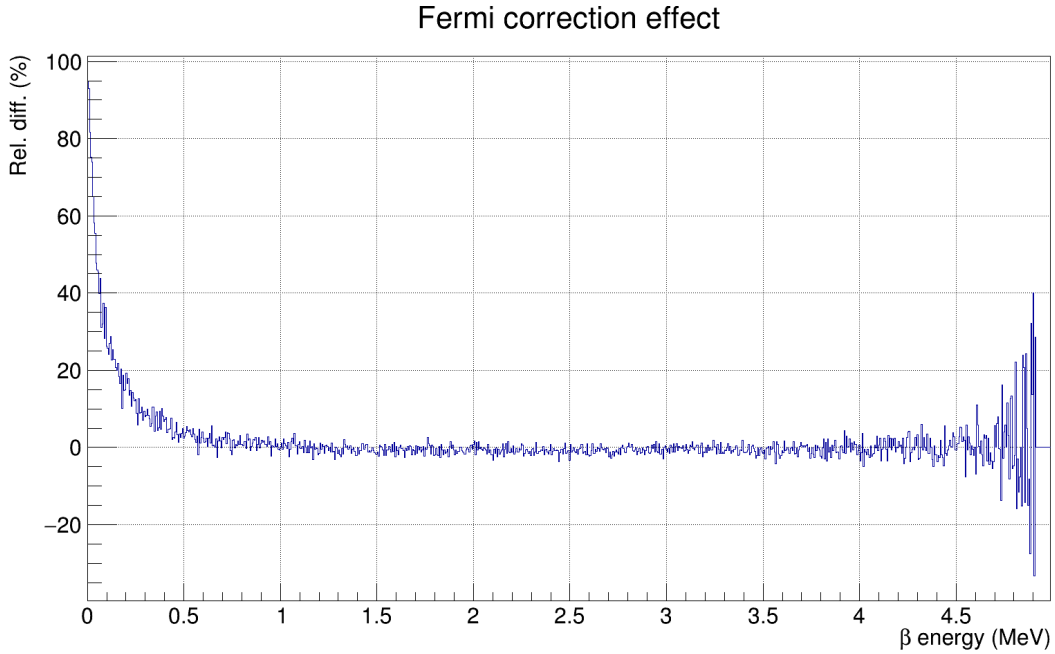

Figure 3.4: Fermi correction effect in $^{35}Ar^{+}$ β^{+} decay. We see here the relative difference of events count when the Fermi correction is not enabled and when it is, as a function of the β energy. The number of events with low-energy electrons collapses when we activate the correction. (The discrepancies above 4.5 MeV are due to low statistics at the end-point.)

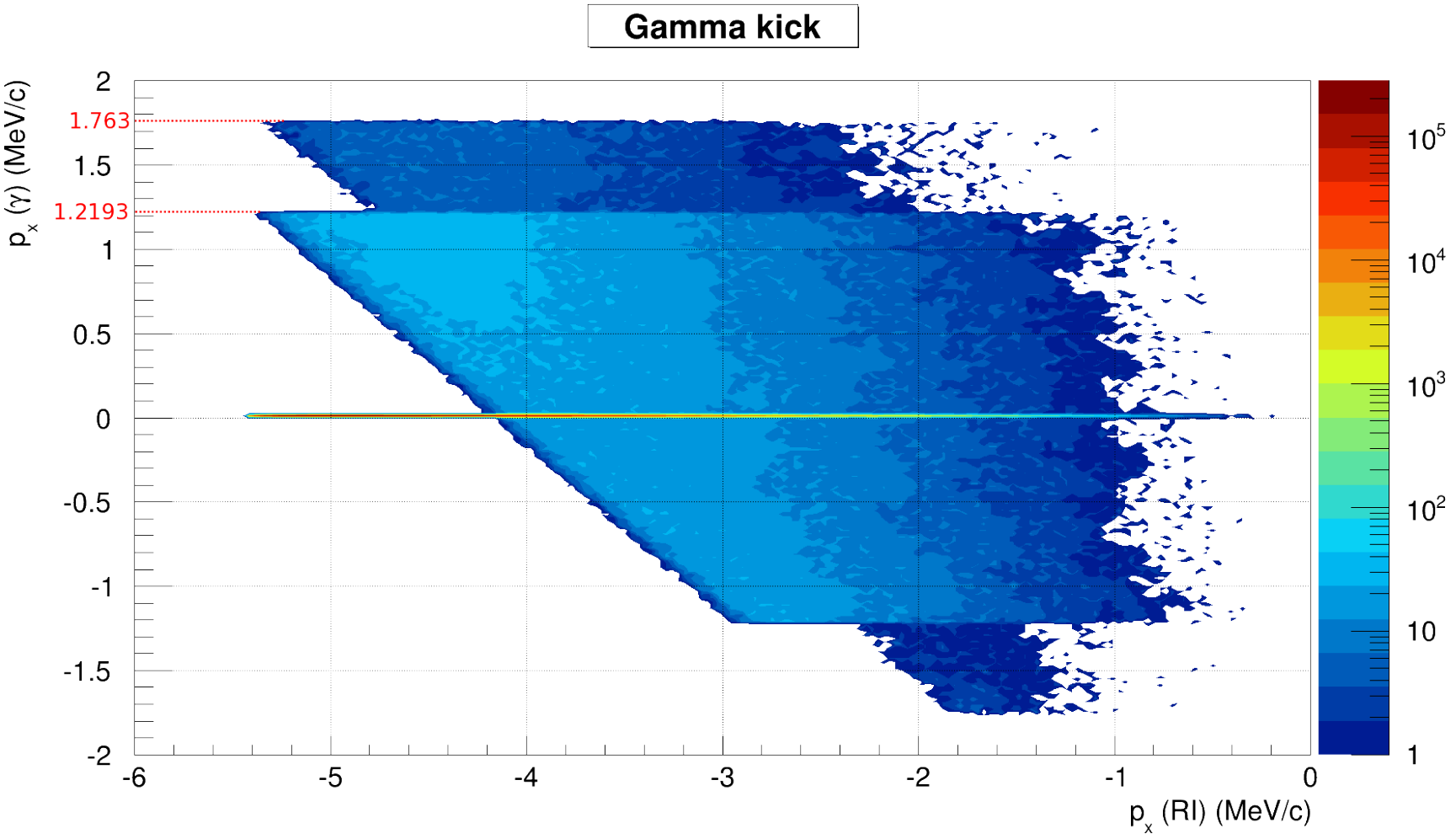

Figure 3.5: γ kick effect in the decay of $^{35}Ar^{+}$. The plot shows the γ momentum x-component as a function of the RI momentum x-component. Since the RI detector is toward $-x$ and a geometric cut was simulated here (angle of acceptance of 1.0 rad $\simeq 60^{o}$), we see only RIs going in the accepted cone. Most of the events are on the line where there is no γ excitation. There are less events with a negative x-component for the γ since they contribute to a kick on the RI toward the direction where it is not accepted (and vice-versa). The two simulated γ energy thresholds are pictured in red.

3.2.2 Clouda

With the β decay generator giving the initial Q-value distribution between the decay products, we need to anchor their positions in the laboratory frame. This is done with the program CLOUDA which purpose it is to provide not only the positions, but also the velocities of the trapped ions at decay time. A concise overview of CLOUDA was published recently [Fabi15]. The microscopic modeling logic is done through three interactions:

- **EM fields:** CLOUDA can simulate either a Paul or a Penning trap.
- **Buffer gas:** As said before, a buffer gas is continuously injected in the trap to thermalize the cloud. We will describe as a second part the modeling of the collisions between ions and atoms (the ions being the decaying particles of interest while the atoms are the neutral buffer gas bodies).
- **N-body:** The third piece is the simulation of the N-body effect, since between 10^2 and a few 10^5 charged ions are confined together in a small volume.

This last effect was the basic reason to choose GPU computation. Indeed, the functioning N-body calculator embedded in CLOUDA does not make any approximation and computes the full effect at each timestep. We will show that when the number of ions is low enough, the N-body has barely no effect and can be deactivated. The usage of GPUs remains handy in this last case since the computation throughput is extremely high, making the simulation to a fully thermalized state (once again, described microscopically) possible in a few minutes.

Although CLOUDA was first designed to simulate a trapped ion cloud, during the course of its development it has been equipped with powerful steppers as we will discuss below. The program is thus able to perform pure tracking of charged particles as well - all on GPUs. We discuss such an aspect in the buffer gas section and more specifically in the different models assessment.

To say a word on geometry, it is worth noting that no smart management has been included in the package yet. In the harmonic field description (section 3.2.2.1), a specific radius is defined beyond which ions are killed. This is the only geometrical cut done and it is hardcoded. It is foreseen to either include primitive functions input to describe ideal geometries or take advantage of the GPU texture memory which was designed to work with images and geometries.

Let us first discuss the choices that were made to solve the equations of motion.

Stepper The EM fields and the N-body effects[6] are computed through the integration of the second order differential equation of motion. In a numerical context, the method to perform this is an important question requiring to be addressed properly since the integration variable, time, is discretized using a given timestep (Δt). For each of the three implemented steppers, we reduced the second order to two first order differential equations.

$$\frac{d^2\mathbf{r}}{dt^2} = \mathbf{a} \tag{3.1}$$

becomes:

$$\frac{d\mathbf{v}}{dt} = \mathbf{a} \qquad \frac{d\mathbf{r}}{dt} = \mathbf{v} \tag{3.2}$$

with $\mathbf{r}$, $\mathbf{v}$ and $\mathbf{a}$ the position, velocity and acceleration of a given ion. This actually yields six equations, since we need to compute each dimension-component individually at each timestep.

[6] The case of the buffer gas is quite different. An elastic collision will abruptly change only the velocity vector of a given ion without modifying its acceleration. The stepper takes this into account when solving the position vector as a function of the velocity vector.

With these generalities in mind, let us take a closer look at our three integration methods:

- **Euler** is the most basic stepper. It is easy to implement and understand, although it is not expected to provide a good numerical stability for long integration times. It solves equations 3.2 in the following way:

$$\begin{aligned} \mathbf{v}_{i+1} &= \mathbf{v}_i + \frac{d\mathbf{v}}{dt} \times \Delta t \\ &= \mathbf{v}_i + \mathbf{a}(t_i, \mathbf{r}_i) \times \Delta t \end{aligned} \tag{3.3}$$

$$\begin{aligned} \mathbf{r}_{i+1} &= \mathbf{r}_i + \frac{d\mathbf{r}_{i+1}}{dt} \times \Delta t \\ &= \mathbf{r}_i + \mathbf{v}_{i+1} \times \Delta t \end{aligned} \tag{3.4}$$

  with i the i^{th} timestep and $\mathbf{a}(t_i, \mathbf{r}_i)$ being the function computing the acceleration at time t_i for the position vector $\mathbf{r}_i$

- The **Leapfrog** stepper is a little more sophisticated than its Euler counterpart and provides a few assets [Youn13]. Its symplectic feature makes it stable on long times, *i.e.* it respects the Liouville's theorem, and enables time reversibility. Moreover, it is almost as simple (and efficient) as Euler. The name *leapfrog* comes from the way the velocity is evaluated at half timesteps while the position is computed at integer timesteps. In CLOUDA, it is implemented in this manner:

$$\delta\mathbf{v} = \mathbf{a} \times \frac{\Delta t}{2} \tag{3.5}$$

$$\mathbf{v}_{i+1/2} = \mathbf{v}_i + \delta\mathbf{v} \tag{3.6}$$

$$\mathbf{r}_{i+1} = \mathbf{r}_i + \mathbf{v}_{i+1/2} \times \Delta t \tag{3.7}$$

$$\mathbf{v}_{i+1} = \mathbf{v}_{i+1/2} + \delta\mathbf{v} \tag{3.8}$$

  At the end of each timestep, we bring back the velocity to an integer timestep value. Although this operation could be skipped and done only when data is recorded, it is useful and not that costly to keep a clear track of the ions at each timestep. It is worth noting that an approximation is made here on the acceleration: we compute it at the next half timestep without taking into account the position of the ions at this same time. Indeed, computing the N-body effect requires the position vector of all the ions.

- The **4^{th} order Runge-Kutta (RK4)** is a widely used stepper [Pres07]. By properly adding the weighted contributions of partial steps, this integrator is quite powerful in that the approximation it provides tends to keep a low numerical error ($\mathcal{O}((\Delta t)^4)$). For a given set of initial conditions and a vector $\mathbf{x}$ such that:

$$\frac{d\mathbf{x}}{dt} = f(t, \mathbf{x}) \tag{3.9}$$

  The next step for this variable is computed as:

$$\mathbf{x}_{i+1} = \mathbf{x}_i + \frac{\Delta t}{6}(\mathbf{k_1} + 2\mathbf{k_2} + 2\mathbf{k_3} + \mathbf{k_4}) \tag{3.10}$$

  where:

$$\mathbf{k}_1 = f(t_i, \mathbf{x}_i) \tag{3.11}$$

$$\mathbf{k}_2 = f(t_i + \frac{\Delta t}{2}, \mathbf{x}_i + \mathbf{k}_1 \times \frac{\Delta t}{2}) \tag{3.12}$$

$$\mathbf{k}_3 = f(t_i + \frac{\Delta t}{2}, \mathbf{x}_i + \mathbf{k}_2 \times \frac{\Delta t}{2}) \tag{3.13}$$

$$\mathbf{k}_4 = f(t_i + \Delta t, \mathbf{x}_i + \mathbf{k}_3 \times \Delta t) \tag{3.14}$$

In our case, we need to solve two equations (see equation 3.2) and because of the N-body calculation and the constraints brought by the usage of GPU, the method was adapted accordingly using a "crossover" logic:

$$\mathbf{k}_1^r = \mathbf{v}_i \qquad \mathbf{k}_1^v = \mathbf{a}\left(t_i, \mathbf{r}_i\right) \tag{3.15}$$

$$\mathbf{k}_2^r = \mathbf{v}_i + \mathbf{k}_1^v \times \frac{\Delta t}{2} \qquad \mathbf{k}_2^v = \mathbf{a}\left(t_i + \frac{\Delta t}{2}, \mathbf{r}_i + \mathbf{k}_1^r \times \frac{\Delta t}{2}\right) \tag{3.16}$$

$$\mathbf{k}_3^r = \mathbf{v}_i + \mathbf{k}_2^v \times \frac{\Delta t}{2} \qquad \mathbf{k}_3^v = \mathbf{a}\left(t_i + \frac{\Delta t}{2}, \mathbf{r}_i + \mathbf{k}_2^r \times \frac{\Delta t}{2}\right) \tag{3.17}$$

$$\mathbf{k}_4^r = \mathbf{v}_i + \mathbf{k}_3^v \times \Delta t \qquad \mathbf{k}_4^v = \mathbf{a}\left(t_i + \Delta t, \mathbf{r}_i + \mathbf{k}_3^r \times \Delta t\right) \tag{3.18}$$

where $\mathbf{a}$ requires a full half-updated vector for all ions for the N-body effect. In eq. 3.18, $\mathbf{k}_4^r$ requires $\mathbf{k}_3^v$ and $\mathbf{k}_4^v$ requires $\mathbf{k}_3^r$ and so forth, thus, the "crossover" logic.

As we will see when taking a closer look at the drift velocities stability as a function of the stepper and the timestep (section 3.2.2.3), the particular systems CLOUDA simulated for the LPCTrap needs are not really sensitive to the stepper accuracy *to some extent*. The power of a stepper resides in providing the most accurate solution for an important number of simulated timesteps. Since we are in the setting where buffer gas constantly "resets" the trajectories of the ions, there is no time for an important numerical error to accumulate. However, CLOUDA could serve other purposes where a working RK4 could be important. The Euler stepper being the fastest, it was used for most of the tests described in this work – once again, we ensured that it returned the same results as the RK4 for our different configurations.

3.2.2.1 EM Fields

In order to confine the ion bunch, a trapping field is required. Although more efforts were dedicated to the Paul trap, CLOUDA is able to simulate a Penning trap as well for which only an ideal description is available. The Paul trap can be modeled using either an ideal field or a realistic field. Of course, in the former case the computing time is highly reduced when compared to the latter case but the approximation is rather crude. Indeed, as we will see the ideal field does trap ions but the full study of the final trapped cloud profile shows important discrepancies between the ideal and realistic (harmonic) field (see section 3.2.2.5). In this section we will present the basic modeling done with the ideal field. We will then detail the method to include all the contributions actually present during experiments. This will yield a complete realistic field for which the integration in CLOUDA will finally be discussed. The test of the ideal Penning trap will be closing this section.

Paul trap The way a Paul trap operates was presented in the last chapter, section 2.2.4. We remind equation 2.12, which governs the equation of motion for all three dimensions as a function of the Mathieu parameters:

$$\begin{aligned} \frac{d^2x}{d\tau^2} + \ (a + 2q\cos(2\tau))x = 0 \\ \frac{d^2y}{d\tau^2} + \ (a + 2q\cos(2\tau))y = 0 \\ \frac{d^2z}{d\tau^2} - 2(a + 2q\cos(2\tau))z = 0 \end{aligned} \tag{3.19}$$

where a and q, the Mathieu parameters, and τ are:

$$a = \frac{2e\phi_0}{mr_0^2\pi^2 f_{RF}^2} \qquad q = \frac{e\phi_1}{mr_0^2\pi^2 f_{RF}^2} \qquad \tau = \pi f_{RF} t \tag{3.20}$$

In the LPCTrap case, we work at constant Mathieu parameters. Thus, changing the trapped ion will imply changing f_{RF} accordingly to accommodate the new mass. Speaking of them, let us remind the parameters as well, obviously adjustable in the simulation package:

- m: The mass of the trapped ion
- r_0: The size of the Paul trap (radius at which the potential is equal to V_0, see equation 2.6)
- f_{RF}: The frequency at which the RF potential ϕ_1 is applied
- ϕ_0: The constant potential
- ϕ_1: The RF potential

The configuration in the $^{35}Ar^{+}$case for LPCTrap is:

- $m = 34.9752576$ u
- $r_0 = 12.5$ mm
- $f_{RF} = 0.7$ MHz
- $\phi_0 = 0$ V
- $\phi_1 = 60$ V

Equation 3.19 shows that the applied RF is described with a cosine function[7] with the argument $2\pi f_{RF}t$. We will call this argument the Radio-Frequency Phase (RFP) and multiple observables will depend on its modulo that we will represent between 0 and 2π. Presently, the applied RF is reproduced with a mathematical cosine function in the simulation. It will be required to implement the "true RF", *i.e.* the one recorded during the experiments to lower the approximation done on this factor.

Two potentials are defined here: ϕ_0 and ϕ_1. ϕ_0 is a constant potential and should include all "background" contributions from elements situated around the Paul trap. The same could be said for ϕ_1, the RF potential which was designed to provide a potential as purely quadrupolar as possible. We detail below how these potentials are treated for the ideal and realistic field.

Ideal field The strict configuration presented above leads directly to an analytical treatment of the equation of motion (eq. 3.19) using the potential shown in fig. 2.7c. This potential is purely quadrupolar, infinite and no ambient electric field is considered – three approximations that the realistic field discussed below is meant to avoid. We will call this configuration the ideal case and its analytical nature provides a very fast treatment of the motion in terms of computation time.

Realistic field One can avoid making the three approximations just mentioned using a realistic description of the fields:

- **Perfectly quadrupolar:** Other non-quadrupolar contributions are actually non-negligible, albeit small.
- **Infinite:** The trap is limited in space and ions travelling too far from its center are, in fact, lost by collisions on electrode surfaces.
- **No ambient field:** The trapping electrode rings are not the only components contributing to the total electric field in the trap region since all the other conducting parts of the trap contribute as well.

Computing and using the realistic field constitute two distinct parts. A first work of precalculation is done prior to the simulation itself in order to include all the real contributions around the experimental Paul trap we will be simulating. We will first show how this precalculation is done. Secondly, the usage in CLOUDA will be detailed.

[7] cosine for the potentials and sine for the fields

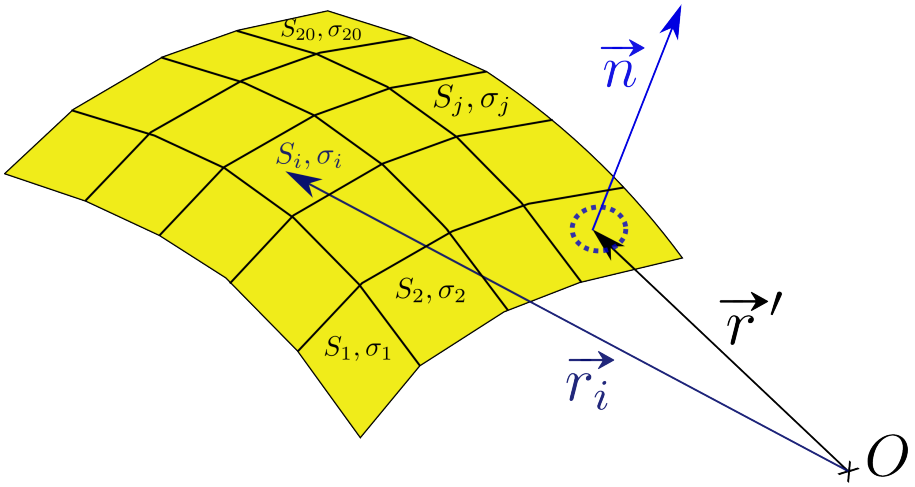

Figure 3.6: BEM cells geometrical aspects.

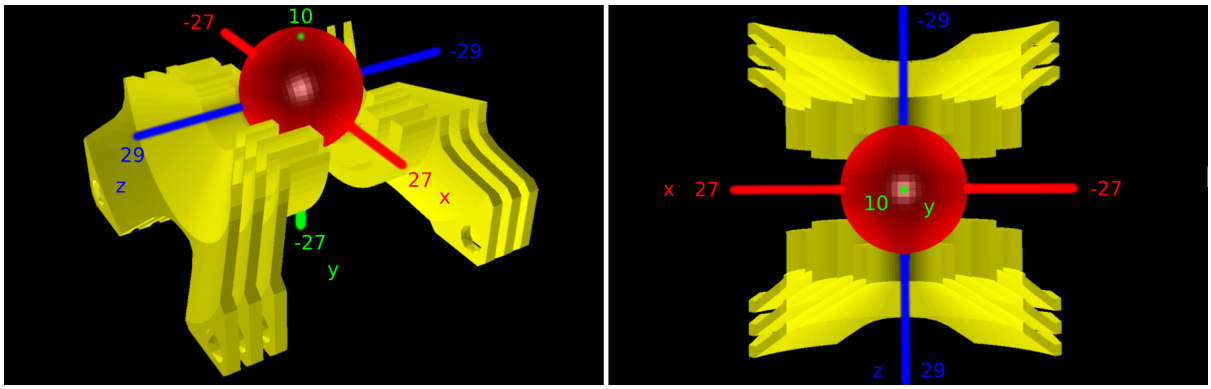

Figure 3.7: Harmonic field domain of definition. The red sphere represents the boundaries inside which the field can be synthesized.

Using the full realistic geometry around the Paul trap and all the potentials applied on the relevant volumes, one can compute all contributions to the EM field in the Paul trap vicinity. Two very different tools were available in our context to achieve this: SIMION which is based on Finite Differences (FD) or ELECTROBEM, a homemade C++ program which is based on Boundary Element Method (BEM). ELECTROBEM was chosen as the appropriate tool since it requires less memory for the same precision [Quem14]. In order to increase the precision with less computations, symmetry around $y = 0$ was assumed. We remind that y is the axis from the floor to the ceiling in the LPCTrap context. This symmetry is true if we neglect the contribution of a few plates that are far away from the trap center.

The geometry is made of specific components of the set-up carefully chosen to include all relevant contributions to the electric field. The BEM requires the geometry to be meshed, so all volumes are represented by a collection of cells (19 048 cells in our case using the symmetry around y). Each cell has an associated charge density, considered constant. Fig. 3.6 pictures the cells geometry. The superposition principle implies that the distribution of the charge densities generates a potential in all space written as:

$$\Phi_i = \frac{1}{4\pi\epsilon_0} \sum_j \int_{S_j} \frac{\sigma_j(\mathbf{r}')}{|\mathbf{r_i} - \mathbf{r}'|} dS' \tag{3.21}$$

where Φ_i is the potential at any point i in space due to the cells j, $\mathbf{r_i}$ the position of the cell receiving contributions from all the j cells, $\mathbf{r}'$ the position of the current cell j with a surface S_j and σ_j the charge density of cell j. For any point in space and especially for the center of each cell, we can thus write all the potentials due to the N cells in a matrix form:

$$\begin{pmatrix} \Phi_1 \\ \Phi_2 \\ \vdots \\ \Phi_{N_c} \end{pmatrix} = \begin{pmatrix} \mathcal{Q}_{1,1} & \mathcal{Q}_{1,2} & \cdots & \mathcal{Q}_{1,N_c} \\ \mathcal{Q}_{2,1} & \mathcal{Q}_{2,2} & \cdots & \mathcal{Q}_{2,N_c} \\ \vdots & \vdots & \ddots & \vdots \\ \mathcal{Q}_{N_c,1} & \mathcal{Q}_{N_c,2} & \cdots & \mathcal{Q}_{N_c,N_c} \end{pmatrix} \begin{pmatrix} \sigma_1 \\ \sigma_2 \\ \vdots \\ \sigma_{N_c} \end{pmatrix} \tag{3.22}$$

where Φ_i becomes the known electrode potentials, σ_i are the unknown constant charge densities of each cell (considered constant) and $\mathcal{Q}_{ij}$ contains the information on the geometry (and a few constants):

$$\mathcal{Q}_{ij} = \frac{1}{4\pi\varepsilon_0} \int_{S_j} \frac{1}{\|\mathbf{r_i} - \mathbf{r}'\|} \, dS' \tag{3.23}$$

The charge densities are the unknowns of the system. Using iterative methods [Quem14] on the system represented by equation 3.22, we solve the σ_i. With all the σ_i known, we may retake the superposition principle to compute the potential (or the field) in any point in space. We thus now have access to realistic fields for our simulated set-up.

Now the question of how this may be used in CLOUDA rises. Two solutions were thought of: a harmonic synthesis of the field at runtime or the interpolation through a pre-calculated field map. The harmonic synthesis was chosen because of its lesser memory usage (but higher number of operations, this is discussed at the end of the section). The usage of the harmonic synthesis first needs the definition of a region where our synthesized field will be available, a constraint brought by the harmonic development we will reach. In the LPCTrap case, we chose a sphere centered at the trap center with a radius $r_0 = 10$ mm as shown on fig. 3.7, knowing that a sphere of radius $r_0 = 12.5$ mm would touch the electrodes. We then use a routine named SHTNS [Scha13] which takes as input a list of points where the field is computed on the chosen sphere surface. SHTNS outputs the spherical harmonic coefficients $\mathcal{A}_{\ell m}$ and $\mathcal{B}_{\ell m}$. These coefficients fully characterize the field of our system and are valid inside the sphere. Now that we have this coefficient set, we can use it at runtime to compute the field at the position of any ion requiring it inside the chosen sphere. The solution of the Laplace's equation:

$$\nabla^2 \Phi(r, \theta, \varphi) = 0 \tag{3.24}$$

can be written as the following harmonic development:

$$\Phi(r, \theta, \varphi) = \sum_{\ell=0}^{\infty} \left(\frac{r}{r_0}\right)^{\ell} \sum_{m=0}^{\ell} \sqrt{\frac{2\ell+1}{4\pi} \frac{(\ell-m)!}{(\ell+m)!}} P_\ell^m(\cos\theta) \left(\mathcal{A}_{\ell m} \cos(m\varphi) - \mathcal{B}_{\ell m} \sin(m\varphi)\right) \tag{3.25}$$

where (r, θ, φ) are the spherical coordinates of a given ion (where the field should be synthesized), r_0 is the chosen sphere convergence radius, $P_\ell^m(\cos\theta)$ are the associated Legendre functions of the first kind and $\{\mathcal{A}_{\ell m}, \mathcal{B}_{\ell m}\}$ are the harmonic coefficients set mentioned above. We notice that the constraint on the sphere radius r_0 appears here explicitly since for any $r > r_0$, divergences begin to occur. Furthermore, the computing time constraint forces us to stop the first sum to some $\ell_{\max}$ – the choice of which must be thoroughly studied to minimize any numerical error as shown below.

We only spoke of the *potential* computation, although during a simulation we want to compute the Lorentz force, thus requiring the *field* components $\mathbf{E} = -\nabla\Phi$. The details to compute this gradient directly from $\{\mathcal{A}_{\ell m}, \mathcal{B}_{\ell m}\}$ are developed in appendix 5.2.

The approximation made in the ideal field where the constant potential ϕ_0 is exactly 0 is avoided here since there is an ambient field in the vicinity of the Paul trap, even when the RF field is off. In fact, the process described above is followed twice, yielding two sets of harmonic coefficients: one when the full RF voltage is applied on the Paul trap electrodes ($\mathbf{E}_{V1}$) and one when it is off ($\mathbf{E}_{V0}$). We thus account for the contribution of the ambient field. In order to use this in CLOUDA, one needs to apply the following:

$$\mathbf{E} = (\mathbf{E}_{V1} - \mathbf{E}_{V0}) \times \sin(2\pi f_{RF} t) + \mathbf{E}_{V0} \tag{3.26}$$

In other words, $\mathbf{E}_{V1} - \mathbf{E}_{V0} = E(\phi_1)$ and $\mathbf{E}_{V0} = E(\phi_0)$ (see equation 2.6).

To study the effect of the chosen $\ell_{\max}$, 10^4 points are randomly selected in a ball of radius $r'_0 \leqslant r_0$. For each point, we calculate the difference between the BEM field and the harmonic field for each field component (E_x, E_y, E_z) and represent them using three distributions. We then extract the RMS of each distribution as a function of the $\ell_{\max}$ value. This was done for three values of r'_0 (5, 7.5 and 10 mm) to check the effect of approaching the electrodes on the synthesized field precision. Indeed, we are interested in knowing if a more extended cloud requires a higher ℓ_{max} value and if so, by how much – the thermalization stage implying for the ions to venture "far" from the trap center comparing to the final cloud size. The results are shown in fig. 3.8. Since the trapped cloud has a RMS in each dimension smaller than 2 mm in most cases, $\ell_{\max} = 12$ is selected as a compromise between a reasonable accuracy of the reconstructed field (discrepancies of a few 10^{-5}) and the computing time. Indeed, a larger $\ell_{\max}$ implies to go further in the sums shown in eq. 3.25, thus increasing computing time.

The BEM computed field reproduces the same secondary Paul traps that were observed in earlier SIMION simulations. Fig. 3.9 pictures E_z along the z-axis. The RF cosine applied on it renders the three points at $E_z = 0$ Paul traps location, the main one being centered at $z = 0$, since only these points will remain stable during the RF oscillation. It is now worth mentionning that to prevent any divergence from the $(r/r_0)^l$ term, thus avoiding the infinite potential approximation, any ion going beyond r_0 is artificially killed. Since the secondary Paul traps are beyond 10 mm, the value of r_0, they do not appear in the simulations. This being said, it is possible to go further and compute additionnal smaller spheres along the z-axis so that other sets of harmonic coefficients could be defined and used, making possible for a few ions to reach these secondary Paul traps. On the experimental side, they are negligible since they are situated in the electrodes center, thus, the detection solid angle is null for all pratical purposes. Consequently, no secondary Paul traps are simulated for now.

Using the same BEM, we could have computed the realistic field using another method than the harmonic synthesis. It is possible to compute a *field map* of the Paul trap with a given 3D space meshing and interpolate at runtime in that map instead of using a *harmonic synthesis*. Since the initial information comes from the same BEM, it is unlikely that the results of both methods would be different. The question risen here is more one of performance, playing with the balance between memory usage and number of operations. On the one hand, a field map would take advantage of a special memory embedded in CUDA, the *texture memory*, which allows for native and efficient interpolation for a given map. Although there would not be an important sum as in eq. 3.25, the memory usage of a map would be extensive and would increase with the resolution of the map. On the other hand, the spherical harmonic coefficients take advantage of another special memory, the *constant memory* which allows for quick readings for all threads, but is rather small – too small to contain something as large as a field map – yet large enough to contain the harmonic coefficients. Although the memory usage remains small in the harmonic case, the number of operations required to synthesize the field at a given point in space is higher than in the map case. The harmonic field also brings the constraint of the convergence sphere while the field map does not. The latter is not implemented in CLOUDA but is in development. It will be interesting to study the impact on performance this brings.

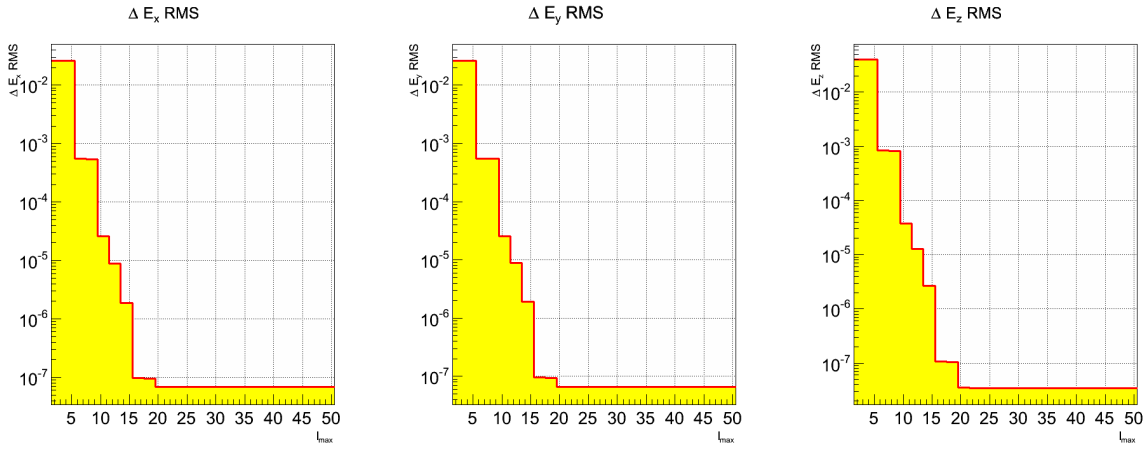

(a) $r'_0 = 5$ mm

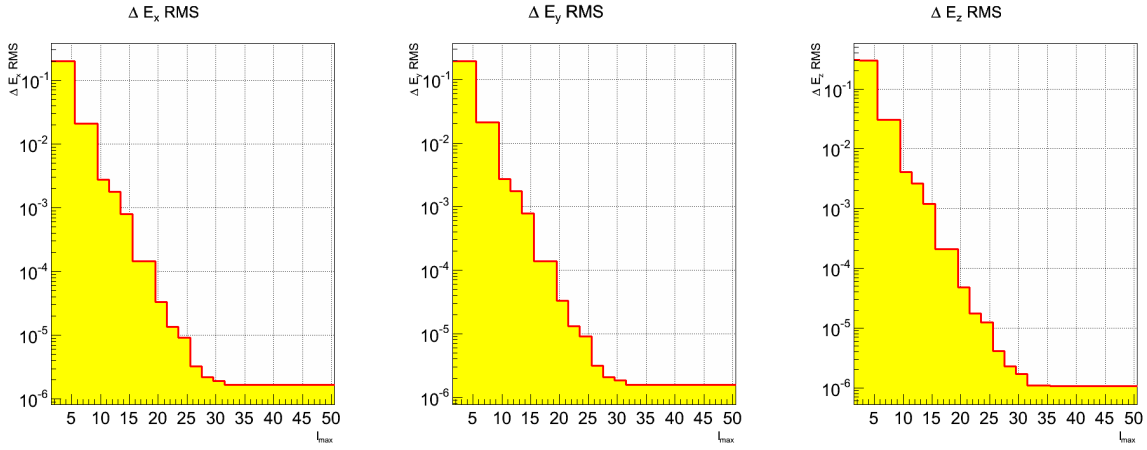

(b) $r'_0 = 7.5$ mm

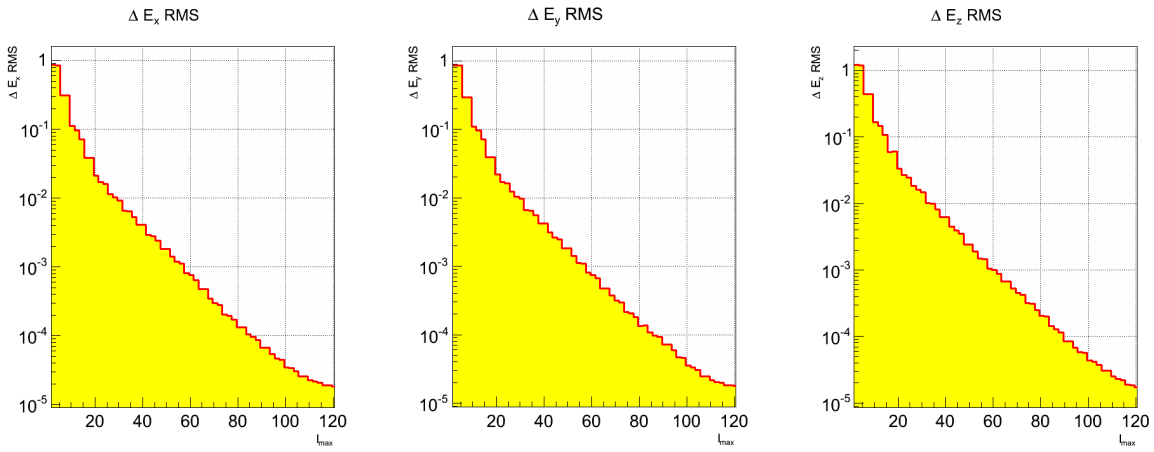

(c) $r'_0 = 10$ mm

Figure 3.8: Harmonic field - $\ell_{\max}$ effect on synthesized field discrepancies compared to the one obtained with the BEM. In all cases, $r_0 = 10$ mm and the differences are shown for fields synthesized in a smaller subsphere of radius r'_0.

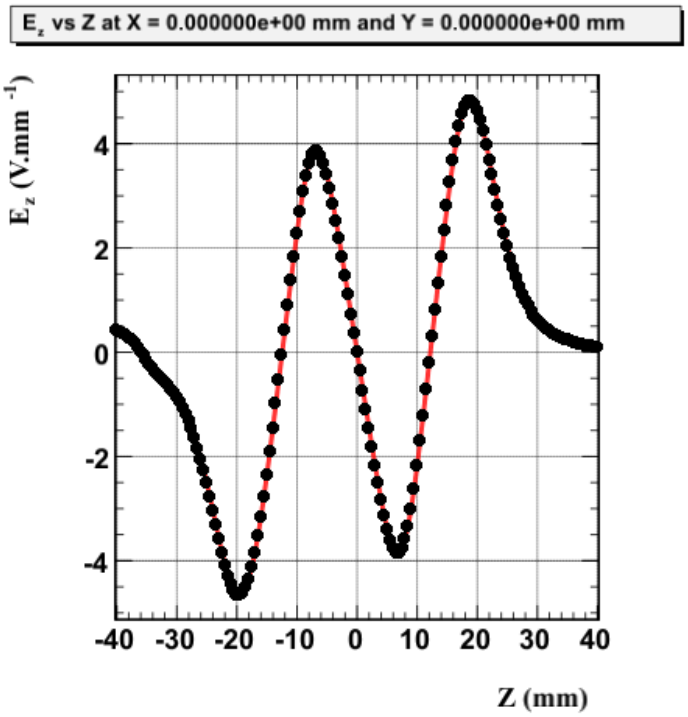

Figure 3.9: Harmonic field - Secondary Paul traps appearing for $E_z = 0$ V.mm^{-1} at $z = 0$ mm and $z \simeq \pm 12.5$ mm.

Penning trap Instead of an electrodynamic RF field, a Penning trap works with the combination of an electrostatic and a magnetostatic field [Dehm89]. Typical geometries are shown in fig. 3.10a. The electric field has the same form as the Paul trap field without a RF potential ($\phi_1 = 0$):

$$\mathbf{E} = \frac{V_0}{2d^2}(\mathbf{x} + \mathbf{y} - 2\mathbf{z}) \qquad d^2 = \left(\frac{z_0^2 + r_0^2/2}{2}\right) \tag{3.27}$$

with V_0 the quadrupole potential and d the trap size related to z_0 and r_0, the axial and radial size of the trap. The magnetic field is simply:

$$\mathbf{B} = B_z\ \hat{\mathbf{z}} \tag{3.28}$$

Knowing the two fields, we can compute the acceleration from the Lorentz force.

$$\mathbf{a} = \frac{q}{m}(\mathbf{E} + \mathbf{v} \times \mathbf{B}) \tag{3.29}$$

$$\mathbf{a} = \frac{q}{m}\left(\mathbf{E} + \begin{vmatrix} \hat{\mathbf{x}} & \hat{\mathbf{y}} & \hat{\mathbf{z}} \\ v_x & v_y & v_z \\ 0 & 0 & B_z \end{vmatrix}\right) \tag{3.30}$$

$$\mathbf{a} = \frac{q}{m}\left[\frac{V_0}{2d^2}(\mathbf{x} + \mathbf{y} - 2\mathbf{z}) + (v_y B_z)\hat{\mathbf{x}} - (v_x B_z)\hat{\mathbf{y}}\right] \tag{3.31}$$

yielding:

$$\begin{aligned} a_x &= \frac{q}{m}\frac{V_0}{2d^2}x + \frac{qB_z}{m}v_y \\ a_y &= \frac{q}{m}\frac{V_0}{2d^2}y - \frac{qB_z}{m}v_x \\ a_z &= -\frac{q}{m}\frac{V_0}{d^2}z \end{aligned} \tag{3.32}$$

It is expected that through the superposition of these fields, the following equation holds for an ideal Penning trap [BG86]:

$$\omega_\pm = \frac{1}{2}\left(\omega_c \pm \sqrt{\omega_c^2 - 2\omega_z^2}\right) \tag{3.33}$$

It is possible to show that, at first order, the trapped ions will follow a movement that can be decomposed in three separate eigenmotions:

- **Magnetron:** A rotation in a plane perpendicular to the z axis (magnetic field axis) with frequency:

$$\omega_- \simeq \omega_m = \frac{V_0}{2B_z d^2} \tag{3.34}$$

- **Cyclotron (reduced):** A swift rotation around the magnetic field lines with frequency:

$$\omega_+ \simeq \omega_c = \frac{qB_z}{m} \tag{3.35}$$

- **Axial:** A harmonic oscillation along the z axis with frequency:

$$\omega_a = \sqrt{\frac{qV_0}{md^2}} \tag{3.36}$$

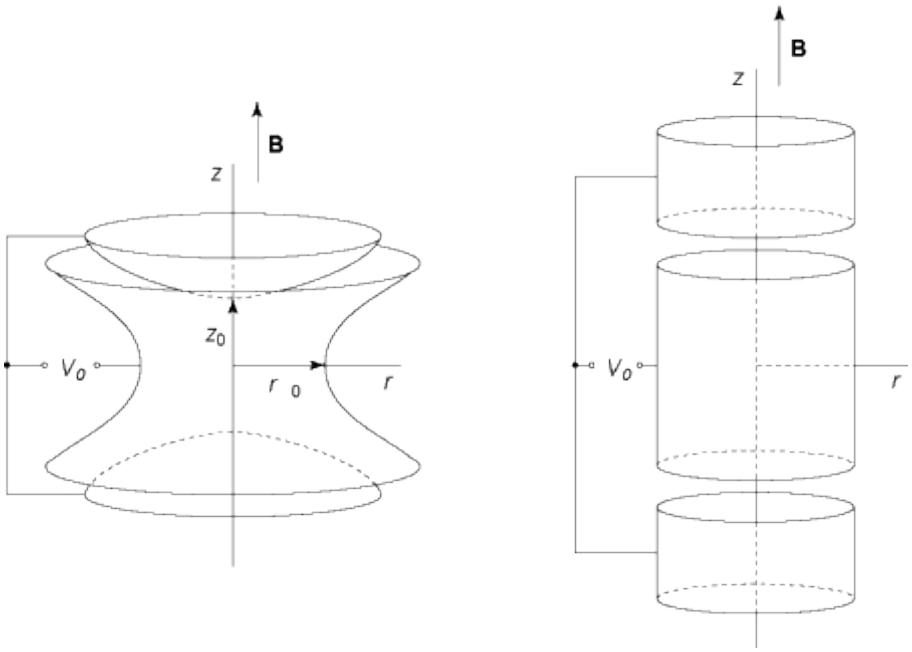

(a) Penning trap geometries (taken from [CoMT15])

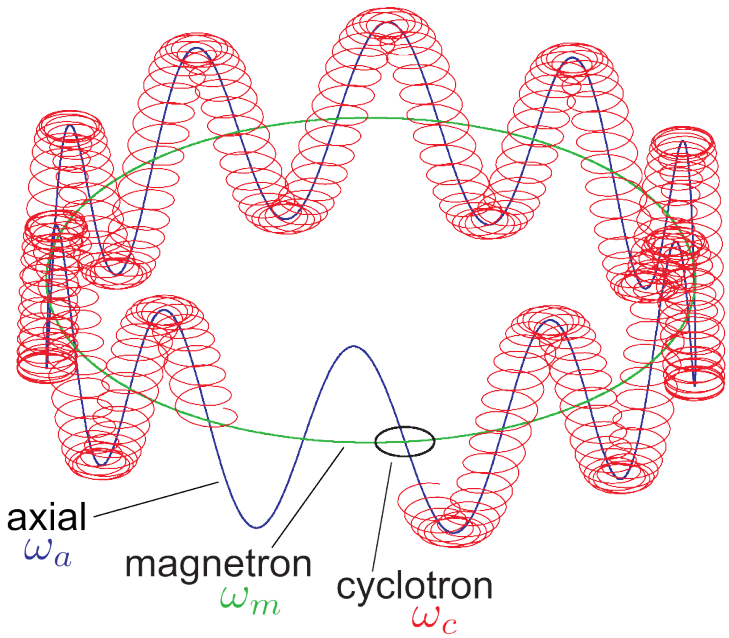

(b) Penning trap eigenmotions (adapted from [VG12])

Figure 3.10: Penning trap features

Fig. 3.10b shows the motion of a single ion in an ideal Penning trap. The expected eigenfrequencies were compared with the fitted ones and a good agreement has been found, as shown in fig. 3.11. The configuration for this simulation was the following:

- $\Delta t = 10$ ps
- $B_z = 24.0$ T (see footnote[8])
- $U_0/d^2 = 7.2 \times 10^5$ V.m^{-2}
- $m = 34.9752576$ u
- $q = 1+$
- $N = 1$ ion

Penning traps are thus available and working in CLOUDA, although they were not studied thoroughly in the context of this work.

[8] Huge field, only used for this demonstration purpose.

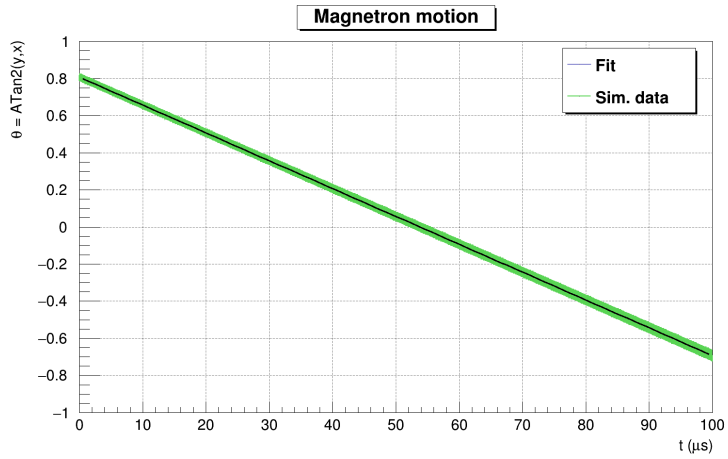

(a)

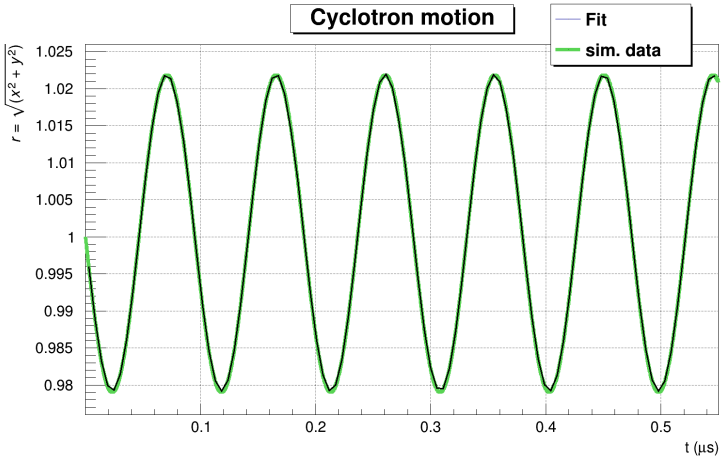

(b)

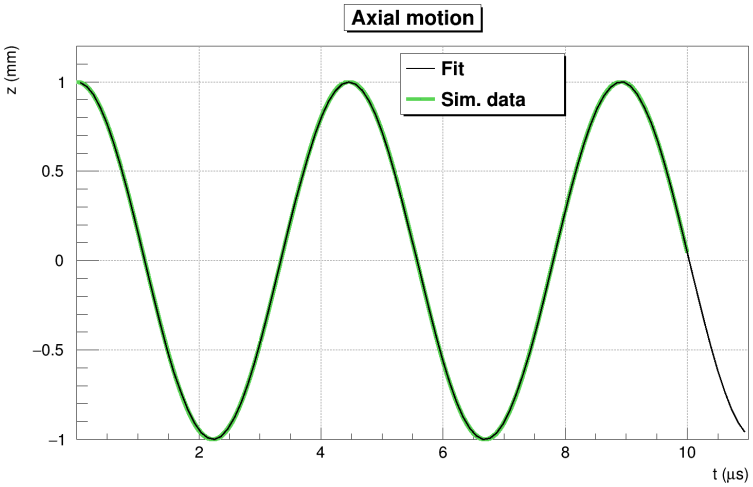

(c)

Figure 3.11: Penning motions fits

3.2.2.2 Buffer gas – Models description

An important part of this work is the thorough simulation of the trapped ion cloud in the experimental Paul trap from a microscopic point of view. The simulated ions will always be in some EM field, constantly undergoing an acceleration. At the same time, buffer gas cooling occurs to countereffect the energy increase, ensuring that the cloud is reaching and keeping a thermalized cold state. Each ion is henceforth individually simulated and the collisions with the atoms of the buffer gas are modeled carefully at each timestep. The present section introduces all the models implemented in the simulation package. The numerical stakes and the way to test the models and confront them to experimental data are developped in section 3.2.2.3. Four more or less complex microscopic models, were developed: Hard Spheres (HS), *Classical*, *Full* and *Cold gas*. Two ion-atom couples were studied: $Li^+ + He$ and $Ar^+ + He$.

Before entering the details of each model, let us present the general procedure that is followed regardless of the used model. At each timestep and for each ion, the interaction with the buffer gas is divided into two separate steps. The collision probability is computed first to check whether a collision occurs. If so, the resulting scattering is computed in what is the second step presented below. If no collision happens, the ion proceeds on its current track without alteration from the buffer gas. Whichever the outcome is, the whole process starts over at the next timestep.

Collision probability In the first step, the collision probability is always equal to:

$$p = 1 - \exp\left(-\frac{v.\Delta t}{\lambda}\right) \tag{3.37}$$

where v is the current ion velocity, Δt is the global simulation timestep and λ is the mean free path. We immediately see that a high-velocity ion will be more likely to collide with a buffer gas atom. The effect of Δt is studied in section 3.2.2.3, although we can mention here that it is a constant during a whole simulation since we do not work with adaptative timesteps. We detail below, for each model, how the collision frequency ν is computed. This quantity is linked to the mean free path with $\lambda = v/\nu$.

Collision effect In the second step, actually computing the collision means finding the scattering angle θ between the inital and the final momentum vector of the ion in the center of mass frame. The computation of θ is different for each model and we detail for each of them below. The atom itself is not simulated: Its velocity is generated from a Maxwell-Boltzmann distribution *if* a collision occurs and exists only to compute the collision, "disappearing" afterwards. We indeed consider the atoms to form an ideal gas. A rejection method is applied on the atom velocity vector in order to account for the higher probability an ion has of hitting a high velocity atom rather than a slow one, in terms of the relative speed between the ion and the atom. Following the logic presented in [Manu07]:

1. Randomize v_x, v_y and v_z of the atom from normal distributions.
2. Compute the relative velocity norm between the considered ion and the just-drawn atom.
3. Defining σ^2_{atom} as the variance of the velocity component gaussians, compute the ratio between this relative velocity and $(v_{\text{ion}} + 3\sqrt{3}\sigma_{\text{atom}})$, yielding a normalized number. Indeed, it is highly unlikely to randomize an atom for which one of its component is as large as $3\sigma_{\text{atom}}$, this value is thus considered the maximum. The factor $\sqrt{3}$ accounts for the three dimensions.
4. Apply a rejection on this normalized ratio. Draw a random number uniformly between 0 and 1. If this random number is smaller than the ratio, accept this atom. Reject otherwise and start over at the first step.

This method ensures not only that the components of the generated atoms are gaussians, but it favors higher relative velocity as well (see fig. 3.12).

Now that we established the global logic, we will detail each model and present how the two quantities depending on them, the mean free path λ and the scattering angle θ, are computed.

It is important to note that we will use *atomic units* (a.u.) in this section, not to be mixed up with *arbitrary units* (arb. units).

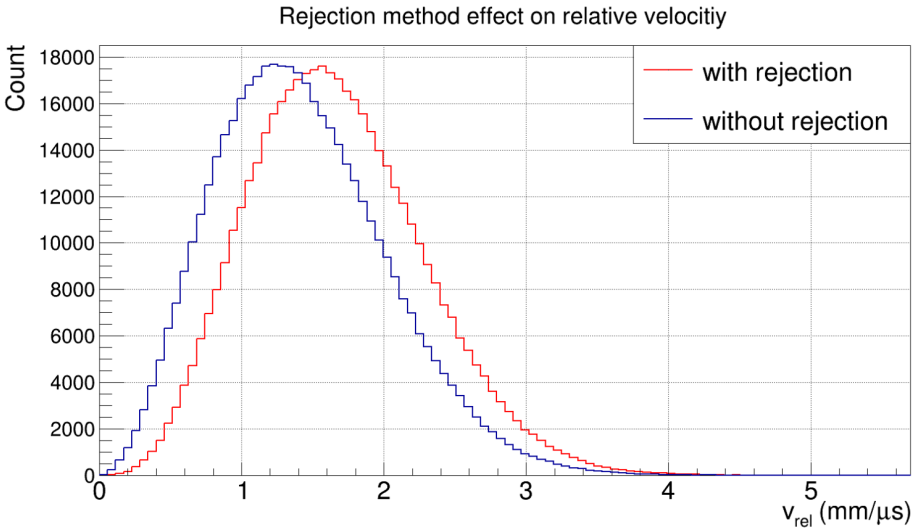

Figure 3.12: Rejection method effect on the generated ion-atom relative velocity.

Hard spheres (HS) Although this is the most basic model, it is simple to understand and to develop while remaining a reference case. Both the ion and atom are considered to be perfectly spherical balls for which a given collision conserves both energy and momentum (classical elastic collision).

Collision probability Given the radii of the balls, assumed to be the Van Der Walls radii (data taken in [Mant09]), we immediately have the maximum impact parameter ($b_{\max} = r_{\text{ion}} + r_{\text{gas}}$) for a collision. The cross section is thus equal to $\pi b_{\max}^2$. As said above, the buffer gas is assumed to follow a Maxwell-Boltzmann distribution. Although there are more atoms with speeds around the most probable speed (v_{mp}), a collision is more likely to occur with atoms going faster than this speed

$$v_{mp} = \sqrt{\frac{2\ k_B\ T_{\text{gas}}}{m_{\text{gas}}}}, \tag{3.38}$$

with k_B the Boltzmann constant. We take this into account by following the reasoning developped in [Manu07] which leads to equation 3.39 that we discuss below in the context of the *Classical* model.

Scattering angle A randomization is done on the linear distribution of impact parameters (see fig. 3.13a). Using momentum and energy conservation, it can be shown that the scattering angle is $\theta = \pi - 2\arcsin(b/b_{\max})$ (see fig. 3.13b). The sign of the result is randomized to have equal chances of being either positive or negative (see fig. 3.15b for a schematic angle definition).

Realistic models Three different realistic models are implemented in the simulation code Clouda (see section 3.2.2): one classical (named *Classical*) and two quantum models (*Full & Cold gas*). We followed the reasonings developed in [Rist12] for their integration in our simulation package. Realistic models are less easily grasped than to the HS model, although the same two-steps global logic detailed at the beginning of this section applies.

***Classical* – Collision probability** In the HS model, the collision probability is a constant depending on the maximum impact parameter $b_{\max}$ which itself depends on the provided radii of the ion and the atom. In the *Classical* model, $b_{\max}$ is defined as well, yet no radii are. Our system is indeed not modeled as two hard spherical balls, it is rather becoming two interacting potentials. In this scenario, defining $b_{\max}$ still makes sense in that it becomes the maximum range we consider the interaction to occur. We show in fig. 3.14a the cross section obtained with our usual[9] $b_{\max} = 45$ a.u. as the blue curve. Once again, this is a constant cross section not depending on the relative speed between the treated ion and atom (we will see hereinafter that it is different for the quantum models). The equation yielding

[9] 45 a.u. was found out to be a good equilibrium between the inclusion of most of the effectful collisions and the number of collisions to compute.

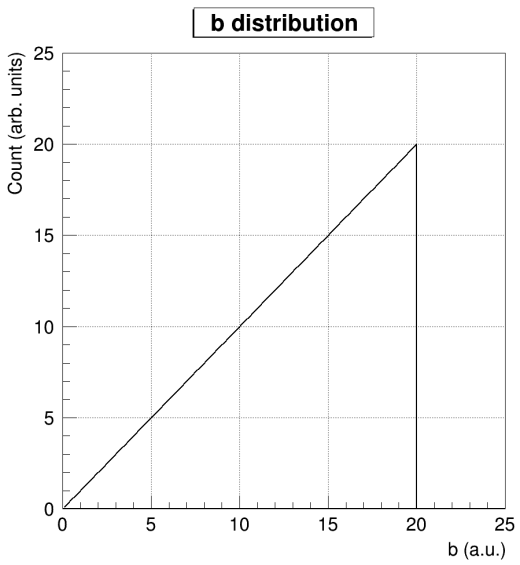

(a) Impact parameter distribution with $b_{\max} = 20$ a.u.

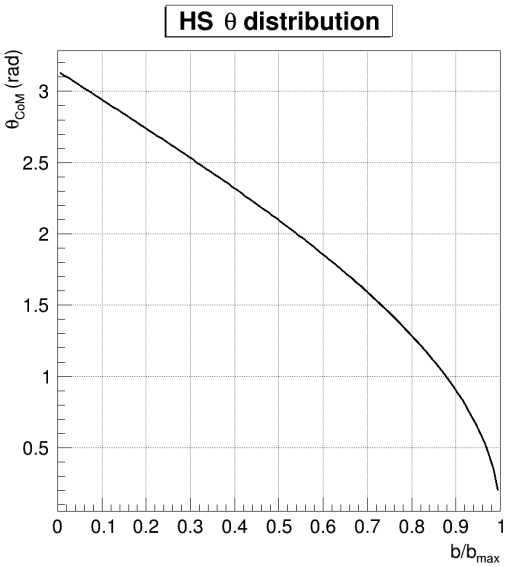

(b) θ distribution as a function of the impact parameter in the HS model.

Figure 3.13: HS model features

the collision frequency ν for the HS and the *Classical* model is derived in [Manu07] and corresponds to equation 16 of [Rist12]. Using our notation, it is as follows:

$$\nu(v) = \rho_{\text{gas}}\ \pi\ b_{\max}^2\ v_{mp} \left[\left(\frac{v}{v_{mp}} + \frac{v_{mp}}{2v} \right) \text{erf}\left(\frac{v}{v_{mp}} \right) + \frac{1}{\sqrt{\pi}} \exp\left(- \left(\frac{v}{v_{mp}} \right)^2 \right) \right] \tag{3.39}$$

where ρ_{gas} is the buffer gas density[10], $\pi b_{\max}^2$ is the constant cross section, v is the ion speed and v_{mp} is the atom most probable speed defined in equation 3.38 above. The collision frequency thus depends linearly on the constant cross section $\pi b_{\max}^2$. We remind that the issue here is to compute the mean free path $\lambda = v/\nu$ to be injected in equation 3.37.

***Full* & *Cold gas* – Collision probability** The *Cold gas* model is an approximation of the *Full* model in which we consider that $v_{mp} = 0$. As we will see, this yields a simplified expression for ν. Staring once more at fig. 3.14a reveals that, unlike the *Classical* model, the quantum models cross section (red curve) depends on the relative speed between the ion and the atom. Numerical needs impose once again the definition of a range to avoid computing effectless long-range interactions. In the present case, this is not done using a $b_{\max}$ value, it is done with the definition of a maximum and a minimum relative speed[11] (between the ion and the atom). Fig. 3.14a pictures the range chosen to include the vast majority of our systems possibilities. Equations 4 and 6 of [Rist12] defines the collision frequency for the *Full* and *Cold gas* models. Using our notation:

- *Full*:

$$\nu(v) = \frac{\rho_{\text{gas}}}{\sqrt{\pi}\ v_{mp}\ v} \int_0^{+\infty} \sigma(x)\ x^2 \left\{ \exp\left[- \left(\frac{x - v}{v_{mp}} \right)^2 \right] - \exp\left[- \left(\frac{x + v}{v_{mp}} \right)^2 \right] \right\} dx \tag{3.40}$$

- *Cold gas*:

$$\nu(v) = \rho_{\text{gas}}\ \sigma(v)\ v \tag{3.41}$$

where $x = v - v_{\text{atom}}$ is the relative speed between the ion and the atom[12] and $\sigma(v)$ or $\sigma(x)$ is the cross section of the collision as a function of the ion velocity or the relative velocity. The simplification

[10] We assume the buffer gas follows an ideal gas law as mentionned earlier.

[11] Actually, the choice is made using the available energies in the center-of-mass frame. This can easily be converted to relative speeds which are more useful in our case with $E_{CM} = 0.5\mu v_{rel}^2$ (with μ the reduced mass).

[12] We remind that a specific atom is randomized from a MB distribution when a collision occurs.

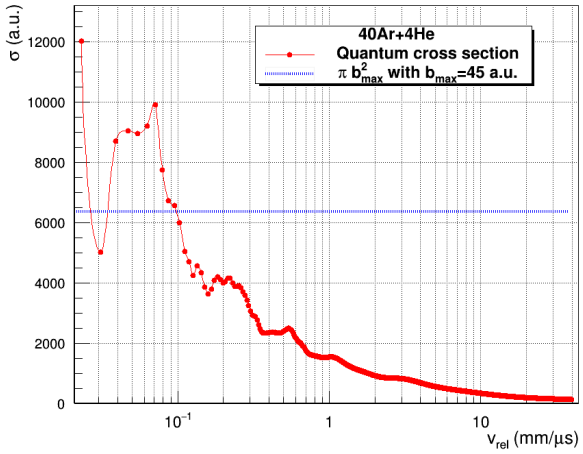

(a) Cross sections in $Ar^+ + He$.

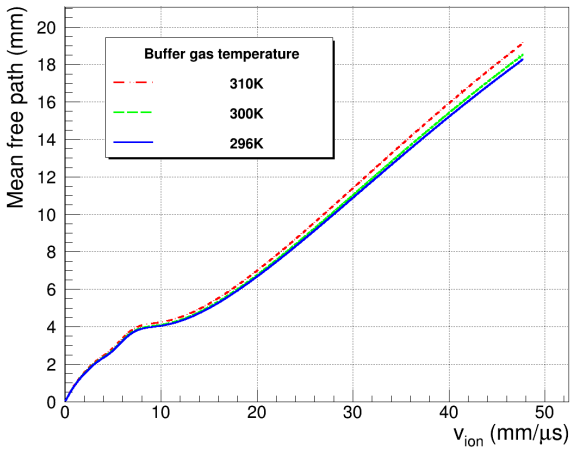

(b) Mean free path in $Li^+ + He$ for the *Full* model.

Figure 3.14: Realistic models probability-related features

granted by the cold gas approximation is obvious here. The *Full* equation can be seen as summing up the contributions of all possible relative velocities weighted by their specific cross section. The variable cross sections are pre-calculated using realistic potentials and are provided as tabulated values in which we interpolate [Pons15]. In order to avoid the resolution of the integral in the *Full* case at each timestep, a pre-calculation is done prior to the simulation and tabulated values are established in which we interpolate as well. We obviously do not integrate to infinity, we rather limit the integration with the cross section limit itself. The range in which the cross section is defined is the domain of definition where most of the simulated ions will fall in[13]. We show in fig. 3.14b the effect the buffer gas temperature has on the mean free path. Indeed, the pre-calculation of the integral must be redone if a new buffer gas temperature is to be used in the desired simulation (dependence on v_{mp}).

With the mean free paths λ now defined, let us take a closer look at the scattering angles.

***Classical* – Scattering angle** If a collision occurs according to the conditions defined above (mean free path), an impact parameter b is drawn in the range $[0; b_{\max}]$ according to the distribution shown in fig. 3.13a. Depending on the available energy in the center of mass frame and on b, θ is fetched in yet other pre-calculated tables [Pons15]. We show in fig. 3.15a the dependence of θ on b and E_{CM}. As we can see, $b_{\max} = 45$ a.u. is an appropriate choice since for $b = b_{\max}$, θ is null or almost so – except for a few very low energy cases. Two remarkable features appear on this last figure. For $E < 0.025$ eV, we see *orbiting* with $|\theta|$ being greater than π, meaning that the ion and the atom make multiple turns around one another before being scattered. Moreover, for $E > 0.025$ eV this *orbiting* transforms in the *rainbow effect* with the characteristic range of θ starting at π for frontal collisions followed by a slow drip towards negative values of θ before returning to 0. Fig. 3.15b schematically represents the interaction in the Argon and Helium system, expliciting the geometry of θ.

***Full* & *Cold gas* – Scattering angle** Same as above, if a collision occurs, a scattering angle θ must be fetched in another pre-calculated table [Pons15] which is the same for both the *Full* and *Cold gas* models. Although θ will still depend on the available energy in the center of mass frame, no impact parameter is defined at all in the quantum context. We thus turn to equation 34 of [Rist12], which is:

$$\frac{\int_0^{\theta} \sigma^d(v,\theta)\sin(\theta)d\theta}{\int_0^{\pi} \sigma^d(v,\theta)\sin(\theta)d\theta} = r \tag{3.42}$$

where σ^d is the differential cross section and r is a random number generated uniformly between 0 and 1. In a way, a renormalization is performed on all relevant impact parameters and this translates as the ratio presented in equation 3.42. Consequently, for the quantum models, θ depends on the available energy in the center of mass frame and the random number r. Fig. 3.16 shows the distribution of all possible θ values.

[13] An ion not falling in it is considered to be at the closest border.

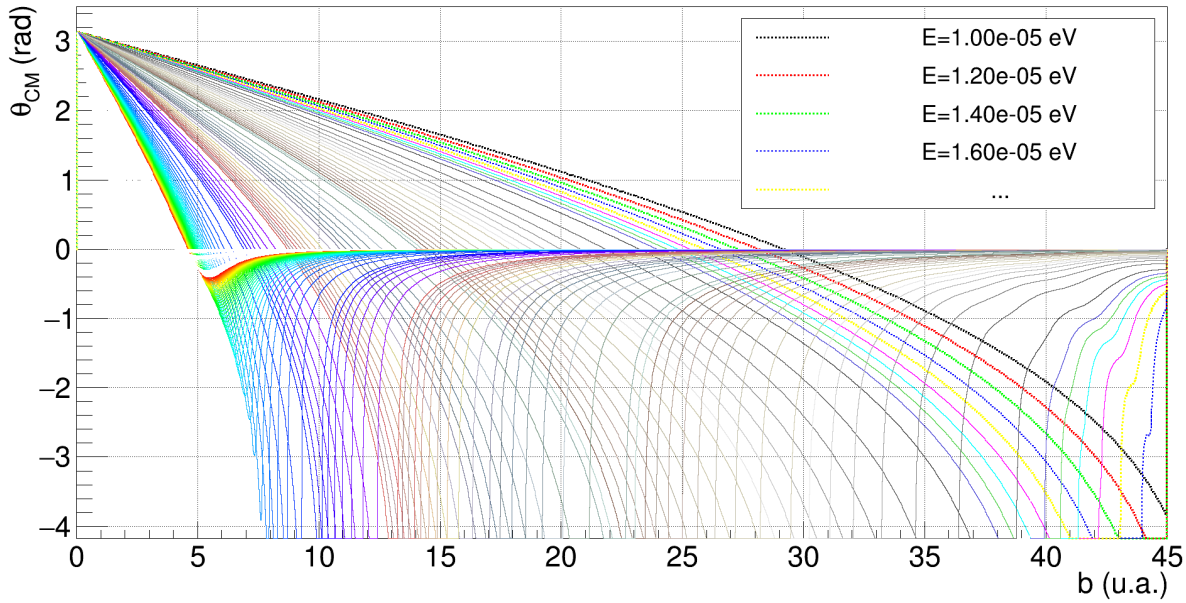

(a) Example of θ distribution in *Classical* model for different relative energies in the case of the $^{35}Ar^{+}$ + ^{4}He system. We can see that the cut chosen at 20 a.u. is appropriate since in the chosen energy range most of the angles are very small or null for this b – except for a few very low energy cases [Pons15].

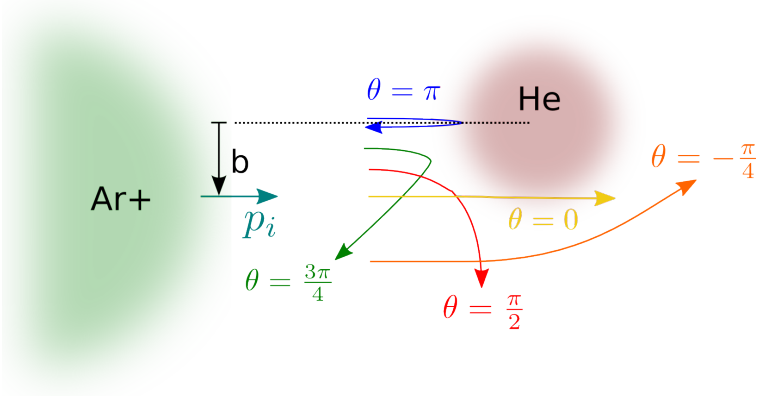

(b) θ schematic representation. The involved atom and ion must be seen as interacting potentials, not solid objects.

Figure 3.15: *Classical* model features.

Excited State The work on the modeling addressed here was done for systems relevant to the LPCTrap experiments. As of now, this means the $^{7}Li^{+}$+^{4}He and $^{40}Ar^{+}$+^{4}He. In the second case, the σ and π states are infinitely degenerated and are thus equiprobable. The σ state exists along the z axis (binding axis) while the π state, the excited one, can equally exist along the x and y axis. Consequently, in the simulations of this system, the fundamental and excited collisions have a probability of respectively one third and two third to occur [Pons15].

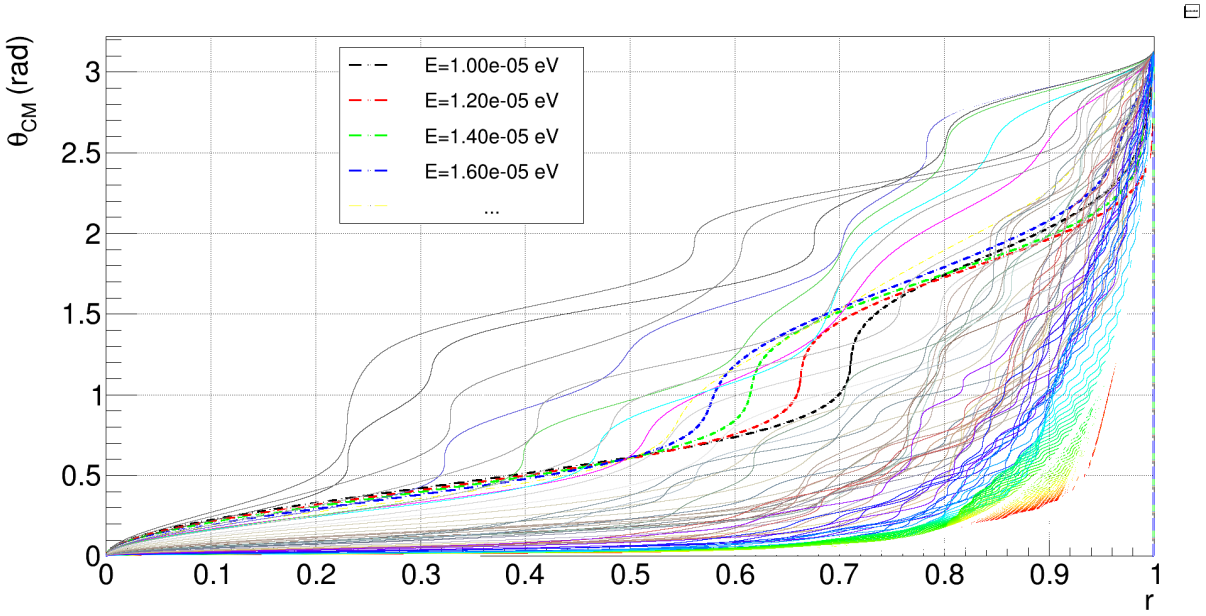

(a) θ distribution in quantum models for different relative energies in the case of the $^{35}Ar^{+} + {}^{4}He$ system [Pons15]. The randomization is not done on the impact parameter, but on a ratio r (see text for details).

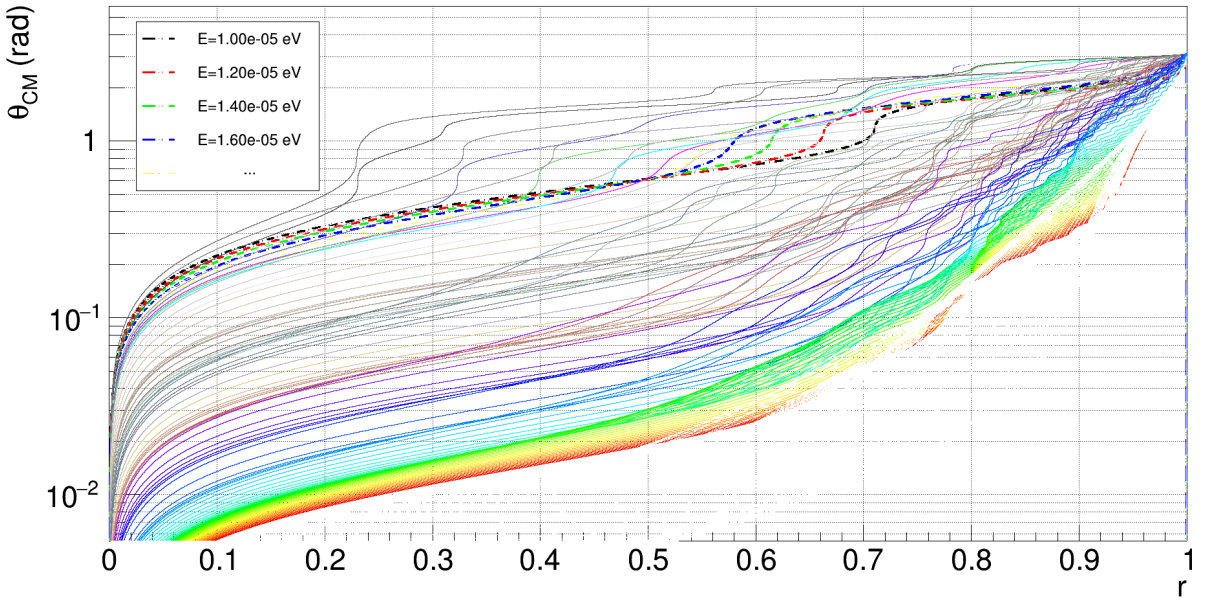

(b) Same as 3.16a in logarithmic scale.

Figure 3.16: θ distribution features in quantum models.

3.2.2.3 Buffer gas – Models assessment

This section will detail the method to assess the models used, including the comparison with available experimental data.

The ion-atom systems we implemented and tested are chosen among the available experimental data to be as close as possible to the relevant systems for the LPCTrap experiments [Elli76; Vieh95]. We can confront our model to two different kinds of data: drift velocities and diffusion coefficients (see below for detail). For both of these tests, another electric field was implemented in CLOUDA. It is an ideal, uniform and infinite electric field toward the x axis. Since the experimental data are presented as a function of a given *Townsend* (Td) value, the ideal electric field can be set as such. We remind here that 1 Td is the ratio of the electric field strength to the buffer gas density and corresponds to 10^{-21} V.m^2. For a chosen Td value and buffer gas pressure and temperature, the program will set the field accordingly.

The concept of thermalization, which we mentionned in section 2.2.4, is rather important here. The system needs time to reach an equilibrium state we call thermalization. CLOUDA does not generate the initial ion distribution. It is provided by an external routine named BOLTZMANN and many settings are possible. Further details are given in the "initial state effect" section below.

In order to assess a model, one needs to ascertain that thermalization is reached before extracting any observables. Moreover, a check is required to ensure that the results will be the same regardless of the initial state and that the timestep is chosen small enough for the results to converge. Thus, we will first describe the method to find the thermalization time, then check the initial state effect and end with the validation of the chosen timestep.

Typically, the simulations in this context are configured in the following way:

- **Buffer gas (atoms):** $T_{\text{gas}} = 300$ K, $p_{\text{gas}} = 1$ Pa
- **Studied system:** $^{40}\text{Ar}^+ + {}^4\text{He}$ or $^7\text{Li}^+ + {}^4\text{He}$
- **Field:** E/ρ in $[2; 200]$ Td
- **Timestep:** $\Delta t = 1$ ns
- **Number of ions:** $N = 16384$ ions
- **Initial state (ions):**
  - **Positions:** All ions are inside a ball of radius $r = 1$ μm.
  - **Velocities:** The vectors are generated according to a Maxwell-Boltzmann distribution with $T_{\text{init}} = 100$ K ($\simeq 1.3 \times 10^{-2}$ eV).

Thermalization time Each model was characterized using different configurations through the study of two different distributions to extract the thermalization time for both the lowest and highest experimental Td values. The first distribution is the ion cloud mean energy evolution ($E_K(t)$) while the second one is the drift velocity evolution ($v_d(t)$). All fits on these distributions were performed using the following exponential function:

$$X(t) = A - B\exp(-(at^2 + bt)) \tag{3.43}$$

where $X(t)$ is either $E_K(t)$ or $v_d(t)$ and A, B, a and b are the fit parameters. It has been found that the second order contribution might provide a better fit in some cases, although it is sometimes null. The time constant τ is then extracted from this exponential fit and the cloud is considered thermalized whenever 10τ has been reached:

$$\text{"linear"}(a = 0) \qquad \tau = \frac{\ln(2)}{b} \tag{3.44}$$

$$\text{"quadratic"} \qquad \tau = \frac{-b + \sqrt{b^2 + 4a\ln(2)}}{2a} \tag{3.45}$$

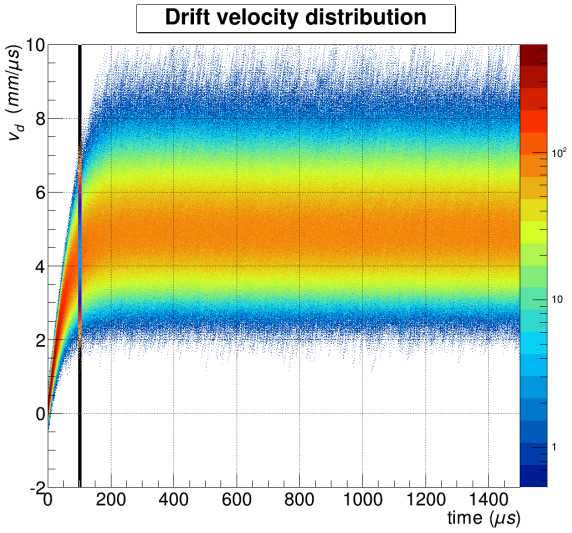

(a) v_x distribution.

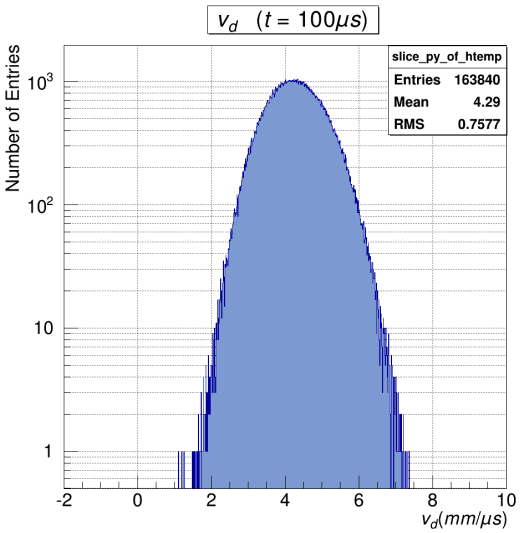

(b) Projection of the v_x distribution on the y axis around $t = 100$ μs, the mean value is extracted.

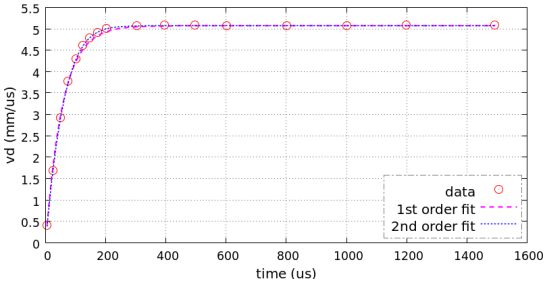

(c) Mean v_x values fit.

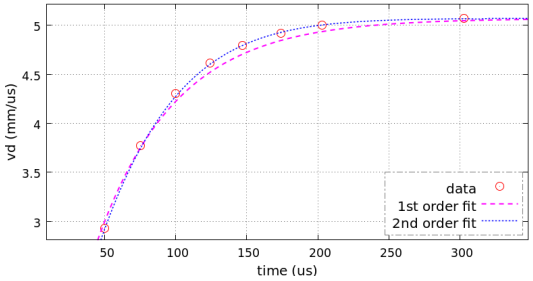

(d) Mean v_x values fit (zoom).

Figure 3.17: Thermalization from v_d ($^{40}Ar^{+}$+^{4}He system at 130 Td, *Classical* model).

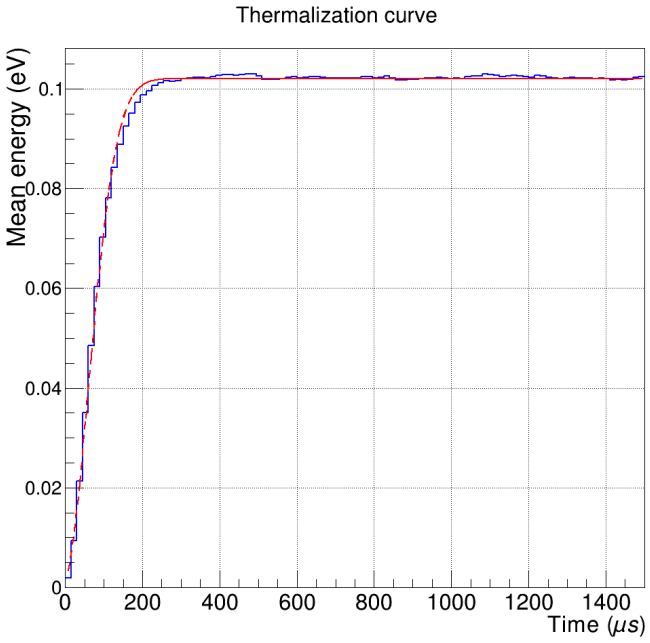

Figure 3.18: Thermalization from $E_K(t)$. The calculated energy is shown with the solid blue curve while the fit result is the dashed red curve.

Let us take a closer look at a fit process example, say, for the *Classical* model in the $^{40}Ar^{+}+^{4}He$ system at 130 Td and 300 K. We begin with the obtained v_x distribution for all ions shown on fig. 3.17a. Around twenty projections on the y axis are taken on the time range, *e.g.* fig. 3.17b features the projection we obtain around $t = 100$ μs. We then take the mean value of each projected distribution which corresponds to v_d at the given time. Finally, on fig. 3.17c and 3.17d, we show the data points (all the mean values) extracted with this method and the fits performed on them. In this case, the fit results are $a = 2.74 \times 10^{-5} \pm 1.97 \times 10^{-6}$ (7.19%) and $b = 1.69 \times 10^{-2} \pm 1.64 \times 10^{-4}$ (0.97%), yielding $\tau_{v_d} = 38.60 \pm 0.036$ (0.09%) μs. Thermalization is thus reached at $t = 386.0$ μs. Neglecting the second order contribution would yield $\tau_{v_d} = 41.01 \pm 0.57$ (1.39%) μs, setting the thermalization at 410.1 μs. Being cautious leads to keep the highest value since both fits are quite accurate. Indeed, this is not always the case and in a few examples the second order contribution becomes much more important, utterly casting aside the linear fit.

The extraction of the thermalization time from the energy distribution is done in the same way. The mean energy of the ion cloud as a function of time is shown in fig. 3.18 along with the 2^{nd} order fit result. Formula 3.45 is used to extract the time constant, yielding $\tau = 65.44$ μs. This gives a thermalization time of 654.4 μs, which is much higher than what was found using v_d. The large difference between the two times is not well understood. As a safety precaution, we choose a final value of 800 μs for this specific case of the *Classical* model in the $^{40}Ar^{+}+^{4}He$ system at 130 Td and 300 K.

This twofold method must be repeated for all four models (HS, *Classical*, *Full* and *Cold gas*), for the extrema Td values and for two ion-atom systems. Since the Lithium data for v_d, D_T and D_L were gathered at different temperatures, a more extensive simulation work has to be done accordingly. Indeed, the temperature is yet another important parameter for it has an impact on the mean free path value (see fig. 3.14b). The achieved results are summed up in table 3.1.

System	**Model**	$\mathbf{T_{atom}}$ **(K)**	$\mathbf{E/\rho}$ **(Td)**	$10.\tau_{v_d}$ (μs)	$10.\tau_E$ (μs)	Chosen $10.\tau$ (μs)
$^{40}Ar^+ + ^4He$	HS	300	5	528.3	375.1	600.0
$^{40}Ar^+ + ^4He$	HS	300	130	216.8	377.1	600.0
$^{40}Ar^+ + ^4He$	*Classical*	300	5	644.7	500.3	800.0
$^{40}Ar^+ + ^4He$	*Classical*	300	130	410.1	654.4	800.0
$^{40}Ar^+ + ^4He$	*Full*	300	5	586.6	466.2	800.0
$^{40}Ar^+ + ^4He$	*Full*	300	130	401.7	713.3	800.0
$^{40}Ar^+ + ^4He$	*Cold gas*	300	5	707.3	731.2	800.0
$^{40}Ar^+ + ^4He$	*Cold gas*	300	130	396.6	684.4	800.0
$^{7}Li^+ + ^4He$	HS	296	10	98.0	115.7	200.0
$^{7}Li^+ + ^4He$	HS	296	120	42.4	74.2	200.0
$^{7}Li^+ + ^4He$	*Classical*	296	10	137.6	140.6	400.0
$^{7}Li^+ + ^4He$	*Classical*	296	120	146.1	287.6	400.0
$^{7}Li^+ + ^4He$	*Full*	296	10	130.4	142.1	400.0
$^{7}Li^+ + ^4He$	*Full*	296	120	145.1	281.0	400.0
$^{7}Li^+ + ^4He$	*Cold gas*	296	10	128.9	205.3	400.0
$^{7}Li^+ + ^4He$	*Cold gas*	296	120	146.3	288.4	400.0
$^{7}Li^+ + ^4He$	HS	300	2	110.0	98.28	200.0
$^{7}Li^+ + ^4He$	HS	300	200	33.70	58.19	200.0
$^{7}Li^+ + ^4He$	*Classical*	300	2	133.0	80.4	400.0
$^{7}Li^+ + ^4He$	*Classical*	300	200	121.7	237.2	400.0
$^{7}Li^+ + ^4He$	*Full*	300	2	116.3	85.0	400.0
$^{7}Li^+ + ^4He$	*Full*	300	200	115.2	217.5	400.0
$^{7}Li^+ + ^4He$	*Cold gas*	300	2	120.9	181.8	400.0
$^{7}Li^+ + ^4He$	*Cold gas*	300	200	122.3	238.4	400.0
$^{7}Li^+ + ^4He$	HS	310	10	100.1	113.5	200.0
$^{7}Li^+ + ^4He$	HS	310	120	44.3	77.9	200.0
$^{7}Li^+ + ^4He$	*Classical*	310	10	142.6	145.1	400.0
$^{7}Li^+ + ^4He$	*Classical*	310	120	152.7	301.0	400.0
$^{7}Li^+ + ^4He$	*Full*	310	10	141.7	150.0	400.0
$^{7}Li^+ + ^4He$	*Full*	310	120	151.4	291.5	400.0
$^{7}Li^+ + ^4He$	*Cold gas*	310	10	139.6	217.8	400.0
$^{7}Li^+ + ^4He$	*Cold gas*	310	120	153.0	301.7	400.0

Table 3.1: Thermalization results for all studied systems. The last column is chosen high as a safety precaution and equal in the same model for configuration ease reasons. Only drift velocities are available for the Argon-ion system between 5 and 130 Td. In the case of the Lithium-ion system, available data includes D_L at 296 K, v_d at 300 K and D_T at 310 K ranging from 10 to 120 Td for the diffusion coefficients and from 2 to 200 Td for the drift velocities.

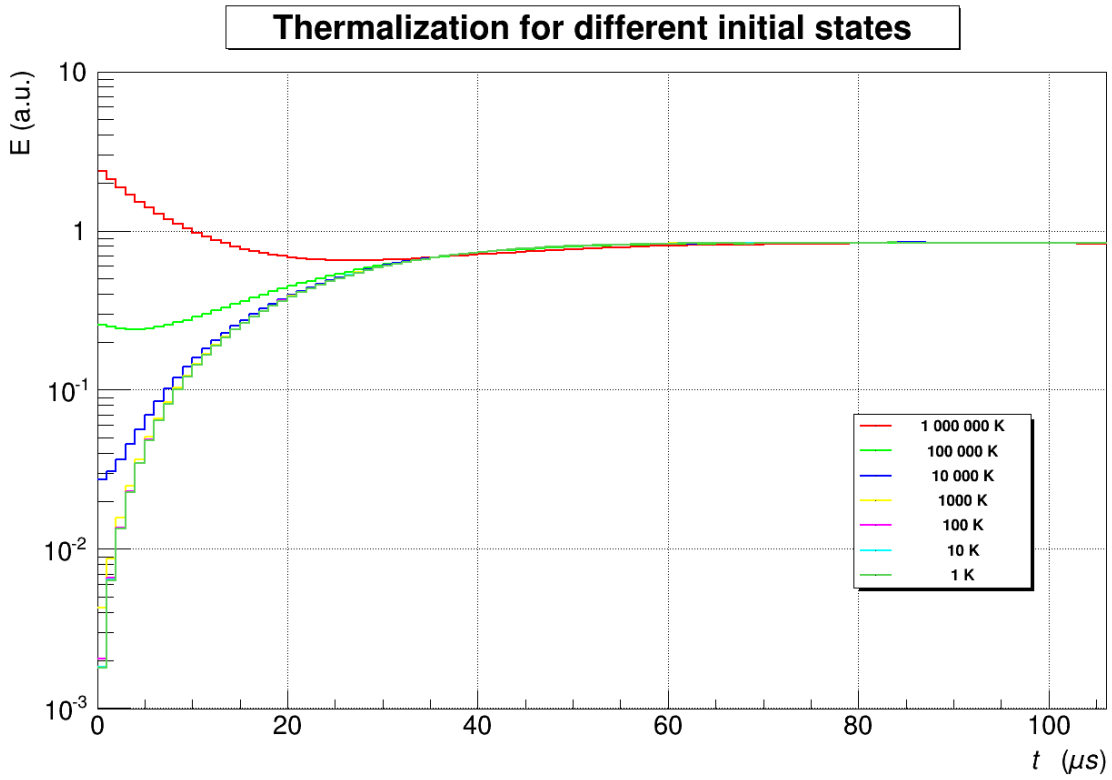

Figure 3.19: Initial temperature effect on thermalization.

Initial state effect Now that thermalization has been properly defined, we can take a look on the impact the initial state has on thermalization. The BOLTZMANN routine generates an initial distribution independently from CLOUDA from which we pick a given number of ions. This ensures to always work with the same initial state when studying different aspects of CLOUDA. BOLTZMANN is adjustable with several parameters:

- The number of ions to generate;
- The temperature yielding the velocity distribution;
- The spatial shape of the volume where the N ions are contained and its dimensions.

Each initial state includes more than one million ions (2^{20}), well above what will be actually used in the simulations presented here[14]. We show in fig. 3.19 the thermalization plots for different initial temperatures ranging from 1 K to 10^6 K for ions in a ball of radius 1 μm. Three shapes were studied: a uniform ball, a gaussian ball (the ion density follows a three-dimensional gaussian distribution) and a tube along the electric field. The results in table 3.2 shows the thermalization times and the final v_d. As expected, the latter is always the same once thermalization is done. This *reset* on the phase space justifies that the simulation starts in the Paul trap since all information prior to this moment is lost with the thermalization process.

Timestep validation The timestep is explicitly appearing at two different places. It shows up both in the equation of motion resolution through any of the three steppers (e.g. eq. 3.3) defined earlier and in the collision probability computation of eq. 3.37. For a given scenario, a comparison has thus been made between the three steppers for four different Δt. The drift velocity and the collision probability was recorded in each case. The data shown in table 3.3 underlines that the results start converging for a timestep of 1 ns, regardless of the stepper. Indeed, when there is buffer gas, the constant reinitialization of the velocity vector happening after each collision prevents any error to accumulate. In other words,

[14] CLOUDA is especially designed to work with the N-body effect, a realistic harmonic field as we will see below and a realistic buffer gas. In principle, staying on more basic interactions would allow the user to go beyond that amount of ions, depending on his hardware.

Initial shape	**Init. temp (K)**	$10.\tau_{v_d}$ (μs)	$10.\tau_E$ (μs)	**Final v_d (mm/μs)**
Ball ($r = 1$ μm)	1	115.4	217.5	12.41
Ball ($r = 1$ μm)	10	114.8	217.5	12.41
Ball ($r = 1$ μm)	10^2	115.3	217.5	12.41
Ball ($r = 1$ μm)	10^3	115.2	217.2	12.41
Ball ($r = 1$ μm)	10^4	114.4	214.9	12.41
Ball ($r = 1$ μm)	10^5	104.6	185.2	12.41
Ball ($r = 1$ μm)	10^6	123.3	230.7	12.41
Ball ($r = 1$ μm)	10^2	115.3	217.5	12.41
Tube $r = 1$ μm ; $h = 5$ μm	10^2	115.0	216.9	12.41
Gaussian ball $r = 1$ μm ; FWTM= $2r$	10^2	115.3	217.4	12.41

FWTM = Full Width at Tenth Max

Table 3.2: Initial state effect on thermalization time. This was done using the $^7Li^+ + ^4He$ system at 300 K and 200 Td. As expected, the final drift velocity is always the same, regardless of the initial state, thus vindicating the need to wait for full thermalization.

Stepper	**Δt** (ns)	**Final v_d (mm/μs)**	**Collision proba. (%)**
Euler	100	13.65	26.2
Euler	10	12.52	2.9
Euler	1	12.42	0.29
Euler	0.1	12.42	0.029
Leapfrog	100	13.65	26.2
Leapfrog	10	12.52	2.9
Leapfrog	1	12.42	0.29
Leapfrog	0.1	12.42	0.029
RK4	100	13.58	26.2
RK4	10	12.51	2.9
RK4	1	12.42	0.29
RK4	0.1	12.42	0.029

Table 3.3: Timestep study. For any stepper, the convergence in the results is achieved at 1 ns. The linear dependence between the timestep and the collision probability may be interpreted as an inverse factor on the mean free path (see equation 3.37).

in a pure tracking scenario, say for an ion in an electric field without buffer gas, steppers would vary in precision and the choice of it would be crucial.

Drift velocities For some ion-atom couple, we dip an initial ion bunch in a uniform electric field and wait for the system to reach thermalization. In this case, thermalization could be seen as an equilibrium between the acceleration provided by the field and the deceleration resulting from the collisions with the buffer gas atoms. At this point, the mean velocity of the ions is called the *drift velocity* (v_d). We note that v_d is only defined for a uniform field and does not have any sense in a dynamic trapping RF field. Nevertheless, fig. 3.20 shows LPCTrap regions. This is done considering the mean energy of the ions (~ 0.1 eV) and computing v_d such that $0.1\ eV = \frac{1}{2}mv_d^2$, knowing that the ions may, in principle, sweep all the velocities from 0 to the v_d value in the dynamic trapping field.

The v_d we obtained are confronted with the experimental data in fig. 3.20 for the $^{40}Ar^+ + ^4He$ system. The first remarkable feature is the gap between the data and the HS results. This is not surprising since we know that this approximation is crude: the ion and the atom are not hard spheres at all. This being said, we tried to modify the ion and atom radii to better account for experimental data, but the shape of the curve does not fit. Regarding the realistic models, we see they agree much better with data. Although there is a systematic offset in the low Td values excluding the *Full* model out of the experimental error bars, starting at 45 Td all the three realistic models are inside this error. The trend followed by the three models is in any case mimicking the experimental data one. Fig. 3.21 exhibits the results for the $^7Li^+ + ^4He$ system which are rather similar.

Diffusion coefficients Using the same Townsend drift field as above (uniform in the x direction) and after thermalization is reached, we start to record the standard deviation evolution ($\sigma(t)$) of both the transverse (D_T) and the longitudinal (D_L) position distributions for all ions. They are linked in the following way:

$$\sigma_x^2 = \frac{D_L}{2} \times t + b \tag{3.46}$$

$$\sigma_y^2 = \sigma_z^2 = \frac{D_T}{2} \times t + b \tag{3.47}$$

A linear fit on the simulated data yields the diffusion coefficients, where b is a fit parameter related to the initial conditions. We will be presenting our results as they are in the literature:

- ρD_L for the longitudinal coefficent, ρ being the buffer gas density.
- D_T/K for the transverse coefficient, $K = v_d/E$ being the mobility of the ions.

Before presenting the results themselves, let us step into the details of a specific coefficient extraction. As an example, we will extract D_L in the case of the *Classical* model at a buffer gas temperature of 296 K and at 120 Td. We note that since no data is available for these coefficients in the Argon case, we will only focus on the Lithium-Helium system.

One must note that we will be performing a linear fit on the evolution of the square RMS of the ions distribution in x in order to extract the slope. This RMS evolves quite slowly, meaning that in order to perform that linear fit correctly, we will be running long simulations to feed the fit with well-separated points. The usual simulations in this work go up to 1 ms, a time long enough to provide most of the interesting characteristics of a thermalized state. In the case of the diffusion coefficients, because of this RMS slow evolution, simulations were performed until ~ 10 ms, implying long computation times. Moreover, the initial state for all ions was set to $\mathbf{r} = \mathbf{v} = \mathbf{0}$, allowing the system to naturally grow its own gaussian distributions.

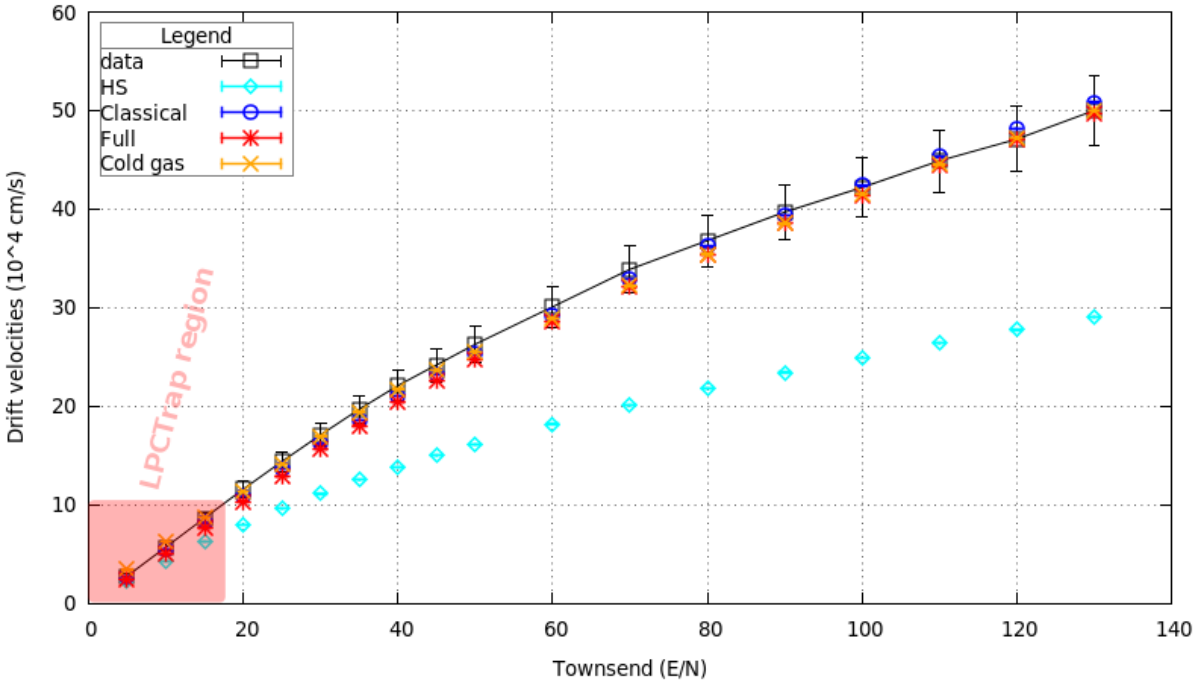

(a) Overview

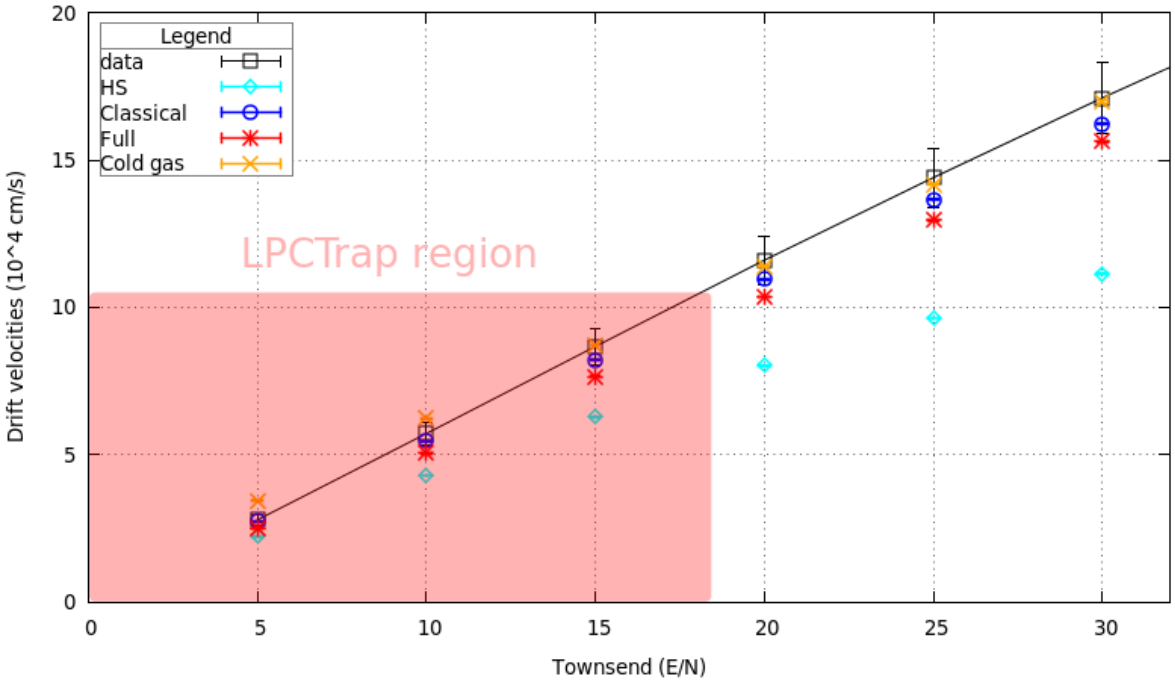

(b) Zoom

Figure 3.20: Drift velocities in the $^{40}Ar^{+}+^{4}He$ system

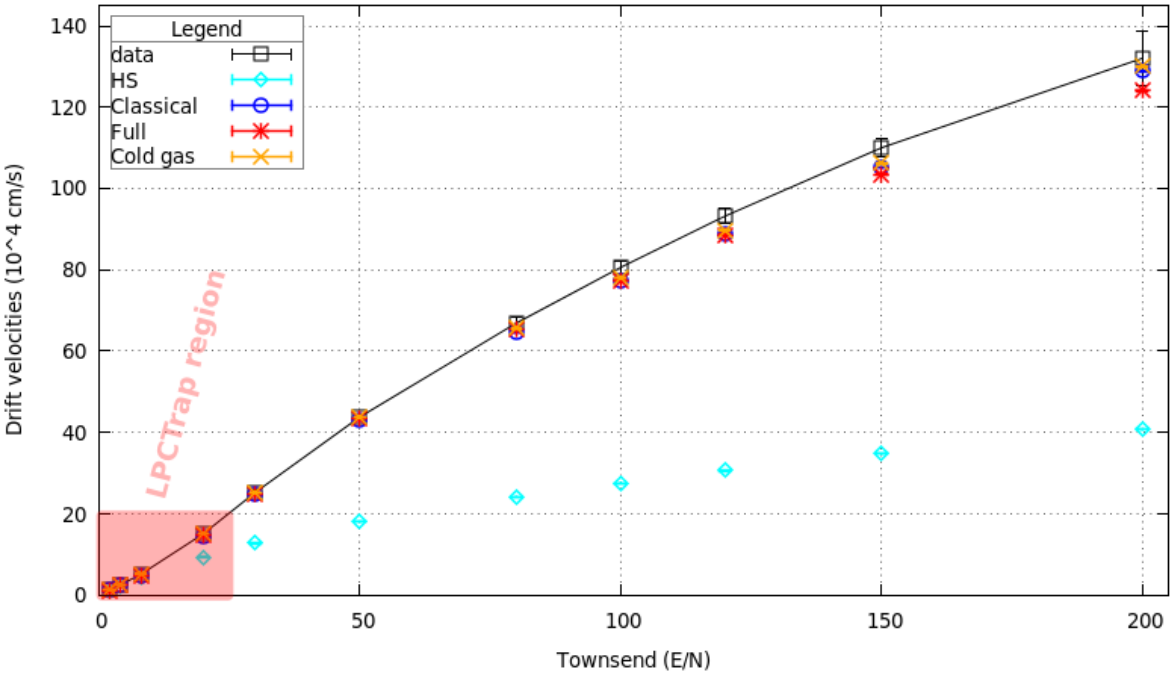

(a) Overview

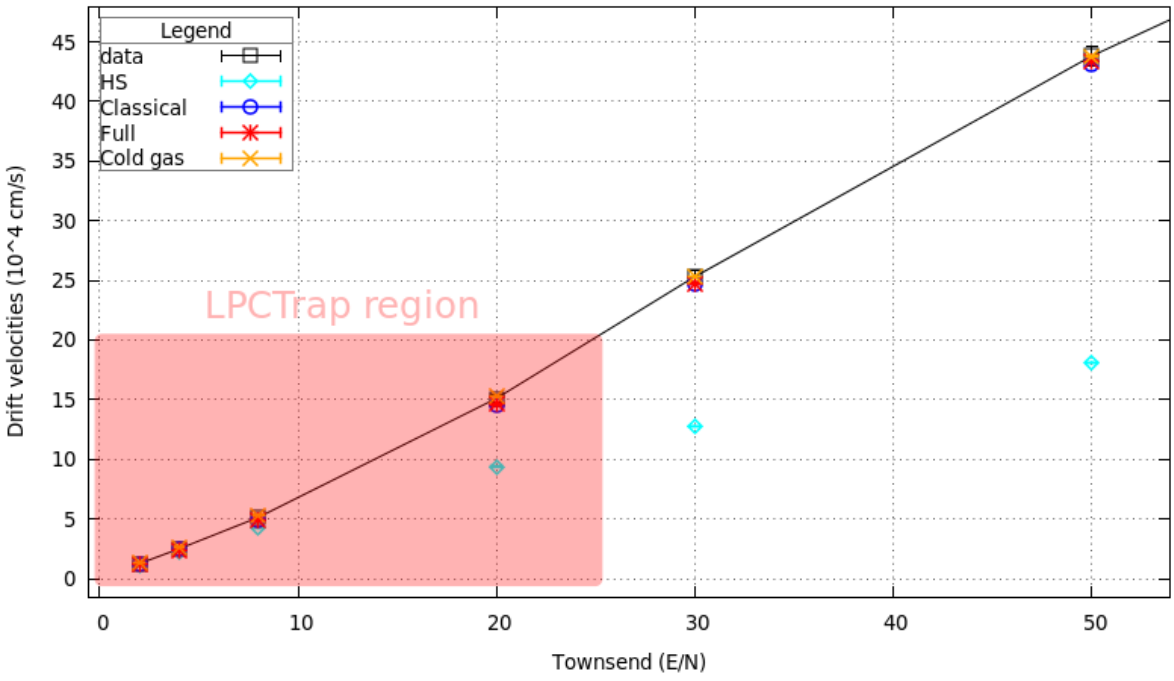

(b) Zoom

Figure 3.21: Drift velocities in the $^{7}Li^{+}+^{4}He$ system

The fit was done on simulated data using ten thick slices of the x distribution as a function of time. By "thick slices", we mean that each distribution from which the RMS is extracted is in fact made of ten consecutive distributions, so that statistical noise is lowered. In numerical words, each time a recording begins, ten consecutive timesteps are saved instead of just one as is done for other simulations. Typically, this leads to a global distribution as shown in fig. 3.22a where the ten slices are shown in the zoom of fig. 3.22b. Now, for each thick slice we project the distribution on the y axis (which is the position in x). We then perform a gaussian fit on the obtained distribution. The square *sigma* of this last gaussian fit is the first point for the linear fit mentionned above. We show in fig. 3.23 typical gaussian fits for three different number of ions cases. We note that the reduced χ^2 suggests these distributions are not real gaussians. In fact, these distributions are made of one gaussian for each summed slice, the correct distribution is thus made of ten similar gaussians.

After ten gaussian fits performed on several datasets with a different number of ions, we are able to construct the plot shown in fig. 3.24 which shows both the square RMS as a function of time and the linear fits results. Indeed, it is important to verify the effect of changing the number of ions has on the fit error. The summary of this check is shown in table 3.4 for D_L and in table 3.5 for D_T. In the case of D_L, $N = 32768$ was found out to be a good compromise between computation time and fit accuracy. This particular convergence study was done using a limited energy range during the first tests. Since the ions really belong to a wider energy range, the collisions occuring below 5×10^{-3} eV and above 5.5 eV were approximated at the time. We assume here that the convergence on the D_L and D_T values as a function of the number of ions remains the same, albeit the coefficient values themselves change.

All this extraction procedure must be followed for twelve Td values and for the four available buffer gas models. Since experimental data for D_L was obtained at 296 K and at 310 K for D_T, all that is described in the previous sentence must be done twice. The final results compared with experimental data are shown in fig. 3.25 for D_L and fig. 3.26 for D_T.

Globally, the quantum models are in good agreement with the data. Regarding the *Classical* model, we note a good agreement at low Td in both cases but a gap appears starting at 60 Td for D_T and 50 Td for D_L, although the trend is correct. During the development of Clouda, the energy ranges covered by the theoretical tables increased. At first, they were not describing all the possible collisions and, thus, approximations were made. It was found out that these tables needed to cover a wider energy ranges, *i.e.* the approximations brought an important error. The results presented here are with such wider tables. More than the angular distribution, the main difference between the *Classical* model and the quantum ones is the collision probability which depends on the cross section. As shown in fig. 3.14a, the *Classical* cross sections are very large, especially at high energies. The foreseen way to correct the discrepancies on D_L and D_T for the *Classical* model is to use the quantum cross sections and change the maximum impact parameter value (b_{max}) accordingly. Indeed, $\sigma = \pi b_{max}^2$ corresponds to a classical cross section. Using the quantum cross section implies a dependence on the ion velocity. One can then compute $b_{max} = \sqrt{\sigma/\pi}$ as the maximum impact parameter for a specific collision. The diffusion angle would then be fetched in the tables of the *Classical* model as it is already done.

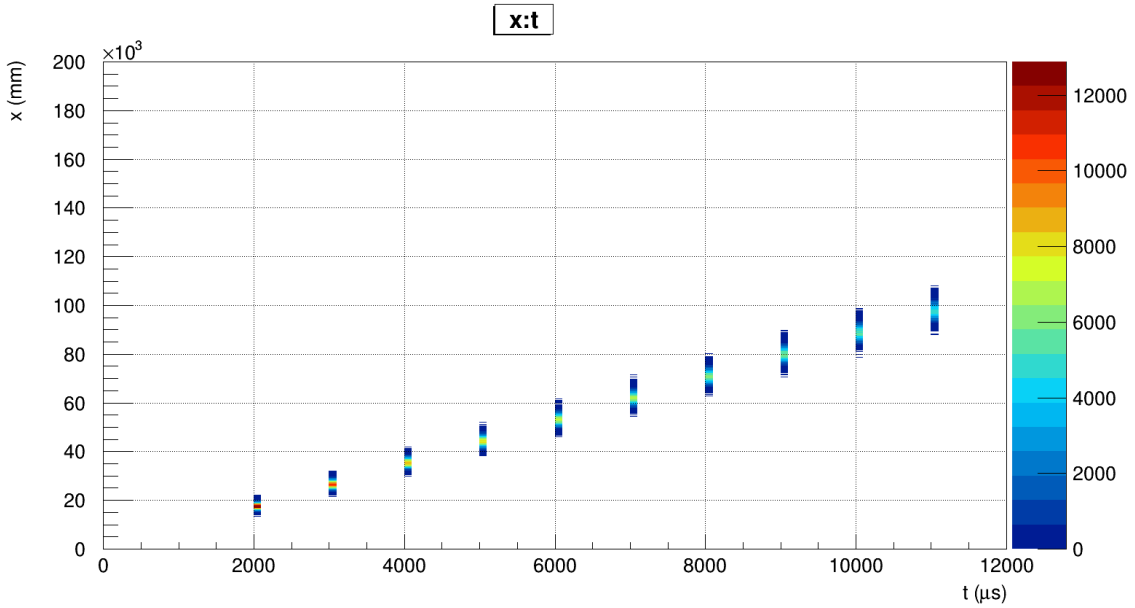

(a) Typical distribution of x vs t ($N = 16384$).

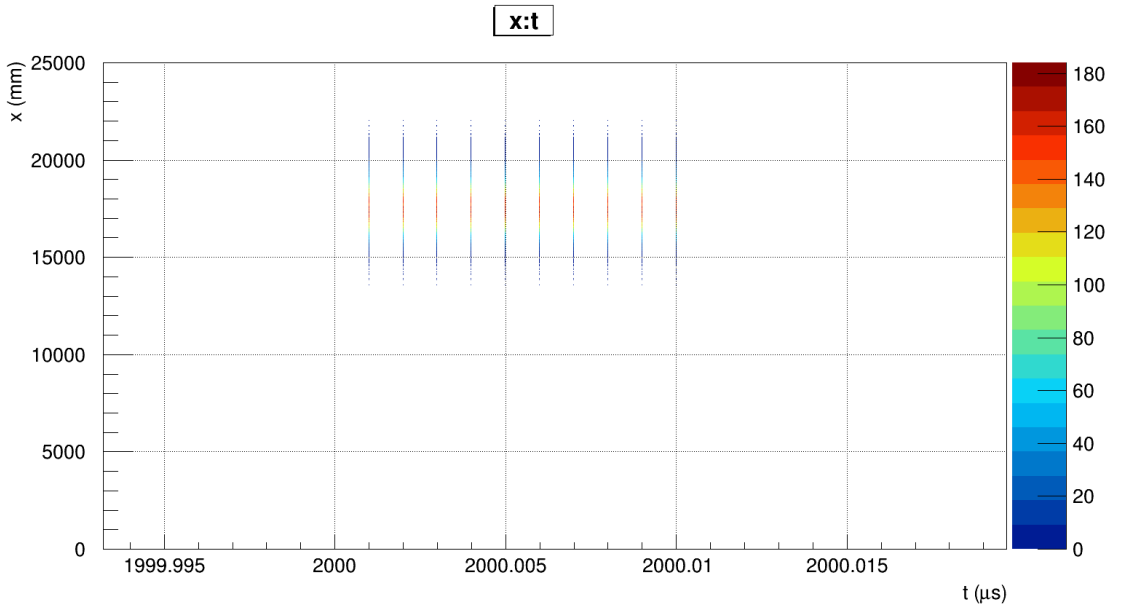

(b) Zoom on fig. 3.22a revealing the ten slices (see text).

Figure 3.22: D_L recorded data

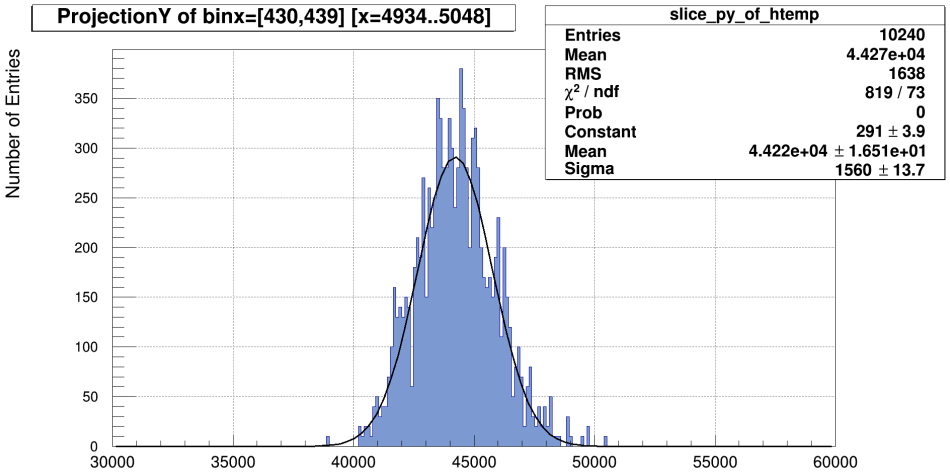

(a) $N = 1024$

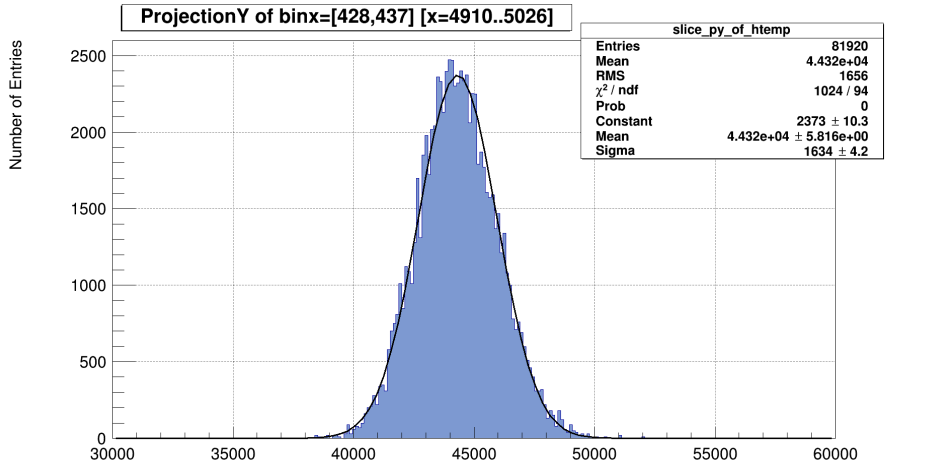

(b) $N = 8192$

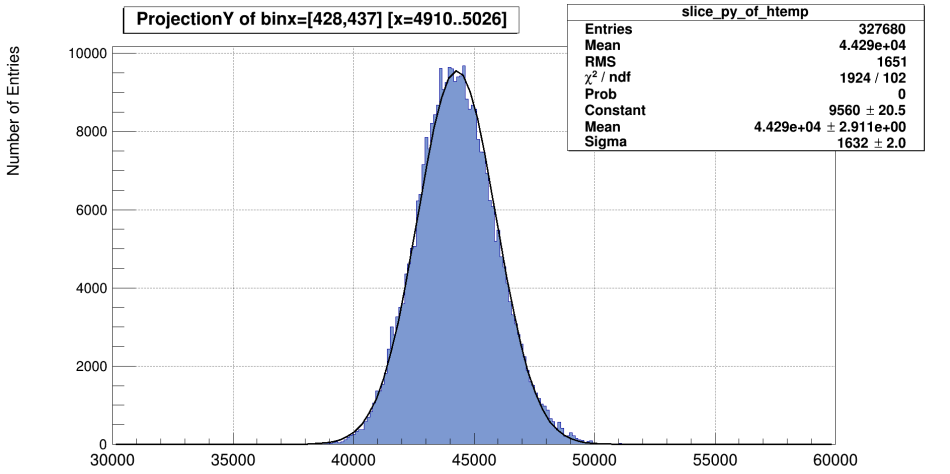

(c) $N = 32768$

Figure 3.23: D_L: Examples of gaussian fit on y-projection of position distribution.

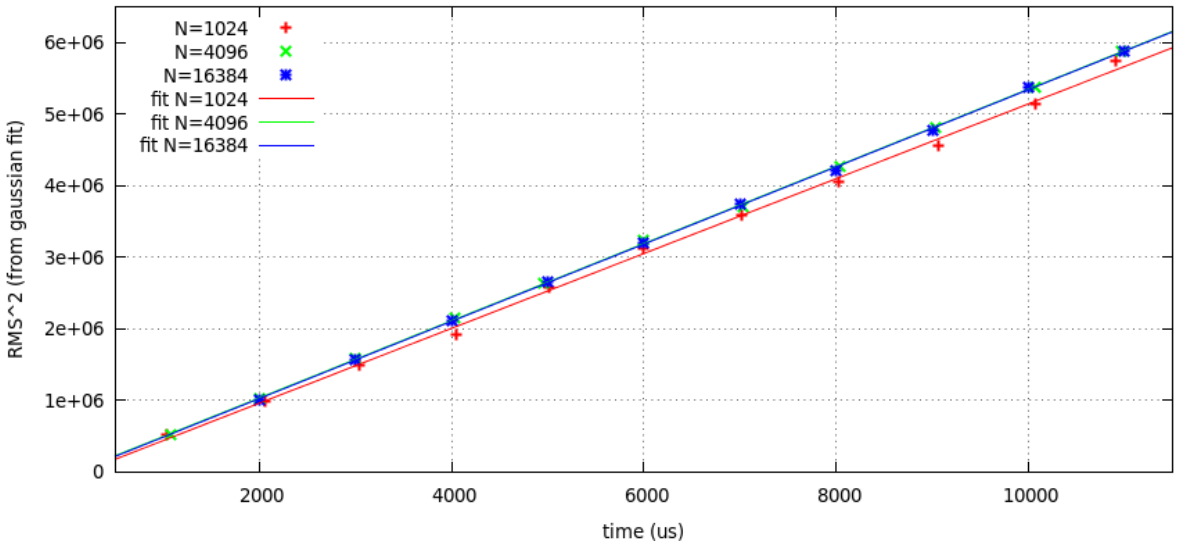

Figure 3.24: D_L: Final linear fit example for three different numbers of ions at 120 Td.

N (ions)	$\rho.D_L$	Fit error (abs)	Fit error (rel)	Computing time (GTX TITAN black)
1024	619.90	23.12	3.73%	18m
4096	670.89	7.58	1.13%	20m
8192	670.24	4.71	0.70%	23m
16384	668.95	3.30	0.49%	32m
32768	677.67	1.73	0.26%	48m
65536	686.30	1.27	0.19%	1h18
131072	679.26	1.26	0.19%	2h17m
262144	678.63	0.90	0.13%	4h13m
Exp. data	791.0	39.55	5.00%	N/A

Table 3.4: The effect of the number of ions on the D_L value. For the experimental data the "fit error" corresponds to the experimental error. We note that these results were done with an older limited energy range, the point being the convergence on the results as a function of the number of ions.

N (ions)	axis	D_T/K	Fit error (abs)	Fit error (rel)
1024	y	796.11	12.62	1.59%
1024	z	758.70	15.42	2.03%
4096	y	824.89	10.95	1.33%
4096	z	789.80	9.79	1.23%
8192	y	817.31	9.76	1.19%
8192	z	822.65	3.16	0.38%
16384	y	827.33	5.33	0.64%
16384	z	835.06	2.76	0.33%
32768	y	845.98	3.92	0.46%
32768	z	844.91	1.27	0.15%
65536	y	844.43	2.1072	0.25%
65536	z	846.57	0.6631	0.08%
131072	y	852.71	1.40	0.16%
131072	z	851.74	0.34	0.04%
262144	y	852.81	0.64	0.07%
262144	z	858.15	0.75	0.09%
Exp. data	N/A	855.00	25.65	3.00%

Table 3.5: The effect of the number of ions on the D_T value. The computing times are the same as for D_L (see table 3.4). We note that these results were done with an older limited energy range, the point being the convergence on the results as a function of the number of ions.

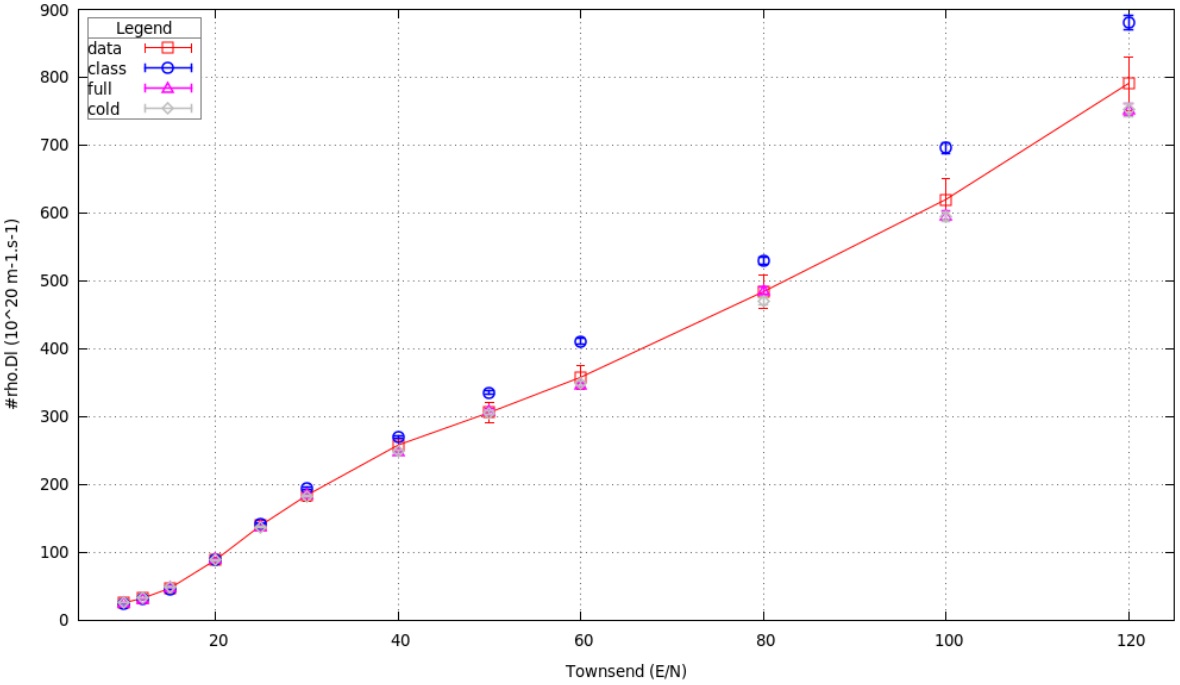

Figure 3.25: D_L results

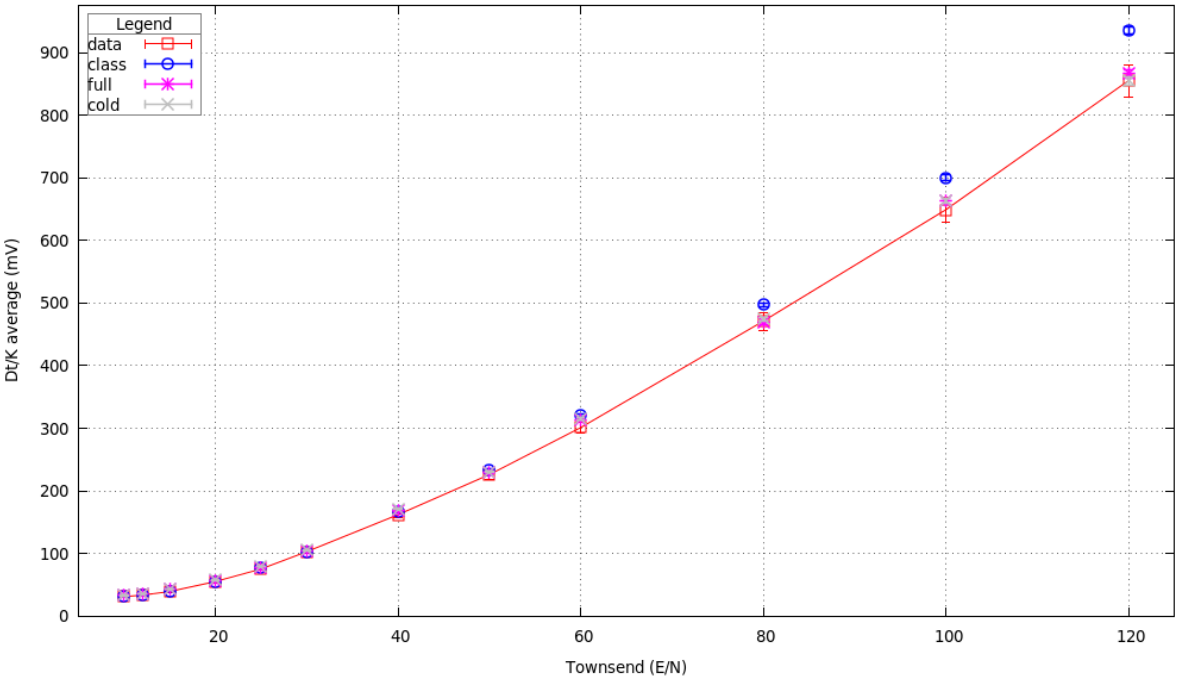

Figure 3.26: D_T results

3.2.2.4 N-body

The third effect that CLOUDA computes is the space charge since at least several thousands of ions are confined in a small volume, thus repelling each other. We remind that the final goal here is to reproduce accurately the ToF of the RI. Of course, it strongly depends on the position of the decaying vertex. If the N-body has a strong effect and enlarges the cloud in a non-negligible way, it will be required to take it into account. Initially, this was the component of the whole simulation package that justified the usage of GPUs. Indeed, computing the exact Coulomb force scales in $\mathcal{O}(N^2)$. For several million timesteps and a few hundred thousand ions, using classical CPUs was not a reasonable option because of the required computing throughput. GPUs are both an efficient and cheap solution to grant access to the needed simulations. In the introduction of this chapter, we already mentionned a few words on the GPU usage. In this section, we will thus only focus on the N-body effect implementation while in the next section we will discuss the impact it has on the final cloud profiles.

Multiple solutions were developed in the past few decades to address the specific problem of pairwise interactions fast computing. The applicability of such solutions ranges from in-trap ions Coulomb repulsion [VG11], our specific case, to global galactic behavior [Nyla07] and includes biomolecular predictions [YBKB11]. Depending on the chosen solution, the computation may scale from $\mathcal{O}(N^2)$ to $\mathcal{O}(N \log N)$ to $\mathcal{O}(N)$. The difference is twofold. First, the required accuracy sets limits on the allowed approximations since the usual tradeoff applies: one needs to find the proper equilibrium between results accuracy and computational efficiency. Second, the challenge the complexity of a given algorithm imposes is non-negligible in terms of implementation. Usually, the more efficient a given algorithm is, the harder it is to implement and make it work properly.

In the beginning, these algorithms were designed to work on parallel CPUs, later to be adapted on GPUs. For instance, Cruz *et al.* [CLB11] give a good introduction of this whole problematic through the presentation of the Fast Multipole Method (FMM) developed in 1987 [GR87][15]. The FMM is perhaps the most efficient way to address our issue at hand, but it is not the simplest. It is based on the idea that local contributions should not be approximated, whereas distant interactions could. Thus, the division of space at each timestep in quadrants, sub-quadrants and so on through a sophisticated tree-like data structure (hierarchical decomposition) allows to label a contributor as "local" or "distant". A step to compute distant approximation is then made. In the FMM case, multipole expansions are used to compute contributing potentials [GR87]. In the Barnes-Hut case, through the usage of yet another hierarchical decomposition of space, the contributions of distant sources are approximated by their center-of-mass weighted by their global charge/mass [BH86]. One only needs to perform a final summation of all contributions in order to have a well-approximated N-body effect. This yields an algorithm complexity of $\mathcal{O}(N)$ for FMM and $\mathcal{O}(N \log N)$ for Barnes-Hut.

The Tile Calculation (TC) algorithm, designed for gravitation modeling, is provided in the CUDA samples [Nyla07]. This algorithm computes "naively" all the N^2 pairwise interactions. Its interest lies in that it was designed specifically to work with CUDA, whereas it is not the case for the two solutions presented above. In fact, the TC scales in an optimized $\mathcal{O}(N^2)$ since the pattern used to scan the contribution of all bodies takes advantage of several technical facilities available in CUDA, *e.g.* the shared memory coupled with a given thread repartition through specific thread block sizes. This algorithm was adapted for Coulomb computation and implemented in CLOUDA. A Barnes-Hut logic was tested in CLOUDA, but it causes crashes that are not understood yet. More time would be required to fully investigate this issue.

There are other available solutions. For instance, SIMBUCA [VG11] is using the Chamomile Scheme (CS) [HI07], which also takes advantage of the shared memory. The difference with the TC is the sequence in which all the interactions are computed. In the CS, a first block of ions is sent to all threads/ions (one thread per ion) via the shared memory. Once all threads have computed the contribution of all ions in the current block, the next block is received and computed and so on. In the TC, each block computes the effect another block has on its threads/ions. Once all blocks are computed, they are "passed to the neighbor". Details are given in the cited references: [Nyla07] and [HI07]. In any case, both algorithms scale in a differently-optimized $\mathcal{O}(N^2)$.

[15] In this reference, older solutions are presented in the introduction. These includes mesh algorithms like Particle-in-cells. Depending on the local contributor density, they may be good solutions as well, although they still scale in $\mathcal{O}(N \log N)$.

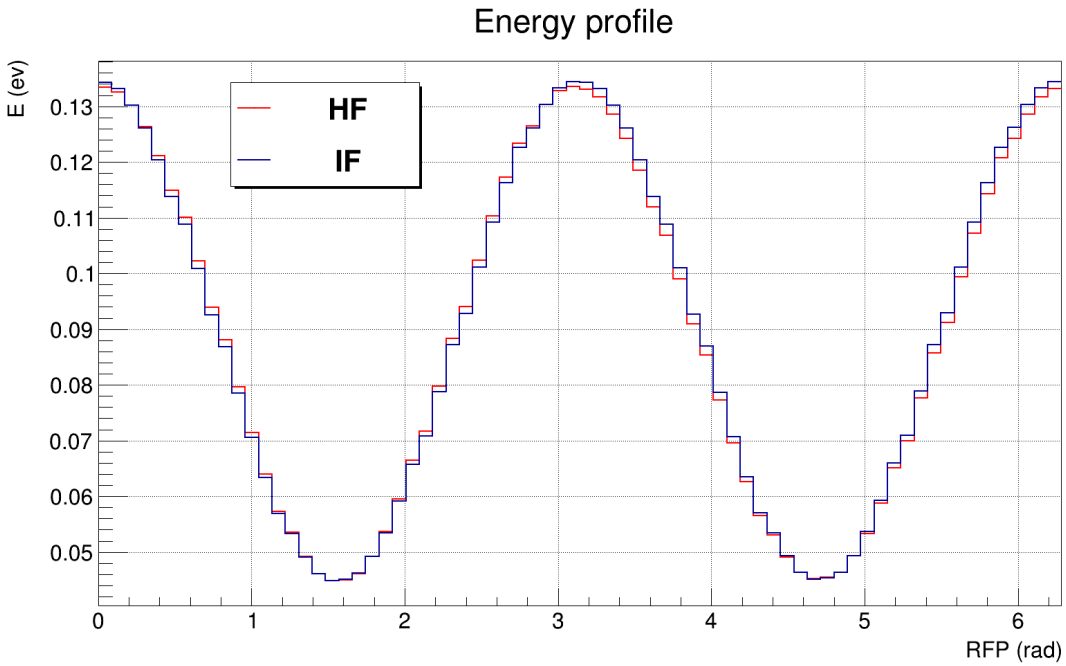

Figure 3.27: Fields effect – Energy profile (72 samples)

3.2.2.5 Cloud profiles

Now that we have described the possible interactions, we can take a look on the impact they have on the shape of the thermalized cloud. In order to compare the effect one interaction or another has on the trapped ion cloud, we will first wait for thermalization to occur using the mean energy of all the ions as described in the buffer gas section above. Obviously, we are now using the trapping field, thus, drift velocities are not defined in such a context. We will then behold the impact a specific sub-interaction has on the cloud profile. The cloud profile or phase space will be shown as six distributions (one for each dimension) as a function of the RFP[16] (see EM field description).

Field effect A comparison between the ideal field (IF) and the harmonic synthesized field (HF) is done with the following configuration:

- $N = 16384$ ions
- **System:** $^{35}Ar^{+} + {}^{4}He$
- **Buffer gas model:** HS
- **N-body:** deactivated
- $\Delta t = 1.0$ ns
- $p = 1$ Pa
- **Thermalization:** A safe thermalization time was found to be 600 μs for both fields.

On fig. 3.27 we see that there is not much difference in the final energy. The disparities rather lie in the phase space where its overview is shown in fig. 3.28. This last figure pictures the RMS of each dimension as a function of the RFP split in 72 samples. We show the full phase space for two of those samples in fig. 3.29 ($\frac{\pi}{2}$) and fig. 3.30 (π).

[16] RadioFrequency Phase

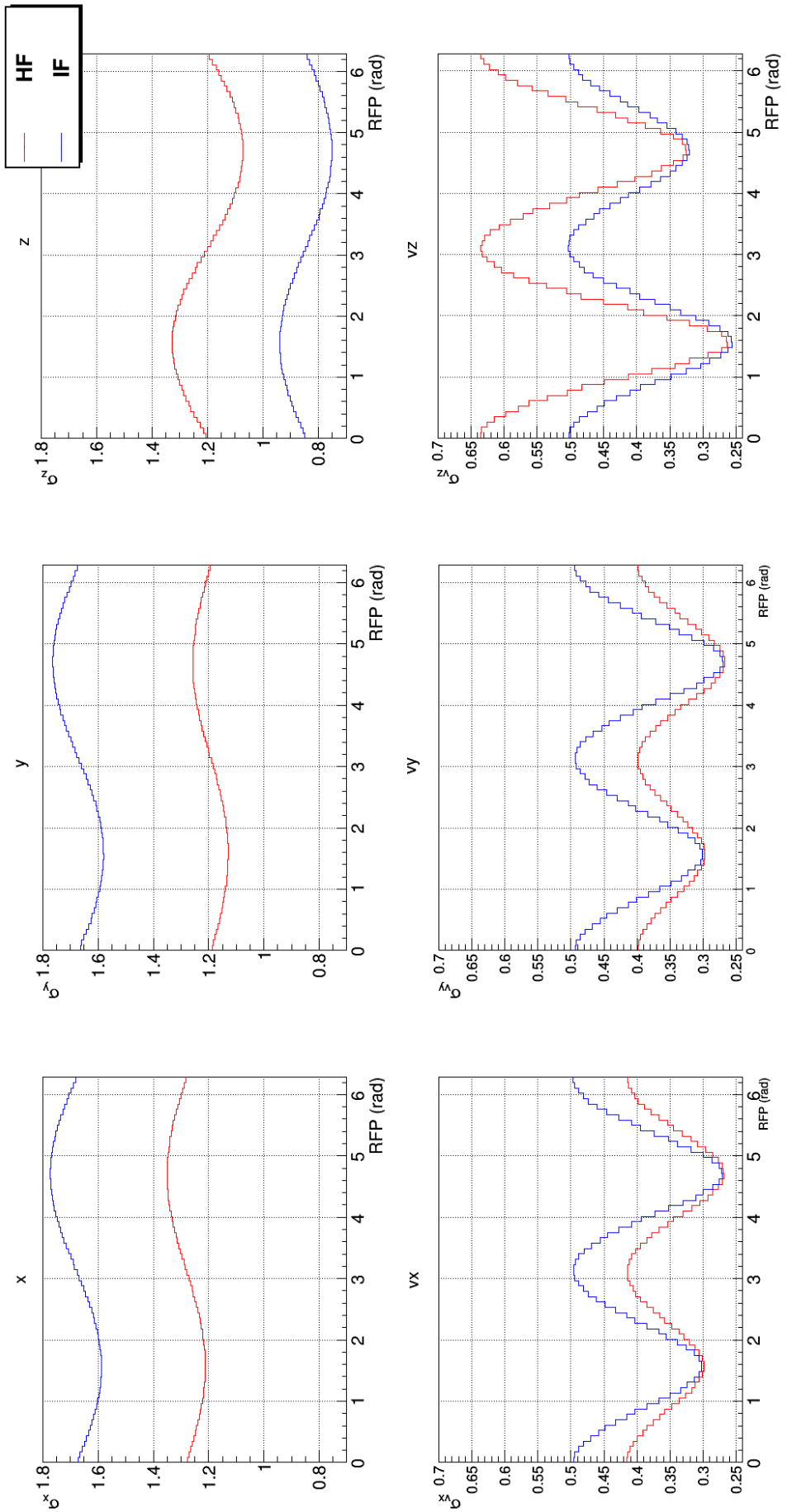

Figure 3.28: Fields effect – Phase space profiles. The RMS of each dimension is shown as a function of the RFP (72 samples).

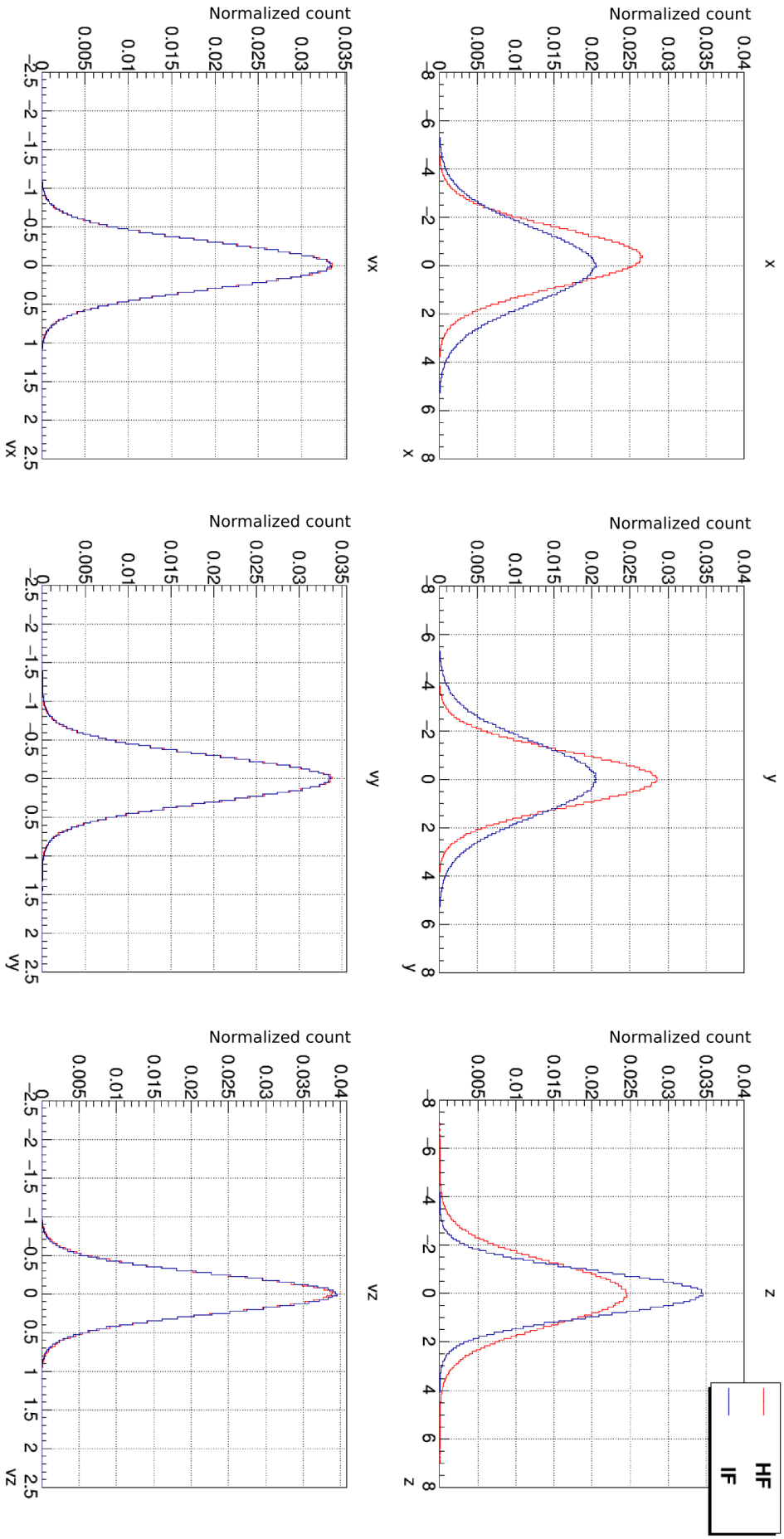

Figure 3.29: Fields effect – Phase space profile taken around $\frac{\pi}{2}$.

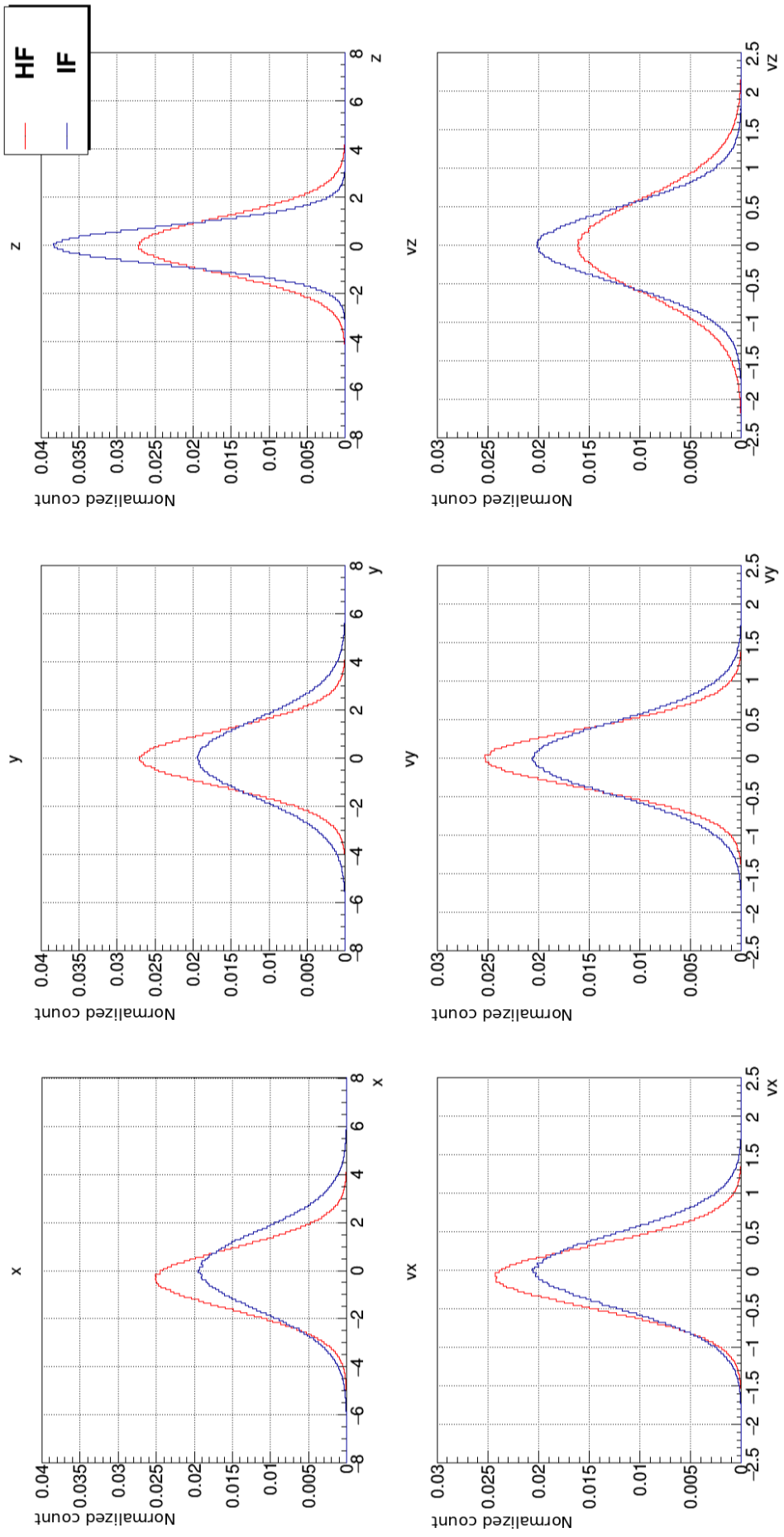

Figure 3.30: Fields effect – Phase space profile taken around π.

What constitutes the signature of a 3D Paul trap is the "phase opposition" between $\{x, y\}$ and $\{z\}$. Indeed, eq. 2.12 explicits that the sign between the z motion is $-$ whereas it is $+$ for x and y. This aspect appears in each distribution where the extrema are inverted when comparing these dimensions at $\frac{\pi}{2}$ and $\frac{3\pi}{2}$ in fig. 3.28. For example, we see that in the velocities RMS as a function of the RFP, the absolute minimum is at $\frac{3\pi}{2}$ for v_x and v_y, while it is at $\frac{\pi}{2}$ for v_z. This is reversed for the relative minima. Another similarity between the IF and the HF is the trend followed by the RMS curves.

Regarding the discrepancies in the RMS distributions, we observe that there is roughly a factor 2 between $\{x, y\}$ and $\{z\}$ for the IF case, physically meaning that the cloud is twice as long in the $\{x, y\}$ direction than it is in $\{z\}$. It is different in the HF case, where the cloud gets a little bigger (not twice as much) in the $\{z\}$ dimension when compared to $\{x, y\}$. Concerning the velocities, although they are rather close to each other in all directions for the IF case, they are $1.5\times$ higher in v_z compared to v_x and v_y for the HF case. Apart from the RMS distribution, we see that in the two specific phase distributions (fig 3.29 and fig. 3.30), the HF causes the cloud center in x to show a negative offset. Keeping in mind that x is the detection axis, we know that the collimators for the β telescope and the RI detection device are not only different in shape, but they are also not at the same distance from the Paul trap center. The realistic modeling includes this aspect.

The number of inequalities is high enough to consider that the IF is not a good approximation in order to reach a realistic cloud shape. Indeed, let us remind that CLOUDA serves no other purpose than providing a set of vertices fixed in the laboratory frame for the initial decays of the radioactive ions of interest. Since the TOF of the RI is the most important observable in the LPCTrap context, having a fine description of the sources location is of utmost importance. Consequently, in order to properly describe the shape of the trapped ion cloud, the usage of a realistic field through a harmonic synthesis is required. CLOUDA does not support field maps, although it could certainly be an interesting add-on in the future. Indeed, we showed here that a realistic field modeling is required, but compared only an ideal with a harmonic field. Checking from a third perspective, namely a precalculated field map, could provide an essential input and shed even more light on that aspect.

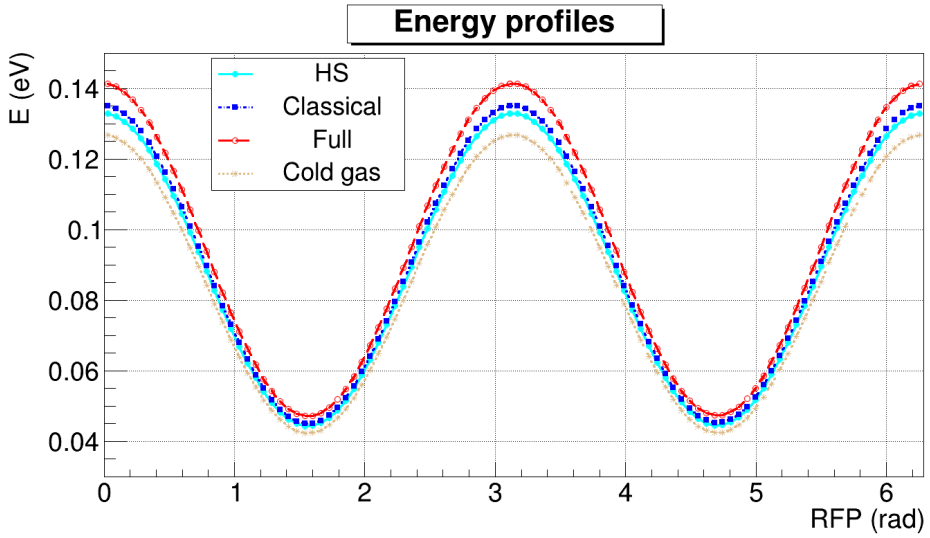

Figure 3.31: Buffer gas effect – Energy profile (100 samples)

Buffer gas effect Fig. 3.31 and 3.32 illustrate the impact the chosen buffer gas model has on the final cloud profile as a function of the RFP. This was done using the following configuration:

- $N = 16384$ ions
- **System:** $^{35}Ar^{+} + {}^{4}He$
- **Trapping field:** Ideal
- **N-body:** deactivated
- $\Delta t = 1.0$ ns
- **Thermalization:** A safe thermalization time was found to be 1000 μs for all models.

We first see that the two classical models, HS and *Classical*, yield very similar results whether from the phase space or the energy point of view. The two quantum models, *Full* and *Cold gas*, return respectively a hotter and colder cloud when compared to the middle one resulting from the classical models. The fact that the *Cold gas* model implies a colder cloud is no suprise at all since this is what this approximation is about: the atoms are at rest. What is more interesting is that although the drift velocities returned by the HS model are less (see fig. 3.20 and 3.21), the impact this model has on the cloud is comparable to realistic potentials and, as said above, is quite similar to the effect of the *Classical* model.

Knowing that the *Cold gas* model is based on a strong approximation, we could cast it aside from the list of the *best* model, *i.e.* the most likely to reproduce the real experimental cloud. This leaves us with the HS and *Classical* model on the one hand and with the *Full* model on the other hand. From the classical models, it is reasonable to exclude the HS because of the unrealistic aspect of it, implying wrong drift velocities. We are thus left with one realistic classical model (*Classical*) and one realistic quantum model (*Full*). At the time of writing, discrepancies appear in the *Classical* case for the diffusion coefficient while the *Full* model reproduces all the experimental data so far with a good agreement. Obviously, better accounting for experimental evidence constitutes an important criterion to consider when choosing a specific model. *Full* thus seems to be the proper model to use. This being said, it would be interesting to check the effect the *Classical* model has on the final RI TOF, since this remains the final objective of this simulation package.

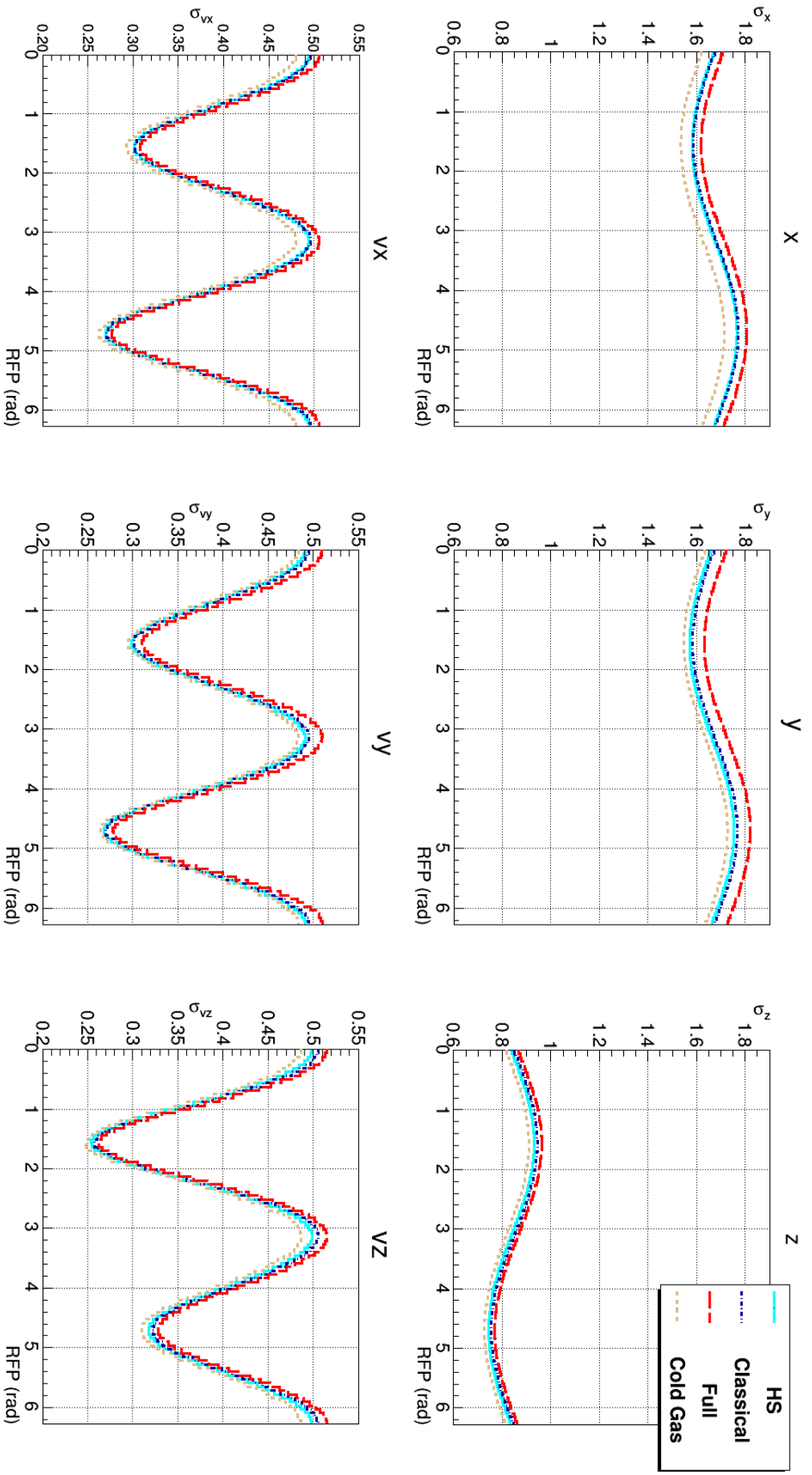

Figure 3.32: Buffer gas effect – Phase space profiles. The RMS of each dimension is shown as a function of the RFP (100 samples).

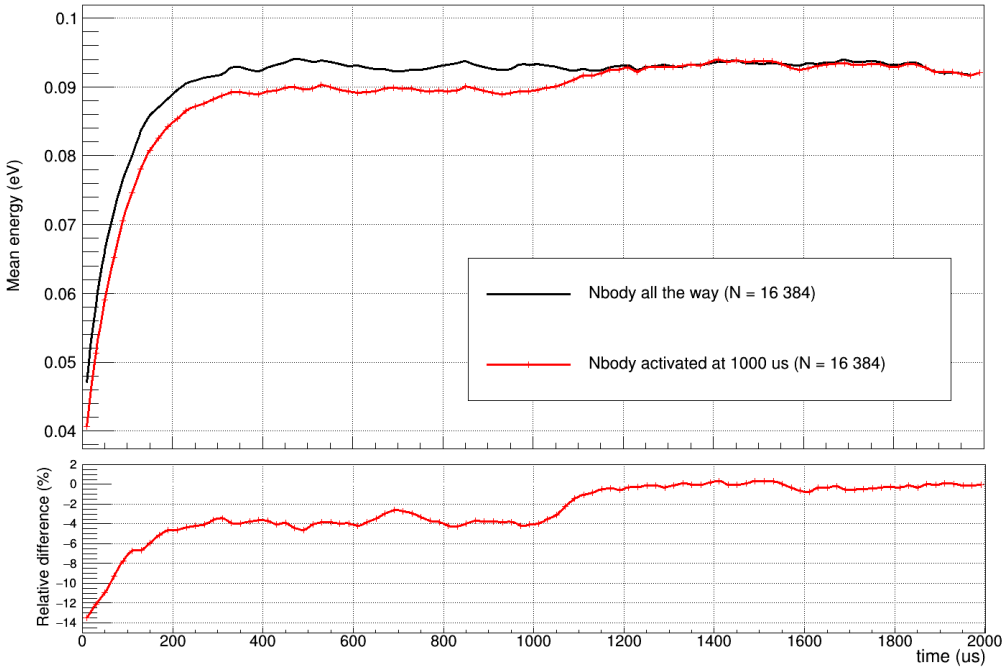

Figure 3.33: N-body effect – delayed activation.

N-body effect In order to check the impact the N-body effect has on a given cloud profile, we need to compare multiple simulations for different numbers of ions. All simulations have this configuration:

- N in [1024 ; 65 536] ions, $^{35}Ar^{+}$ + ^{4}He couple
- Buffer gas: Hard Spheres, $T = 300$ K
- Field: Ideal Paul trap
- $\Delta t = 1$ ns

First of all, $t = 600$ μs was found to be a safe thermalization time. The N-body effect being the most costly from a computational time point of view by far, we tested a delayed activation of that effect. Hopefully, the re-thermalization from the N-body contribution takes less time that the one from the buffer gas collisions. Fig. 3.33 shows that this was not the case. Indeed, one needs to wait a similar time for that re-thermalization to occur. In the specific example we show, N = 16 384 ions were simulated. In the first case, labelled "all the way", N-body was activated from the beginning while in the other case, with the very same configuration, it was activated at $t = 1000$ μs. The initial thermalization takes respectively $t = 10\tau = 406.64$ μs and $t = 10\tau = 428.83$ μs. Re-thermalization takes $t = 6\tau' = 445.75$ μs. The difference between the final energy prior to and right after re-thermalization is about 0.004 eV, waiting $6\tau'$ is thus enough to reach a suppression of $0.004/2^6 \simeq 6.0 \times 10^{-5}$ - which is about the same as waiting 10τ when running from 0.04 eV to 0.1 eV yielding a suppression of $0.06/2^{10} \simeq 6.0 \times 10^{-5}$. In the end, nothing is gained using the re-thermalization technique.

The cloud energy profiles are shown in fig. 3.34. They are all compared to a default case where the N-body effect was deactivated. Non-negligible differences arise with the number of ions. Indeed, as it is shown in the relative difference plot on the bottom of the figure, for 2048 ions, a 1% maximum difference appears. This is a very important result. First, the N-body effect is thus non-negligible at all. Second, during an experiment, the number of trapped ions changes during a cycle, whether it is from radioactive decay or collisions with surrounding volumes. With N depending on the time, the cloud shape will depend on the time as well and, ergo, the ToF of the RI. Moreover, the number of ions initially injected in the trap is not constant and depends of the losses between the injection in the RFQCB and the injection in the Paul trap – it even depends of the fluctuation of the incoming beam itself. This will be important to keep in mind during the analysis phase.

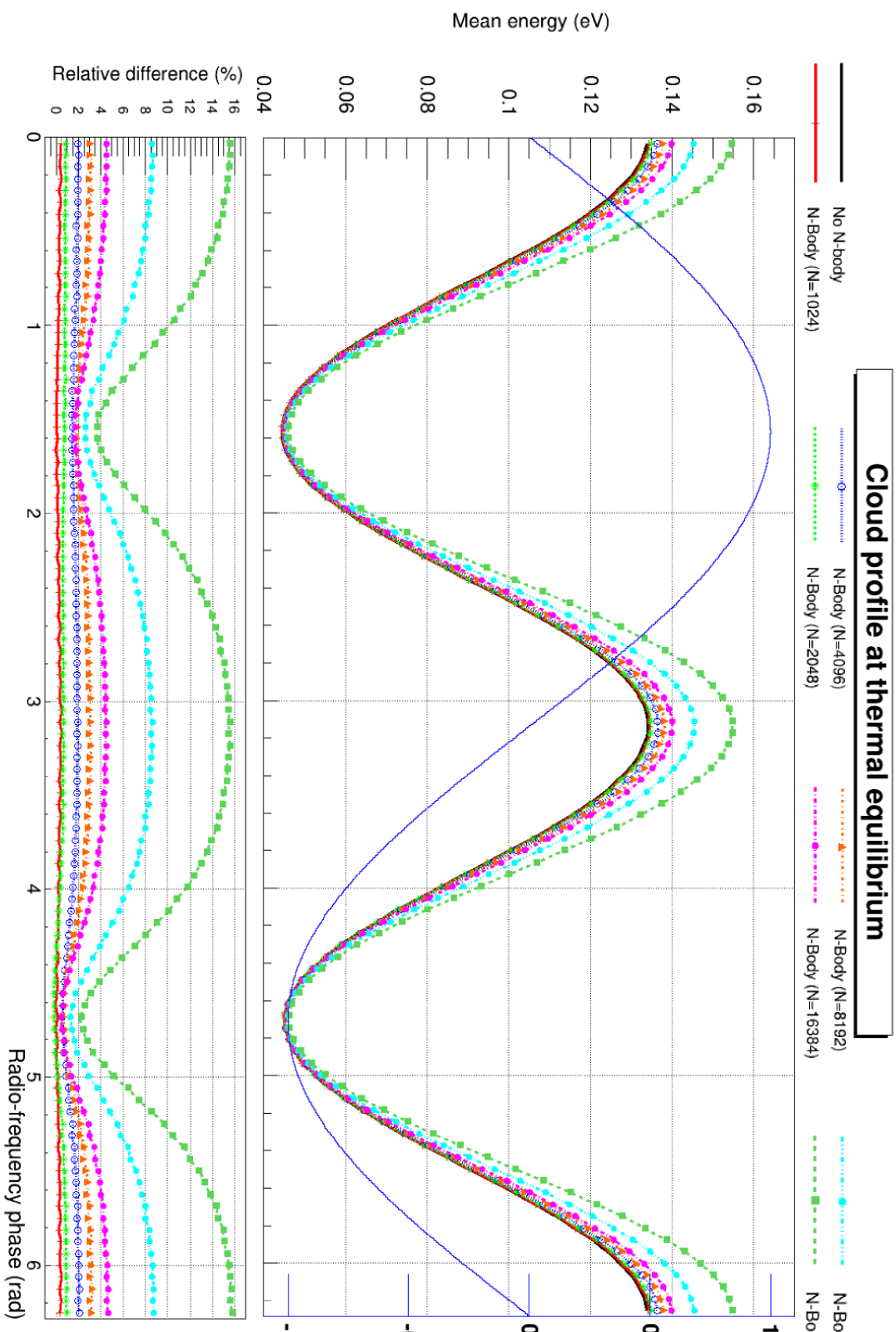

Figure 3.34: N-body – Energy profile (100 samples). The distinct blue curve shows sin(RFP) with its $y-$ axis on the right-hand side.

3.2.2.6 Conclusion

CLOUDA is a powerful tool to simulate the dynamics of a trapped ion cloud, whether it is in a Paul or Penning Trap, and embeds realistic microscopic ion-atom collision models which are mostly in good agreement with experimental data (drift velocities and diffusion coefficient). The N-body effect coming from the Coulomb repulsion of the space charge is working as well through an optimized $\mathcal{O}(N^2)$ algorithm: the so-called Tile Calculation. Exhaustively, CLOUDA includes:

- EM Fields:
  - Paul trap: ideal and harmonic field implemented. Field map in development.
  - Penning trap: ideal field implemented.
- Buffer gas:
  - Classical: *Classical* model from realistic potentials (Li + He and Ar + He systems) and hard spheres implemented (any system).
  - Quantum: *Full* and *Cold gas* models from realistic potentials implemented for the Li + He and Ar + He systems.
- N-body: Tile calculation implemented. Barnes-Hut in development.

Most realistic cloud We show the profile of the most realistic cloud simulated here for LPCTrap in fig. 3.35 and 3.36. It was achieved in 1h21m of computing time (GTX TITAN black) with the following configuration:

- Thermalization set at 1000 μs.
- System: $^{35}Ar^{+}+^{4}He$
- Initial state: ions inside a ball of radius $r = 1$ mm at 100 K.
- $N = 8192$ ions.
- Field: Paul trap, harmonic synthesis (153 ions died because they went beyond $r_0 = 10$ mm).
- Buffer gas: *Full* model at 300 K ($p = 1$ Pa).
- N-body: Enabled.

It thus includes the asymmetry between x and y from the harmonic description of the surrounding potentials, the N-body effect which increases the RMS of all phase space distribution and the mean energy and the thermalization from a realistic microscopic description of the ion-atom collisions through the *Full* quantum model.

Optimization A few computing times have been mentioned throughout this section. Because the N-body effect is the most greedy to compute, modern GPUs are being used to solve the dynamics of the relevant system. We can now compute the cloud profiles shown in the N-body effect section, resulting in an important step for the global analysis. However, computing the full interactions of 65536 ions could be considered the maximum loadout the GPUs can take while keeping a reasonable computing time (a few days). To gain an increased number of iterations per second (a decreased computing time), a few optimizations are possible. Let us discuss a few points in this regard:

- Changing the algorithm which computes the **N-body effect** is mandatory. Indeed, although it is optimized, the so-called Tile Calculation still scales in $\mathcal{O}(N^2)$. Implementing a working Barnes-Hut or even an ExaFMM would be very beneficial. The N-body effect on the cloud could also be checked with a "mega-charge scaling" method, as it is done in SIMBUCA. The idea is to set a factor on the electric charge of the ions and lower the number of ions. The ensuing statistical study would then, in principle, yield a profile for more ions that are actually simulated.
- Preliminary tests showed that completing the implementation of the **field map** would result in a gain of an order of magnitude in the computing time of the realistic field. In other words, the realism of the harmonic synthesis would be ensured with the speed of the ideal field.

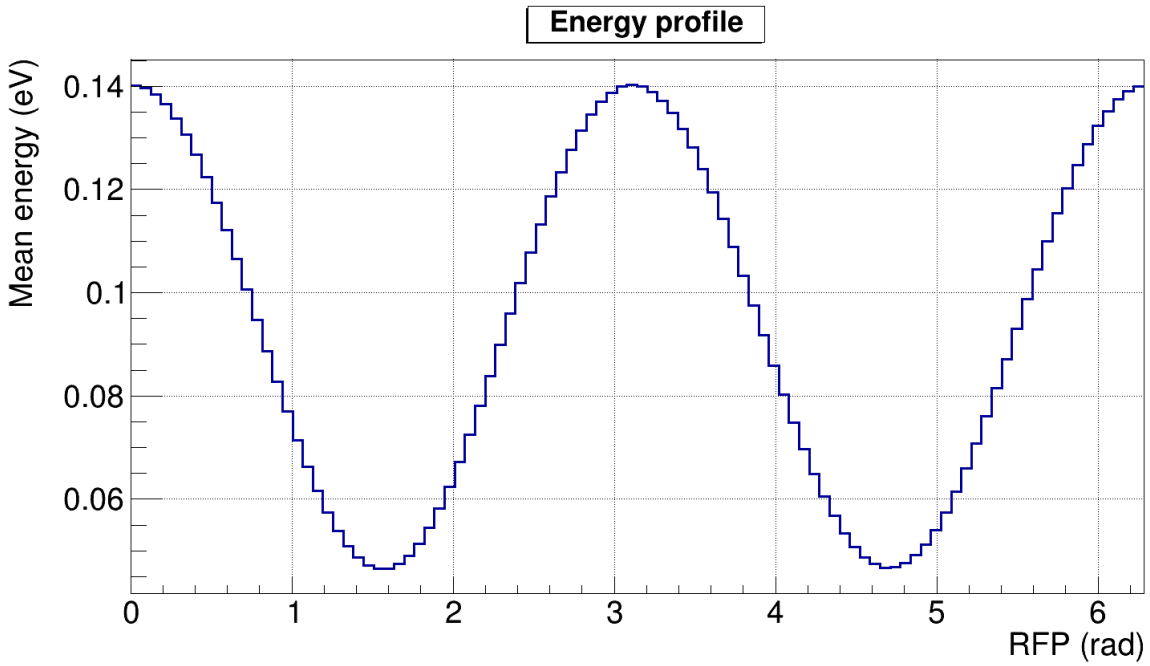

Figure 3.35: Most realistic cloud – Energy profile (100 samples).

- No serious tests were done to find the optimal balance in the thread repartition/block size logic. A major issue in CUDA is to properly allocate the computing threads in their block structure. For now, the default structure of the old TC routine is hardcoded. Digging deeper in this aspect would provide additional insight and has the potential to decrease the computing time without (too) much efforts while keeping the precision intact.
- A quick profiling of the GPU code using the Nvidia tools showed that the subroutine computing the **buffer gas** effect takes most of the computing power when the N-body effect is disabled. The number of pre-computations is probably already at its maximum. For instance, the integral that must be performed in the *Full* model is tabulated and a quick interpolation is done using the texture memory which is rather swift.

Simbuca No formal comparison was done between SIMBUCA and CLOUDA. Both programs objective is to simulate the dynamics of a trapped ion cloud, using a Penning trap in the SIMBUCA case and a Paul trap in the CLOUDA case. CLOUDA computes everything on the GPU side and has a microscopic description of the buffer gas cooling while SIMBUCA computes only the N-body effect, by far the most expensive one, on the GPUs and has a statistical description of the buffer gas cooling. The N-body algorithm in itself is quite different with the Tile Calculation in the CLOUDA case and the Chamomile Scheme for SIMBUCA. With the now-working Penning trap in CLOUDA, a comparison should be done to check if any differences rise in the results.

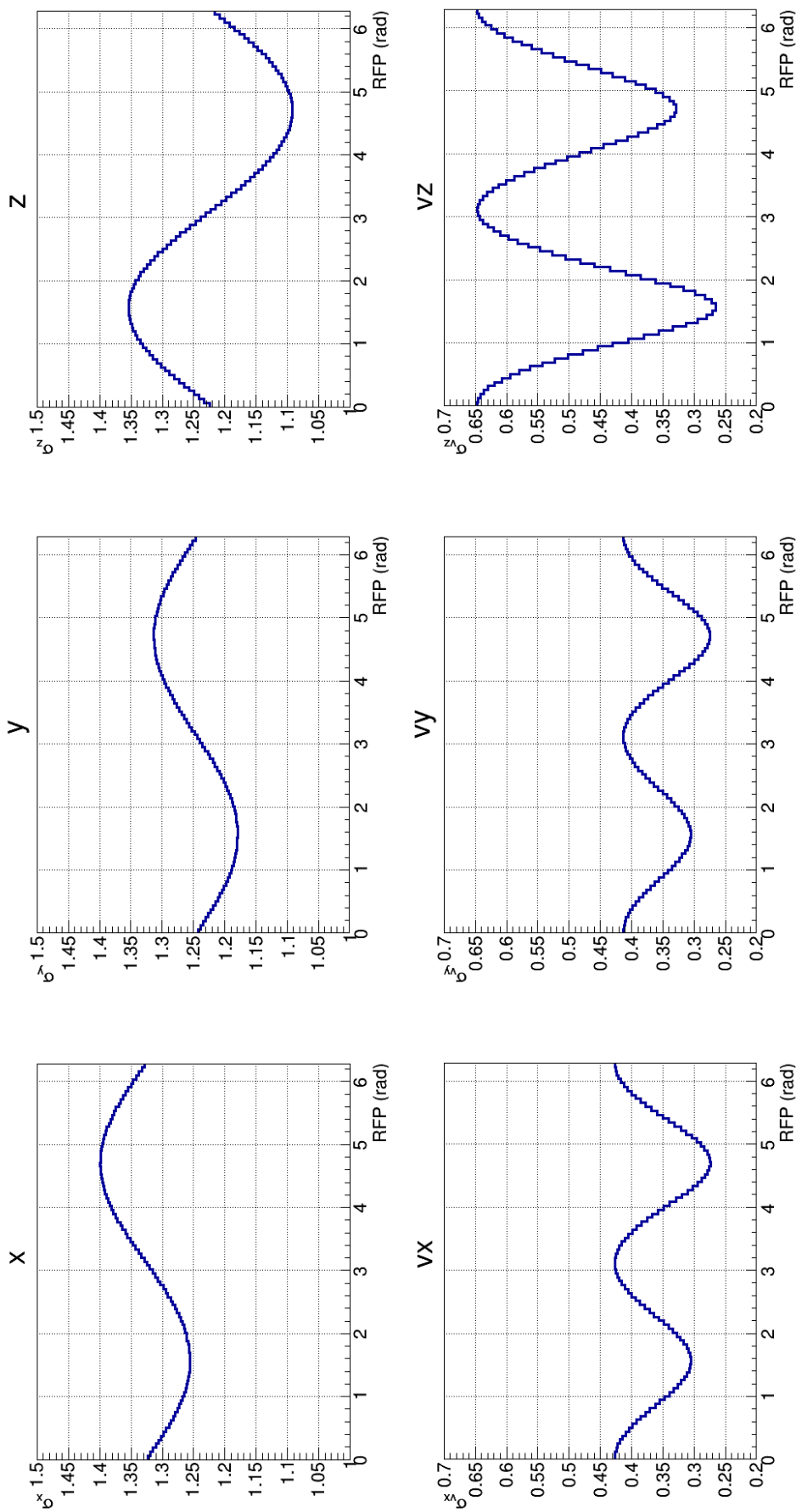

Figure 3.36: Most realistic cloud – Phase space profiles. The RMS of each dimension is shown as a function of the RFP (100 samples).

3.3 Tracking & Detection

Getting back to fig. 3.1 shows that at this point we are in the purple region: the in-trap decay event. Indeed, both the Q-value distribution among the decay products and the positions and velocities of the decaying vertices are provided by the β-decay generator and CLOUDA. All this information constitutes the prerequisite for tracking. As said before, neither the neutrino nor any γ will be tracked. We will thus focus on the recoil ion on the one hand and on the β particle on the other hand, since the TOF of the RI remains *the* observable we want to study.

LPCTrap's geometry is back-to-back, implying that not all events will be detected in coincidence. Indeed, only those falling in two acceptance cones (solid angles), one for each particle, will be detectable. This is a first order approximation because the main issue with the β particle is its tendency to scatter, possibly to the β telescope. With the proper modeling of the trapped cloud, this scattering is yet another important systematic effect that must be addressed in the LPCTrap context.

As was mentionned briefly in the introduction of this chapter, the tracking is performed using the BAYEUX package. BAYEUX wraps multiple tools required to perform a complete simulation. To adapt to the specific LPCTrap problematics, a declination of the global package was developed and is named LPCTRAPSW[17]. Let us discuss the separate tools embedded in this package.

3.3.1 Geometry

A very convenient feature of BAYEUX is the geometry management, done with the sub-package *geomtools*. All relevant volumes for the simulation are defined following a mother/daughter logic that could be represented by a tree. The root is the "world" volume and it contains a few daughters: the first vertices in the tree. For example, one of them is the β telescope. Going further in this specific branch, the vertex of the β telescope is itself a mother containing daughters, *e.g.* the DSSSD and so on. With an "on-board" GNUPLOT support, *geomtools* allows a user to define its geometry properly, then immediately visualize it without any GEANT4 implied. Moreover, it is possible to visualize only specific sub-volumes because of the mother/daughter logic. The package still being in development, not all subvolumes can be grouped this way. For instance, the RI ensemble is directly linked to the world while the elements of the β telescope are linked to the "β telescope" subvolume.

In order to provide all the relevant volumes where a β scattering can occur, the geometry of LPCTrap was accurately defined as per the "true" technical blueprints. Fig. 3.37 shows the center of the detection chamber where the Paul trap sits. The top figure shows a picture of the trap as it is in the chamber while the bottom figure shows the simulated geometry, from approximately the same angle. In both cases, the beam comes from the right, the large bottom collimator is the entrance to the β telescope and the thin top collimator is the entrance to the RI detection ensemble. It is important to keep in mind that this is a schematic view of the set-up, the zoom being approximately the same. A few volumes do not have exactly the same shape as in the real set-up, but this is not an issue since it concerns only volumes not contributing much to the β scattering, according to simulations. We note the central spheres in the simulated geometry which are a virtual representation where cuts can occur. For instance, the harmonic synthesis is valid only in a 10 mm sphere (see section 3.2.2.1) outside of which divergences occur. Fig. 3.38 shows another perspective of the compared detection chambers. The β telescope geometries are shown in fig. 3.39 and a global geometry is pictured in fig. 3.40.

The concept of "variant" position is also implemented in the package. Indeed, the exact position of the MCPPSD, for example, is known only to some extent. Such a systematic effect can be studied with the "variants" position and check the impact it has on the final ToF. Obviously, the longer the distance between the Paul trap and the detector, the longer it takes to reach the latter.

[17] Stands for LPCTrap SoftWare

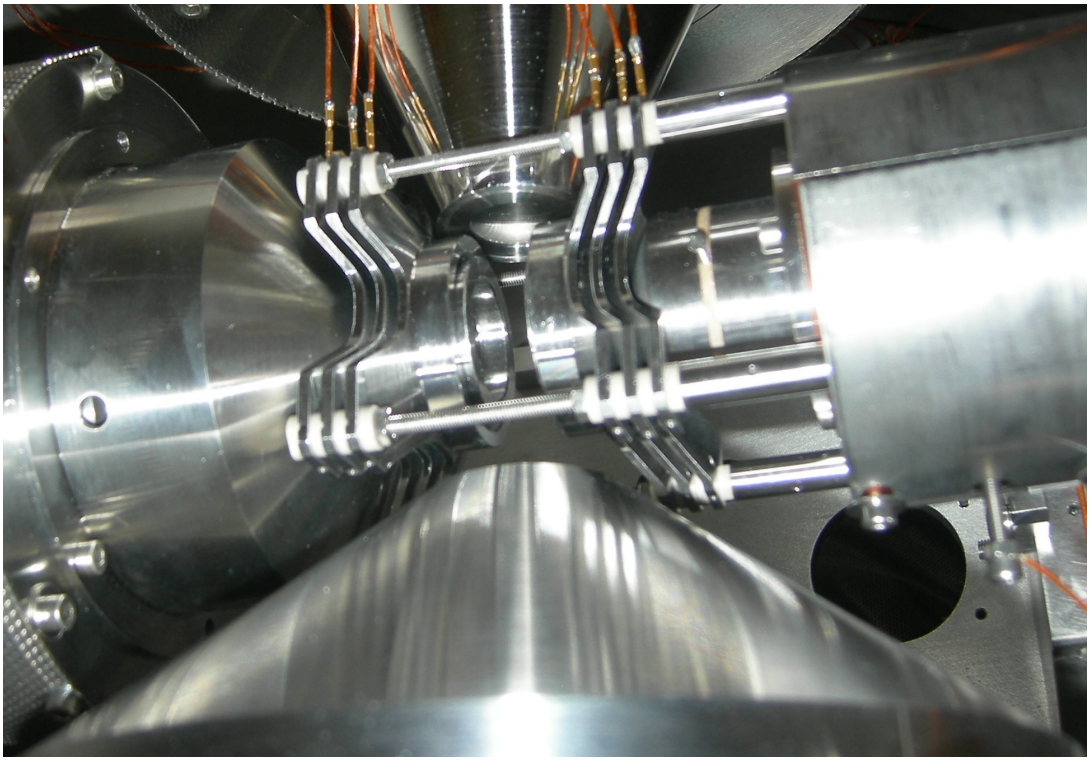

(a) "True" geometry

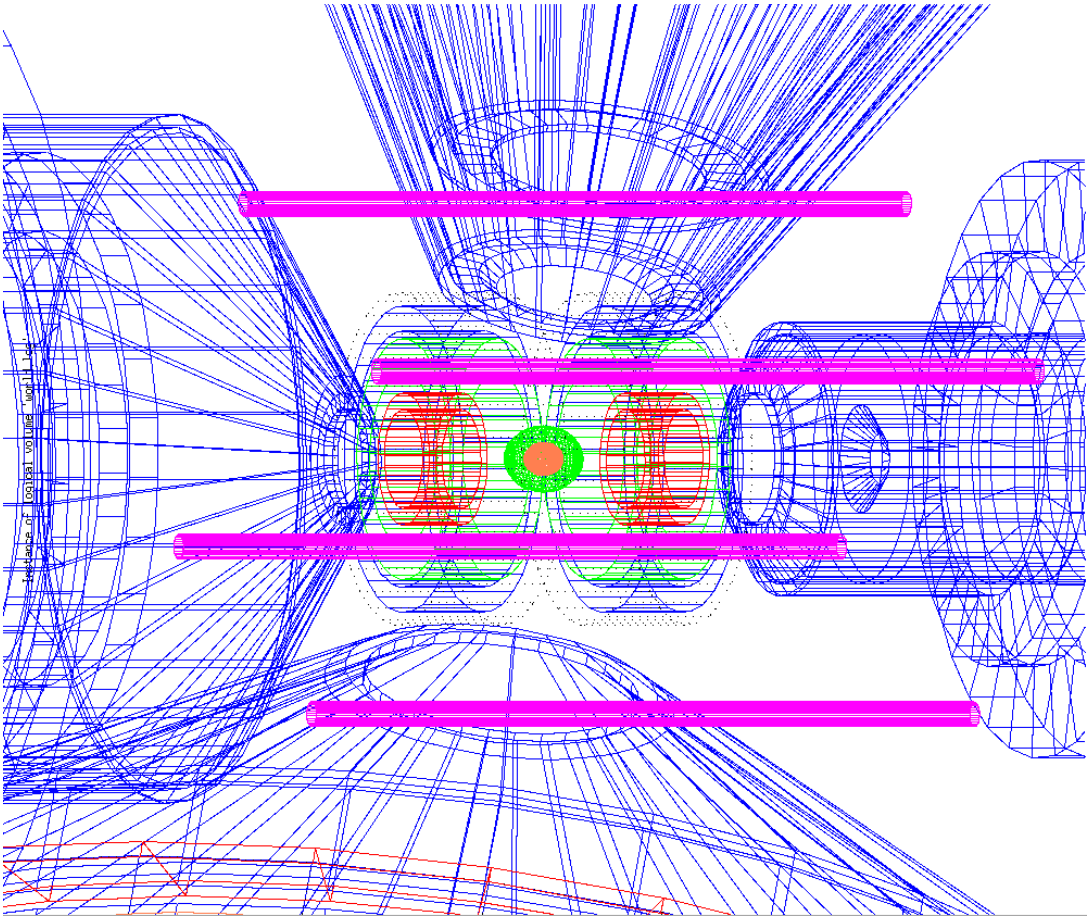

(b) Simulated geometry. The pink support bars are 71 mm long.

Figure 3.37: Paul trap geometry

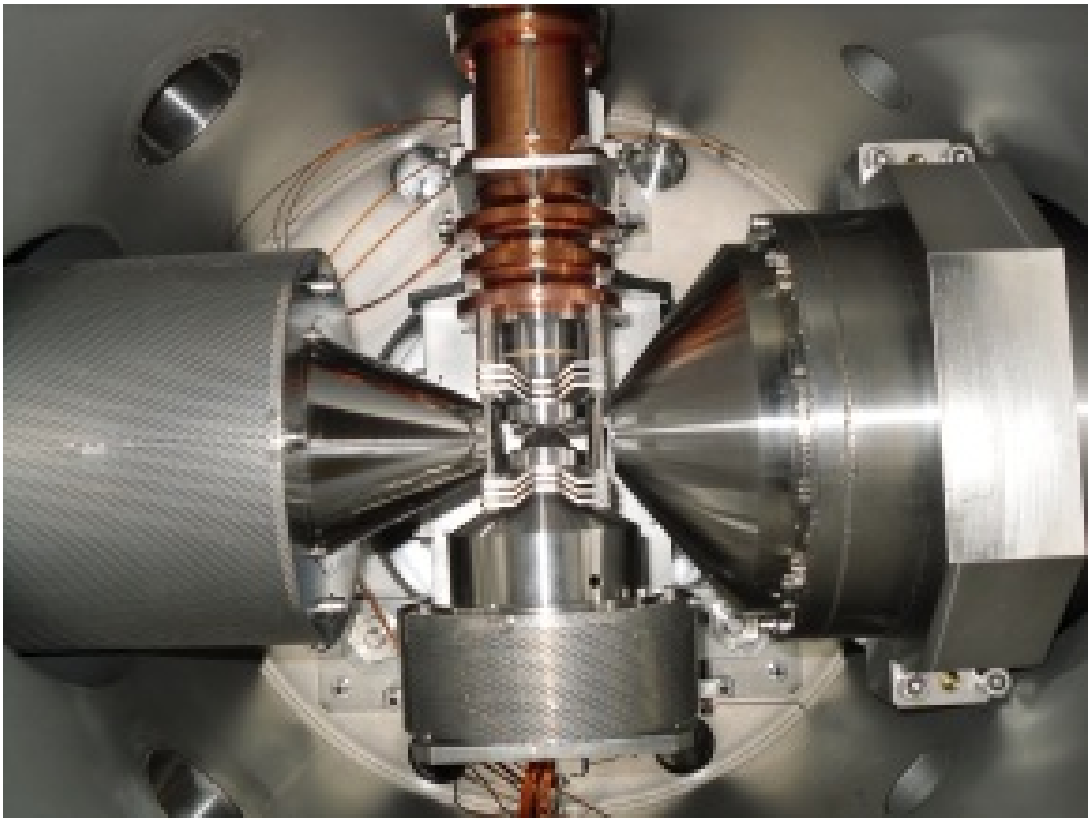

(a) "True" geometry

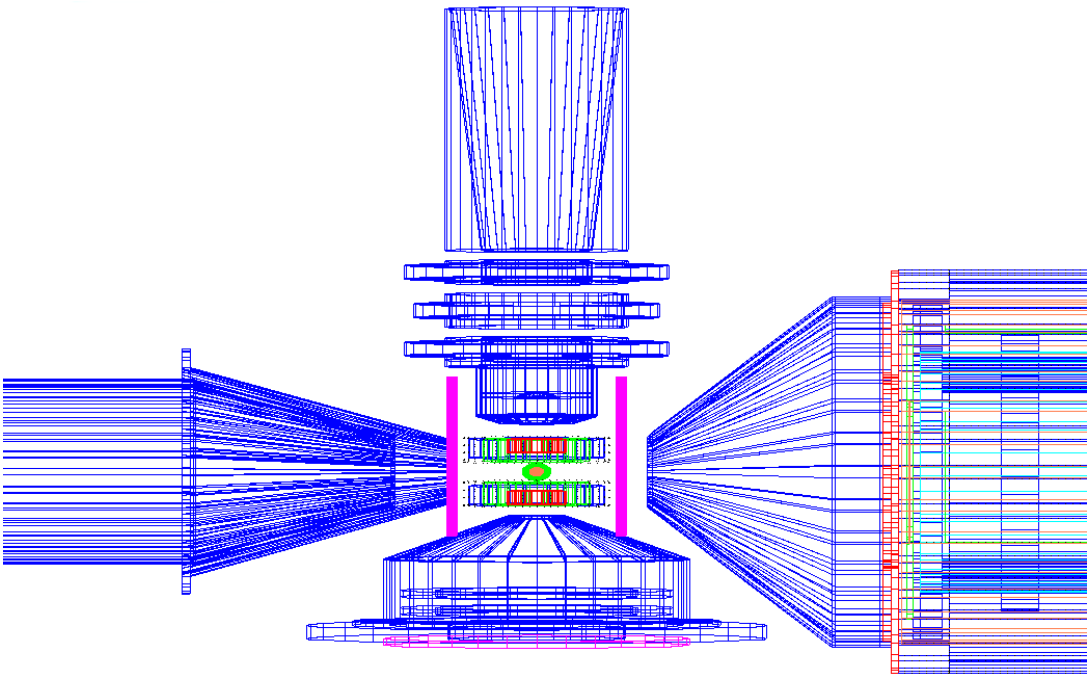

(b) Simulated geometry. The pink support bars are 71 mm long.

Figure 3.38: Paul trap geometry (Further away)

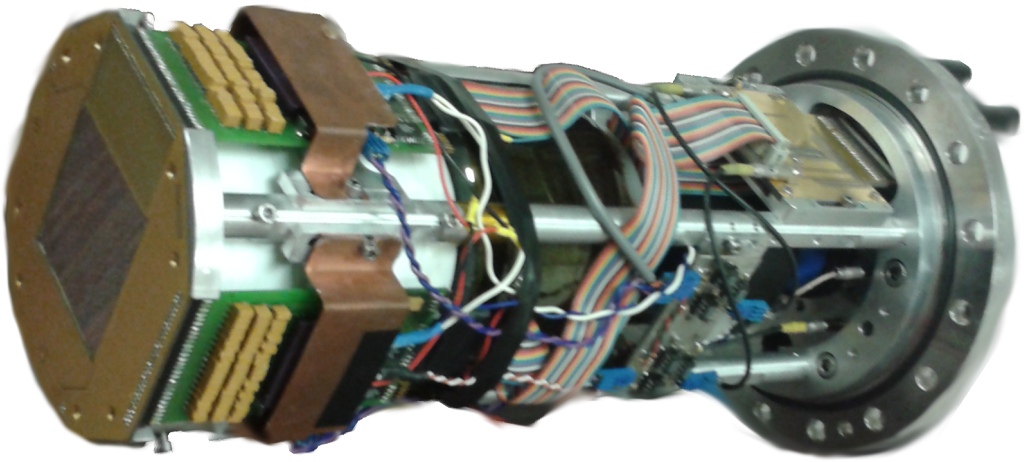

(a) "True" geometry

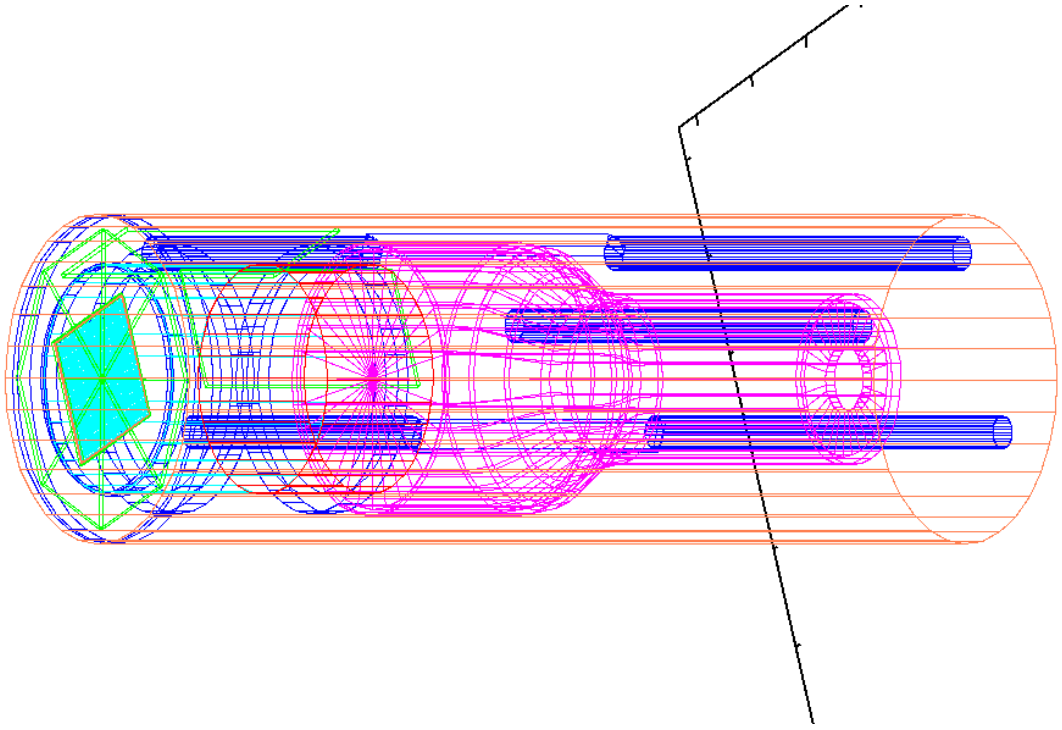

(b) Simulated geometry. The DSSSD represented by the cyan square is 62×62 mm^2.

Figure 3.39: β telescope geometry

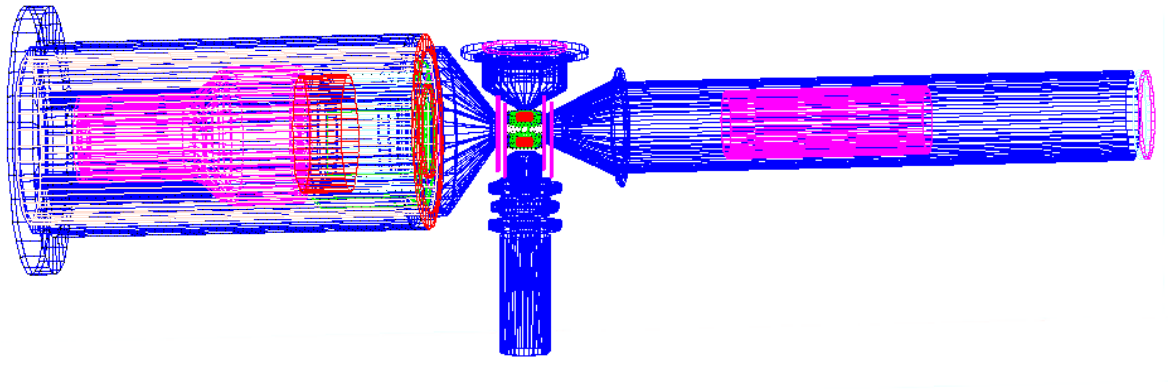

Figure 3.40: Global simulated geometry. The pink support bars are 71 mm long.

3.3.2 EM Fields

LPCTrapSW provides the required tools to simulate ions in arbitrary EM fields. Along with analytical fields, field maps and harmonic fields input are available. It is obviously the user's responsability to provide either the map or the harmonic coefficients, though. For either a realistic or an ideal field, a time-dependent term can be added to account for dynamic components - an RF field for instance. Although most of the RI tracking happens behind the first collimator in the long free flight tube, the trapping RF field has a non-negligible effect on the final TOF since it changes the rising edge of the TOF peaks, depending on the current RFP.

3.3.3 Tracker

The core MC simulation is done with Geant4 [Agea03], which is embedded in Bayeux. On multiple points, especially on the configuration of the physics models, Geant4 lacks an exhaustive documentation. The wrapping that Bayeux provides adds an interface which is a partial solution to this latter issue in itself.

In Geant4, the mean free path computation of a given ion changes the effective charge of the ion in some specific cases. Thus, simulating an ion in an extensive vacuum implies that the tracking of that ion will not be correct since the charge is not the proper one. This is yet another tracking logic, which is justified in the relevant Geant4 cases, that Bayeux controls.

On the β particle side, the models included in Geant4 will address the modeling of the scattering, an important systematic effect.

3.3.4 Data analysis

Once a simulation is set, one can define multiple filters to construct multiple datasets. Let us define this through a short example.

A β particle enters a plastic scintillator, thus depositing its energy at multiple points. Each interaction may create delta-rays which could themselves interact at multiple points. Filters could be defined as "only the integrated energy deposited by the entering β", "all the individual energies deposited by the β" or "the delta-rays detailed tracks". Moreover, it is possible to define a plane where to record the position of the ions as they pass through. The Geant4 simulation occurs, yielding its results. The user then has access to the multiple datasets depending on the defined filters. This is yet another ease-of-use tool provided by Bayeux.

3.4 Conclusion

Although all the elements of the extensive simulation are converging, no final ToF are available yet since the implementation of a few aspects are still ongoing. More specifically, the β decay generator is done and working, although one could question the importance of implementing any or all order-α corrections. The CLOUDA program is fully functionnal. Multiple upgrades are foreseen in the near future, they are detailed in the conclusion of the CLOUDA section. In the tracking part, the LPCTrap implementation through BAYEUX still lacks some checks and service classes. They are well-advanced though and the coupling of the results CLOUDA outputs to the input accepted by BAYEUX is ready. In a way, once final checks on the geometry, the EM fields and the data recording filters are done on the tracking side, there are no anticipated complications to finally reach ToF spectra. When this starts to yield results, it will be necessary to check that all systematic effects that can be accounted for in the simulation are tested and their impact quantified. Fully realistic ToF will hence be available to confront to the experimental data – thus yielding the possibility to extract a value for $a_{\beta\nu}$ with a well-controlled error on it.

Chapter 4

Perspectives

Résumé français – Ce court chapitre aborde deux aspects expérimentaux différents. En premier lieu, les probabilités de Shake-Off de l'ion $^{35}Ar^{+}$ sont extraites en utilisant le lot de données de 2012. Ce faisant, le processus d'analyse de données LPCTrap est approché. On présente d'abord les spectres obtenus en-ligne qui permettent le contrôle du bon déroulement d'une expérience. Pour extraire les probabilités de Shake-Off, il est nécessaire de faire des coupures pour "nettoyer" le spectre en temps de vol de l'ion de recul qui reste la distribution centrale de LPCTrap. On constate qu'une analyse relativement simple permet d'extraire avec une excellente approximation les probabilités de Shake-Off du cas étudié, confirmant la qualité des lots de données LPCTrap. On aborde ensuite ce qui est attendu avec les lots de données à analyser à la lumière des nouvelles simulations, en terme de précision relative sur $a_{\beta\nu}$. En deuxième partie, le futur expérimental anticipé de LPCTrap est décrit. À court terme, une évolution minimale est envisagée où l'idée est d'augmenter le nombre de détecteurs et de passer à une acquisition numérique. À plus long terme, le projet WINNINGMOTIONS est prévu et permettra d'extraire une valeur pour D, un paramètre de corrélation différent de $a_{\beta\nu}$ qui permet notamment de chercher de nouvelles sources de violation CP.

Contents

4.1 Initial data analysis – ^{35}Ar

The LPCTrap experiments impose two data analysis steps. The first one includes the basic usual calibration and some background subtraction. The second requires more powerful tool and the use of a part of the data themselves. Apart from calibration data (using known sources), the raw data can be interpreted either with or without a condition on the coincidence detection of the two decay products. This section will overview a part of the first step, presenting the different available spectra. We will reach a rough estimate of the Shake-Off (SO) probabilities from a Time-of-Flight (TOF) spectrum. For this purpose, we will be focusing on data coming from the 2012 $^{35}Ar^{+}$ experiment.

4.1.1 Online monitoring

During the experiment, when a run takes place, a dedicated monitoring computer receives a sample of the data in real-time and one can see several relevant spectra grow. The constructed spectra do not

guarantee the inclusion of all the statistic counts and only separated spectra are constructed once and for all (it is not possible to apply any post-filters).

A MCPPSD, the so-called extraction detector, is located on the beam axis after the Paul trap. It is used, during an on-going run, to estimate the size of the just-ejected cloud. This quantity is expected to vary with the LIRAT beam itself, taking into account the possible degradation being set on the beam or the bunch. Another source of variation is known and requires monitoring. One can observe a collapse of the cloud size when the LN2 level attached to the RFQCB is getting low, thus expliciting quite easily the requirement for a LN2 refill.

Finally, the control station of LPCTrap allows the access to the current accelerator settings and the control of relevant LIRAT components. As an example, a Faraday cup (CF14) may be lowered in the beam to check its total intensity. Coupled with a silicon diode of LPCTrap, one may measure the intensity of β emitters in the beam (see section 2.2.1).

4.1.2 Interpreted raw data

Once the raw (binary) data is saved on the disks, a routine encodes them in usable objects such as ROOT datatree. For one event, multiple recording of different signals occurs as was listed briefly in section 2.3.3. Let us summarize and complete these different recordings:

- **Nrun** The run number. Some runs were made for calibration purposes or include a specific failure (on the LPCTrap or accelerator side) which rendered the data hardly usable. Being able to trim the data according to this criterion is useful.
- **ADC_cycle** The timestamp inside the cycle. Fig. 4.1 shows two typical spectra. The red one shows unanticipated fluctuations that were due to a excessive instant count. Reducing the number of trapped ions (to reach some 1000 triggers/s) was found to be a good solution to retrieve the expected shape presented as the blue curve.
- **TDC_RF** This is the RFP[1] modulo 2π. The TOF has a slight dependence on it. Indeed, the RI may receive a kick if the trapping potential escape direction is toward the detection setup and vice-versa. This influence must be taken into account during the careful analysis of a given dataset.
- β **telescope**

  QDC_beta The signal coming from the photomultiplier coupled to the plastic scintillator is the acquisition START. A cut is usually done in what is actually the energy of the β particle, avoiding low energy related background.

  V550_qsi The signals coming for the DSSSD strips. There are 64×2 signals for 60×2 strips. We work with the signal of each individual strip for each run. This integrated signal has a similar shape for each spectrum. When a trigger occurs, all strips are read and, most of the time, no energy is deposited in them except where the β passed. This results in a dominating pedestal, corresponding to $E = 0$ and to a separated structure corresponding to the energy deposited by the passing β. Since the strips are thin and for the β energies at stake, we consider the deposited energy to peak on a specific constant value. Two fits are thus performed in order to calibrate the DSSSD. The first one follows a gaussian function and its mean is the channel at $E = 0$. The second fit is done on the β signal itself using a homemade function:

$$f(N_{\text{channel}}) = A \times \exp\left(\frac{-e^{-z} - z + 1}{D}\right) \tag{4.1}$$

  with $z = (N_{\text{channel}} - B)/C$ and A, B, C and D are the fit parameters.

- **MCPPSD**

  QDC_gal The main signal coming from the MCPPSD (and not its delay lines) is the TOF STOP. It is also the START signal to reconstruct the position of the ion on the MCPPSD using the four signals below, each of which provides its own STOP. We will be presenting linear combination of those since they are more useful.

[1] Radio-Frequency Phase, see section 2.2.4.

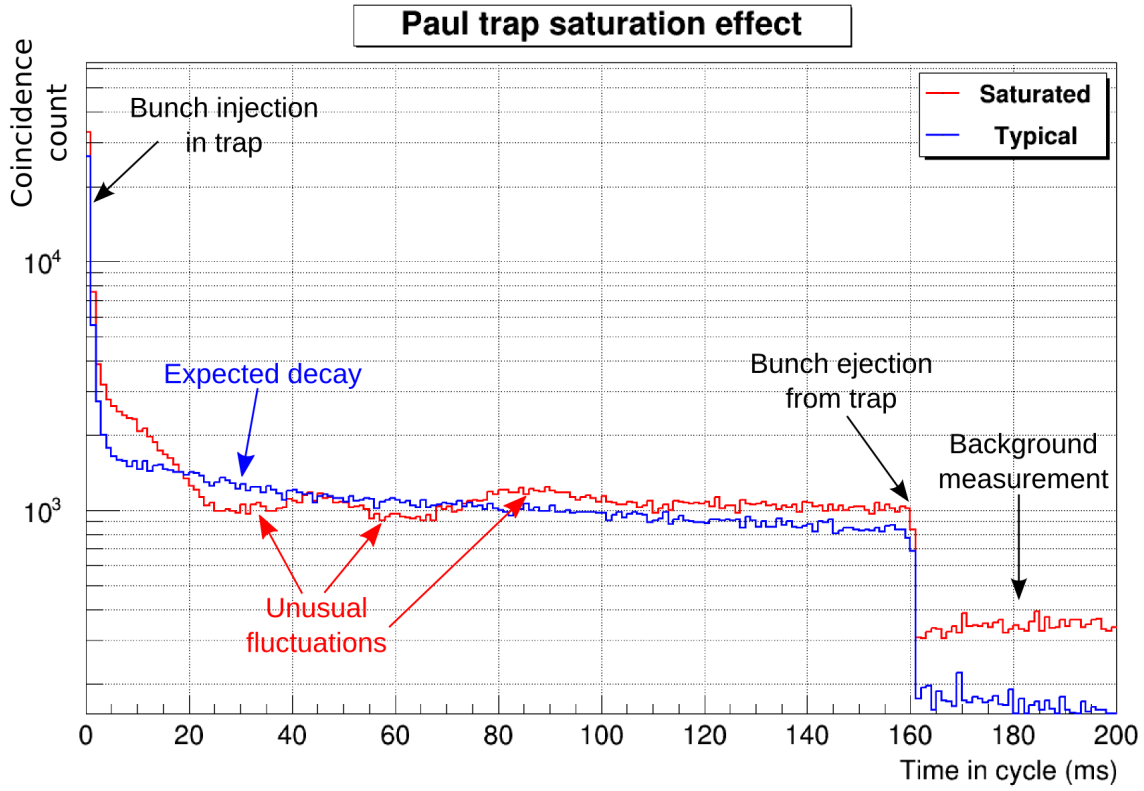

Figure 4.1: Calibrated cycle timestamp. The blue and red curves correspond, respectively, to runs 21 and 6. The red curve presents fluctuations that were found to disappear when the injected bunch size was reduced. The blue curve is a "healthy" run. For each true data run, the total cycle length was 200 ms, where the first 160 ms were the detection subcycle and the last 40 ms were the background measurement. Indeed, at each cycle, a background measurement is performed, enabling a clean cut of it in the TOF spectrum.

TDC_x1 + TDC_x2 The length of wire x.

TDC_x1 - TDC_x2 The position where the β hit in x.

TDC_y1 + TDC_y2 The length of wire y.

TDC_y1 - TDC_y2 The position where the β hit in y.

A cut on the sums allows to jettison absurd non-physical signals The differences can be used to reconstruct the positions where RIs were detected.

- **TDC_tof** This is the main TOF of the Recoil Ion (RI) and it is discussed below.

The LPCTrap experiments yield an important number of observables that are very useful not only to allow a fine analysis, but to immediately note when an undesired effect happens as well. Moreover, the constraint brought on the required simulations is an asset allowing a better global control.

4.1.2.1 TOF

Our working ROOT datatree here was constructed only with coincidences from the raw data. The obtained TOF spectra (see fig. 4.2a), one for each run, present a distinct signature around $t_{\text{real}} = 0$: the spike which corresponds to $^{35}Ar^{+}$ decaying in the MCPPSD. Since the β is usually relativistic, its velocity is orders of magnitude higher than the RI's. Decaying in the MCPPSD thus yields the negative TOF the β particle took to travel to the β telescope (STOP immediately sent by the RI before START sent by the β). This almost-null TOF generates the so-called spike and we use it to compute the "true zero position", *i.e.* the channel number coding a real time of zero. We will use this offset later on.

Two runs, one prior to and one after the experiment, were dedicated to the calibration of the TDC

Charge state	Estimation	Published result [Cour13b]
1+	75.86%	74.75% ± 1.07%
2+	17.87%	17.24% ± 0.44%
3+	5.21%	5.71% ± 0.27%
4+	1.06%	1.58% ± 0.21%

Table 4.1: SO Estimation

encoding the TOF. Using a Time Calibrator[2] (TC), an artifically-flat TOF spectrum was filled with counts separated by 1 ns. Almost all the channels were populated using this signal, furnishing a high number of points to perform a linear fit, the TOF spectrum being indeed calibrated linearly. The calibration points are subtracted from the calibration curve, yielding the linearity flaw of the TDC coding the TOF that we will need to add to the data (see fig. 4.2b).

With the offset from the spikes, the calibration curve equation and the linearity flaw, one can properly calibrate the TOF spectrum. It was said earlier that during a 200 ms cycle, 160 ms were dedicated to the "true" measurement and 40 ms to the background measurement. The background thus recorded is subtracted from the TOF spectrum. Moreover, the injection phase shown in fig. 4.1 is associated with an important background. A cut at 10 ns is thus performed as well to eliminate more background. With such a first-order cleaned TOF spectrum, we may, for instance, compute roughly the SO probabilities (see fig. 4.2c). Of course, we do not account for false coincidences, tails of each charge state peak overflowing in its neighbor and so on, still the estimate is comparable to the published result [Cour13b] as shown in table 4.1. We note that the published results are based on the 2011 data and the present estimation is done using the 2012 data. The good agreement between this simple analysis and the published results shows that the corrections brought by a full analysis remain low, although they are required to ensure a proper error control.

[2] Ortec 462

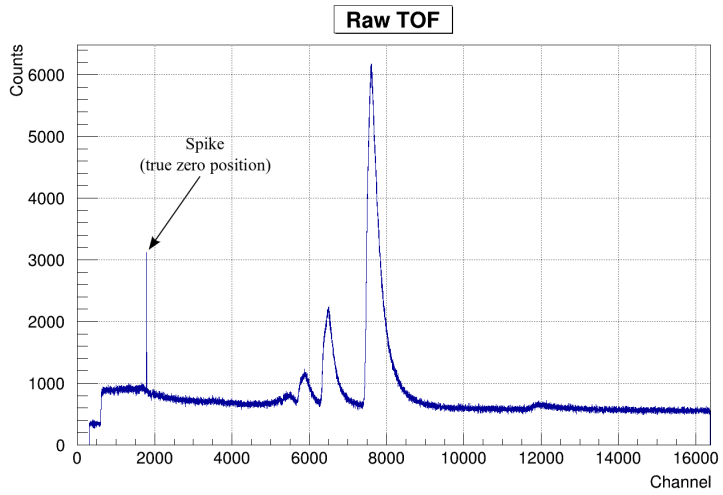

(a) Raw TOF

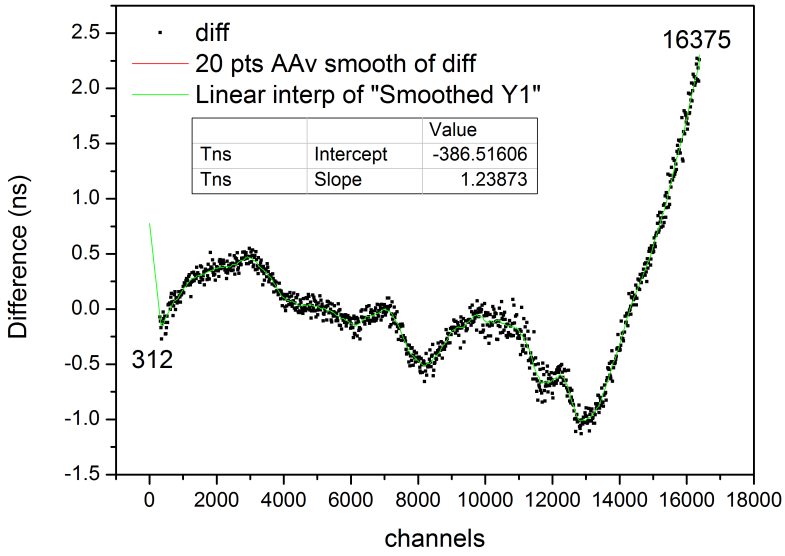

(b) Linear flaw and calibration of the TOF. The obtained linear fit parameters are shown as "slope" and "intercept".

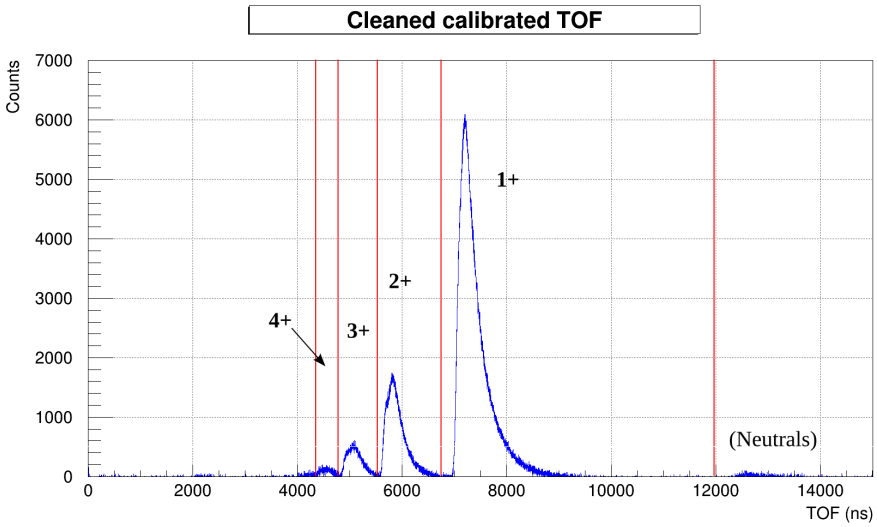

(c) Calibrated and 1st-order cleaned TOF. The red lines represent the chosen integral regions to compute the SO probabilities.

Figure 4.2: TOF spectra

4.1.3 Expectations

A first check on the recordings coming from the 2012 experiment shows no failure that could jeopardize the dataset. In fact, a first analysis was completed, allowing to extract the SO probabilities of the $^{35}Ar^{+}$ system [Cour13b]. However, the analysis to extract $a_{\beta\nu}$ requires a more detailed study since the searched physics is thinner and, ergo, more sensitive to effects that do not have a noticeable impact in the SO analysis framework.

The gathered data during the past campaigns are expected to reach a high precision (see section 3.2 in [LiHI15]). Indeed, two major requirements when compared to past experiments were recently fulfilled:

- First, the years of experience on the well-tested LPCTrap device henceforth allows a high control on the bunch themselves, allowing the maximization of the trapped cloud size through a fine tuning of the different settings. As we showed in this section, this reached a point where a saturation was even observed, producing ill-effects observed with the event timestamps.
- Second, the detailed simulation where every systematic effect is addressed is being accomplished. At the time of writing, the convergence on the development of the whole simulation package is reaching an important milestone. The β decay generator and a first version of CLOUDA are operational. As soon as the tracking program gets fully functional[3], one might expect the first TOF, where a careful control of all relevant contributions is established, to be available soon.

  This being said, once the development of the simulation package is indeed achieved, the thorough usage of it will require time in order to assess all the effects a sub-module has on the final TOF. Of course, as of now, only intermediate results were checked inside each module. For example, we know that changing the buffer gas model in CLOUDA has an effect on the final cloud shape. What we do not know, is the impact these different models bring in the final TOF spectrum. The same could be said for the EM field modeling, the method to choose a proper statistic dataset, the effect of the γ in the final TOF and so on.

The analysis of the dataset at LPCTrap are expected to yield a relative statistical precision of [LiHI15]:

- $^{6}He^{+}$: 0.45%
- $^{35}Ar^{+}$: 0.13%
- $^{19}Ne^{+}$: 10.50% (we note that the SM value is ~ 0.0438 in this case)

[3] The asked accuracy and form of the EM fields at LPCTrap required several development efforts in the BAYEUX package.

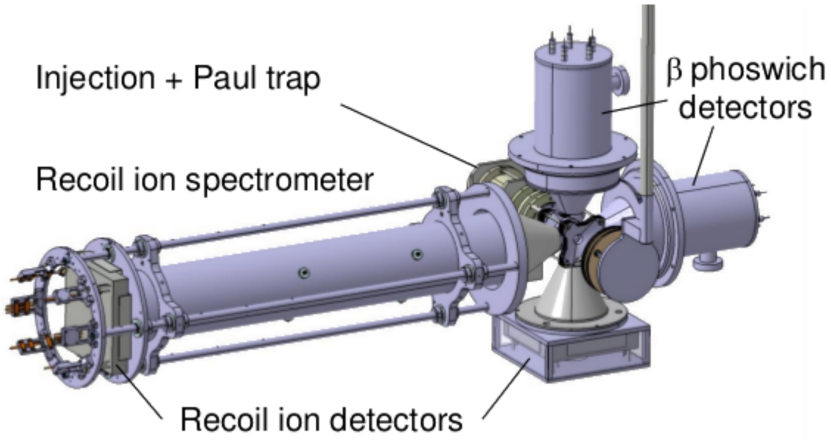

Figure 4.3: Minimal upgrade layoutof the LPCTrap detection set-up

4.2 Experimental future: LPCTrap 2.0

The future of LPCTrap is foreseen in two steps. The first "minimal upgrade" aims at gaining statistics to increase the precision on the measurements we are able to perform today or work with less intense beams. The second upgrade is part of the WINNINGMOTIONS[4] project where an extended collaboration and the coupling with laser beams is required.

4.2.1 Minimal upgrade

LPCTrap is based on the RI TOF measurement performed with a β telescope and a MCPPSD as fully described in section 2.3. Three aspects are part of the minimal upgrade:

- Double the number of detectors as pictured in fig. 4.3.
- Replace the β telescope technology (DSSSD+scintillator) with *phoswiches*. We remind that phoswiches are two opticaly-coupled scintillators.
- Change the current analogic acquisition for the FASTER[5] system.

Although they allow the position reconstruction, the analogic silicon strips have numerous drawbacks. First, the backscattering of the β particle is an important systematic effect – lowering the Z of its detector (from silicon to plastic scintillators) should help in reducing the amount of backscattered events. Second, the DSSSD issue rate is rather high, whether the origin of it is the failure of a controller-chip or a specific strip. Third, the deadtime of the β telescope is high which was not an issue at the beginning of LPCTrap but is becoming one, as discussed in the previous section.

With the upgrade to phoswiches, we will be conserving the position sensitivity using a segmented detector. The two scintillators, characterized by different decay constants and following the $\Delta E - E$ logic, will be used to discriminate between γs and βs.

With such a scheme, a gain of a factor $\sim$4 on the global statistics is expected.

[4] Weak INteraction Novel INvestiGations Measuring the Orientation of Trapped IONS
[5] http://faster.in2p3.fr/

4.2.2 WINNINGMOTIONS

WINNINGMOTIONS is a common project between GANIL, LPC Caen, IPNL (Lyon), IKS Leuven, ISOLDE and the University of Manchester. The basic idea is to couple a laser array, such as COLLAPS (ISOLDE), to polarize ions confined in an upgraded version of LPCTrap.

The updated setup will allow to access polarization-dependent correlation parameters (see expression 1.36), D being the aimed one. This parameter allows to check for new sources of CP-violation, the mechanism responsible for the matter/antimatter asymmetry. The best constraints on D for now come from the free neutron decay (2×10^{-4}) and the ^{19}Ne (6×10^{-4}) with the Standard Model value being D= 0. WINNINGMOTIONS objective is to reach 10^{-4} or below through the study of $^{23}Mg^{+}$, an ion with well-known optical pumping schemes and with a high production rate at SPIRAL. The polarization degree is expected to be over 99%. The aimed precision level is nearing the final state interaction effects D_{FSI}. Measuring these effects was never done at this precision, this providing a very interesting input. Fig. 4.4a shows a possible upgrade in the WINNINGMOTIONS framework while fig. 4.4b presents the detection layout in the detection plane.

At the same time, theoretical efforts are included in this endeavor as it is necessary to properly interpret the results and place them in the global effort to test the SM through the *weak* interaction. The project was recently submitted to the French ANR.

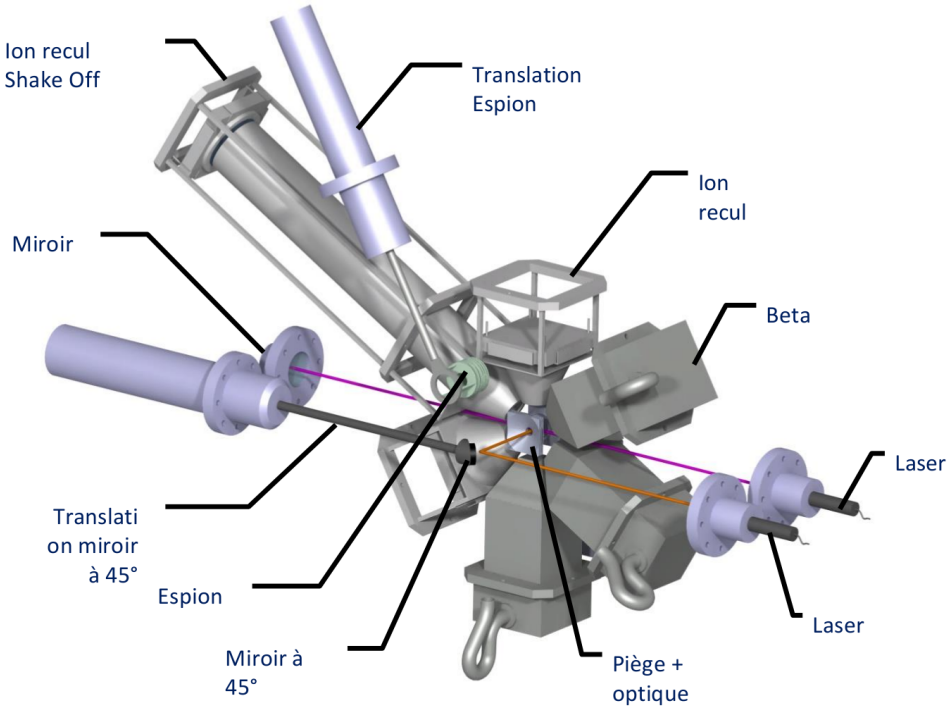

(a) WINNINGMOTIONS ion trap surrounded by its detectors.

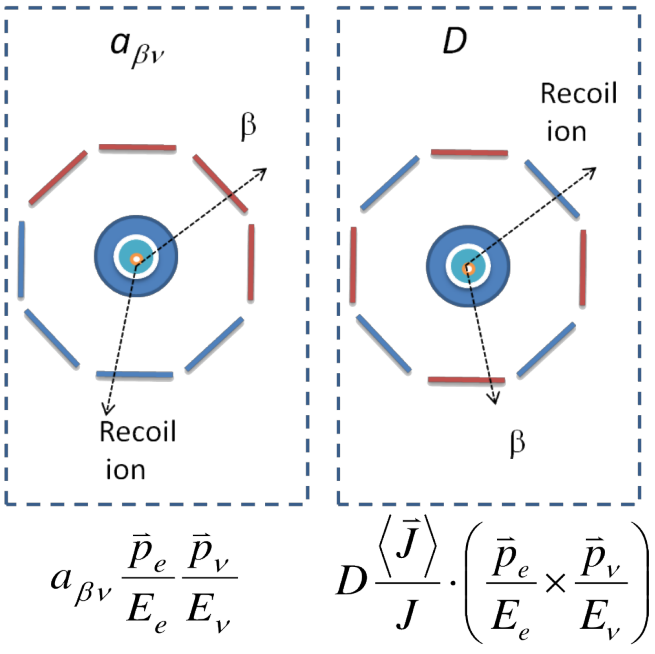

(b) WINNINGMOTIONS detection plane schemelayout.

Figure 4.4: WINNINGMOTIONS features

Conclusion

The present work began with a review of the modern knowledge on the Weak interaction. A state of the art was given as well for which the conclusion is manifest. LPCTrap belongs to the precision measurements community in which all the current experiments are hindered by the proper control of the slightest systematic effects. Whether it is from fundamental theory (higher-order corrections) or more concrete modeling as is achieved in the present work, an important effort is required to ascertain the exact contribution of systematic effects and reduce them as much as possible. In this regard, a full simulation package was developed in the LPCTrap framework where all aspects are studied.

A proper β decay generator was developed. Initially a stand-alone module, it is now embedded in the more general Bayeux package which we address below. The generator works for any β emitter, as long as its decay scheme and tabulated Fermi correction is provided. A Von Neumann rejection method allows to populate an arbitrary large set of decays for chosen values of $a_{\beta\nu}$, accounting for possible γ emissions. The full algorithm accomplishing this is given. Although the generator is fully working, the question of the relevance of including higher-order corrections to the decay itself is still open.

The program Clouda, the major part of this work, was then detailed. Its objective is the thorough modeling of the trapped ion cloud dynamics. Three interactions are simulated in this context. First, the confining EM fields were addressed. Clouda computes Paul and Penning traps where for the former both an ideal and realistic field is available while for the latter only an ideal description is working. Field maps, which will bring the precision of the realistic field with the low computing time of the ideal description, are being developed. It was shown that the proper modeling of the fields has a non-negligible effect on the final cloud profile. The careful study of the buffer gas modeling was then approached. A first work to assess the four implemented models was accomplished successfully, yielding results in excellent agreement with experimental data for the drift velocities and good agreement for the diffusion coefficients. The so-called *Full* model reproduces best the experimental data. The *Classical* model shows discrepancies for high Td values in the diffusion coefficients, we suggest to look deeper in the cross section modeling in order to correct this. The effect the models have on the trapped ion cloud was then checked and we showed non-negligible differences appearing here as well. Last but not least, the effect of the N-body space charge was studied. The usage of GPU was mandatory to address this specific problem. For now, only an optimized $\mathcal{O}(N^2)$ algorithm is implemented, the so-called Tile Calculation. A Barnes-Hut is being tested, albeit unstable for yet unknown reasons. Fast Multipole Methods (FMM) would provide an incredible increase in the computational throughput, lowering the complexity of the algorithm to some $\mathcal{O}(N)$. We showed that increasing the number of ions in the Paul trap yielded non-negligible differences in the mean energy profile once again. We may conclude that the final reconstructed TOF is expected to greatly vary according to the enabled Clouda interactions. Indeed, the realism now modeled was never reached before and should contribute to a better control on the final results.

The tracking of the decay products with the Bayeux package is expected to yield its first results very soon. The full geometry is translated in the simulation context as well as all the relevant EM fields on the RI side.

An initial data analysis of the $^{35}Ar^{+}$ dataset was approached. As long as the simulations are not fully functionnal, it will be hard to extract $a_{\beta\nu}$ from the data – unlike the Shake-Off (SO) probabilities that were published recently. The future prospects of LPCTrap were finally discussed. It is foreseen to begin a new experimental program where the study of the triple correlation parameter D will be the main target, opening up new theoretical, experimental and simulation possibilities.

Conclusion (Français)

Ce travail a débuté avec une revue de la connaissance moderne de l'interaction Faible. Un état de l'art fut également fourni où la conclusion est manifeste. LPCTrap appartient à la communauté des mesures de haute précision pour lesquelles toutes les expériences sont soumises au contrôle fin du moindre effet systématique. Que ce soit du côté théorique fondamental (corrections d'ordre supérieur) ou du côté de la modélisation concrète telle qu'accomplie dans ce travail, un effort important est nécessaire pour valider la contribution exacte des effets systématiques pour les réduire le plus possible. A cet égard, une application de simulation complète fut développée dans le contexte de LPCTrap où tous les apsects sont étudiés.

Un générateur de décroissances β approprié fut développé. Initialement module autonome, il est désormais intégré dans l'application Bayeux qui est plus générale et que nous abordons ci-dessous. Le générateur fonctionne pour n'importe quel émetteur β à condition de fournir le schéma de décroissance et la correction de Fermi tabulée. Une méthode de réjection de Von Neumann permet de peupler un lot de données de décroissances arbitrairement grand pour des valeurs choisies de $a_{\beta\nu}$ en tenant compte des désexcitations γ possibles. L'algorithme complet qui accomplit cette tâche est donné. Bien que le générateur fonctionne parfaitement, la question d'inclure ou non les éventuelles corrections d'ordre supérieur à la décroissance elle-même reste ouverte.

Le programme Clouda qui constitue le coeur de ce travail est ensuite détaillé. Son objectif est la modélisation fine de la dynamique du nuage d'ions piégés. Trois interactions sont simulées dans ce contexte. Il a d'abord fallu s'intéresser aux champs électromagnétiques de piégeage. Clouda peut simuler des pièges de Paul et de Penning où dans le premier cas une modélisation idéale et réaliste est disponible, alors que dans le deuxième cas seulement la description idéale fonctionne. Des cartes de champs sont en développement et devraient permettre d'obtenir la précision du champ réaliste avec le temps de calcul réduit de la description idéale. Il a été démontré que la modélisation adéquate des champs induit un effet non négligeable sur le profil du nuage final. L'étude attentive de la modélisation du gaz tampon a alors été approchée. Une première étude pour éprouver les quatre modèles implémentés a été réalisée avec succès, donnant des résultats en excellent accord avec les données expérimentales pour les vitesses de dérive et en bon accord pour les coefficients de diffusion. En effet, il était attendu que les deux modèles quantiques soient les plus réalistes et, ainsi, reproduiraient parfaitement les données expérimentales. Bien que l'accord soit bon, des écarts apparaissent aux grandes valeurs de Townsends – un problème qui est en cours de résolution au moment de la rédaction. L'effet que les modèles ont sur le nuage d'ions piégés fut alors vérifié et nous avons démontré que des différences non négligeables apparaissent ici aussi. Finalement, l'effet à N-corps de la charge d'espace fut étudié. L'utilisation de cartes graphiques est incontournable pour répondre à cette problématique. Pour l'instant, seulement un algorithme en $\mathcal{O}(N^2)$ optimisé est implémenté : le "calcul en tuile". Un Barnes-Hut est en test, mais instable pour des raisons encore inconnues. Les "méthodes multipolaires rapides" pourraient fournir un apport signiticatif en termes de temps de calcul, diminuant la complexité de l'algorithme à quelques $\mathcal{O}(N)$. Nous avons démontré que l'augmentation du nombre d'ions dans le piège de Paul induit encore une fois des différences non négligeables dans le profil de l'énergie moyenne. Nous pouvons conclure que le temps de vol reconstruit varie grandement selon les interactions activées dans Clouda. En effet, le réalisme désormais implémenté n'a jamais été pris en compte auparavant et devrait contribuer à un meilleur contrôle de l'incertitude sur les résultats finaux.

La traque des produits de décroissance par l'application Bayeux devrait fournir ses premiers résultats dans un futur proche. La géométrie complète est traduite dans le contexte numérique ainsi que tous les champs électromagnétiques d'intérêt du côté ion de recul.

Une analyse initiale du lot de données $^{35}Ar^{+}$ a été menée. Tant que l'ensemble des simulations n'est pas complètement fonctionnel, il sera très difficile d'extraire $a_{\beta\nu}$ des données – à l'inverse des probabilités de Shake-Off qui ont récemment été publiées. Les perspectives du futur de LPCTrap ont finalement été présentées. Il est prévu de débuter un nouveau programme expérimental où la cible centrale devient l'étude du paramètre de corrélation triple D, ouvrant de nouvelles possibilités théoriques, expérimentales et numériques.

Appendices

5.1 Optimized LPCTrap tuning

$^{6}He^{+}$

Paul trap	$V_{3\ inj}$	130 V
	$V_{4\ inj}$	300 V
	$T_{3\ inj}$	6.10 μs
	$T_{4\ inj}$	6.0 μs
	V_{12RF}	127 Vpp
	$f_{12\ RF}$	1.15 MHz
	$T_{12\ RF}$	4.75 μs
	V_5	12 V
	V_6	12 V
	$V_{3\ extr.}$	300 V
	p_{H2}	4.0×10^{-6} hPa
PD2	V_{PD2}	818 V
	V_{Lp}	270 V
	T_{PD2}	11.5 μs

PD1	V_{Lc}	410 V
	Cycle length	200 ms
	V_{PD1}	8981 V
	T_{PD1}	6.0 μs
RFQCB	V_{Li1}	-1000 V
	V_{Li2}	-750 V
	V_{HT}	9920 V
	V_{Ls}	0 V
	p_{H2}	7.7×10^{-3} hPa
	V_{RF}	410 Vpp
	f_{RF}	1.88 MHz

$^{35}\mathbf{Ar}^{+}$

V1	1.8
V2	4.998
V3	4.949
Li1	-1 kV
Li2	-750 kV
F (RFQCB)	840 kHz
gaz (RFQCB)	10.0 cc/mn
V_{RF}	4.0 V
V_{HT}	10095 V
V_{PD1}	9175 V (200 ms)
V_{PD2}	818 V (718V in lens mode)
L_{Chien}	395 V

D1	9.99	R1	
D2		R2	14.24
D3	0	R3	30.65
D4	9.99	R4	28.87
D5	9.99	R5	2.33
D6	9.99	R6	28.78
D7	0.79	R7	0.15
D8	160	R8	8.38
D9		R9	1000
D10	0.15	R10	0.15
D11	0.15	R11	0.15
D12	0.15	R12	0.15
D13	0.15	R13	0.15

$^{19}\mathbf{Ne}^{2+}$

V1	1.499
V2	4.993
V3	4.949
L1	-1.107 kV
L2	-1.151 kV
L3	-1 kV (with PD1)
L4	110 V (with PD1)
F (RFQCB)	1254 kHz
gaz (RFQCB)	5.0 cc/mn
V_{RF}	4.2 V
V_{HT}	9858 V
V_{PD1}	8929 V (200 ms)
V_{PD2}	823.5 V (100V in lens mode)
L_{Chien}	400 V
p_{trap}	1.0×10^{-5} mbar

D1	9.99	R1	
D2		R2	10.24
D3	0	R3	21.96
D4	9.9792	R4	18.26
D5	9.98	R5	4.84
D6	9.98	R6	18.17
D7	0.79	R7	0.15
D8	160	R8	4.87
D9		R9	1000
D10	0.15	R10	0.15
D11	0.15	R11	0.15
D12	0.15	R12	0.15
D13	0.15	R13	0.15

5.2 Realistic fields – Field components

In section 3.2.2.1 we develop the method to integrate realistic fields in CLOUDA simulations. We only show equations for the potential, although in the simulation we require the field components in order to solve the Lorentz force. We give the needed expressions in this appendix [Quem14].

The electric field can be written as:

$$\mathbf{E}(\rho,\theta,\varphi) \;=\; -\nabla\Phi(\rho,\theta,\varphi)$$

For the spherical coordinates ρ, θ and φ.

$$\begin{aligned}
E_\rho(\rho,\theta,\varphi) &= \sum_{n=1}^{\infty}\left(\frac{\rho}{r_0}\right)^{n-1}\left[\mathcal{A}_{\ell 0}\,P_\ell^0 \;+\; \sum_{m=1}^{n} P_\ell^m\;\left(\mathcal{A}_{\ell m}\,\cos(m\varphi) \;-\; \mathcal{B}_{\ell m}\,\sin(m\varphi)\right)\right]\\
E_\theta(\rho,\theta,\varphi) &= \sum_{n=1}^{\infty}\left(\frac{\rho}{r_0}\right)^{n-1}\left[\mathcal{A}_{\ell 0}\,D_\ell^0 \;+\; \sum_{m=1}^{n} D_\ell^m\;\left(\mathcal{A}_{\ell m}\,\cos(m\varphi) \;-\; \mathcal{B}_{\ell m}\,\sin(m\varphi)\right)\right]\\
E_\varphi(\rho,\theta,\varphi) &= -\sum_{n=1}^{\infty}\left(\frac{\rho}{r_0}\right)^{n-1}\;\sum_{m=1}^{n} m\;L_\ell^m\;\left(\mathcal{A}_{\ell m}\,\sin(m\varphi) \;+\; \mathcal{B}_{\ell m}\,\cos(m\varphi)\right)
\end{aligned}$$

where:

$$\mathcal{A}|\mathcal{B}_{\ell m} \;=\; \frac{1}{r_0}\sqrt{\frac{2\ell\;+\;1}{4\pi}\frac{(\ell\;-\;m)!}{(\ell\;+\;m)!}}\;A|B_{\ell m}$$

The field components depend on the functions P, D and L which we detail here. The associated Legendre functions of 1st kind from recurrence relations can be written as:

$$\begin{aligned}
(\ell-m+1)P_{\ell+1}^m(\cos\theta) &= \cos\theta\,(2\ell+1)\,P_\ell^m(\cos\theta) \;-\; (\ell+m)\,P_{\ell-1}^m(\cos\theta)\\
P_m^m(\cos\theta) &= (-1)^m(2m-1)!\,\sin^{\frac{m}{2}}\theta\\
P_{m+1}^m(\cos\theta) &= \cos\theta\,(2m+1)\,P_m^m(\cos\theta)\\
P_0^0(\cos\theta) &= 1
\end{aligned}$$

and:

$$L_\ell^m(\cos\theta) = \begin{vmatrix} 0 & \text{if} \quad m=0\\ -\frac{1}{2m}\left[P_{\ell+1}^{m+1}(\cos\theta) \;+\; (\ell-m+1)(\ell-m+2)\,P_{\ell+1}^{m-1}(\cos\theta)\right] & \text{if} \quad m\neq 0\end{vmatrix}$$

$$D_\ell^m(\cos\theta) = \begin{vmatrix} 0 & \text{if} \quad \ell=0,\ m=0\\ P_\ell^1(\cos\theta) & \text{if} \quad \ell>0,\ m=0\\ (\ell-m+1)L_{\ell+1}^m(\cos\theta) \;-\; (\ell+1)\;\cos\theta\;L_\ell^m(\cos\theta) & \text{if} \quad m>0\end{vmatrix}$$

5.3 β decay generator full algorithm

We present the full algorithm that was used to generate the β decay sets as it was introduced in section 3.2.1. It is based on a rejection method embedding a Von Neumann alogrithm. A sample set containing 10^7 $^{35}Ar^+$ decay events is shown in fig. 5.5 and was computed with both the gamma de-excitation and the Fermi correction enabled.

A first initialization phase performs the following:

- Load nuclei (mass, Q-value)
- Load 'a' values to compute
- Set angular cut
- Set number of sets to accept
- Gamma de-excitation requested ? If yes, provide the decay scheme (gamma energies and branching ratios)
- Perform Fermi correction ? If yes, provide tabulated data

We will be describing the main loop that generates all sets using informal pseudo code:

```
for each value of 'a'
{
   while number of sets to accept is not fulfilled
   {
      // We start with the setting of the effective Q-value to use.
      // A possible gamma emission would reduce this quantity.

      if(do not perform gamma de-excitation)
      {
         Q_betaDecay = Q
      }
      else if(last decay was not achieved) [Von Neumann algorithm]
      {
         Q_betaDecay =
            Q - E_gamma_that_has_been_selected_previously_and_must_done
            (possibly 0, in any case do not re-roll a new decay)
      }
      else
      {
           Roll a new decay:
           - Set E_gamma according to branching ratios
              (possibly 0) and compute Q_value
           - Flag this decay as "to be achieved" [Von Neumann algorithm]
      }

      // Now that the Q-value is set, we want to distribute it
      // between the decay products. "K" means "kinetic energy".

      Compute K_RI_max according to the Q-value (K_RI_min is 0)

      Randomize K_RI in [0;K_RI_max]

      Compute K_beta_min_acceptable and K_beta_max_acceptable
         as a function of randomized K_RI

      Compute K_beta_max according to the Q-value (K_beta_min is 0)
```

```
        Randomize K_beta in [0; K_beta_max]

40      if(K_beta is not in [K_beta_min_acceptable; K_beta_max_acceptable])
        {
           Reject event and start over [Rejection method]
        }
        else: go on
45
        // Now that we have the kinematics of the decay products,
        // we need to add the effect of 'a'

        Compute the probability 'p' for this event according to the current 'a'
50         value (see section on "correlation parameters" in Chap. 1 for details
           on the dependence of the kinematic distribution on 'a'). If the Fermi
           correction is enabled, take it into account for the computation of 'p'.

        Roll a dice on 'p'
55
        if(roll is a failure)
        {
           Reject event and start over [Rejection method]
        }
60      else: go on


        // The test for 'a' has been passed. Now, we check the angular cut imposed
        // on the decay product directions. This is useful to avoid the inclusion
65      // of an important number of events that won't reach the detectors in the
        // tracking phase due to the geometrical efficiency.

        Set event randomly in laboratory frame (set x,y,z coordinates of each
           momentum vector)
70
        if(event is not compatible with requested angular cut)
        {
           Reject event and start over [Rejection method]
        }
75      else: go on

        Check that energy and momentum is conserved (with the neutrino and
           the eventual gamma)

80      Accept event and save it

        Consider decay achieved (for the initial Q value ifs)
           [Von Neumann algorithm]

85    } end while number of sets to accept is not fulfilled
   } end for each value of 'a'
```

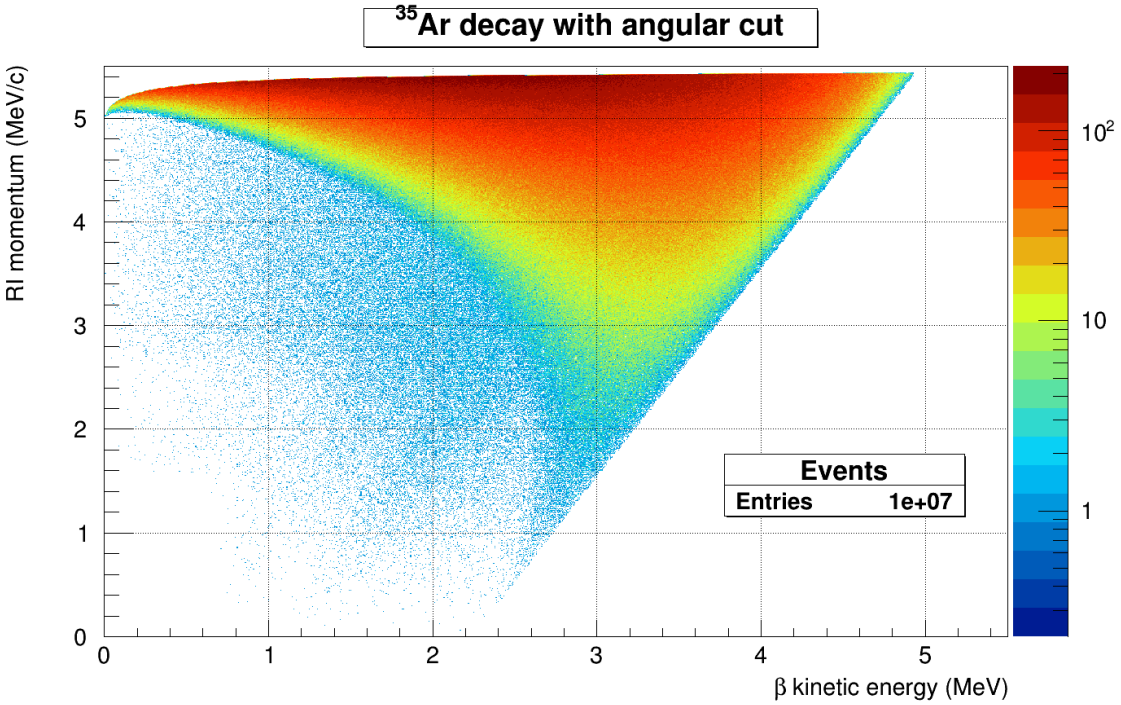

Figure 5.5: β decay generator kinematic sample. The recoil ion momentum is randomized first, imposing boundaries on the possible β kinetic energy which is set second.

Bibliography

[Aad12] G. Aad et al. "Observation of a new particle in the search for the Standard Model Higgs boson with the {ATLAS} detector at the {LHC}". In: *Phys. Lett. B* 716.1 (2012), pp. 1–29. DOI: http://dx.doi.org/10.1016/j.physletb.2012.08.020.

[Abea95] F. Abe et al. "Observation of Top Quark Production in $\overline{p}p$ Collisions with the Collider Detector at Fermilab". In: *Phys. Rev. Lett.* 74.14 (1995), pp. 2626–2631.

[Adel99] E.G. Adelberger et al. "Positron-Neutrino Correlation in the $0^+ \to 0^+$ Decay of ^{32}Ar". In: *Phys. Rev. Lett.* 83.3101 (1999).

[Agea03] S. Agostinelli et al. "Geant4 - a simulation toolkit". In: *Nucl. Instr. Meth. Phys. Res. A* 506 (2003), pp. 250–303.

[Ahma01] Q. R. Ahmad et al. "Measurement of the Rate of $\nu_e + d \to p + p + e^-$ Interactions Produced by ^8B Solar Neutrinos at the Sudbury Neutrino Observatory". In: *Phys. Rev. Lett.* 87.071301 (2001).

[Amal84] E. Amaldi. "From the discovery of the neutron to the discovery of nuclear fission". In: *Physics Reports* 111.1–4 (1984), pp. 1–331. DOI: http://dx.doi.org/10.1016/0370-1573(84)90214-X. URL: http://www.sciencedirect.com/science/article/pii/037015738490214X.

[Ande33] C.D. Anderson. "The Positive Electron". In: *Phys. Rev.* 43 (1933).

[Aube74] J. J. Aubert et al. "Experimental Observation of a Heavy Particle J". In: *Phys. Rev. Lett.* 33 (Dec. 1974).

[Auer09] N. Auerbach. "Coulomb corrections to superallowed β decay in nuclei". In: *Phys. Rev. C* 79.035502 (2009).

[Augu74] J. -E. Augustin et al. "Discovery of a Narrow Resonance in e^+e^- Annihilation". In: *Phys. Rev. Lett.* 33 (1974).

[Aviv12] O Aviv et al. "Beta decay measurements from 6 He using an electrostatic ion beam trap". In: *Journal of Physics: Conference Series* 337.1 (2012).

[Bae14] S Baeßler et al. "New precision measurements of free neutron beta decay with cold neutrons". In: *J. Phys. G: Nucl. Part. Phys.* 41.114003 (2014).

[Ban04] G. Ban et al. "Transport and cooling of singly-charged noble gas ion beams". In: *Nucl. Instr. Meth. Phys. Res. A* 518 (2004), pp. 712–720.

[Ban13] G. Ban et al. "Precision measurements in nuclear β-decay with LPCTrap". In: *Ann. Phys.* 525.8-9 (2013).

[Bec96a] H. Becquerel. "Emission of New Radiations by Metallic Uranium". In: *Compt. Ren.* 122.1086 (1896).

[Bec96b] H. Becquerel. "On the Invisible Radiations Emitted by Phosphorescent Substance". In: *Compt. Ren.* 122.501 (1896).

[Behr14] J.A. Behr. *β decay correlations with TRIUMF's neutral atom trap*. Solvay Workshop 2014. 2014.

[Beri12] J. Beringer (Particle Data Group) et al. "2013 Review of Particle Physics". In: *Phys. Rev. D* 86.010001 (2012 and 2013 partial update for the 2014 edition).

[BG14] J.A. Behr and A. Gorelov. "β-decay angular correlations with neutral atom traps". In: *J. Phys. G: Nucl. Part. Phys.* 41.114005 (2014).

[BG86] L.S. Brown and G. Gabrielse. "Geonium theory: Physics of a single electron or ion in a Penning trap". In: *Rev. Mod. Phys.* 58.1 (1986).

[BH86] J. Barnes and P. Hut. "A hierarchical O(N log N) force-calculation algorithm". In: *Nature* 324.4 (1986).

[BJ95] W.E. Burcham and M. Jobes. *Nuclear and Particle Physics*. Longman Scientific & Technical, 1995.

[Cabi63] N. Cabibbo. "Unitary Symmetry and Leptonic Decays". In: *Phys. Rev. Lett.* 10.12 (1963).

[CC15a] CEA/CNRS. *An introduction to the SPIRAL project by A. Villari*. 2015. URL: http://pro.ganil-spiral2.eu/laboratory/ganil-accelerators/spiral/introduction (visited on 04/05/2015).

[CC15b] CEA/CNRS. *The LIRAT low-energy beam facility at SPIRAL*. 2015. URL: http://pro.ganil-spiral2.eu/laboratory/experimental-areas/lirat (visited on 04/05/2015).

[Chat12] S. Chatrchyan et al. "Observation of a new boson at a mass of 125 GeV with the {CMS} experiment at the {LHC}". In: *Phys. Lett. B* 716.1 (2012), pp. 30–61. DOI: http://dx.doi.org/10.1016/j.physletb.2012.08.021.

[CJ14] J. Chadwick. "The Intensity Distribution in Magnetic Spectrum of β-Rays of Radium B + C". In: *Verhandl. Dtsch. phys. Ges* 16 (1914), p. 383.

[CJ32] J. Chadwick. "The Existence of a Neutron". In: *Royal Society of London Proceedings Series A* 136.830 (1932), pp. 692–708.

[CJH64] J. H. Christenson et al. "Evidence for the 2π Decay of the K_2^0 Meson". In: *Phys. Rev. Lett.* 13.4 (1964), pp. 138–140.

[CLB11] F.A. Cruz, S.K. Layton, and L.A. Barba. "How to obtain efficient GPU kernels: An illustration using FMM & FGT algorithms". In: *Comput. Phys. Commun.* 182 (2011), pp. 2084–2098.

[CNT68] T.A. Carlson, C.W. Nestor Jr., and T.C. Tucker. In: *Phys. Rev.* 169.27 (1968).

[CoMT15] MLLTRAP collaboration. *Penning traps*. URL: http://www.ha.physik.uni-muenchen.de/research/nuclear-science/nuclear-masses/mlltrap/layout/traps/index.html (visited on 09/02/2015).

[Cour12] C. Couratin et al. "First Measurement of Pure Electron Shakeoff in the β Decay of Trapped $^6He^+$ Ions". In: *Phys. Rev. Lett.* 108.243201 (2012).

[Cour13b] C. Couratin et al. "Electron shakeoff following the β^+ decay of trapped $^{35}Ar^+$ ions". In: *Phys. Rev. A* 88.041403 (2013).

[Cour13a] C. Couratin. "Mesures de précision avec LPCTrap et développements techniques à GANIL : corrélation angulaire bêta-neutrino ($a_{\beta\nu}$) et probabilité de shakeoff dans la décroissance de l'$^6He^+$, étude de la production de nouveaux faisceaux á SPIRAL." PhD thesis. Université de Caen Basse-Normandie, 2013.

[CPJ63] T.A. Carlson, F. Pleasonton, and C.H. Johnson. "Electron Shake Off following the β^- Decay of ^{6}He". In: *Phys. Rev.* 129.5 (1963).

[Dari04] G. Darius. "Etude et mise en oeuvre d'un dispositif pour la mesure du paramètre de corrélation angulaire dans la désintégration du noyau ^{6}He". PhD thesis. Université de Caen Basse-Normandie, 2004.

[Dehm89] H.G. Dehmelt. "Experiments with an isolated subatomic particles at rest". In: *Nobel lecture* (1989).

[Dela02] P. Delahaye. "Etudes et tests preliminaires a une mesure de la correlation angulaire $\beta - \nu$ dans la desintegration du noyau ^{6}He a l'aide d'un piege de Paul". PhD thesis. Université de Caen Basse-Normandie, 2002.

[Dhal13] A. Dhal et al. "Probing Fundamental Interactions By An Electrostatic Ion Beam Trap". In: *Acta. Phys. Pol. B* 44.3 (2013).

[Dira28] P.A.M. Dirac. "The Quantum Theory of the Electon". In: *Proc. Roy. Soc.* 117 (1928), pp. 610–624.

[Elli76] H.W. Ellis, R.Y. Pai, and E.W. McDaniel. "Transport Properties Of Gaseous Ions Over A Wide Energy Range". In: *Atomic Data and Nuclear Data Tables* 17 (1976), pp. 177–210.

[Fabi14] X. Fabian et al. "Precise measurement of the angular correlation parameter $a_{\beta\nu}$ in the β decay of ^{35}Ar with LPCTrap". In: *EPJ Web of Conferences* 66 (2014), p. 08002.

[Fabi15] X. Fabian et al. "Using GPU parallelization to perform realistic simulations of the LPCTrap experiments". In: *Hyperfine Interactions* (2015). ISSN: 0304-3843.

[Fein41] E.L. Feinberg. In: *Sov. Phys. JETP* 4.423 (1941).

[Ferm34] E. Fermi. "Versuch einer Theorie der β-Strahlen". In: *Z. Phys.* 88 (1934), pp. 191–171.

[FGM58] R.P. Feynman and M. Gell-Mann. "Theory of the Fermi Interaction". In: *Phys. Rev.* 109.1 (1958).

[Flec08] X. Fléchard et al. "Paul Trapping of Radioactive $^6He^+$ Ions and Direct Observation of Their β Decay". In: *Phys. Rev. Lett.* 101 (2008).

[Flec11a] X. Fléchard et al. "Measurement of the $\beta - \nu$ correlation coefficient $a_{\beta\nu}$ in the β decay of trapped $^6He^+$ ions". In: *J. Phys. G: Nucl. Part. Phys.* 38 (2011).

[Flec11b] X. Fléchard et al. "Temperature measurement of $^6He^+$ ions confined in a transparent Paul trap". In: *Hyperfine Interactions* 199 (2011).

[FN65] The Nobel Foundation. *The Nobel Prize in Physics 1965*. 2015. URL: http://www.nobelprize.org/nobel_prizes/physics/laureates/1965/ (visited on 04/02/2015).

[Fuku98] Y. Fukuda et al. "Evidence for Oscillation of Atmospheric Neutrinos". In: *Phys. Rev. Lett.* 81.8 (1998), pp. 1562–1567.

[GGS58] M. Goldhaber, L. Grodzins, and A.W. Sunyar. "Helicity of Neutrinos". In: *Phys. Rev.* 109.1015 (1958).

[GIM70] S. L. Glashow, J. Iliopoulos, and L. Maiani. "Weak Interactions with Lepton-Hadron Symmetry". In: *Phys. Rev. D* 2.7 (1970), pp. 1285–1292.

[Glas61] S.L. Glashow. "Partial-symmetries of weak interactions". In: *Nuclear Physics* 22.4 (1961), pp. 579–588.

[Gluc97] F. Glück. "Order-α radiative correction calculations for unoriented allowed nuclear, neutron and pion β decays". In: *Comp. Phys. Comm.* 101 (1997), pp. 493–502.

[Gluc98] F. Glück. "Order-α radiative correction to ^{6}He and ^{32}Ar β decay recoil spectra". In: *Nucl. Phys. A* 628 (1998), pp. 493–502.

[GGMa07] M.C. Gonzalez-Garcia and M. Maltoni. "Phenomenology with massive neutrinos". In: *Physics Reports* 460 (2007), pp. 1–129.

[GM01] W. Greiner and B. Müller. *Gauge Theory of Weak Interactions*. Springer-Verlag, 1996.

[GA14] M. Gonzalez-Alonso. *Nuclear β decay and LHC: an Effective Field Theory approach*. Solvay Workshop 2014. 2014.

[GMAA05] A. Gorelov et al. "Scalar Interaction Limits from the β-ν Correlation of Trapped Radioactive Atoms". In: *Phys. Rev. Lett.* 94 (2005), p. 142501.

[GR87] L. Greengard and V. Rokhlin. "A Fast Algorithm for Particle Simulations". In: *J. Comput. Phys.* 73 (1987), pp. 325–348.

[Heis32] W. Heisenberg. "On the Structure of Atomic Nuclei. I." In: *Z. Phys.* 77 (1932).

[Herb77] S. W. Herb et al. "Observation of a Dimuon Resonance at 9.5 GeV in 400-GeV Proton-Nucleus Collisions". In: *Phys. Rev. Lett.* 39.5 (1977), pp. 252–255.

[HG01] E.M. Henley and A. García. *Subatomic physics*. 3rd ed. World Scientific Publishing Co. Pte. Ltd., 2007.

[HI07] T. Hamada and T. Iitaka. "The Chamomile Scheme: An Optimized Algorithm for N-body simulations on Programmable Graphics Processing Units". In: *arXiv* (2007).

[Hols14] B.R. Holstein. "Precision Frontier in semileptonic weak interactions: theory". In: *J. Phys. G: Nucl. Part. Phys.* 41.114001 (2014).

[HT14] J.C. Hardy and I.S. Towner. "The measurement and interpretation of superallowed 0+ → 0+ nuclear β decay". In: *J. Phys. G: Nucl. Part. Phys.* 41.114004 (2014).

[HT15] J. C. Hardy and I. S. Towner. "Superallowed $0^+ \to 0^+$ nuclear β decays: 2014 critical survey, with precise results for V_{ud} and CKM unitarity". In: *Phys. Rev. C* 91.025501 (2015).

[JPC63] C. H. Johnson, Frances Pleasonton, and T. A. Carlson. "Precision Measurement of the Recoil Energy Spectrum from the Decay of He^6". In: *Phys. Rev.* 132 (3 1963), pp. 1149–1165.

[JTW57b] J.D. Jackson, S.B. Treiman, and H.W. Wyld Jr. "Coulomb corrections in allowed beta transitions". In: *Nucl. Phys.* 4 (1957), pp. 206–212.

[JTW57a] J.D. Jackson, S.B. Treiman, and H.W. Wyld Jr. "Possible Tests of Time Reversal Invariance in Beta Decay". In: *Phys. Rev.* 106.3 (1957).

[KM73] M. Kobayashi and T. Maskawa. "CP-Violation in the Renormalizable Theory of Weak Interaction". In: *Prog. Theor. Phys.* 49.2 (1973), pp. 652–657.

[Lere15] A. Leredde. *Mesure de precision du parameter de corrélation angulaire dans la décroissance d^6He piégés par laser*. LPC Caen Seminar. 2015.

[Levi53] J.S. Levinger. In: *Phys. Rev.* 90.11 (1953).

[Li13] G. Li et al. "Tensor Interaction Limit Derived From the $\alpha - \beta - \bar{\nu}$ Correlation in Trapped ^{8}Li Ions". In: *Phys. Rev. Lett.* 110.092502 (2013).

[LiHB05] E. Liénard et al. "Performance of a micro-channel plates position sensitive detector". In: *Nucl. Instr. Meth. Phys. Res. A* 551.2–3 (2005), pp. 375–386.

[LiHI15] E. Liénard et al. "Precision measurements with LPCTrap at GANIL". In: *Hyperfine Interactions* (2015). DOI: 10.1007/s10751-015-1198-9.

[LiUH10] E. Liénard. Habilitation a diriger des recherches. Universite de Caen Basse-Normandie. 2010.

[Lind04] M. Lindroos. *Review of the ISOL Method*. Tech. rep. CERN-AB-2004-086. revised version submitted on 2004-09-28 17:19:32. Geneva: CERN, 2004. URL: http://cds.cern.ch/record/793447.

[LVGM10] Haozhao Liang, Nguyen Van Giai, and Jie Meng. "Isospin symmetry-breaking corrections for superallowed β decay in relativistic RPA approaches". In: *Journal of Physics: Conference Series* 205.012028 (2010).

[LY56] T.D. Lee and C.N. Yang. "Question of Parity Conservation in Weak Interactions". In: *Phys.Rev.* 104.254 (1956).

[Mant09] M. Mantina et al. "Consistent van der Waals Radii for the Whole Main Group". In: *J. Phys. Chem. A* 113.19 (2009), pp. 5806–5812.

[Manu07] D. Manura. *Additional Notes on the SIMION HS1 Collision Model*. Scientific Instrument Services. 2007.

[Math68] E. Mathieu. "Mémoire sur le mouvement vibratoire d'une membrane de forme elliptique." In: *J. Math. Pures Appl.* (1868), pp. 137–203.

[Maug14] F. Mauger. "The Bayeux library and the SuperNEMO software". GDR Neutrino Meeting, Orsay, June 18, 2014. 2014.

[Mehl13] M. Mehlman et al. "Design of a unique open-geometry cylindrical Penning trap". In: *Nucl. Instr. Meth. Phys. Res. A* 712 (2013).

[Mehl15] M. Mehlman et al. "Status of the TAMUTRAP facility and initial characterization of the RFQ cooler/buncher". In: *Hyperfine Interactions* (2015), pp. 1–10. DOI: 10.1007/s10751-015-1187-z.

[Melc14] D. Melconian. *β-decay Correlations Measurements using Ion and Laser Traps*. Solvay Workshop 2014. 2014.

[Mend13] M.P. Mendenhall et al. "Precision measurement of the neutron β-decay asymmetry". In: *Phys. Rev. C* 87.032501 (2013).

[M07] A. Méry et al. "Search for tensor couplings in the weak interaction". In: *Eur. Phys. J. Special Topics* 150.1 (2007). DOI: 10.1140/epjst/e2007-00354-9.

[MA07] A. Méry. "Mesure du coefficient de corrélation angulaire $\beta - \nu$ dans la décroissance de ^{6}He à l'aide d'un piége de Paul". PhD thesis. Université de Caen Basse-Normandie, 2007.

[Migd41] A.B. Migdal. "Ionization of atoms accompanying α and β-decay". In: *Zh. Eksp. Teor. Fiz.* 207.11 (1941).

[MS06] W.J. Marciano and A. Sirlin. "Improved Calculation of Electroweak Radiative Corrections and the Value of V_{ud}". In: *Phys. Rev. Lett.* 96.032002 (2006).

[Mull14] P. Müller. *Lil'a with laser trapped ^{6}He.* Solvay Workshop 2014. 2014.

[Mund13] D. Mund et al. "Determination of the Weak Axial Vector Coupling λ=g_A/g_V from a Measurement of the β-Asymmetry Parameter A in Neutron Beta Decay". In: *Phys. Rev. Lett.* 110.172502 (2013).

[NA37] Seth H. Neddermeyer and Carl D. Anderson. "Note on the Nature of Cosmic-Ray Particles". In: *Phys. Rev.* 51.10 (1937), pp. 884–886.

[NCGA13] O. Naviliat-Cuncic and M. Gonzalez-Alonso. "Prospects for precision measurements in nuclear β decay in the LHC era". In: *Annalen der Physik* 525.8-9 (2013), pp. 600–619. DOI: 10.1002/andp.201300072. URL: http://dx.doi.org/10.1002/andp.201300072.

[Nyla07] L. Nyland, M. Harris, and J. Prins. *GPU Gems 3.* Addison-Wesley Professional, 2007, pp. 677–695.

[NS09] O. Naviliat-Cuncic and N. Severijns. "Test of the Conserved Vector Current Hypothesis in $T = 1/2$ Mirror Transitions and New Determination of $|V_{ud}|$". In: *Phys. Rev. Lett.* 102.142302 (2009).

[O14] K.A. Olive et al. "Review of Particle Physics". In: *Chin. Phys. C* 38.090001 (2014).

[Paul30] W. Pauli. *Open letter to the group of radioactive people at the Gauverein meeting in Tübingen.* Open Letter. 1930.

[Paul90] W. Paul. "Electromagnetic traps for charged and neutral particles". In: *Rev. Mod. Phys.* 62.3 (1990), pp. 531–540.

[Perl75] M. L. Perl et al. "Evidence for Anomalous Lepton Production in $e^+ - e^-$ Annihilation". In: *Phys. Rev. Lett.* 35.22 (1975), pp. 1489–1492.

[Poca14] D. Pocanic et al. "Experimental study of rare charged pion decays". In: *J. Phys. G: Nucl. Part. Phys.* 41.114002 (2014).

[Pons15] B. Pons. *Private communication.* 2015.

[Poro15] T. Porobić et al. "Space-charge effects in Penning ion traps". In: *Nucl. Instr. Meth. Phys. Res. A* 785 (2015), pp. 153–162. DOI: http://dx.doi.org/10.1016/j.nima.2015.02.057. URL: http://www.sciencedirect.com/science/article/pii/S0168900215002673.

[Pres07] William H. Press et al. *Numerical Recipes 3rd Edition: The Art of Scientific Computing.* 3rd ed. New York, NY, USA: Cambridge University Press, 2007. ISBN: 0521880688, 9780521880688.

[Quem14] G. Quéméner. "Private communication." 2014.

[ReCo53] F. Reines and C.L. Cowan Jr. "Detection of the Free Neutrino". In: *Phys. Rev.* 92.3 (1953).

[Robe15] H. Robertson et al. *CENPA Annual Report.* http://www.npl.washington.edu/webfm_send/1247. Seattle, University of Washington. 2015.

[Rodr06] D. Rodríguez et al. "The LPCTrap facility: A novel transparent Paul trap for high-precision experiments". In: *Nucl. Instr. Meth. Phys. Res. A* 565 (2006), pp. 876–889.

[Ron14] G. Ron. *Measuring $a_{\beta\nu}$ in ^{6}He using an Electrostatic Ion Trap.* Solvay Workshop 2014. 2014.

[Rist12] Z. Ristivojevic and Z.L. Petrović. "A Monte Carlo simulation of ion transport at finite temperatures". In: *Plasma Sources Sci. Technol.* 21.035001 (2012).

[Ruth99] E. Rutherford. "Uranium Radiation and the Electrical conduction Produced by it". In: *Philos. Mag.* 47.109 (1899).

[SBNC06] N. Severijns, M. Beck, and O. Naviliat-Cuncic. "Tests of the standard electroweak model in nuclear beta decay". In: *Rev. Mod. Phys.* (2006).

[Scha13] N. Schaeffer. "Efficient spherical harmonic transforms aimed at pseudospectral numerical simulations". In: *Geochemistry, Geophysics, Geosystems* 14.3 (2013), pp. 751–758. ISSN: 1525-2027. DOI: 10.1002/ggge.20071.

[Scie03] N.D. Scielzo et al. "Recoil-ion charge-state distribution following the β^+ decay of ^{21}Na". In: *Phys. Rev. A* 68.022716 (2003).

[Scie04] N. D. Scielzo et al. "Measurement of the $\beta-\nu$ Correlation using Magneto-optically Trapped ^{21}Na". In: *Phys. Rev. Lett.* 93.102501 (2004).

[Scie14] N. Scielzo. *Beta-decay correlations in $^{8}Li/^{8}B$.* Solvay Workshop 2014. 2014.

[Seve08] N. Severijns et al. "$\mathcal{F}t$ values of the $T = 1/2$ mirror β transitions". In: *Phys. Rev. C* 78.055501 (2008).

[Sev14a] N. Severijns. "Correlation and spectrum shape measurements in β-decay probing the standard model". In: *J.Phys. G : Nucl. Part116. Phys.* 41.114006 (2014).

[Sev14b] N. Severijns. "Correlation and spectrum shape measurements in β-decay probing the standard model". In: *J. Phys. G: Nucl. Part. Phys.* 41.114006 (2014).

[SM58] E.C.G. Sudarshan and R.E. Marshak. "Chirality Invariance and the Universal Fermi Interaction". In: *Phys. Rev.* 109.5 (1958).

[SNC11] Nathal Severijns and Oscar Naviliat-Cuncic. "Symmetry tests in nuclear beta decay". In: *Annual Review of Nuclear and Particle Science* 61 (2011), pp. 23–46.

[Ster15] M. G. Sternberg et al. "Limit on Tensor Currents from ^{8}Li β Decay". In: *Phys. Rev. Lett.* 115.182501 (2015).

[Ster13] M.G. Sternberg. PhD thesis. University of Chicago, 2013.

[TH08] I. S. Towner and J. C. Hardy. "Improved calculation of the isospin-symmetry-breaking corrections to superallowed Fermi β decay". In: *Phys. Rev. C* 77 (2 Feb. 2008), p. 025501. DOI: 10.1103/PhysRevC.77.025501. URL: http://link.aps.org/doi/10.1103/PhysRevC.77.025501.

[Thom97] J.J. Thomson. "Cathode Rays". In: *Philos. Mag.* 44.293 (1897).

[VG11] S. Van Gorp et al. "Simbuca, using a graphics card to simulate Coulomb interactions in a penning trap". In: *Nucl. Instr. Meth. Phys. Res. A* 638 (2011), pp. 192–200.

[VG12] S. Van Gorp. "Search for physics beyond the standard electroweak model with the WITCH experiment". PhD thesis. KU Leuven, 2012.

[Velt11] Ph. Velten. "Mesure du paramètre de corrélation angulaire bêta-neutrino dans la décroissance de l'^{6}He." PhD thesis. Université de Caen Basse-Normandie, 2011.

[Vett08] P. A. Vetter et al. "Measurement of the β-ν correlation of ^{21}Na using shakeoff electrons". In: *Phys. Rev. C* 77.035502 (2008).

[Vieh95] L.A. Viehland. "Transport Properties Of Gaseous Ions Over A Wide Energy Range, IV". In: *Atomic Data and Nuclear Data Tables* 60 (1995), pp. 37–95.

[Wils68] F.L. Wilson. "Fermi's Theory of Beta Decay". In: *Am. J. Phys.* 36.12 (1968), p. 1150.

[WSL59] R.F. Wuerker, H. Shelton, and R.V. Langmuir. "Electrodynamic Containment of Charged Particles". In: *J. Appl. Phys.* 30.3 (1959).

[Wu57] C. S. Wu et al. "Experimental Test of Parity Conservation in Beta Decay". In: *Phys. Rev.* 105 (1957), pp. 1413–1415.

[WV96] L. Wauters and N. Vaeck. "Study of the electronic rearrangement induced by nuclear transmutations: A B-spline approach applied to the β decay of ^{6}He". In: *Phys. Rev. C* 53.497 (1996).

[YBKB11] R. Yokota et al. "Biomolecular electrostatics using a fast multipole {BEM} on up to 512 gpus and a billion unknowns". In: *Comput. Phys. Commun* 182.6 (2011), pp. 1272–1283.

[YCFG14] A.R. Young et al. "Beta decay measurements with ultracold neutrons: a review of recent measurements and the research program at Los Alamos National Laboratory". In: *J. Phys. G: Nucl. Part. Phys.* 41.114007 (2014).

[Youn13] P. Young. *The leapfrog method and other symplectic algorithms for integrating Newton's laws of motion.* 2013. URL: http://physics.ucsc.edu/~peter/242/leapfrog.pdf (visited on 08/09/2015).

[Zwei64] G. Zweig. *An SU3 Model For Strong Interaction Symmetry And Its Breaking.* online. CERN, Geneva. Jan. 1964.

Mesures de précisions dans le contexte de l'interaction faible: développement de simulations réalistes pour le dispositif LPCTrap installé au GANIL.

Résumé
Cette thèse s'inscrit dans l'effort déployé pour mesurer le paramètre de corrélation angulaire bêta-neutrino $a_{\beta\nu}$ dans trois décroissances bêta nucléaires ($^{6}He^{+}$, $^{35}Ar^{+}$et $^{19}Ne^{+}$). La structure V-A de l'interaction faible prévoit que $a_{\beta\nu}$ = +1 pour les transitions de Fermi pures et $a_{\beta\nu}$ = -1/3 pour les transitions de Gamow-Teller pure. Une mesure fine de ce paramètre pour tester un écart à ces valeurs peut révéler l'existence de courants exotiques. Par ailleurs, la mesure de ce paramètre dans le cas de transitions mirroirs permet d'extraire le premier élément de la matrice de Cabibbo-Kobayashi-Maskawa (CKM), V_{ud}. Le dispositif LPCTrap, installé au GANIL, est conçu pour préparer un faisceau continu d'ions à l'injection dans un piège de Paul dédié. Ce dernier permet de disposer d'une source quasi-ponctuelle à partir de laquelle les produits de désintégrations sont détectés en coïncidences. C'est par l'étude de la distribution du temps de vol des ions de recul que sont extraits la valeur de $a_{\beta\nu}$ et, depuis 2010, les probabilités de Shake-Off (SO) associées. Cette étude nécessite la simulation complète des expériences LPCTrap. La majeure partie du présent travail est dédiée à de telles simulations, en particulier à la modélisation de la dynamique du nuage d'ions piégés. Le programme Clouda, qui profite des unités de calcul graphique (GPU), a été développé dans cette optique et sa caractérisation complète est présentée ici. Trois aspects importants sont abordés: le champ de piégeage électro-magnétique, les collisions réalistes entre les ions et les atomes de gaz tampon et l'effet de la charge d'espace. La présente étude démontre l'importance de ces simulations pour accroître le contrôle des erreurs systématiques sur $a_{\beta\nu}$.

Mots clés : Interactions faibles, désintégration bêta, Corrélations angulaires (Physique nucléaire), Simulations par ordinateur, CUDA (Informatique), Interactions ion-atome, Charge d'espace, Synthèse harmonique

Precision measurements in the weak interaction framework: development of realistic simulations for the LPCTrap device installed at GANIL.

Abstract
This work belongs to the effort presently deployed to measure the angular correlation parameter $a_{\beta\nu}$ in three nuclear beta decays ($^{6}He^{+}$, $^{35}Ar^{+}$et $^{19}Ne^{+}$). The V-A structure of the weak interaction implies that $a_{\beta\nu}$ = +1 for a pure Fermi transition and $a_{\beta\nu}$ = -1/3 for a pure Gamow-Teller transition. A thorough measurement of this parameter to check any deviation from these values may lead to the discovery of possible exotic currents. Furthermore, the measurement of $a_{\beta\nu}$ in mirror transitions allows the extraction of V_{ud}, the first element of the Cabibbo-Kobayashi-Maskawa (CKM) matrix. The LPCTrap apparatus, installed at GANIL, is designed to ready a continuous ion beam for injection in a dedicated Paul trap. This latter device allows to have a quasi-ponctual source from which the decay products are detected in coincidence. It is from the study of the recoil ion time-of-flight (TOF) distribution that $a_{\beta\nu}$ is withdrawn and, since 2010, the associated Shake-Off (SO) probabilities. This study requires the complete simulation of the LPCTrap experiments. The major part of this work is dedicated to such simulations, especially to the modeling of the trapped ion cloud dynamic. The Clouda program, which takes advantage of graphics processing unit (GPU), was developed in this context and its full characterization is presented here. Three important aspects are addressed: the electromagnetic trapping field, the realistic collisions between the ions and the buffer gas atoms and the space charge effect. The present work shows the importance of these simulations to increase the control of the systematic errors on $a_{\beta\nu}$.

Keywords: Weak interactions (Nuclear physics), Beta decay, Angular correlations (Nuclear physics), Computer simulation, Ion-atom collisions, Space charge, Harmonic synthesis

Discipline : Physique (Constituants élémentaires et physique théorique)

Laboratoire de Physique Corpusculaire – U.M.R. 6534
ENSICAEN – 6, boulevard Maréchal Juin 14050 Caen Cedex – France